NASA Contractor Report 185118

The Measurement of Boundary Layers on a Compressor Blade in Cascade

Volume I—Experimental Technique, Analysis, and Results

William C. Zierke and Steven Deutsch

Pennsylvania State University
State College, Pennsylvania

July 1989

Prepared for
Lewis Research Center
Under Grant NSG-3264

National Aeronautics and
Space Administration

Foreword

We would like to extend our appreciation to NASA Lewis for supporting this study (NASA Grant NSG-3624) and to the NASA Lewis personnel for their advice and patience. A special thanks goes to Mr. Nelson Sanger who acted as the grant manager. Nels gave us some valuable advice and showed abundant patience. Mr. Don Boldman also gave some valuable suggestions.

As the heads of the Garfield Thomas Water Tunnel during this study, Professor Blaine R. Parkin and Professor Robert E. Henderson gave valuable support. Many of the other engineers and technicians at the Applied Research Laboratory supported us and helped with the experimental setup. None of this experiment could have been accomplished without the many students who helped with the data acquisition and reduction. Fred Williams, Charlie Allen, Russ Taylor, Rob Synestvedt, Lisa (Shellenberger) Meyer, Ron Merski, and Bruce Kelly all spent many hours on what sometimes seemed to be a never-ending project.

Table of Contents

Nomenclature

A^+	dimensionless effective sublayer thickness in the inner boundary layer
A^+_{eq}	equilibrium value of A^+
A_{film}	surface area of the hot film
AR	aspect ratio
B	integral layer thickness in the Perry and Schofield [1973] theory
c	blade chord length
c_1	empirical constant in the hot-film equation for surface shear stress
c_2	empirical constant in the hot-film equation for surface shear stress
C	law of the wall constant (=5.0)
C_{ab}	correlation coefficient of signals at locations a and b
C_f	skin friction coefficient $= \frac{\tau_w}{\frac{1}{2}\rho U_e^2}$
C_L	lift coefficient $= \frac{\text{lift per unit span}}{\frac{1}{2}\rho V_1^2 c}$
CL	wake centerline
C_p	static-pressure coefficient $= \frac{p - p_1}{\frac{1}{2}\rho V_1^2}$
dB	decibel
D	diffusion factor

E	error between the data and the wall-wake equation
$\mathcal{E}$	voltage across the hot film
f	similarity function;
	characteristic frequency
f_D	Doppler frequency
f_S	frequency shift
F	streamwise pressure gradient function of Abu-Ghannam and Shaw [1980]
FFT	fast Fourier transform
G	Clauser's shape factor
h	convective heat transfer coefficient;
	characteristic height of a roughness element, a downstream-facing step,
	or a separation "bubble"
H_{12}	first shape factor = $\frac{\delta^*}{\theta}$
H_{32}	second shape factor = $\frac{\delta_3}{\theta}$
i	incidence angle = $\beta_1 - \kappa_1$
$\mathcal{I}$	electrical current
k	thermal conductivity
K	kurtosis or flatness
ℓ	turbulence "mixing length"
ℓ_{film}	length of a hot film in the streamwise direction
ℓ_{ref}	reference length
L	distance from the blade surface to the location of $\tau_{\max}$
L.E.	blade leading edge
L_p, L_s	pressure and suction surface length scales from the point of minimum
	velocity to the point where the velocity defect is $\frac{1}{2}(U_e - u_{cl})$
LDV	laser Doppler velocimeter
M	Mach number

n	data point index
N	number of samples;
	number of data points
N_{inv}	number of data points in the inviscid region
N_{max}	maximum number of data points that could possible be in the inviscid region
Nu	Nusselt number = $\frac{h\ell_{\text{film}}}{k}$
p	static pressure
p_e	static pressure at the boundary layer or wake edge
p_T	total or stagnation pressure
P	pressure surface
Q	heat flux
r	radius
R_c	radius of curvature
Re	Reynolds number
Re_c	blade chord Reynolds number = $\frac{cV_1}{\nu}$
$Re_{x,s}$	local Reynolds number for the onset of transition
Re_θ	momentum thickness Reynolds number = $\frac{\theta U_e}{\nu}$
$Re_{\theta,e}$	momentum thickness Reynolds number for the completion of transition
$Re_{\theta,s}$	momentum thickness Reynolds number for the onset of transition
$\mathcal{R}_{\text{film}}$	electrical resistance of the hot film
s	blade spacing
s_u	standard deviation of the sample of the u data
S	skewness;
	suction surface
St	Strouhal number
STAN5	parabolic boundary layer code of Crawford and Kays [1976]

$t_{0.975}$ Student's t score representing all but 2.5% of one tail of the Student's t distribution for a given degree of freedom

t_{max} maximum blade thickness

T_e temperature at the boundary layer edge

T.E. blade trailing edge

T_{film} temperature of the hot film

u streamwise velocity

u^+ dimensionless velocity in the inner boundary layer $= \frac{u}{u_\tau}$

u_τ shear or friction velocity $= \sqrt{\frac{\tau_w}{\rho}}$

U_{BF} maximum backflow velocity

U_e velocity at the boundary layer or wake edge

U_{e_s} velocity at the boundary layer edge near detachment

U_m velocity scale based on the maximum shear stress $= \sqrt{\frac{\tau_{max}}{\rho}}$

U_{ref} reference velocity

U_s velocity scale for the Perry and Schofield [1973] defect law

v normal velocity

V velocity

W wake

$W(\ )$ Coles' universal wake function

x streamwise coordinate;

blade coordinate (see appendix A)

x^+ dimensionless streamwise coordinate in the inner boundary layer $= \frac{x u_\tau}{\nu}$

x_{sb} streamwise length of the separation "bubble"

y coordinate normal to the blade surface or across the wake;

blade coordinate (see appendix A)

y^+ dimensionless coordinate normal to the blade surface in the inner boundary layer $= \frac{y u_\tau}{\nu}$

β flow angle measured from the axial direction;
Falkner-Skan streamwise pressure gradient parameter

β_c Clauser's equilibrium parameter

γ stagger angle

δ boundary layer thickness (where $u = 0.99 U_e$)

δ^* displacement thickness $= \int_0^\infty \left(1 - \frac{u}{U_e}\right) dy$

δ_s^* displacement thickness near detachment

δ_3 energy thickness $= \int_0^\infty \frac{u}{U_e} \left[1 - \left(\frac{u}{U_e}\right)^2\right] dy$

δ_{BF} depth of backflow

δ_d deviation angle $= \beta_2 - \kappa_2$

Δ defect thickness

ϵ fluid turning or deflection angle $= \beta_1 - \beta_2$

η dimensionless streamwise similarity variable;
normalized distance across the wake

θ momentum thickness $= \int_0^\infty \frac{u}{U_e} \left(1 - \frac{u}{U_e}\right) dy$

κ blade metal angle;
lens half angle;
von Karman's mixing length parameter (=0.41)

λ wavelength of the incident laser beams;
length scale in the outer region of a turbulent boundary layer
(in the "mixing length" model)

λ_θ streamwise pressure gradient parameter $= \frac{\theta^2}{\nu} \frac{dU_e}{dx}$

ν kinematic viscosity (0.150 cm^2/sec for air)

ν_t apparent scaler turbulent or "eddy" kinematic viscosity

ξ dimensionless similarity variable normal to the blade surface

Π	Coles' wake parameter
ρ	fluid density (1.205 kg/m^3 for air)
σ	blade solidity $= \frac{c}{s}$
τ_{max}	maximum shear stress
τ_w	wall or surface shear stress
ϕ	camber angle $= \kappa_1 - \kappa_2$
ψ	streamfunction
ω	total-pressure loss coefficient $= \frac{p_{T_1} - p_{T_2}}{\frac{1}{2}\rho V_1^2}$

Subscripts

a	location a
b	location b
c	camber line
cl	at the wake centerline
e	boundary layer or wake edge
inv	inviscid
LE	blade leading edge
m	mean flow
meas	measured
n	data point index
p	pressure surface
s	suction surface
TE	blade trailing edge
x	axial direction
θ	tangential direction
wall	at the wall

ξ	derivative with respect to ξ
0	no flow
1	inlet
2	outlet

Superscripts

	fluctuating quantity;
	derivative with respect to η
—	average over the blade passage;
	time average

Summary

Measurements have been made of the boundary layers and wakes about a highly loaded, double-circular-arc compressor blade in cascade. These laser Doppler velocimetry measurements have yielded a very detailed and precise data base with which to test the application of viscous computational codes to turbomachinery. In order to test the computational codes at off-design conditions, the data have been acquired at a chord Reynolds number of 500,000 and at three incidence angles. Moreover, these measurements have supplied some physical insight into these very complex flows. Although some "natural" transition is evident, laminar boundary layers usually detach and subsequently reattach as either fully or intermittently turbulent boundary layers. These transitional separation "bubbles" play an important role in the development of most of the boundary layers and wakes measured in this cascade and the modeling or computing of these "bubbles" should prove to be the key aspect in computing the entire cascade flow field. In addition, the nonequilibrium turbulent boundary layers on these highly loaded blades always have some region of separation near the trailing edge of the suction surface. These separated flows, as well as the subsequent near wakes, show no similarity and should prove to be a challenging test for the viscous computational codes.

Chapter 1 Introduction

Over the past two decades, techniques for computing complex flows have become increasingly more sophisticated. Steger [1978], Thompson [1980], Rubin and Khosla [1981,1982], Beam and Warming [1982], and Briley and McDonald [1984] have computed viscous flows at reasonable Reynolds numbers; Davis and Werle [1981] and Johnston and Sockol [1984] have studied viscid-inviscid interaction; and Edwards and Carter [1985] and Melnik and Brook [1985] have computed through separated regions. Further, all computations may now involve complex turbulence models, such as the models by Bradshaw, Ferriss, and Atwell [1967] and Launder, Reece, and Rodi [1975]. It is desirable that these techniques find their way into the turbomachinery design process. These numerical techniques are capable of very detailed predictions, but to be used with confidence, they should be tested against very detailed experimental data under typical flow conditions. As turbomachinery testing has generally been concerned with overall turbomachinery performance rather than with the details of the flow field, such data are lacking.

In order to provide the needed data, we have developed a cascade facility in which we can use a one-component laser Doppler velocimeter (LDV) to measure the periodic, two-dimensional flow field about a double-circular-arc, compressor blade in cascade. The boundary layer and near-wake

measurements will provide a very detailed and precise data base for testing new computational methods. The emphasis of this research will be on understanding the physics of this complex flow field so that others can focus their attention on the physical phenomena when developing their computational techniques.

Comparisons of viscous computations are most needed under flow conditions typical of modern compressor blades–especially under off-design conditions. Therefore, measurements of boundary layers and near wakes have been acquired on a highly loaded compressor cascade blade at three incidence angles near a chord Reynolds number (Re_c) of 500,000. The incidence angles of 5.0, -1.5, and -8.5 degrees yield boundary layers with a wide variety of characteristics. Inlet and outlet five-hole probe measurements and blade static-pressure measurements supplement the boundary layer and near-wake profiles. Surface flow visualization and hot-wire and hot-film measurements complement the transition and separation region data. The physical interpretation of the data results from a detailed boundary layer and wake analysis. Before describing this experiment, data, and analysis, we will describe previous boundary layer measurements in both rotating systems and cascades.

Chapter 2 Historical Background

Several researchers have attempted to measure boundary layers on turbomachine blades. Evans [1978] measured boundary layers at four chord (c) locations at midspan on the suction surface of a stator blade ($c = 305.0$ mm and $Re_c = 500,000$). The hot-wire measurements were made in an axial-flow compressor at three time-mean incidence angles on a row of stationary blades preceded by a row of rotating blades. The stator blades cut the wakes of the rotor blades and the rotor wake segments are subsequently transported through the stator passages. Since the wake segments involve low velocity fluid, the boundary layer is subject to a periodically varying freestream, and the blade is subject to a periodically varying incidence angle. Ensemble-averaged velocity profiles eliminate the random unsteadiness caused by turbulence. However, the periodic unsteadiness is preserved. The ensemble-averaged velocity profiles at 30% and 50% chord show that the boundary layers alternate between laminar and turbulent because of the unsteady flow. As a result, the time-mean velocity profiles exhibited a larger boundary layer growth than was expected.

Anand and Lakshminarayana [1978] measured boundary layers on the rotor blades of a rocket pump inducer using a three-sensor hot-wire probe rotating with the blades. Because of

imbalances in the radial pressure force and inertia forces in the blade boundary layer, outward radial velocities develop in a rotor blade boundary layer and inward radial velocities develop in a stator blade boundary layer. Anand and Lakshminarayana [1978] measured a significant outward radial component in the boundary layer velocity and found that this radial migration strongly influenced the chordwise velocity profiles.

Other experimenters have measured the boundary layers on rotor blades of axial-flow fans. Toyokura, Kurokawa, and Kimoto [1982] used rotating three-hole cobra probes to measure the three-dimensional boundary layers at six radial sections (c = 80.0 mm to 199.5 mm and Re_c = 300,000 to 500,000). The outward radial flow seemed to retard the predicted regions of transition and separation. Lakshminarayana, Govindan, and Hah [1982] used rotating miniature "x"-configuration hot-wire probes for boundary layer measurements at five radial locations (c = 152.4 mm and Re_c = 280,000 at midchord). Rotating miniature "x"-configuration hot-wire probes were also used by Pouagare, Galmes, and Lakshminarayana [1985] for numerous boundary layer measurements (c = 123.9 mm to 154.1 mm). In no case could the velocity profiles be very well resolved.

Walker [1982] made measurements similar to those of Evans [1978]. Walker [1982] used a hot wire in an axial-flow compressor to measure boundary layers on a stator (c = 76.0 mm and Re_c = 30,000 to 200,000) downstream of both a row of rotating blades and a row of inlet guide vanes. He tried to correct for wall proximity using a method outlined by Wills [1962], but still had difficulties matching the law of the wall. Low Reynolds number, large adverse streamwise pressure gradients, and rapidly changing boundary conditions (due to the periodic unsteadiness) were given as reasons for the absence of a logarithmic region.

Hodson [1983] made hot-wire measurements in an axial-flow turbine at midspan on a rotor blade (c = 114.5 mm and Re_c = 315,000) downstream of a stator row. Once again, the periodic unsteadiness seemed to cause the boundary layer characteristics to vary between laminar and

turbulent at some chordwise locations. Profile losses were larger than expected and this too was attributed to the unsteady flow.

Only one set of blade boundary layer measurements taken with an LDV exists from a turbomachine. Jessup, Schott, Jeffers, and Kobayashi [1985] used a one-component LDV to measure the boundary layers along the suction surface of a propeller blade (c = 141.0 mm and $Re_c = 730,000$) operating in a water tunnel. They focussed the LDV measurement volume at a particular point within the water tunnel. Every velocity data point then corresponded to a particular angular position of the rotating propeller blade. An oscilloscope time sweep in conjunction with a magnetic pick-up gave the appropriate angular position. After moving the LDV measurement volume to several axial positions, they extracted the velocity data from measurements close to the blade surfaces. Each data point within a given boundary layer then contained anywhere from 4 to 60 particle counts, a number hardly large enough to yield accurate values of mean velocity and turbulence intensity. Qualitatively, however, their data are quite interesting and shows regions of laminar, transitional, and turbulent flow.

Boundary layer measurements on turbomachine blades have yet to produce velocity profiles with enough detail and precision to compare with viscous computational codes. Therefore, our understanding of the physical nature of these complex, unsteady, three-dimensional boundary layers is far from complete. These flows are characterized by high turbulence levels, as well as by periodic unsteadiness caused by the interaction between stationary and rotating blade rows. "Blockage" effects exist because of the development of the end-wall boundary layers and the consequent contraction of the mainstream flow. The blade boundary layers are also affected by centrifugal and Coriolis forces associated with both the swirl and the blade rotation. The complex blade geometries and the complex flow field, including secondary flows, tip leakage, and trailing vorticity, make the analysis or measurement of turbomachine blade boundary layers very difficult.

Because of these difficulties, many researchers have sought a simpler geometry which retains some of the physics of the flow in which to make their boundary layer measurements. A model that has proven effective in other areas of turbomachinery is the periodic, two-dimensional row of airfoils, commonly referred to as a cascade. Properly realized, a cascade should eliminate all of the complexities of the turbomachine except blade curvature, secondary flow, and the effect of freestream turbulence.

The first attempt to measure boundary layers on cascade blades was made by Peterson [1958]. He used a three-hole cobra probe to measure blade boundary layers in a compressor cascade (c = 123.8 mm and $Re_c = 300,000$). Several boundary layers were measured on both the suction and pressure surfaces for three different incidence angles. In an attempt to better model an actual turbomachine, Peterson [1958] simulated the added diffusion caused by the radial distribution of axial velocity and the consequent streamline deviation. This added diffusion was created in the cascade by placing a perforated metal screen downstream of the blades. The measurements were not taken in the freestream, and therefore, the normal pressure gradient remains unknown. This lack of information leads to a problem in computing the edge velocity (which was probably inferred from the blade static-pressure distribution). The data are quite scattered, especially in the regions near separation, where the cobra probe fails. Peterson [1958] reported no significant differences between measurements with and without the added diffusion.

Pollard and Gostelow [1967] measured boundary layers on compressor cascade blades (c = 152.4 mm and $Re_c = 200,000$) with a Pitot tube to examine the effect of leading edge roughness. Three suction surface boundary layers and one pressure surface boundary layer were measured on both blades with a smooth leading edge and with a leading edge roughened with polythene spheres. With no roughness, laminar separation occurred before transition. It appears that separation of the turbulent boundary layers near the trailing edge would be more likely to occur when leading edge roughness is present. These results agree with the Preston tube skin-friction

measurements of Pollard and Gostelow [1967]. The detail and precision of the data are unknown since no actual data points are given.

Evans [1971] used compressor cascade blades ($c = 304.8$ mm and $Re_c = 500,000$) for boundary layer measurements taken with a hot-wire anemometer probe. A problem with this data is that the blade boundary layers were tripped with a wire at 10% chord. Evans [1971] argued that a turbulent boundary layer over most of the blade would better represent the high turbulence and unsteadiness levels usually encountered in a turbomachine. Instead, the artificially induced boundary layer development is rather misleading.

Problems of contamination, corrosion, erosion, and deposition have led to two investigations that dealt with the effects of surface roughness on cascade blade boundary layers. Bammert and Milsch [1972] measured blade boundary layers in a compressor cascade ($c = 180.0$ mm and $Re_c = 430,000$) with four different blade profiles to parametrically change the pitch, camber, and thickness of the blades. They used emery powder to develop the five roughness grades to be tested. A turbine cascade ($c = 175.0$ mm and $Re_c = 560,000$) was used for the blade boundary layer measurements of Bammert and Sandstede [1980] where four roughness grades were tested. Both investigations used a flattened Pitot tube which allowed measurements to be taken very close to the blade surface. Bammert and Sandstede [1980] used a hot-wire anemometer to confirm the measurements made with the flattened Pitot tube. The studies showed that increasing surface roughness led to increases in both momentum thickness and skin friction and a forward shift of the regions of transition and separation.

Meauzé [1979] used a transonic compressor cascade ($c = 94.9$ mm, $Re_c = 1,660,000$ for $M_1 = 0.70$, and $Re_c = 2,120,000$ for $M_1 = 0.85$) for blade boundary layer measurements. He used total-pressure probes to measure suction surface boundary layers for two inlet Mach numbers and four incidence angles. The flow recompression on the highly cambered blades results in laminar flow separation and subsequent turbulent reattachment. The thin laminar boundary

layers upstream of this separation "bubble" were difficult to measure, so that the total-pressure profiles were only measured for turbulent boundary layers.

The trailing edge boundary layers on both the suction and pressure surfaces of a compressor cascade blade (c = 203.2 mm and Re_c = 478,000) were measured with a hot-film probe by Hobbs, Wagner, Dannenhoffer, and Dring [1982]. The two profiles are very detailed; they show a nearly separated profile on the suction surface, and also a pressure surface profile typical of favorable pressure gradients.

Hodson [1983] has presented blade boundary layer data measured in a turbine cascade (c = 114.5 mm and Re_c = 315,000) with a hot-wire probe. Although no data points are reported, the velocity profiles on the suction surface show laminar flow until 78% chord followed by laminar separation and no reattachment.

Finally, in one of a growing number of experiments designed to evaluate three-dimensional flow effects, Schuls and Gallus [1988] measured the suction surface boundary layers of a compressor blade in an annular cascade (c = 62.6 mm and Re_c = 390,000). Their hot-wire measurements showed that the initially laminar boundary layers transitioned to turbulent near midchord. At midspan, the resulting turbulent boundary layers remained attached when the incidence angle was 2.2 degrees. Closer to the hub, separation occurs over the final 30% chord. Measurements at an incidence angle of 7.2 degrees show this suction surface/hub corner separation covers a larger extent of span and chord. Blade static-pressure measurements, flush-mounted hot-film measurements, and flow visualization help illustrate this three-dimensional feature of the flow.

With one exception, all prior investigations have used hot-wire or pressure probes to make boundary layer measurements.[1] There are three potential problems: first, a periodic two-dimensional cascade flow is difficult to establish and the probe may distort it; second, some

[1] Jessup, Schott, Jeffers, and Kobayashi [1985] did make boundary layer measurements using the LDV technique. Unfortunately, their data points within their propeller blade boundary layer did not contain an adequate number of particle counts.

boundary layers are likely to be small compared to the probe dimensions; and third, separated regions, if present, cannot be conveniently studied. For these reasons, the current study used the LDV technique.[2] The need for optical access to the blade row for the LDV technique places some unique restrictions on the types of flow controls that may be employed in the cascade. In particular, continuous blade pack suction to restrict the side wall boundary layer growth is no longer possible. Therefore, before discussing the LDV results, we will describe the cascade facility and flow.

[2] Elazar and Shreeve [1989] are in the process of completing two-component, LDV measurements of boundary layers on a controlled diffusion blade in cascade.

Chapter 3 Cascade Facility

In order to make LDV boundary layer measurements on a highly loaded cascade compressor blade with a Re_c near 500,000, we needed to modify the existing cascade facility. A description of this facility is given here.

Wind Tunnel

The cascade wind tunnel has a 0.37 m by 0.64 m test section with a maximum air speed of approximately 35 m/sec. Tunnel turbulence control is through a honeycomb with a 3.18 mm cell size, several settling screens in the diffuser section, and a nine-to-one contraction. Over the speed range of 24-35 m/sec, the tunnel operated with a freestream turbulence level of 0.18% $\pm$ 10% as measured by a hot-wire anemometer. Figure 1 shows a schematic of the open return facility.

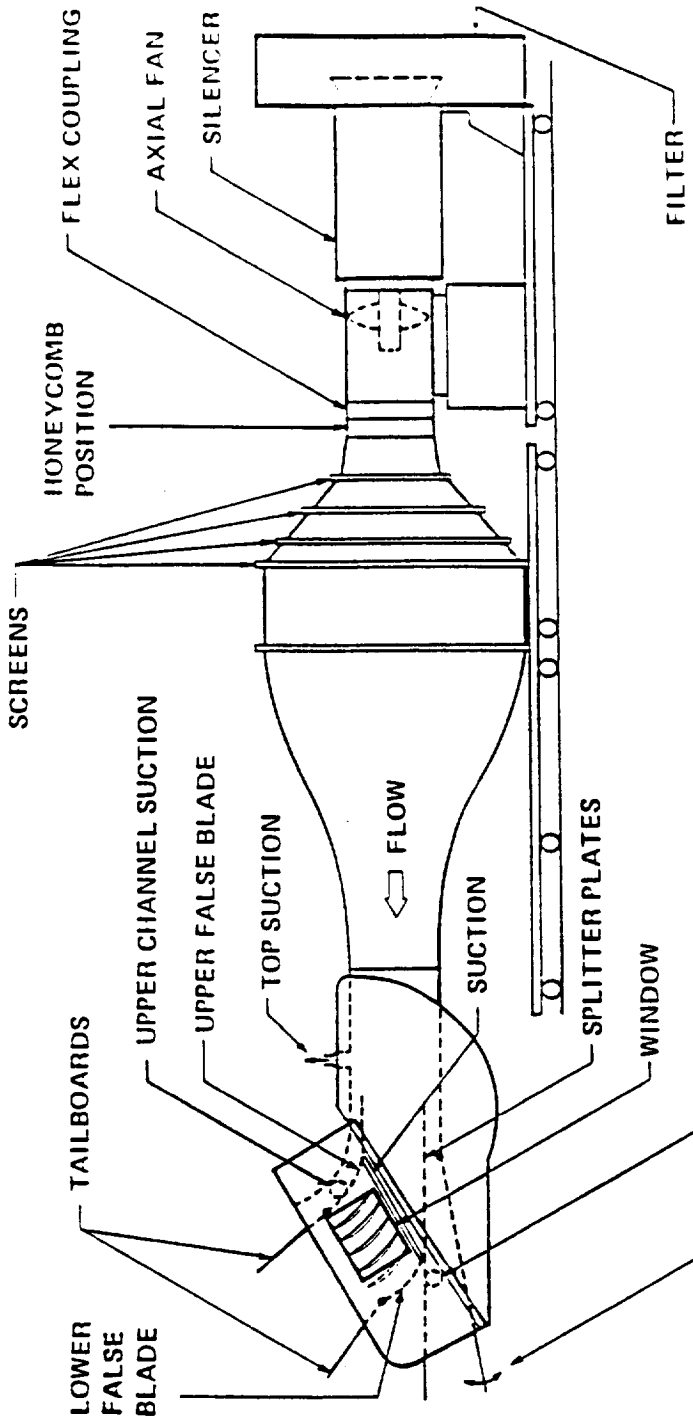

Figure 1. Cascade wind tunnel with flow controls

Test Section

The blade section used in the tests is a compressor blade designed at the NASA Lewis Research Center (see Sanger [1980]). The blade section is a double-circular-arc blade with 65 degrees of camber,[3] a 20.5 degree stagger angle, a solidity of 2.14, and a 228.6 mm chord length. The five cascade blades were made of aluminum and were anodized black to minimize laser reflections. Both the leading and trailing edges were machined to a 0.9144 mm radius. Camber line and thickness relationships necessary to construct the blades (or for computation) are given in appendix A. To insure proper alignment, the blades were carefully positioned in two inserts–aluminum and Plexiglas[4] (on the optics side)–which were in turn mounted to the plywood walls of the cascade test section. The test section is shown in figure 1 and some key aspects of the blade geometry are shown in table 1.

As current computer codes assume a two-dimensional, periodic cascade flow, one must take data in such a flow field for it to be of use. Two-dimensionality, of course, implies that the velocities and angles of the flow are substantially the same in spanwise planes, while periodicity supposes that velocities and flow angles show only minimal variations from blade passage to blade passage, both upstream and downstream of the blade row. For the five-bladed cascade used here, downstream periodicity was taken to mean periodicity over three blade passages centered at the minimum velocity point of the middle blade wake. In order to satisfy the condition of continuity for a two-dimensional, incompressible cascade flow, the axial velocity must be held constant throughout. From a practical standpoint then, flow periodicity and two-dimensionality could

---

[3] The blade was designed to show some trailing edge separation of the suction surface turbulent boundary layer at zero incidence angle. With the available cascade geometry, this leads to a large camber angle.

[4] A glass insert was later placed within the Plexiglas to improve the LDV signal.

Table 1. Blade geometry

c	228.6 mm
s	106.8 mm
$t_{\max}$	12.5 mm
r_{LE}	914.4 μm
r_{TE}	914.4 μm
σ	2.14
AR	1.61
γ	20.5°
κ_1	53.0°
κ_2	-12.0°
ϕ	65.0°

be determined, for a uniform inlet flow, by examining the axial-velocity ratio and flow angles determined at the exit plane. This was quite useful as these outlet measurements could be made simply and quickly, thus allowing us to check the cascade flow daily.

Two-dimensionality and periodicity are normally controlled in cascades by employing blades with a large aspect ratio or by using continuous suction over the entire blade pack.[5] Since we required a rather large chord length to obtain a value of 500,000 for Re_c, we could only use five blades within the cascade test section and our aspect ratio was only 1.61. Also, continuous suction was not possible in the current experiment because of the need for laser access. Alternate flow control was examined in some detail. Returning to figure 1, we note that there are many potentially useful flow controls. That is, it is possible in principle, to control the flow by adjusting the position of the lower false blade, the upper false blade, the variable diffuser, and the tailboards (as well as the relative position of the tailboards), or by adjusting the magnitude (and distribution) of the top suction, side suction, and lower and upper channel suction.

In practice, blade passages adjacent to the lower and upper false blades were each set at nominally one blade spacing. The diffuser was set to minimize the flow angle at the splitter plate. Lower channel suction was not required while top and upper channel suction were provided through the same 5 hp blower, which was run at full power. A baffle system was used to adjust the relative amounts of suction provided at the top and upper channel, and the baffling along with slight adjustments to the upper false blade position were used to insure a horizontal flow at the upper false blade leading edge. The tailboards were most useful in controlling the relative exit angles of the flow; that is, they could be adjusted so that the exit angle across the cascade in a blade-to-blade direction was constant outside of the wake regions. The periodicity, however, was found to be most influenced by the amount and distribution of the sidewall suction. Side suction was provided by a 10 hp centrifugal blower operated at full power. Side suction distribution was

---

[5] Note that the control here seems to be over the growth of channel corner disturbances. An attempt to use a slightly divergent wall, commonly used to compensate for boundary growth, failed.

controlled by a complex baffling system. Six suction ducts were located at a half-blade spacing on either side of each of the blades. Each of the individual ducts had a separate baffle control, and was adjusted by the simple but tedious procedure of changing a baffle position and then examining the resulting outlet flow. Presumably, the control of side suction distribution controlled the size of the sidewall boundary layer at its intersection with the blade pack leading edge line–in a sense controlling the virtual origin of the corner disturbances. Control of sidewall suction distribution then implied a control of the "blockages," caused by corner disturbance contamination, of each blade passage individually and hence control of the individual blade angles of attack. Once set, the stability of the periodicity obtained on a day-to-day basis was excellent.

Chapter 4 Experimental Technique

The measurements of boundary layers on cascade blades required an LDV system specifically adapted to the cascade facility previously described. In addition, several other measuring techniques were required for supplementary measurements.

Pressure Measurements

Static-pressure taps, Pitot-static probes, and five-hole probes were used in conjunction with pressure transducers to measure values of static and stagnation pressure within the cascade flow field. The five-hole probes are capable of resolving the three components of velocity as well as the relative yaw and pitch angles of the flow. Treaster and Yocum [1979] give a complete description of the five-hole probes employed in this study. The probes were calibrated at a speed of 30.5 m/sec in an open jet air facility over the range of pitch and yaw angles of $+30$ degrees to -30 degrees. Reynolds number effects on the probes have been shown to be small (see Treaster and Yocum [1979]).

A nearly real-time data acquisition/reduction system was used for the pressure measurements. The separate pressure transducer signals as well as a test section temperature signal were scanned by a multiplexer/scanner, smoothed on a multimeter through a 100 cycle (1.667 sec) integration, and sent for reduction to a VAX 11/782. Pressures, velocities, and flow angles could be monitored during each test.

Spanwise velocity profiles were measured approximately 36 mm upstream of and parallel to the leading edge line with a five-hole probe and five individual pressure transducers. These inlet surveys were repeated at several blade-to-blade locations, covering a distance of two blade spacings centered near the center blade leading edge. After using these measurements to check the periodicity and two-dimensionality at the inlet, we obtained values of β_1, i, p_1, p_{T_1}, V_1, and V_x averaged over the two blade spacings. The averaging was necessary since we measured some streamline bending due to the presence of the blades.

Outlet five-hole probe surveys were taken at midspan in the blade-to-blade direction covering all the blade passages. The outlet profiles were measured parallel to the trailing edge line and either 31.9% or 52.6% chord downstream of this line. A Pitot-static probe was placed 73 mm upstream of the blade pack leading edge and protruded approximately 50 mm into the flow–well outside of the side-wall boundary layer. The probe was located at a position where V_1 was roughly equal to the average of the inlet velocities measured with the five-hole probe. Using this inlet Pitot-static probe, an outlet five-hole probe, and seven individual pressure transducers, we measured the periodicity of the outlet–specifically observing the variation in axial-velocity ratio and flow turning angle. After verifying the periodicity of the outlet flow, we repeated the outlet surveys at other spanwise locations in order to check the two-dimensionality of the outlet flow. Next, we averaged the five-hole probe measurements at midspan over three blade passages, centered at the minimum velocity point of the center blade wake. If the resulting average axial-velocity ratio lay within 3% of 1.00, the flow was considered adequate. We then

obtained blade-passage averaged values of $\overline{\beta}_2$, $\overline{\delta_d}$, $\overline{p}_2$, $\overline{p_{T2}}$, and $\overline{V}_2$. Measured values of total-pressure loss coefficient, $\overline{\omega}$, and static-pressure rise coefficient, $\overline{C_{p_2}}$ could also be obtained.

A five-hole probe was also used to make detailed measurements of the far wake. The five-hole probe was traversed across the center blade wake repeatedly to give six separate traverses–yielding the average value, u, and the standard deviation of the sample, s_u, at each location, y. For sample sizes less than 30, we use the Student's t test to obtain 95% confidence levels,

$$u \pm \frac{s_u}{\sqrt{N-1}} t_{0.975} ,$$

where N is the number of samples. Tabularized data for the Student's t test yield $t_{0.975} = 2.571$ when the number of degrees of freedom $(N-1)$ is five.

Blade static-pressure distributions were measured using blades instrumented with static-pressure taps and corresponding conveying tubes. Ideally, blade static pressure would be measured on the center blade of the cascade–the one intended for LDV measurements–but the two types of measurements had somewhat conflicting requirements. That is, an aerodynamically smooth (0.8 μm estimated surface roughness) surface was desired for the LDV surveys, while the conveying tubes required for the pressure measurements inevitably led to a somewhat roughened surface. To work around this problem, we instrumented the suction surface of the blade above the center blade and the pressure surface of the blade below the center blade with 24 pressure taps each; we also instrumented the center blade pressure and suction surfaces with 6 and 7 taps, respectively. If the flow was periodic, the pressure distribution could be obtained from the adjacent blades as well as from the center blade. After verifying this periodicity by comparing the results of the pressure distributions from the adjacent blades against the data from the center blade, we interchanged the instrumented center blade with an uninstrumented blade for the LDV surveys. Data acquisition and reduction, for the static-pressure distribution, were similar to that described for the five-hole probe data with the exception that a scanner valve was used to switch the pressure data, hole-by-hole, to a single transducer during data acquisition. During the course

of the experiment, a few of the 24 pressure taps on each surface were found to give erroneous results and these taps were not used any further.

Surface Flow Visualization

Adopting the chemical sublimation method used by Holmes and Obara [1982] and Obara [1988], we used surface flow visualization to help determine the location of the transition and separation regions. Gray [1944] developed the first chemical sublimation method for indicating transition for his low-speed wind tunnel testing. The method involves coating the test surface with a very thin film of a volatile chemical solid. In regions of higher shear stress, the increased mixing implies an increase in the mass transfer coefficient which produces greater rates of sublimation. Holmes and Obara [1982] and Obara [1988] suggested the use of acetone as the solvent and naphthalene as the chemical solid when testing at Mach numbers less than 0.15–0.20.

An air brush was used to coat the blade with a mixture of naphthalene and acetone in a solid-to-solvent volume ratio varying from 1:8 to 1:4. When subjected to a flow, the white particles sublimated in regions of high shear stress exposing the black blade. The white particles remained in regions of low shear stress. Preliminary tests determined the run time sufficient to set up the visualization pattern–ideally, a stable pattern existed during an interval of several seconds. For each run, the center blade was removed, the naphthalene/acetone mixture was applied, and large particles were dusted off. The blade was then replaced in the cascade and removed after the predetermined run time, allowing the sublimation pattern to be photographed. A sufficient number of tests were taken so that a meaningful mean and Student's t test deviation could be obtained.

Later in the study, we also used an oil film method to visualize the flow pattern close to the blade surface. If a very thin coat of oil covers the blade surface, the shear stress within the flow

will carry the oil with it. In most parts of the flow, oil streaks will be left behind, approximating the "wall streamlines." In regions of separation and reattachment, the streamwise pressure gradient strongly affects the oil flow by decelerating the flow, thickening the oil film, and causing the oil film to pile up to form a steep ramp. Thus, the oil film method gives a good indication of the location of separation and reattachment as well as the flow direction elsewhere.

The blade was painted with a thin film of (ashless dispersant) aviation oil. This oil had the advantage that it was naturally florescent when exposed to the ultraviolet light of a black lamp. The flow pattern could be viewed in its transient and steady states while the tunnel was operated. Afterwards, we removed the blade and photographed the steady-state flow pattern under a black lamp before gravity caused the oil pattern to run.

Hot Wires and Hot Films

A continuous flow measurement can be made with the use of heated sensors. Within the flow, we can use a probe supporting a fine wire or a thin metallic film heated with an electric current. The voltage across the hot wire or hot film is a function of the flow velocity. Hot wires were used to measure the freestream turbulence within the cascade. The cylindrical wires were calibrated in an open jet air facility.

To obtain a nearly nonintrusive, continuous measurement of the wall shear stress, we can use hot films flush mounted to the blade surface. A current heats the thin metallic film that is baked on to a substrate which is chosen for its poor heat conduction. The probes are sensitive to cooling through convective heat transfer. Flush-mounted hot films are used rather than flush-mounted hot wires because the films are wide enough to allow the thermal boundary layer to develop over their thickness whereas the wires are too thin. For a flush-mounted hot film in a

laminar boundary layer, Ludweig [1950] and Liepmann and Skinner [1954] derived a relationship for the Nusselt number under forced convection,

$$Nu = \frac{h\ell_{\text{film}}}{k} = \frac{Q\ell_{\text{film}}}{k(T_{\text{film}} - T_e)} \propto (\tau_w)^{\frac{1}{3}} .$$

In an incompressible flow, Liepmann and Skinner [1954] showed that this relationship can be extended to turbulent boundary layers when the thermal boundary layer thickness is smaller than the viscous sublayer.[6] The hot film serves as one arm of a constant temperature anemometer's Wheatstone bridge. Since the heat flux, Q, changes with changing wall shear stress, τ_w, the anemometer changes the current, $\mathcal{I}$, passing through the hot film to ensure a constant film resistance, $\mathcal{R}_{\text{film}}$, and thus a constant film temperature, T_{film}. Therefore, the electrical power of the hot film must equal the rate of heat transfer away from the film,

$$QA_{\text{film}} = \mathcal{I}^2\mathcal{R}_{\text{film}} .$$

We can equate the heat flux from these two equations and multiply by the constant hot-film resistance to obtain:

$$(\tau_w)^{\frac{1}{3}} = c_1\mathcal{E}^2 + c_2 .$$

Thus, the shear stress to the one-third power is proportional to the square of the voltage, $\mathcal{E}$, across the hot film. The constant c_2 accounts for other forms of heat loss such as the heat transfer from the metallic film to the substrate. Liepmann and Skinner [1954] also show that the streamwise pressure gradient may affect the relationship between the heat flux and the shear stress. For most flows, however, this effect may be neglected. Bellhouse and Schultz [1966,1968] validated this relationship experimentally for laminar, turbulent, transitional, and separated shear layers.

The 0.4 mm by 0.9 mm platinum hot films (with a 2.0 μm quartz substrate) were flush mounted to the blade surface using epoxy, with the shorter distance aligned in the direction of the flow. Constant temperature anemometers were used with an overheat ratio of 1.6. The

[6] See chapter 6.

probes were not calibrated to obtain c_1 and c_2. However, immediately before each measurement, we measured the voltage across the hot film without any flow to obtain

$$0 = c_1 \mathcal{E}_0^2 + c_2 .$$

Then, after measuring the voltage with flow, we obtained

$$(\tau_w)^{\frac{1}{3}} = c_1 \left(\mathcal{E}^2 - \mathcal{E}_0^2\right) .$$

An assumption could be made that c_1 was similar for each probe and by setting c_1 equal to one, we could compare the individual probe measurements to obtain trends in the behavior of the shear stress at different locations. The assumption does not affect the trends of the data, but only observations based on the magnitude of the shear stress. Remember, however, that the heat transfer from the hot films with flow is governed by forced convection while the heat transfer from the hot films without flow is governed by free or natural convection.

Later, after measurements and calculations gave us an estimate of the time-average shear stress at the blade surface, we found we could use these estimates to yield a reasonable approximation of c_1. This rough calibration allowed us to obtain estimates of both the trend and magnitude of the data.

Laser Doppler Velocimeter

In a nonintrusive manner, a laser Doppler velocimeter measures the local, instantaneous fluid velocity by detecting the Doppler shift of scattered light from an injected seed particle in the flow. Of course, this technique will only work if the seed particle is small enough to follow a fluid pathline. After a laser emits a singular-frequency light beam, this beam is split in two and the resulting beams are focused at the desired measurement location. The intersecting beams from

this dual beam technique form an ellipsoidal measurement volume consisting of an interference fringe pattern. As the light is scattered off a seed particle within the measurement volume, the frequency of the scattered light changes because of the particle motion. This Doppler frequency shift is linearly proportional to the particle velocity. The scattered light from the two incident beams at two different angles is focussed on a photodetector and mixed to produce a difference or heterodyne frequency which is the Doppler frequency. We can also interpret this dual beam technique in terms of the interference fringes. As a seed particle passes through the light and dark regions of the interference fringe pattern, the photodetector detects a modulation of light intensity at a frequency equal to the Doppler frequency. By knowing the wavelength of the incident laser beams, λ, the half angle of the beams exiting from the converging lens, κ, and the Doppler frequency, f_D, we can determine the fringe spacing and thus the particle velocity normal to the fringe pattern,

$$u = \frac{f_D \lambda}{2\sin(\kappa)} .$$

Since the mixing process in the photodetector gives us a positive Doppler frequency which is the difference of two other frequencies, we cannot distinguish the direction of the seed particle. To eliminate this directional ambiguity, we upshift the frequency of one light beam by 40 MHz with a Bragg cell. This frequency shift occurs when the light beam enters the Bragg cell and is diffracted by travelling acoustic waves. A prism then returns the beam to its original direction. Essentially, the upshift causes the interference fringes to "move" upstream at 40 MHz relative to a stationary seed particle. Later, an electronic downmixer can downshift the collected Doppler signal to achieve the desired frequency shift, f_S. The processed signal will still yield a positive frequency, but before computing the velocity, we subtract f_S. This gives us the true Doppler frequency with a sign corresponding to the direction of the particle velocity.

Before processing the photodetector signal, we can attempt to improve the signal-to-noise ratio–which is degraded by electrical noise and the detection of light from extraneous sources (mostly reflections). One technique to increase the signal-to-noise ratio involves decreasing the

measurement volume by expanding the diameter of the incident laser beams. We can then use a low-pass filter to omit any high-frequency noise and a high-pass filter to omit any low-frequency noise and the low-frequency component or "pedestal" produced from the light intensity modulation.

After the photodetector converts the changes in light intensity into electrical signals, we must process these electrical signals to obtain the flow velocity. If the signal-to-noise ratio is sufficiently high, we can employ a counter processor, which is desirable since this type of signal processor can operate when the rate at which seed particles pass through the measurement volume is either high or low. After converting the electrical signal into pulses for digital processing, the counter processor decides if the pulses have exceeded some predetermined threshold and checks the time for the cycles within the Doppler "burst." The counter processor can then validate whether only a single seed particle has passed over the minimum number of interference fringes and reject any false data. Finally, the digital output signal can send the validated data to a digital computer for further data analysis.

All blade boundary layer and near-wake measurements were made using a single-component LDV. For all the LDV measurements, a specially designed traversing mechanism was used which matched the arc of motion of an optics cradle to that of the blade curvature (two arcs were employed, one for each of the pressure and suction surfaces). All measurements were made in the plane of the local blade normal. Translation of the optics cradle normal to the blade could be accomplished in step intervals as small as 0.0254 mm. Prior to the LDV measurements, a reference distance was established by focusing the LDV measurement volume on an insert which securely fit over the center measuring blade. Narrow lines had been etched on the insert (on arcs matching the blade curvature) to be known distances from the blade surface. Repeatability in establishing a measurement reference was estimated to be ± 0.05 mm, and this uncertainty is probably the major source of scatter in the velocity data.

A five-watt, Spectra-Physics, argon-ion laser was used for the measurements. Power on the blue line (488 nm wavelength) ranged between 0.5 watts and 0.7 watts on a day-to-day basis. Standard TSI backscatter optical components were used: The 371.3 mm focusing lens was chosen to allow the measurements to be made at the blade midspan. Later, we replaced this lens with one having better optical properties (and a 372.0 mm focal length). The ellipsoidal measurement volume was reduced through the use of a (2.71:1) beam expander; the predicted measurement length in the normal to the blade direction was 33 μm. While this length was small when compared to the length scales of the measured turbulent boundary layers, we shall show that it is roughly half the size of the displacement thickness of the smallest measured laminar profile. Where appropriate, optical shifting at 5 MHz was employed. Note that to measure close to the blade surface, we tilted the optical cradle at an angle of roughly 1 degree. Silicon carbide particles having a mean diameter of 1.5 μm were used for laser seeding. In an attempt to maintain a uniform distribution, we injected the silicon carbide particles well upstream of the measurement station. The particles were suspended in a "cloud chamber," which was constructed for this study, and were injected into the tunnel by a small overpressure.

LDV data acquisition and reduction was accomplished by using a direct link to a VAX 11/782 computer. Software allowed selection of the focusing lens half angle, the laser beam wavelength, the frequency shift, the minimum number of cycles employed in the calculation (8 here), and the number of particle counts per run. Initial output was in the form of a velocity histogram. Minimum and maximum velocity limits could be set by two cursors to eliminate obvious noise from the distribution. Final output was mean velocity, local turbulence intensity, and the percent of particle counts employed in the calculations. For most of the profiles measured, the skewness and kurtosis of the distribution were also calculated. The percentage of particle counts employed in the calculation may be used as an indicator of signal-to-noise ratio. At least 98% of the total particle counts were used for measurement stations in the boundary layer; at least 95% were

employed for points in the freestream (the difference in percentages reflects the fact that fewer overall points were used at the freestream locations).

For a counter processor, employed in a highly turbulent flow, the calculation of mean velocity and turbulence intensity may not be straightforward. McLaughlin and Tiederman [1973], Hoessel and Rodi [1977], Giel and Barnett [1979], Edwards [1981], Edwards and Jensen [1983], Johnson, Modarress, and Owen [1984], and Stevenson, Thompson, and Craig [1984] have all discussed the question of velocity bias in a highly turbulent flow. As pointed out first by McLaughlin and Tiederman [1973], the problem arises because more high-speed particles than low-speed particles arrive in the measurement volume during a given measurement interval. A related problem, termed incomplete signal bias by Stevenson, Thompson, and Craig, [1984], can be eliminated by employing a sufficiently high frequency shift.

McLaughlin and Tiederman [1973] describe a correction for the phenomenon (with uniform seeding)–but it requires complete velocity vector information. A more practical one-dimensional correction is also given, but this correction tends to overestimate the error for local turbulence intensities >20%. Edwards [1981] shows that the biasing error can be made negligibly small for the case of a saturated data handling system (taking data at a fixed rate set by the slowest component of the system) by taking the particle density equal to the seeding rate (this assumes a validation circuit for the system). Stevenson, Thompson, and Craig [1984] used equal time interval sampling in a very highly seeded mixing layer as a bias-free test case. As pointed out by Edwards and Jensen [1983], however, very high seeding rates may open the door to other types of errors, for example, by reducing the actual number of statistically independent samples used to form the velocity statistics. Moreover, a very high seeding rate may be very difficult to achieve in precisely those regions in which the bias is expected to be high. Often, in fact, a counter processor is chosen over a tracker processor because of its ability to act at very low seeding rates.

The bias question is obviously quite complex, and a consensus opinion on how to correct data is still lacking. Some issues, such as non-uniform particle seeding, of interest particularly

in air flows, have not yet been the subject of detailed studies (see Hoessel and Rodi [1977] for instance). Giel and Barnett [1979] conducted an experiment favorable to obtaining statistical bias, but no consistent bias was evident–thus further obscuring the bias question. In the current study, we employed simple arithmetic averaging. We note that both Mclaughlin and Tiederman [1973] and Johnson, Modarress, and Owen [1984] show that the overestimate of the mean velocity goes roughly quadratically with turbulence intensity, being 5% for a local turbulence intensity near 20%, and being 12% for a local turbulence intensity near 35%. These numbers should be borne in mind not only when evaluating the data presented here, but also when evaluating any measurements made in highly turbulent flows. The mean velocity here was taken as

$$u = \frac{1}{N}\sum_{n=1}^{N} u_n$$

and the variance as

$$u'^2 = \frac{1}{N}\sum_{n=1}^{N}(u_n - u)^2 .$$

Local turbulence intensity was taken as $\sqrt{u'^2}/u$ and turbulence intensity was taken as $\sqrt{u'^2}/U_e$, where U_e is the edge velocity of the boundary layer or wake.

For many of the boundary layers measured, we monitored the skewness and kurtosis (or flatness) with the idea that a change of shape from the classical distribution in the boundary layer might signal significant velocity bias. No such deviations were observed. We calculated the skewness and kurtosis from

$$S = \frac{1}{Nu'^3}\sum_{n=1}^{N}(u_n - u)^3$$

and

$$K = \frac{1}{Nu'^4}\sum_{n=1}^{N}(u_n - u)^4 .$$

The skewness is a measure of the symmetry of the distribution. For a symmetric distribution, the skewness is zero. The kurtosis is a measure of the concentration of values away from the mean (in the tails of the distribution). For a Gaussian distribution, the kurtosis is three. Figure 2 shows

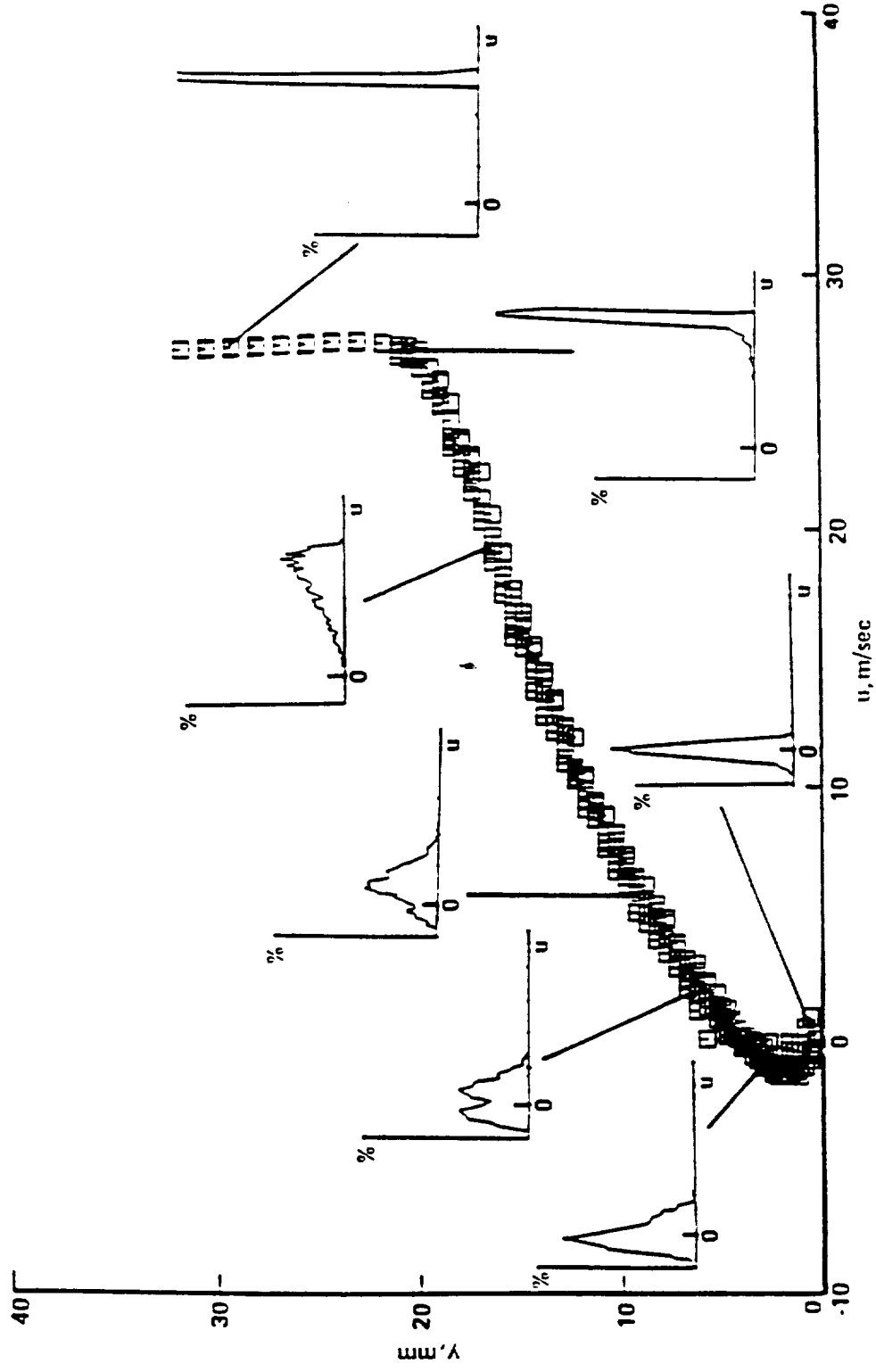

Figure 2. The velocity data from six individual experiments at 90.3% chord on the suction surface at $i = -1.5$ degrees-presented with six representative velocity histograms

the velocity data from six individual experiments along with some typical velocity histograms.[7] Moving from the freestream to the blade surface, we calculated the histogram skewness values as 0.69, -4.19, -0.77, -0.09, 0.34, 1.24, and 3.22 and the histogram kurtosis values as 4.69, 24.5, 3.09, 2.77, 2.88, 7.63, and 42.49. In the freestream, the velocity histogram is quite narrow. Just within the turbulent shear layer, the flow becomes intermittently turbulent. While the velocity usually takes on the maximum value set in the freestream, occasionally, one measures seed particles with a smaller velocity–leading to a negatively skewed histogram with a large kurtosis. In fact, one may find it difficult to differentiate between the actual data in the tail of the histogram and any noise–making this location difficult to measure and requiring a reduction in data rate. As measurements are made closer to the blade surface, the skewness reaches a minimum and then increases towards zero while the kurtosis reaches a maximum and then decreases towards three: A Gaussian distribution is finally obtained as shown in figure 2.

The data here followed the trends shown by Klebanoff [1954], Charney, Mathieu, and Comte-Bellot [1976], Reichert and Azad [1979], Karlsson [1981], and Simpson, Chew, and Shivaprasad [1981b]: The velocity distribution was Gaussian in all regions except where y was between 70% and 120% of the boundary layer thickness (where $S < 0.0$ and $K > 3.0$). For attached turbulent boundary layers, one can measure velocity histograms with $S > 0.0$ and $K > 3.0$ where y is less than 10% of the boundary layer thickness. Here, the blade surface prevents the histogram from obtaining values of velocity less than zero. For the detached turbulent shear layer shown in figure 2, positively skewed velocity distributions can occur farther from the surface. Also, one can measure bimodal velocity distributions when the time-average velocity away from the surface is near zero.

Experience has shown that quite satisfactory repeatability of the mean velocity and turbulence intensity can be guaranteed in boundary layer flows by using 1000 particle counts in regions in which the local turbulence intensity exceeds 5%. In regions of local turbulence intensity of

[7] This data were taken at 90.3% chord on the suction surface for $i = -1.5$ degrees.

less than 5% but more than 2%, 500 points are used, while 200 points are used in regions of less than 2%. More particle counts would be necessary to obtain more accurate values of the skewness and kurtosis. At each chord position, profiles were defined by statistically treating the data for six individual experiments. Six experiments were chosen as the statistics found from six experiments showed less than 1% scatter in the freestream data. Error bands, presented on the LDV data plots, represent 95% confidence levels as determined by a Student's t test.

Chapter 5 Experimental Results

With the use of the experimental technique just described, we measured the flow field about the blades for incidence angles of 5.0, -1.5, and -8.5 degrees. The incoming flow for all three incidence angles contained a freestream turbulence level of 0.18% ± 10% as measured with a hot wire. For this freestream turbulence level, we now present the measurements for all three incidence angles. Detailed analysis of the data is given in chapter 7.

Flow Field for a 5.0 Degree Incidence

The flow field through the cascade of double-circular-arc compressor blades was established at an incidence angle of 5.0 degrees and a Re_c of 505,000 with an observed ±1% variation on a day-to-day basis. The average inlet static and total (gage) pressures were $p_1 = -414.3$ Pa and $p_{T_1} = 246.1$ Pa giving an inlet velocity of 33.11 m/sec. Figure 3 shows a typical outlet flow profile and the equivalent turning angles–as measured with a five-hole probe 52.6% chord downstream of the blade trailing edge. The periodicity of the flow is clearly excellent. The flow turning

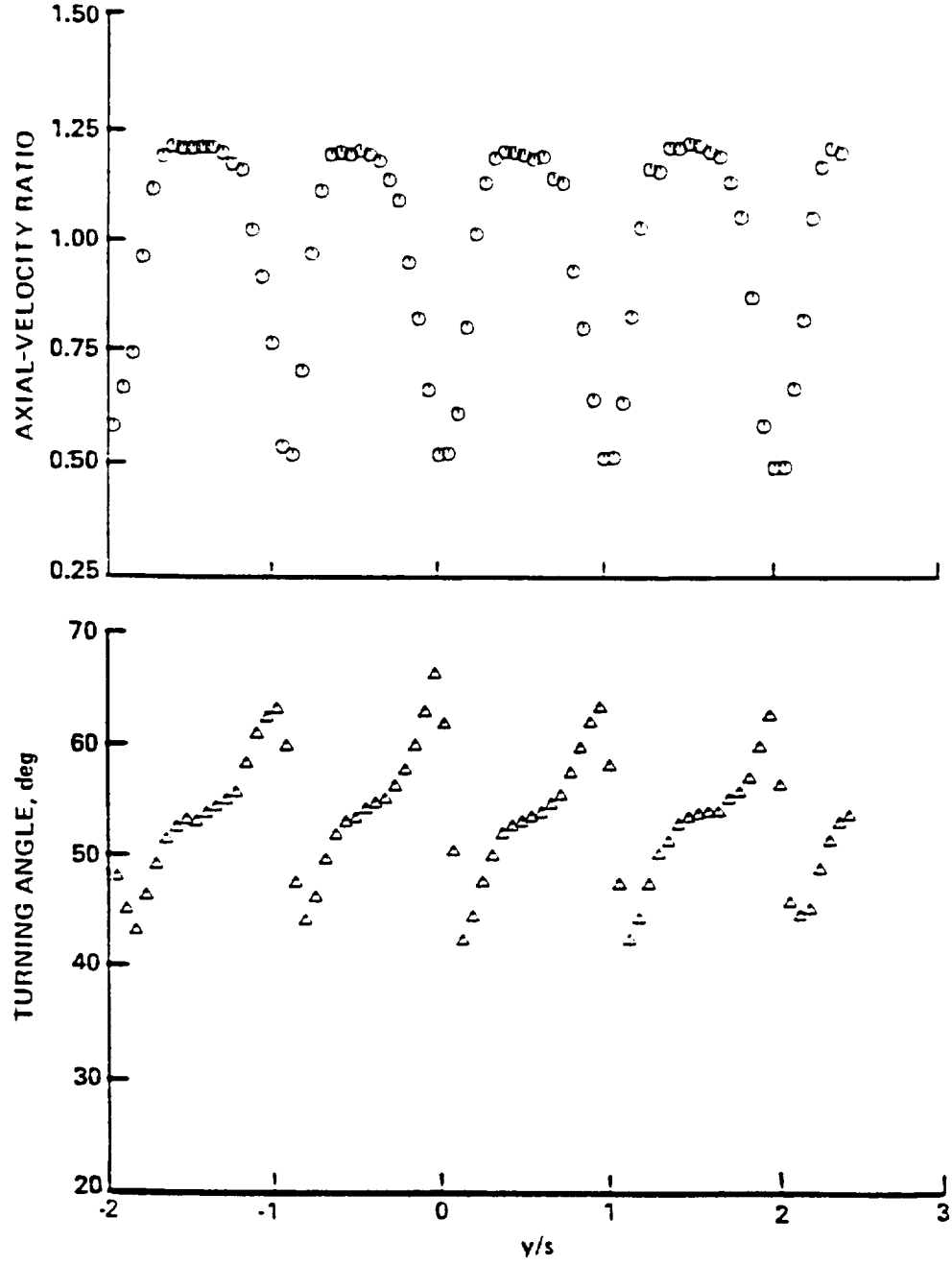

Figure 3. Five-hole probe outlet survey for $i = 5.0$ degrees

angle averaged across the three center blade passages was 54.0 degrees. At this downstream location, different spanwise measurements showed a two-dimensional core flow at least 50 mm wide where the influence of the corner disturbances had not yet been felt. Table 2 summarises the flow conditions for all three incidence angles while figure 4 shows the inlet and outlet velocity triangles.

Measurements have been taken to help quantify the losses in total pressure across the cascade. Additional quantities can be computed to compare with design limits on diffusion rate and static-pressure rise within the cascade. The difference between the blade-passage-averaged flow angle in the outlet flow and the exit blade "metal" angle is the deviation angle. For a 5.0 degree incidence, the deviation angle was measured to be 16.0 degrees, which is very large.[8] Nondimensionalizing by the inlet dynamic pressure, the blade-passage-averaged total-pressure loss coefficient, $\overline{\omega}$, was 0.151 and the blade-passage-averaged static-pressure rise coefficient, $\overline{C_{p_2}}$, was 0.463. Note that the static-pressure rise coefficient was probably affected by the positioning of the tailboards. An equation for the total-pressure loss coefficient was developed by Lieblein and Roudebush [1956] where

$$\overline{\omega} = 2\left(\frac{\theta}{c}\right)\frac{\sigma}{\cos(\overline{\beta}_2)}\left[\frac{\cos(\beta_1)}{\cos(\overline{\beta}_2)}\right]^2\left\{1 - \left[\frac{\theta}{c}\right]\frac{\sigma H_{12}}{\cos(\overline{\beta}_2)}\right\}^{-3}\left(\frac{2H_{12}}{3H_{12} - 1}\right).$$

A value of 0.172 for $\overline{\omega}$ can be calculated from this equation using the flow parameters measured in the outlet flow.[9] The loss in total pressure across the cascade is related to the amount the flow is diffused through the blade passage. Lieblein, Schwenk, and Broderick [1953] derived a diffusion factor where

$$\overline{D} = 1 - \frac{\overline{V}_2}{V_1} + \frac{V_{\theta_1} - \overline{V}_{\theta 2}}{2\sigma V_1} = 1 - \frac{\cos(\beta_1)}{\cos(\overline{\beta}_2)} + \frac{\sin(\beta_1) - \cos(\beta_1)\tan(\overline{\beta}_2)}{2\sigma}.$$

---

[8] Although large, a 16.0 degree deviation angle is not unexpected, since the blades are very highly loaded and the design condition called for a zero degree incidence angle.

[9] This value of $\overline{\omega}$ was computed using the values of momentum thickness (θ) and first shape factor (H_{12}) calculated in the far wake at 152.6% chord. Details of the calculations are shown in chapter 6 on the method of analysis.

Table 2. Flow conditions

i	5.0°	-1.5°	-8.5°
β_1	58.0°	51.5°	44.5°
$\overline{\beta}_2$	4.0°	2.1°	-0.6°
$\overline{\beta}_m$	39.9°	32.9°	25.9°
$\overline{\epsilon}$	54.0°	49.4°	45.1°
$\overline{\delta}_d$	16.0°	14.1°	11.4°
V_1	33.11 m/sec	32.88 m/sec	33.28 m/sec
$\overline{V}_2$	17.59 m/sec	20.48 m/sec	23.74 m/sec
$\overline{V}_m$	22.88 m/sec	24.38 m/sec	26.39 m/sec
V_x	17.55 m/sec	20.47 m/sec	23.74 m/sec
$\overline{\omega}$	0.151[a]	0.094[a]	0.028[a]
		0.071[b]	0.024[b]
	0.172[c]		0.018[c]
$\overline{C}_{p_2}$	0.463	0.473	0.421
C_L	0.952	0.821	0.956
$\overline{D}$	0.658	0.555	0.452
Re_c	505,000	501,000	507,000

[a] measured values

[b] values computed at 131.9% chord

[c] values computed at 152.6% chord

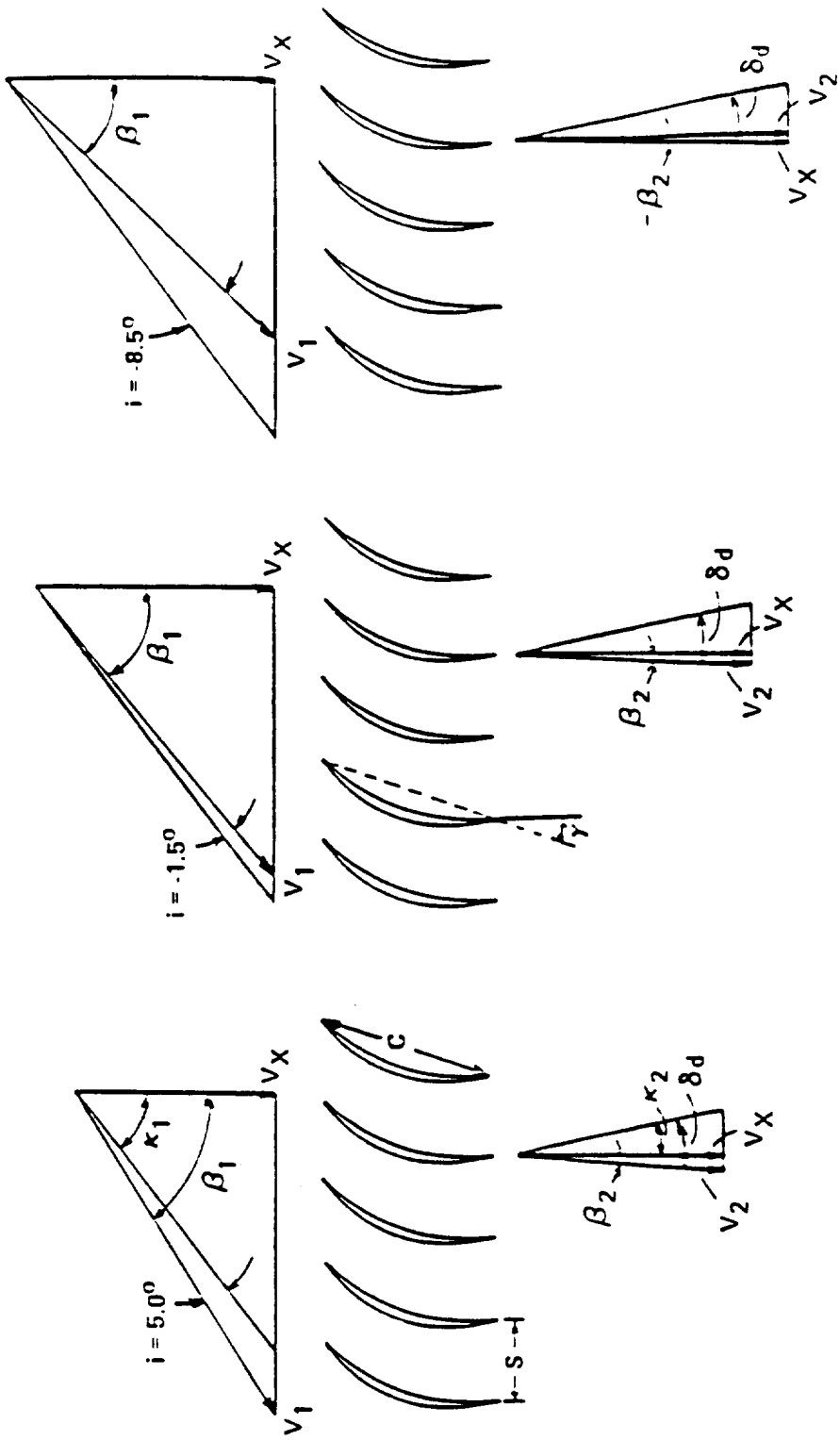

Figure 4. Inlet and outlet velocity triangles

Designers normally place a limit between 0.5 and 0.6 on $\overline{D}$ when designing a blade row (depending upon span location). This limit is based on a large number of cascade performance tests. Values of $\overline{D}$ greater than this limit result in large increases in total-pressure loss because the larger amount of diffusion causes the blade boundary layers to separate. Using a blade-passage-averaged value of the outlet flow angle allows a value of 0.658 for $\overline{D}$ to be computed. This value of $\overline{D}$ indicates a risk of separation.

The blade static-pressure distribution appears in figure 5. The vertical lines in figure 5 indicate the locations at which LDV surveys were made. Integrating this distribution gives a lift coefficient of 0.952. The 5 degree incidence angle dramatically affects the pressure distribution. At the leading edge on the pressure surface, for example, the large positive incidence angle results in a strong acceleration which promises a region of laminar flow. In the region from 6% chord[10] to 68% chord, the flow is subjected to a mildly adverse gradient so that the onset of transition might be expected in this region. The subsequent favorable gradient, however, makes the eventual complete transition to turbulence problematic. The very large adverse pressure gradient at the leading edge of the suction surface implies a leading edge separation. This gradient becomes less severe with downstream distance and vanishes entirely near 80% chord. No pressure gradient is evident over the last 20% chord which indicates a possible separation region–that is, a region which cannot sustain a streamwise pressure gradient. The rapid and continuous changes of pressure on both the pressure and suction surfaces offer little hope of finding equilibrium boundary layers. In addition, the inviscid velocity field within the blade passage will be under the influence of a normal pressure gradient, and one cannot anticipate a constant freestream velocity region.

The chemical sublimation method showed signs of transition on the pressure surface and separation near the trailing edge of the suction surface. Evidence of two-dimensionality was

---

[10] Wherever the term "% chord" appears, it should be understood to mean the percent of surface distance (or arc length, since the surfaces are circular arcs) for the surface under discussion.

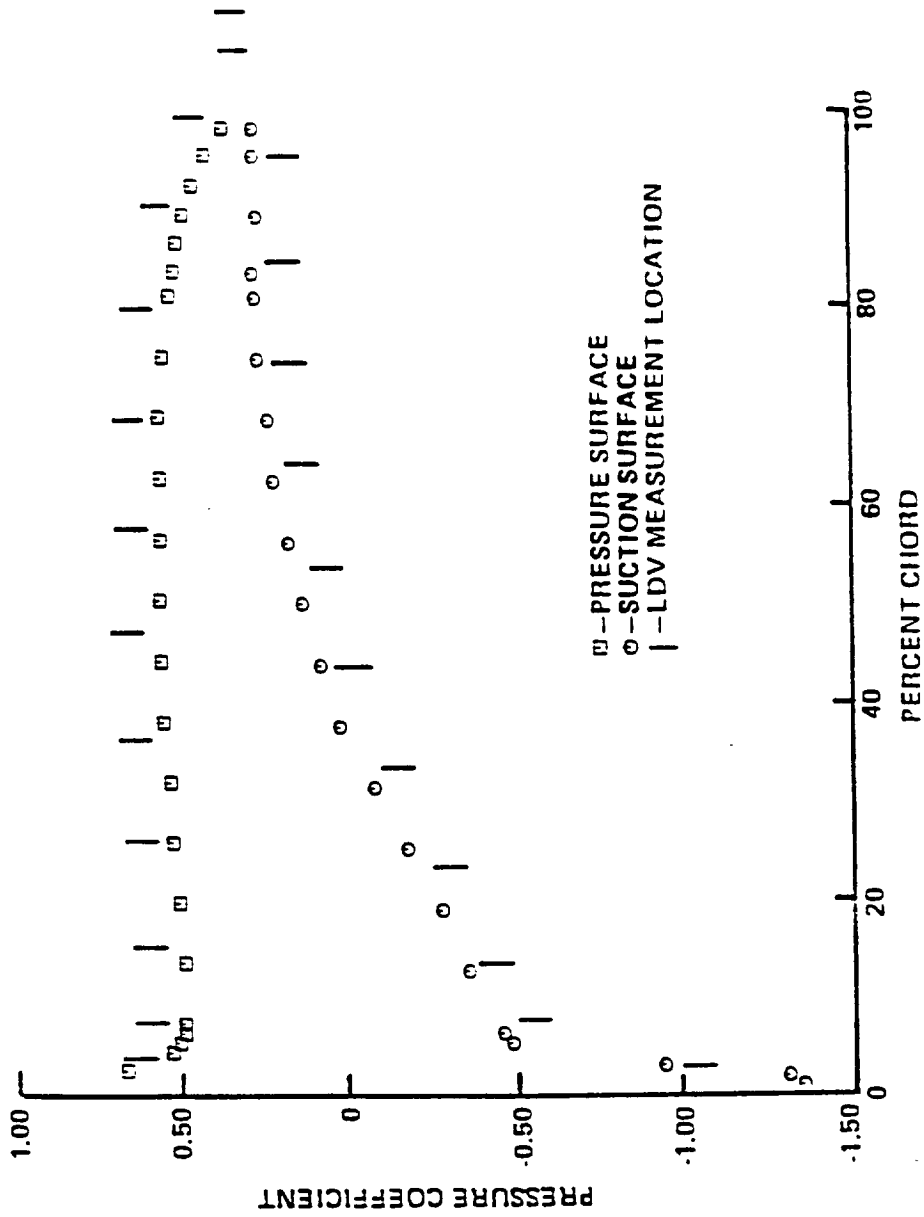

Figure 5. Blade static-pressure distribution for $i = 5.0$ degrees

much more apparent in the suction surface separation pattern than in the pressure surface transition pattern. This is perhaps an indication of the importance of the local surface roughness in determining the transition point for the very thin boundary layers encountered. With 95% confidence, separation was found to occur at 65.5% chord on the suction surface with a deviation of ±3.5% chord. Transition was found on the pressure surface to be at 64.2% ± 3.9% chord to the same level of confidence.

Boundary layer measurements were made at 11 chord locations on the pressure surface of the center cascade blade. To help interpret these velocity profiles, figure 5 shows the measurement locations along with the pressure distribution. The combination of continuously changing pressure and moderate surface curvature signals a complicated nonequilibrium flow field. The measured pressure surface boundary layers are shown in figure 6. The blade-to-blade pressure gradient affects the inviscid region of each profile. This pressure gradient varies from a strong, nonlinear gradient near the leading edge, where the streamlines have a large curvature, to a nominally zero gradient near the trailing edge. As previously noted, each profile was measured six times and the symbols in figure 6 represent velocity data averaged over the six tests. The error bands give 95% confidence levels as determined by the Student's t test. These error bands are quite small, particularly in the inviscid regions. The exception appears at 2.7% chord where the boundary layer is so small that the LDV could only nominally penetrate the layer, and correspondingly, the resolution is poor.

Suction surface boundary layers were taken at 11 chordwise locations on the center blade. Figure 5 shows these chordwise locations as well as the static-pressure distribution. The measured suction surface boundary layers are presented in figure 7. The inviscid regions show the effects of the normal pressure gradient. Note how the large curvature in the streamlines near the leading edge results in a highly curved inviscid region. The 95% confidence bands are quite small for all the boundary layers except in two regions. First, the thin boundary layer at 2.6% chord has a large velocity gradient near the surface; because of this large gradient, the sensitivity to probe

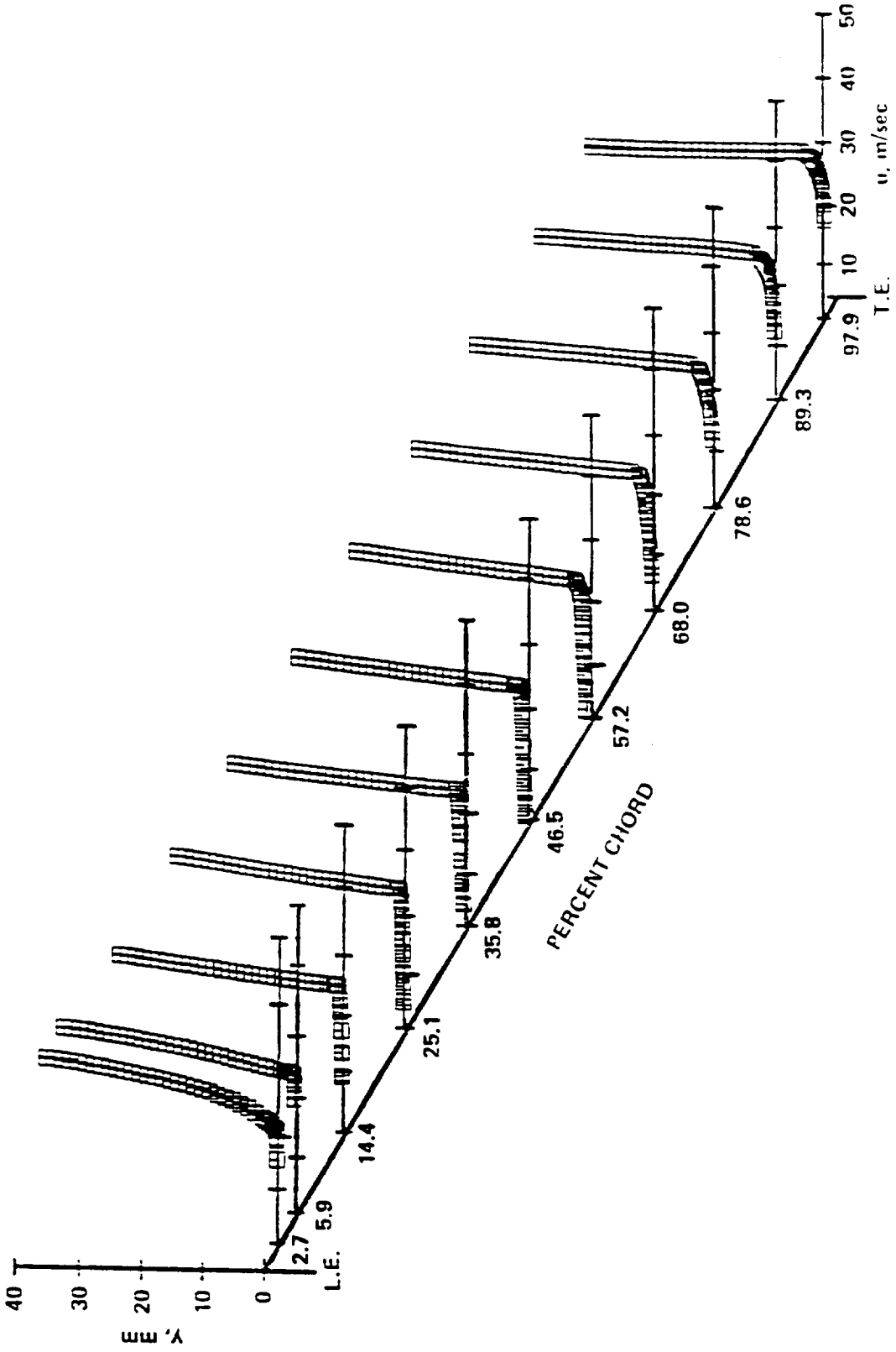

Figure 6. Measured pressure surface boundary layers for $i = 5.0$ degrees

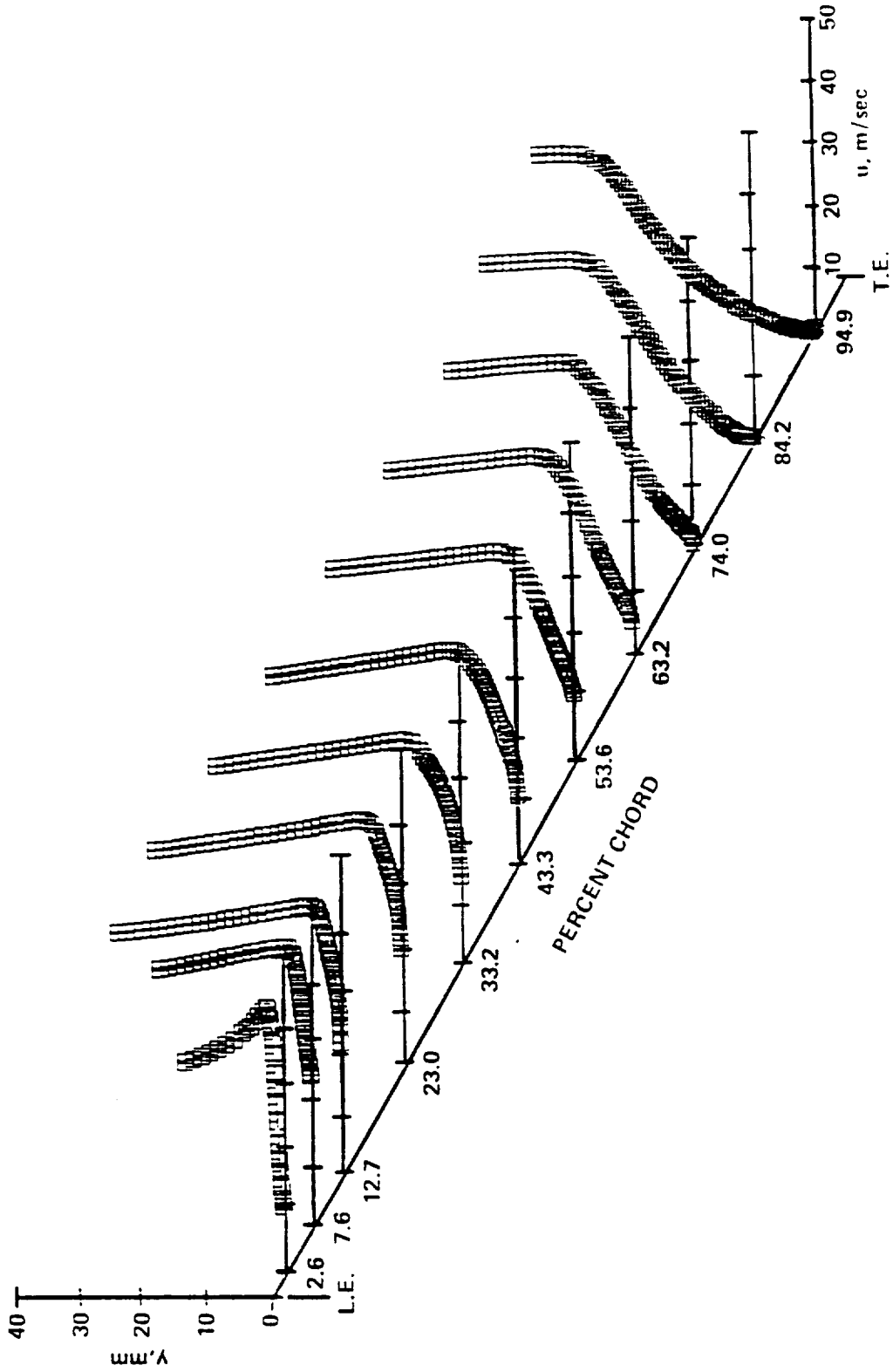

Figure 7. Measured suction surface boundary layers for $i = 5.0$ degrees

placement is heightened, and the measurements are less repeatable. Second, as suspected, the boundary layer at 94.9% chord was separated, and the unsteadiness in the separation process resulted in larger error bands.

Near-wake measurements were made at 105.4% chord and 109.6% chord using the LDV technique. Five-hole probes were used to measure the far wake at 152.6% chord. Figure 8 shows the data points and their 95% confidence bands for all three wake positions. The two near-wake profiles, which are quite similar, are very asymmetric because of the large difference in trailing edge boundary layer thicknesses on the two surfaces of the blade. The separation of the suction surface boundary layer leads to negative mean velocities at the center of the near wake. Other researchers have also measured negative mean velocities in near wakes. Wadcock [1980], using a flying hot wire, measured negative mean velocities in the near wake of an airfoil. Braden, Whipkey, Jones, and Lilley [1983] used a LDV to measure negative mean velocities in the near wake of an airfoil with confluent boundary layers.[11]

For the flow fields at all three incidence angles, the LDV measurements give information on local turbulence intensity and percent backflow as well as the skewness and kurtosis of each velocity distribution. We shall present turbulence intensity and percent backflow in chapter 7 after analyzing the velocity data to obtain U_e.

Flow Field for a -1.5 Degree Incidence

Following the completion of the measurements of the flow field for a 5.0 degree incidence angle, we rotated the entire test section and established a new periodic, two-dimensional flow field. Five-hole probe measurements yielded an incidence angle of -1.5 degrees and a Re_c of

[11] Confluent boundary layers develop on an airfoil with leading edge slats or trailing edge flaps which causes the boundary layers from the various surfaces to interact.

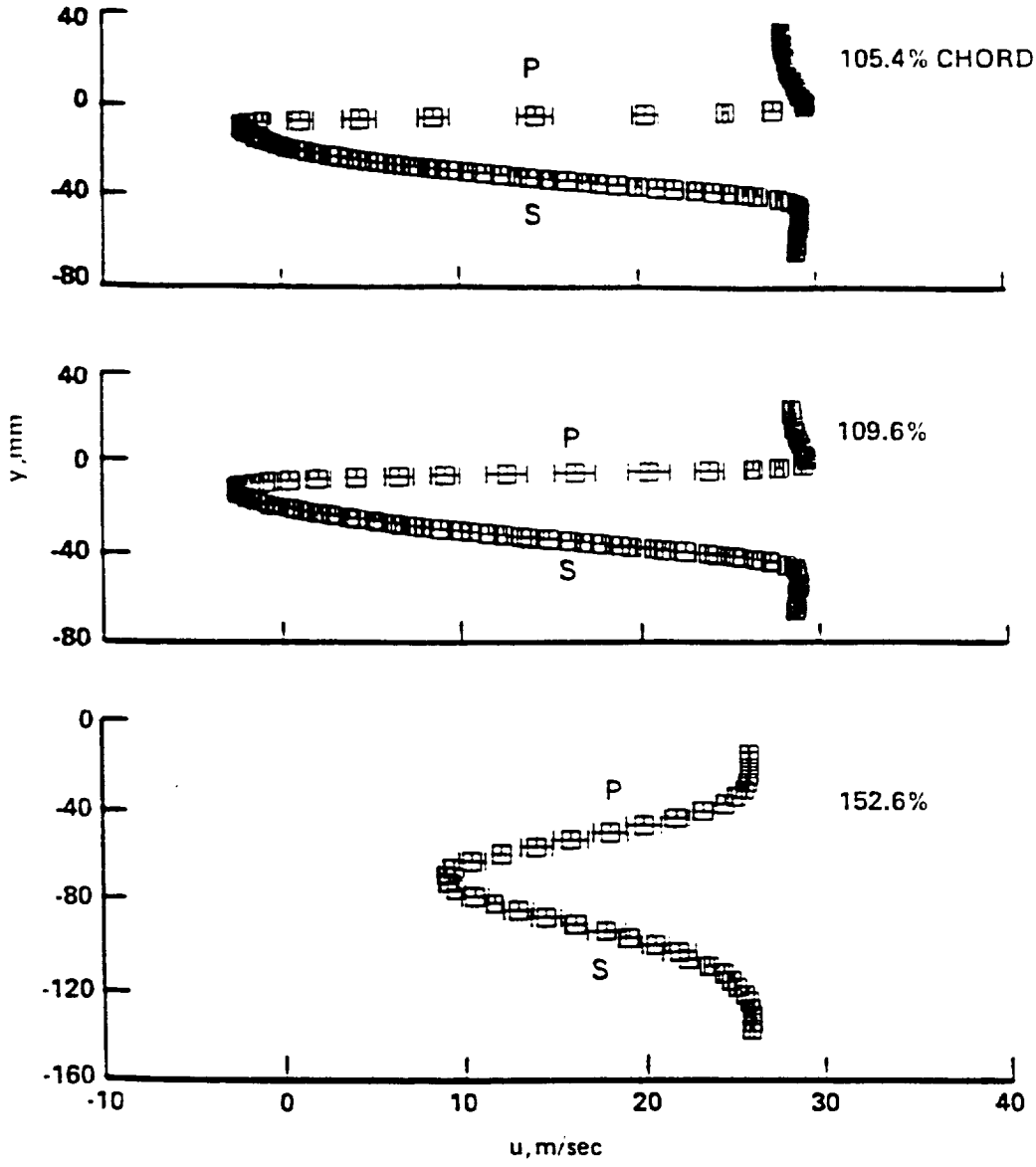

Figure 8. Measured wakes for $i = 5.0$ degrees

501,000. The average inlet velocity of 32.88 m/sec was computed from the (gage) measurements of $p_1 = -382.0$ Pa and $p_{T_1} = 269.6$ Pa. Figure 9 shows a typical outlet flow profile and the equivalent turning angles as measured with a five-hole probe 31.9% chord downstream of the blade trailing edge. After many adjustments of the various flow controls, we found this case to be the closest we could obtain to achieving a periodic, two-dimensional flow field near the design incidence angle of zero degrees.

From figure 9, the flow turning angle averaged across the three center blade passages was 49.4 degrees. The deviation angle was 14.1 degrees. Measurements also give an $\overline{\omega}$ of 0.094 and a $\overline{C_{p_2}}$ of 0.473, while calculations using the equation of Lieblein and Roudebush [1956] give an $\overline{\omega}$ of 0.071. Calculating a diffusion factor of 0.555 shows that while a risk of separation still exists for $i = -1.5$ degrees, the risk is not as great as for the flow field with $i = 5.0$ degrees (where $\overline{D} = 0.658$). Figure 4 shows the velocity triangles for this set of inlet and outlet flow measurements.

The new blade static-pressure distribution appears in figure 10. The vertical lines in figure 10 show the locations of LDV measurements. Integrating this distribution gives a lift coefficient of 0.821. We can compare this pressure distribution with the pressure distribution corresponding to the 5.0 degree incidence angle shown in figure 5. Although the two distributions are similar, one can notice differences which could strongly affect the boundary layers on both the pressure and suction surfaces. For the -1.5 degree incidence, the streamwise pressure gradient near the leading edge of the pressure surface is less favorable and extends only to 3% chord. Downstream, the flow consists of a mildly adverse pressure gradient from 3% chord to 62% chord followed by an increasingly strong acceleration to the trailing edge. The initially laminar boundary layer confronts a slightly stronger adverse pressure gradient for this second incidence angle. Transition should occur in this region with a more probable chance of completion than that of the transition on the pressure surface at the 5.0 degree incidence.

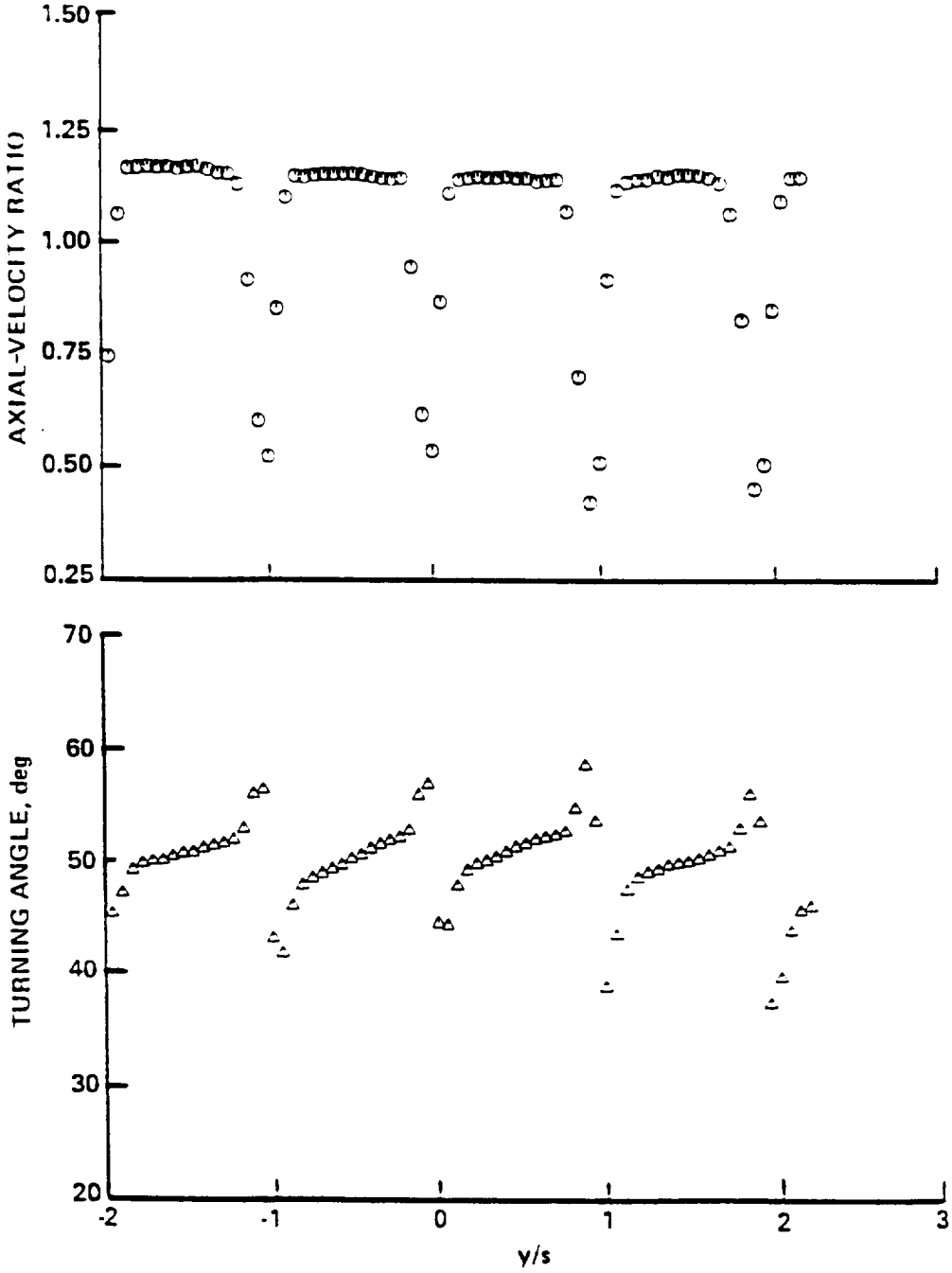

Figure 9. Five-hole probe outlet survey for $i = -1.5$ degrees

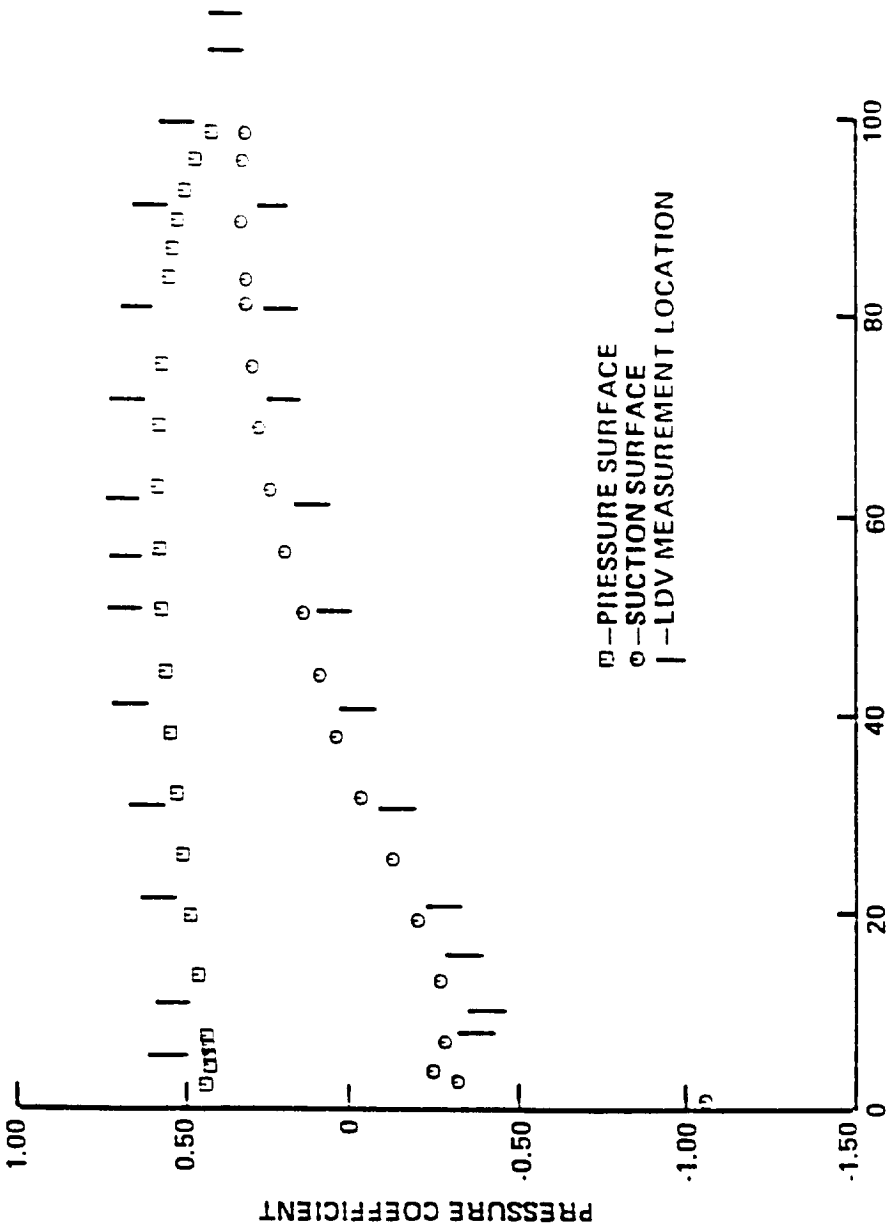

Figure 10. Blade static-pressure distribution for $i = -1.5$ degrees

Once again, the very large adverse pressure gradient at the leading edge of the suction surface implies a leading edge separation. Unlike the flow for the first incidence, however, a small favorable pressure gradient exists on the suction surface from 3% chord to 9% chord. Thus, the flow history of the suction surface boundary layers for the first two incidence angles differs and the boundary layers for the second incidence angle should be thinner. Both pressure distributions show a vanishing adverse pressure gradient near 80% chord indicating a possible separation region near the trailing edge of the suction surface.

Results from the chemical sublimation method corroborate the blade static-pressure distribution on the suction surface. With 95% confidence, a region of low shear stress was found at 45.1% $\pm$ 2.3% chord indicating that separation occurs a little earlier for the -1.5 degree incidence than for the 5.0 degree incidence. On the pressure surface, however, the surface flow visualization gave some surprising results. With the same level of confidence, a region of low shear stress was found between 14.0% $\pm$ 5.5% chord and 38.2% $\pm$ 5.2% chord. Thus, the results indicate a separation region rather than the anticipated transition region.

As shown on the blade static-pressure distribution in figure 10, we measured boundary layers at 12 chord locations on the pressure surface. Figure 11 shows these boundary layer profiles. At this incidence angle, the streamlines near the leading edge show less curvature than they did at the 5.0 degree incidence. Therefore, the inviscid region of the velocity profiles is quite linear. Again, the error bands give 95% confidence bands as determined by the Student's t test. These bands tend to represent the repeatability of measuring at the same spatial location for each of the six tests and are only visible when the boundary layer is very small and the velocity gradient is very large.

Suction surface boundary layers were measured at 11 chordwise locations. Figure 12 shows the velocity profiles and figure 10 shows the location of these profiles relative to the blade static-pressure distribution. Once again, a linear, normal pressure gradient is evident. As expected from

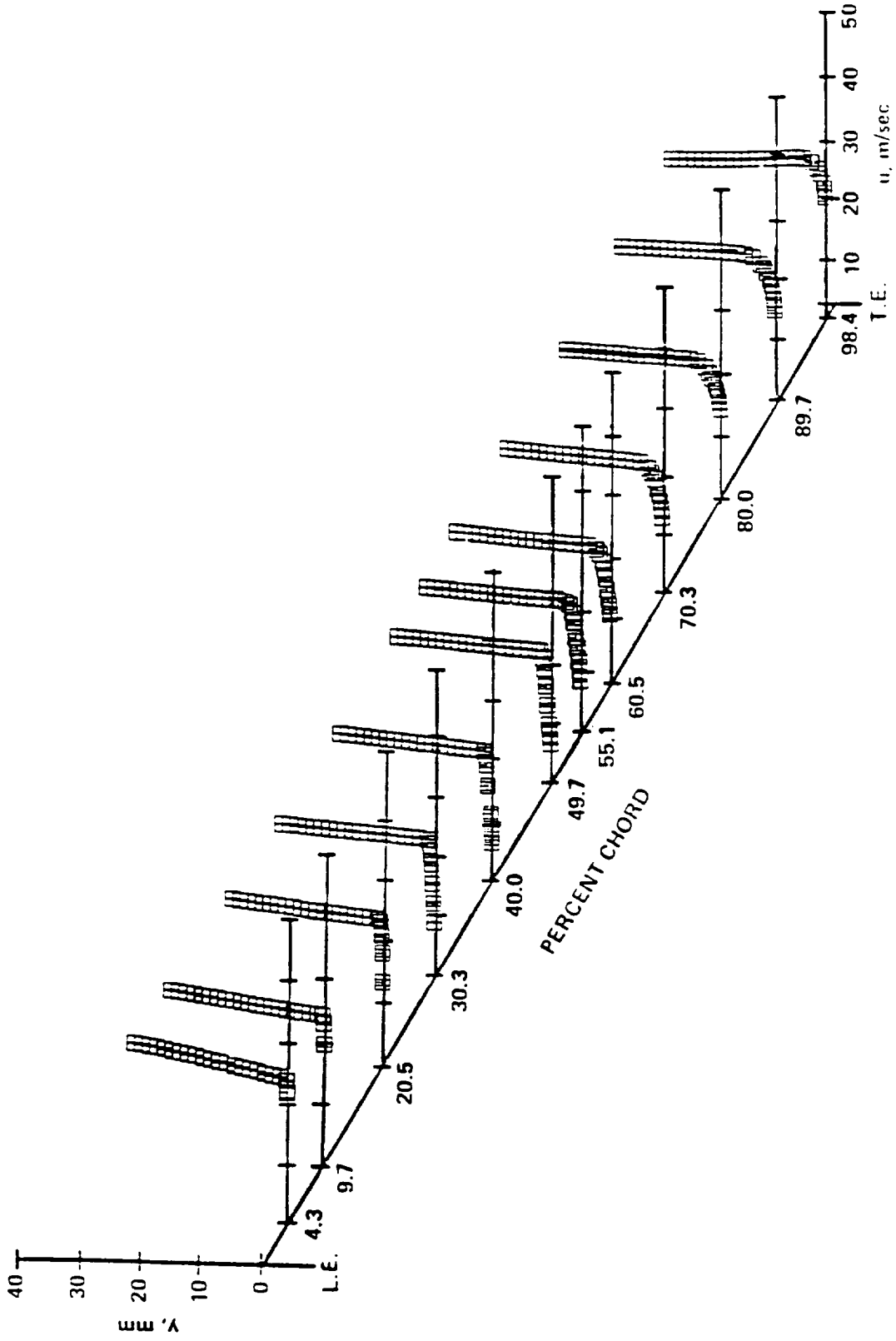

Figure 11. Measured pressure surface boundary layers for $i = -1.5$ degrees

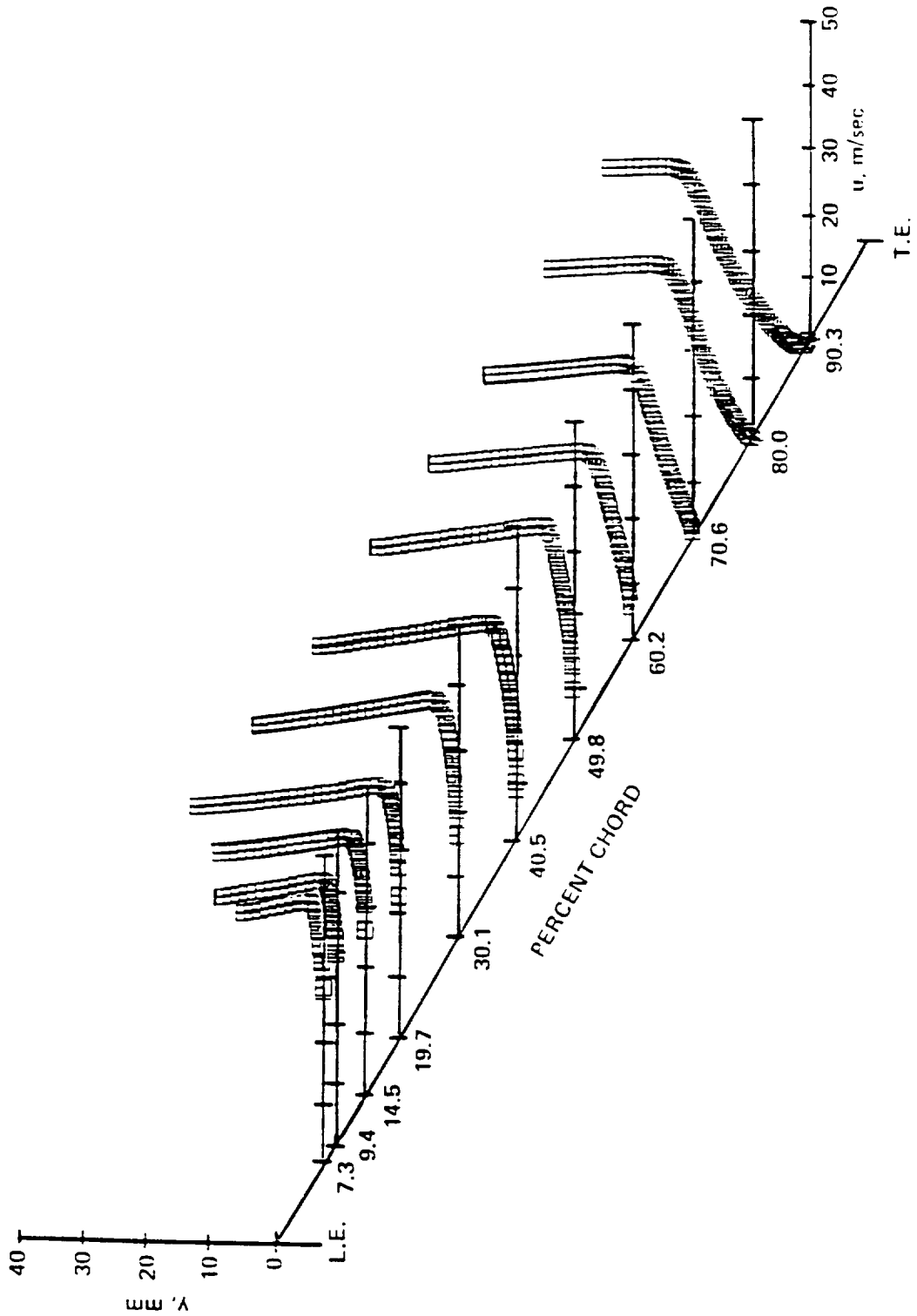

Figure 12. Measured suction surface boundary layers for $i = -1.5$ degrees

the pressure distribution and the surface flow visualization, separation occurs near the trailing edge.

LDV measurements of the near wakes were made at 106.0% chord and 109.7% chord, while five-hole probe measurements of the far wake were made at 131.9% chord. Figure 13 shows the mean values and 95% confidence bands for the measurements of all three wake profiles. Similarly to the 5.0 degree incidence, the near wakes are asymmetric and show negative mean velocities at the wake center. The far wake shows symmetry and a much shallower depth than the near wakes. Surprisingly, however, the width of the far wake is similar to the widths of the two near wakes.

Flow Field for a -8.5 Degree Incidence

A third periodic, two-dimensional flow field was established by once again rotating the entire test section. Inlet five-hole probe measurements yielded an incidence angle of -8.5 degrees and a Re_c of 507,000. The average (gage) measurements of $p_1 = -315.8$ Pa and $p_{T_1} = 351.6$ Pa result in an average inlet velocity of 33.28 m/sec. The outlet flow profile and the corresponding turning angles of figure 14 show a substantially different flow field at this incidence angle than the flow fields that existed at the first two incidence angles. The periodic flow field shows very small wakes as measured with a five-hole probe 31.9% chord downstream of the blade trailing edge–indicating a substantially reduced region of separation.

The five-hole probe measurements give an average turning angle of 45.1 degrees and a $\overline{C_{p_2}}$ of 0.421. The velocity triangles in figure 4 show this reduced turning of the flow. A deviation angle of 11.4 degrees and a $\overline{\omega}$ of 0.028 also indicate a reduced region of separation relative to the values from the first two incidence angles. Using the equation of Lieblein and Roudebush

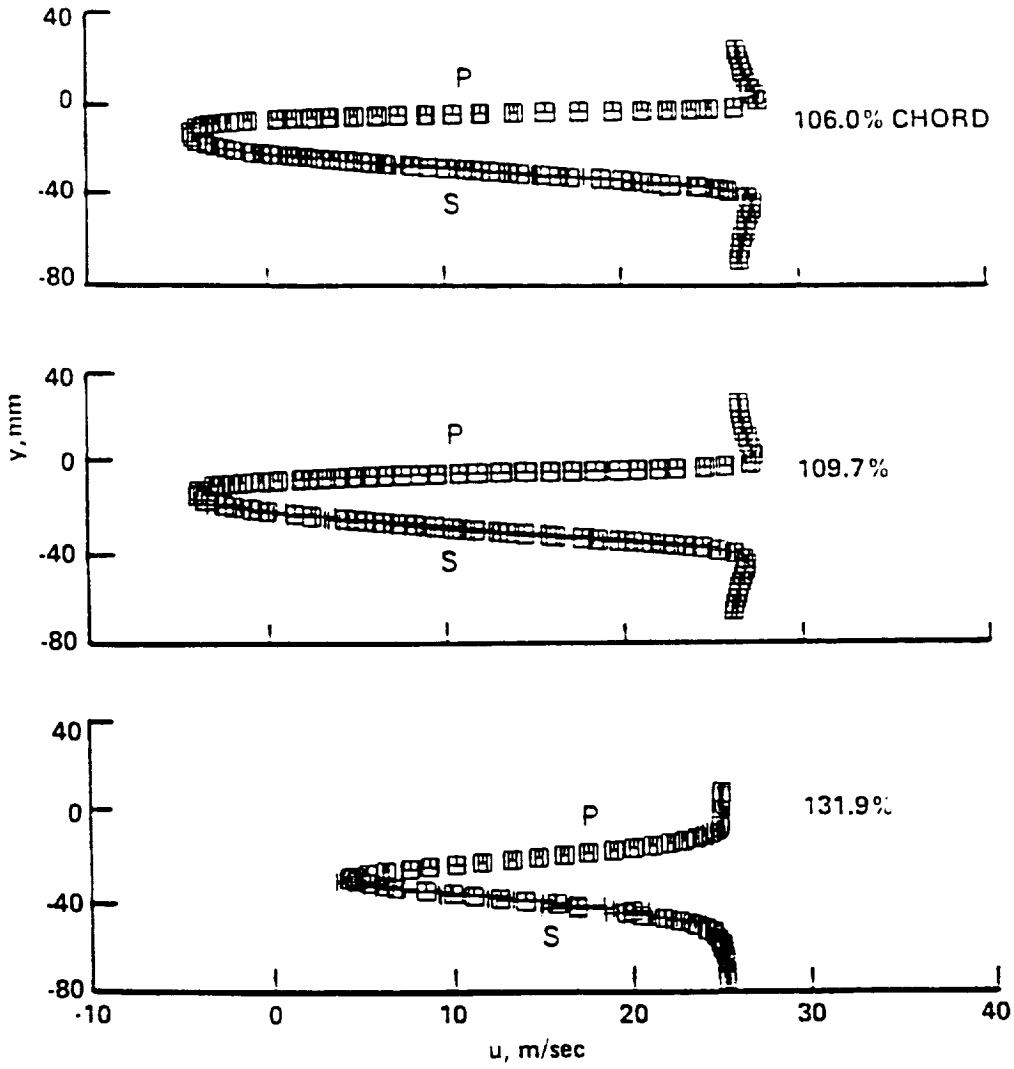

Figure 13. Measured wakes $i = -1.5$ degrees

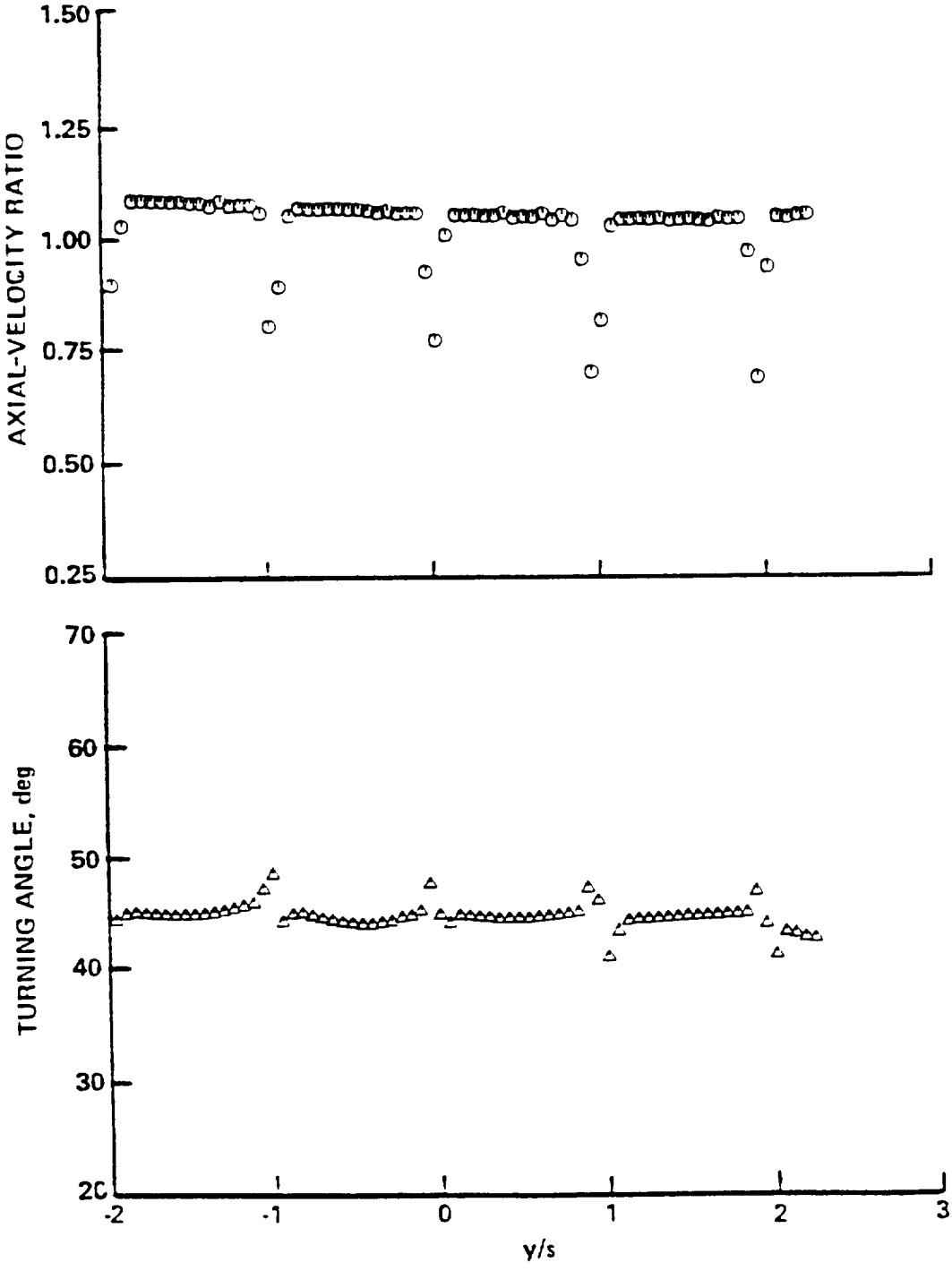

Figure 14. Five-hole probe outlet survey for $i = -8.5$ degrees

[1956], we computed values for $\bar{\omega}$ of 0.024 and 0.018 using the far-wake data at 131.9% chord and 152.6% chord, respectively. A diffusion factor of 0.452 also shows a reduced risk of separation.

The blade static-pressure distribution, as seen in figure 15, for $i = -8.5$ degrees shows the difference in this new flow field even more clearly. Notice that the chord location of maximum blade loading has moved from the leading edge, downstream to about 21% chord. The large adverse streamwise pressure gradient near the leading edge has shifted from the suction surface to the pressure surface. This shift implies that a leading edge separation occurs on the pressure surface for this incidence angle. The adverse gradient on the pressure surface becomes less severe with downstream distance until near 75% chord, where a favorable gradient gradually becomes more pronounced towards the trailing edge. A strong acceleration of the flow exists on the first 18% chord of the suction surface and one would expect laminar boundary layers in this region. Either transition or separation should be expected on the aft 82% chord where the flow decelerates. Unlike the pressure distributions for the first two incidence angles, however, no extended region of zero streamwise pressure gradient exists near the trailing edge of the suction surface indicating no extended region of separation.

For this incidence angle, we attempted two types of surface flow visualization: the chemical sublimation method and the oil film method. Both methods showed a very two-dimensional flow on the pressure surface with only one distinct flow region. The oil film method showed oil accumulating near the leading edge before the pattern of "wall streamlines" formed which indicated a possible separation and reattachment. On the suction surface, however, both methods showed some interesting results. To 95% confidence, the oil film method showed that the flow detached from the surface at 35.3% $\pm$ 2.0% chord and reattached to the surface at 59.8% $\pm$ 2.3% chord. Meanwhile, the chemical sublimation method showed transition to occur at 56.0% $\pm$ 0.8% chord. Evidently, the appearance of a separation "bubble" triggered transition from laminar to turbulent flow. The oil film method also showed a possible separation very near the trailing

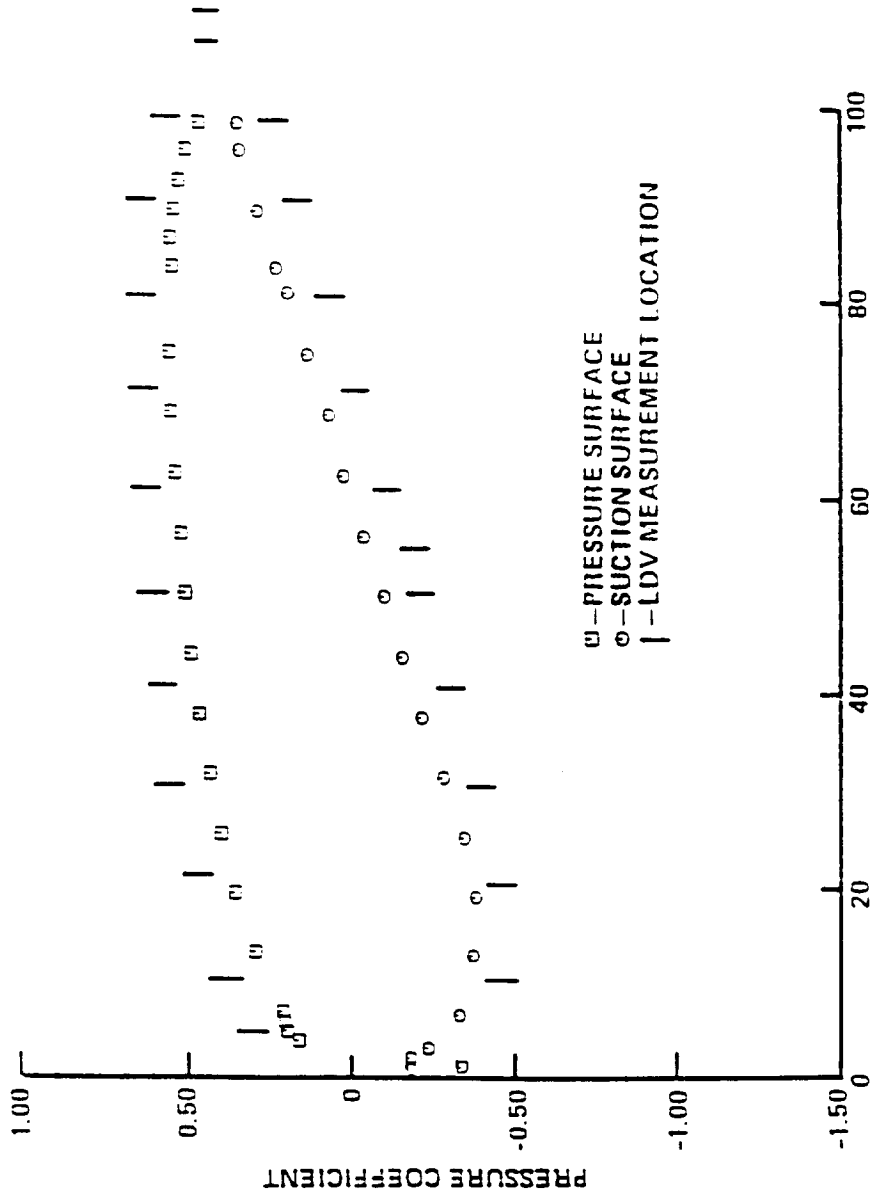

Figure 15. Blade static-pressure distribution for $i = -8.5$ degrees

edge and evidence of the corner disturbances near the side walls. However, both surface flow visualization methods showed an adequate core region of two-dimensional flow.

Figures 16 and 17 show the LDV measured velocity profiles–both mean values and 95% confidence bands–on the pressure and suction surfaces, respectively. The normal pressure gradients are linear as they were when $i = -1.5$ degrees. Near the leading edge of the suction surface, no discernable boundary layer could be measured since the strong acceleration causes the boundary layers to be very thin. Near the 35.3% chord location where the oil film method indicated separation, we found it very difficult to obtain a high data rate. Also, even though we measured no negative mean velocities, we did measure some negative instantaneous velocities. A separation "bubble" seemed to be indicated.

Wakes were measured in two locations in the near wake region and two locations in the far wake region. Figure 18 shows the LDV measurements at 106.0% chord and 109.7% chord and the five-hole probe measurements at 131.9% chord and 152.6% chord. As one might guess, these wake profiles look quite different from the wake profiles for the other two incidence angles. The near wakes are nearly symmetric and show no mean negative velocities–again indicating that no large region of separation occurs at the blade trailing edge. The symmetric far wake profiles become much less deep but change very little in width.

Because of the indications from both the surface flow visualization and the LDV measurements that a large separation "bubble" appeared on the suction surface, we decided to make further measurements with some flush-mounted hot-film probes. The probes were epoxied to the suction surface in the pattern shown in figure 19. The spanwise staggering of the probes prevented the possibility of one probe shedding a wake onto a downstream probe. Also the electrical wires from each probe were taken straight downstream to the trailing edge and not directly to a side wall to minimize any interaction with the other probes. As viewed on an oscilloscope, the direct voltage signals from the probes clearly indicated a sharp transition from small amplitude

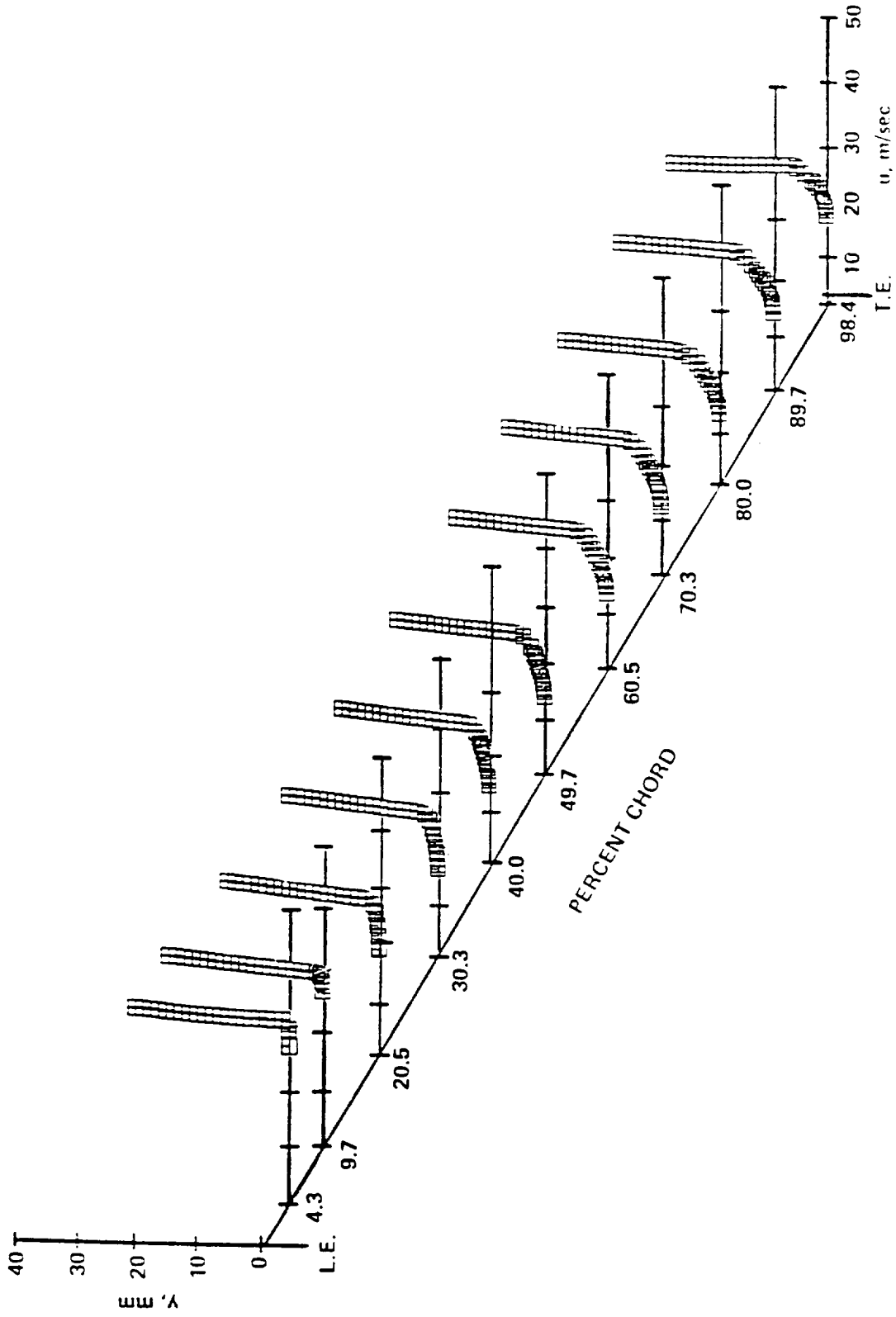

Figure 16. Measured pressure surface boundary layers for $i = -8.5$ degrees

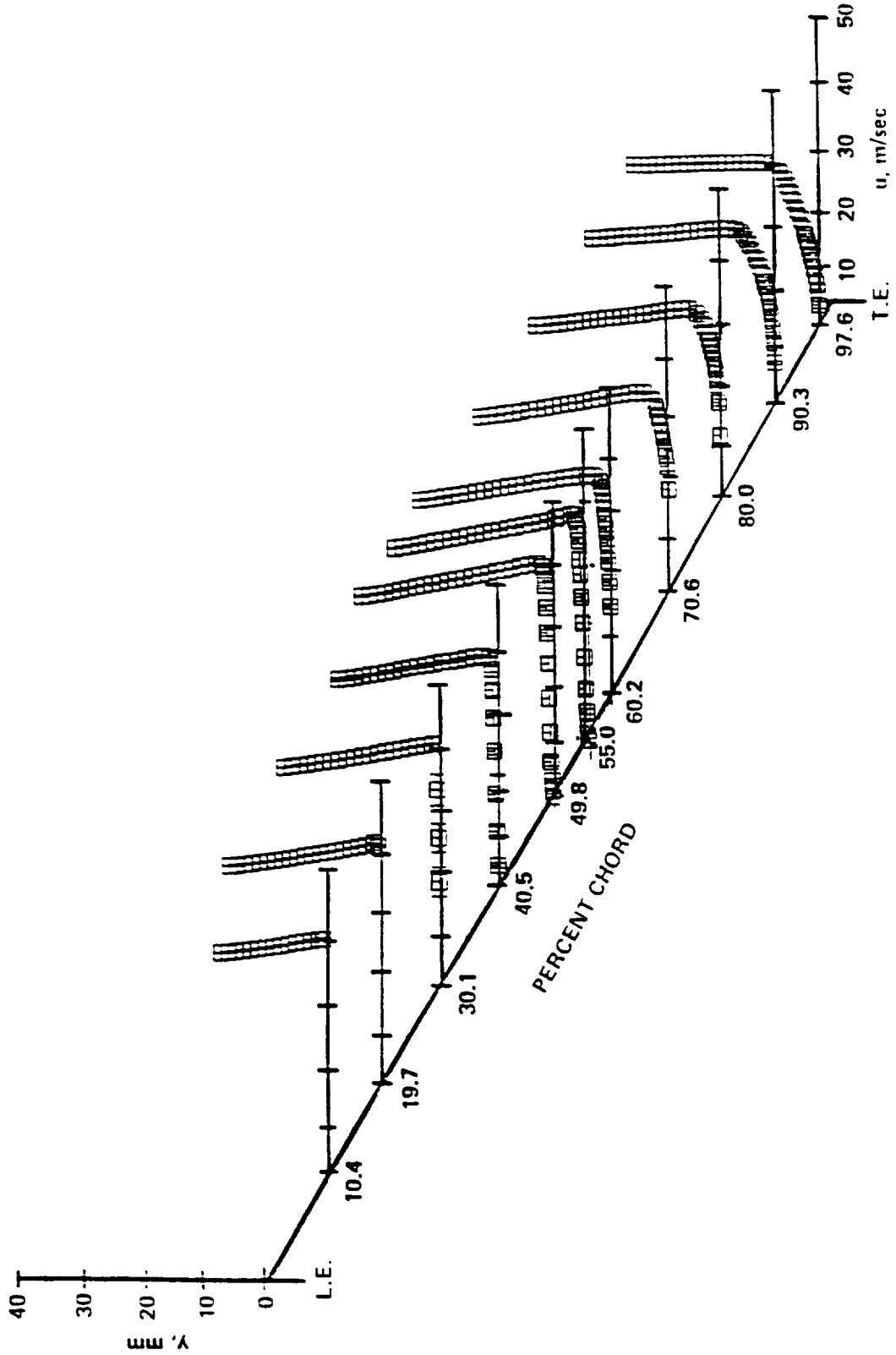

Figure 17. Measured suction surface boundary layers for $i = -8.5$ degrees

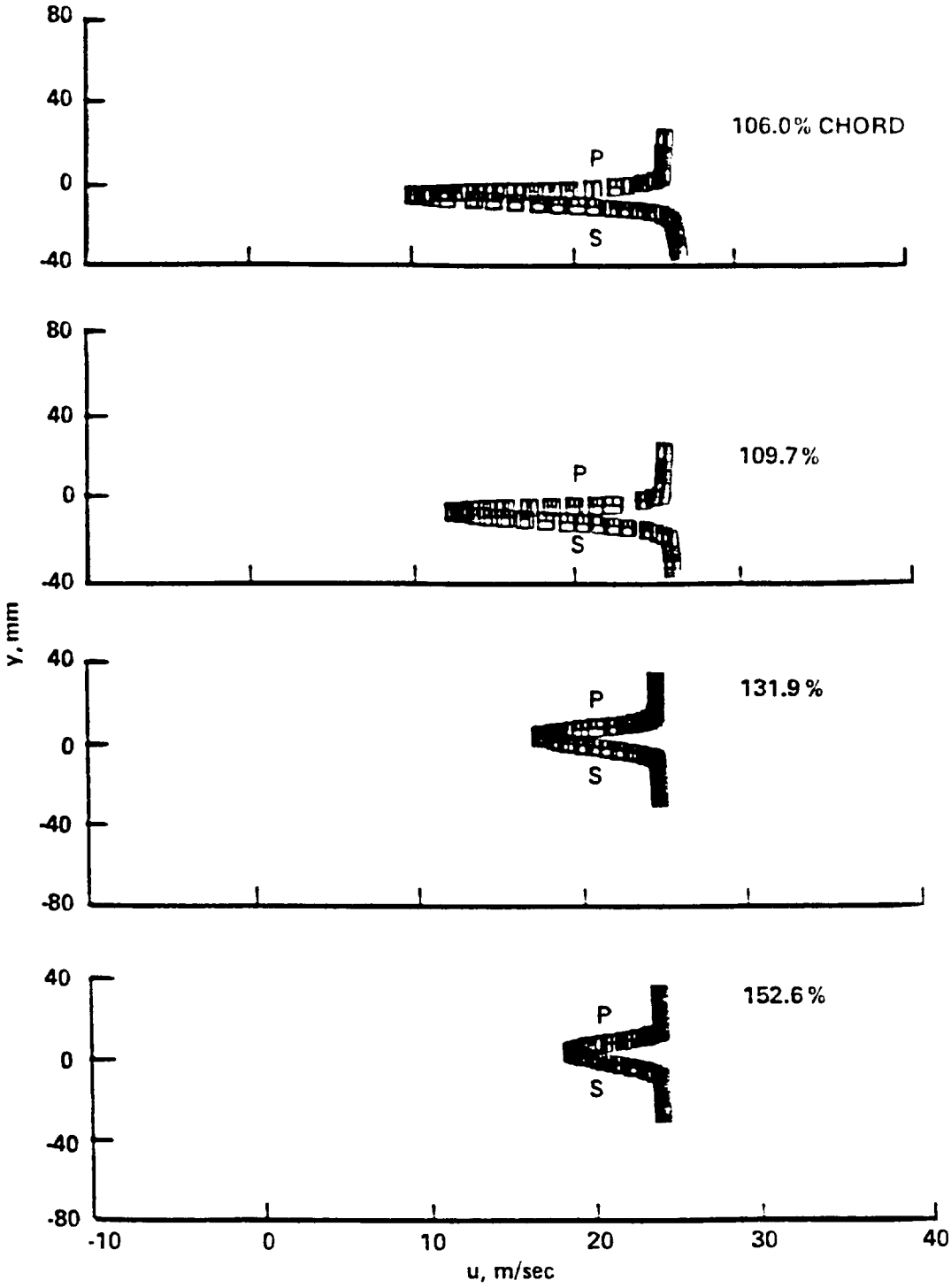

Figure 18. Measured wakes for $i = -8.5$ degrees

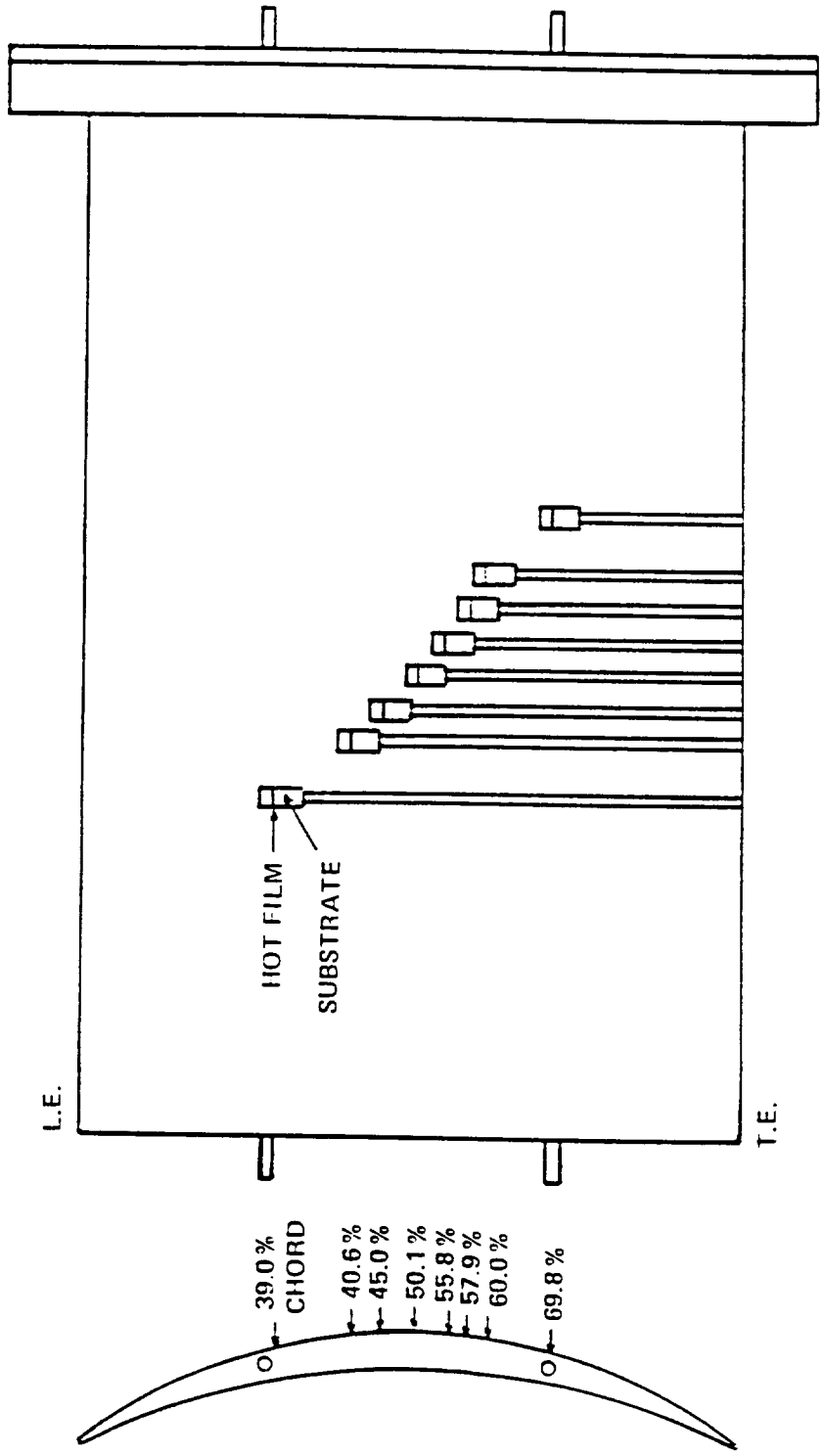

Figure 19. Locations of the flush-mounted hot-film probes on the suction surface for $i = -8.5$ degrees

oscillations to large amplitude oscillations at the probe location of 55.8% chord–indicating a sudden onset of transition. Since the rough calibration of the hot-film signals requires information from the analyzed LDV measurements, we shall wait to further discuss these results.

Chapter 6 Method of Analysis

In the previous chapter, detailed measurements of boundary layers and wakes have been presented. In order for us to better understand the physics of this complex flow field, we need a method to analyze the data. Two typical profiles will be used as examples in explaining this method of analysis. Figures 20a and 21a show these typical profiles. A strong normal pressure gradient affects both of these boundary layers and masks even the most fundamental boundary layer properties. Moreover, experience has shown that even without the complication of a strong normal pressure gradient, the state of the boundary layer (laminar, transitional, or turbulent) is often not self evident and the method for calculating the properties of the layer is often not obvious.

In this chapter, we will present a method of boundary layer analysis which draws on available theoretical and empirical formulations. The analysis describes methods of reconstructing boundary layer profiles from data influenced by a normal pressure gradient, of comparing data against standard laminar and turbulent profiles, and of generating important boundary layer parameters. The analysis encompasses laminar, transitional, turbulent, and separated boundary layers as well as wakes. Finally, we include some fundamentals of the analysis of random data.

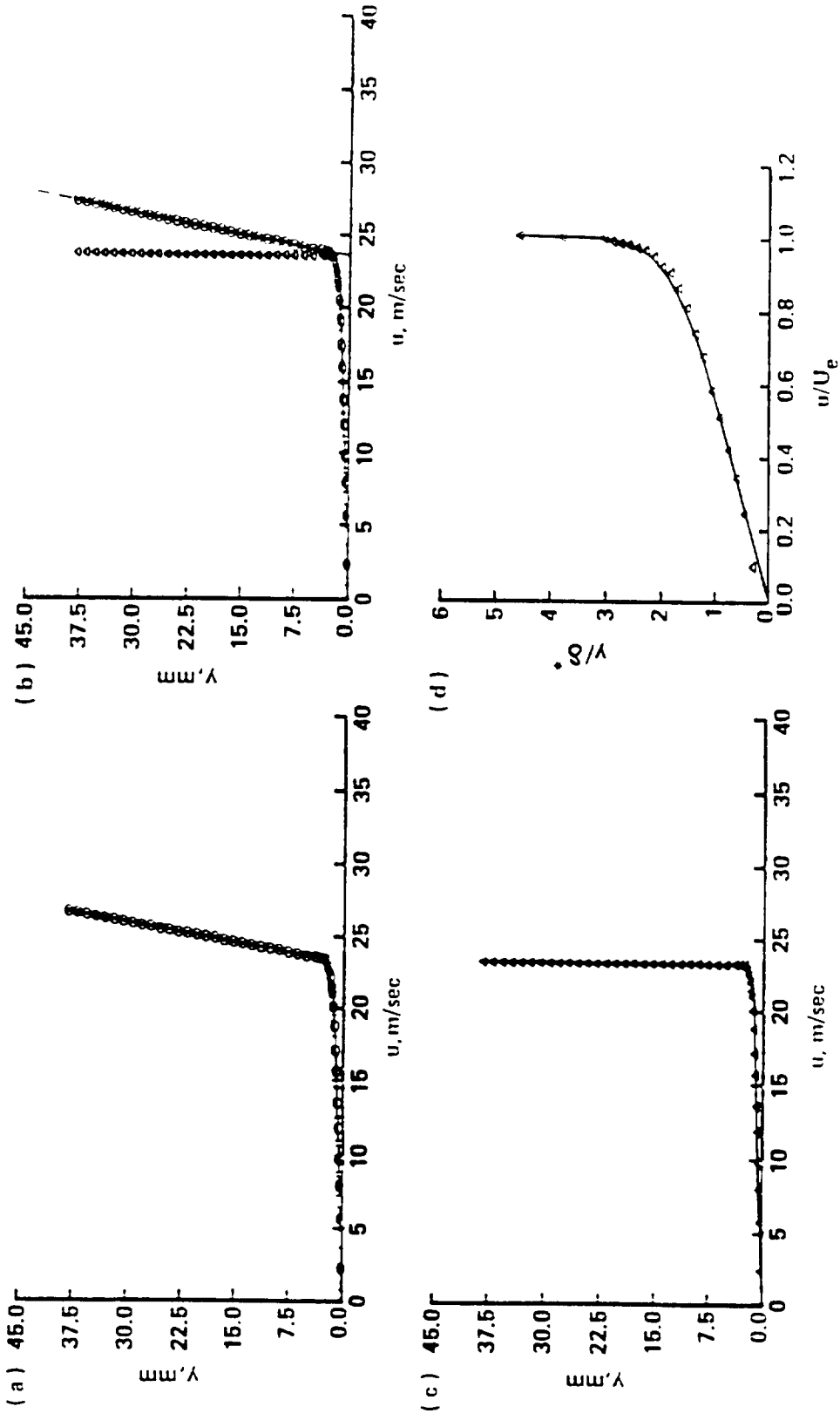

Figure 20. Boundary layer with $\partial p/\partial y < 0$ at 57.2% chord of the pressure surface for $i = 5.0$ degrees: (a) measured velocity profile; (b) boundary layer reconstruction; (c) reconstructed velocity profile with a spline fit; and (d) outer variable plot of the reconstructed velocity profile with a Falkner-Skan solution

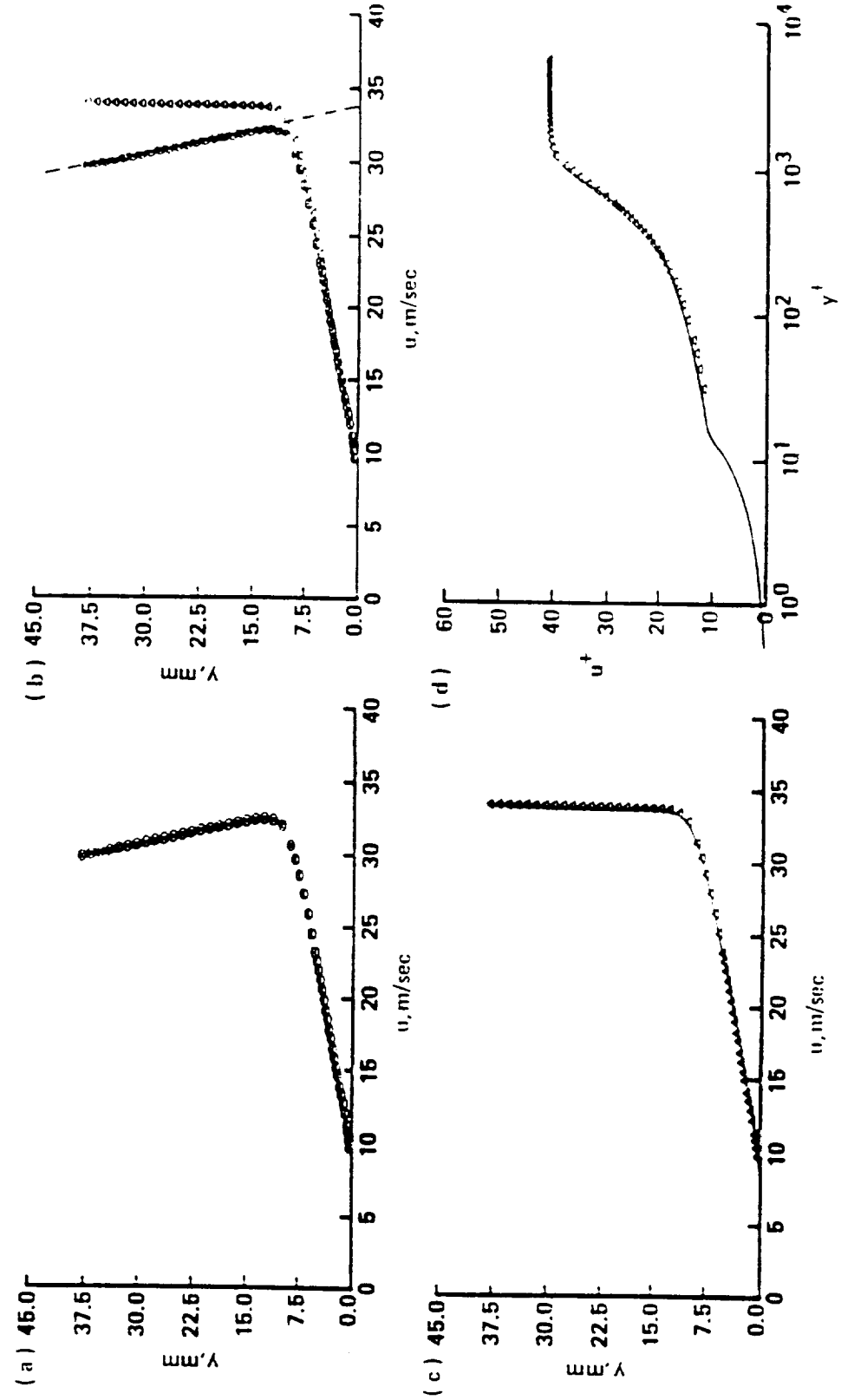

Figure 21. Boundary layer with $\partial p/\partial y > 0$ at 53.6% chord of the suction surface for $i = 5.0$ degrees: (a) measured velocity profile; (b) boundary layer reconstruction; (c) reconstructed velocity profile with a spline fit; and (d) inner variable plot of the reconstructed velocity profile with a fit to the wall-wake equation

Normal Pressure Gradient

Surface curvature, blowing, or suction may induce significant streamline curvature in a flow. Streamline curvature in turn causes a normal pressure gradient which results in a cross streamline gradient in the inviscid velocity profile. As shown in figures 20a and 21a, the freestream velocity does not reach a constant value (the edge velocity, U_e). Boundary layer analyses, however, assume that the location of the boundary layer edge is known and that a constant freestream velocity exists outside the boundary layer. To use or formulate a boundary layer analysis, the procedure must account for the effect of the normal pressure gradient.

Mellor and Wood [1971] and Ball, Reid, and Schmidt [1983] outlined one method which accounts for these effects. The method assumes that the measured velocity profiles represent composite profiles. This implies that each of the profiles has a region where the viscous effects predominate, a region in which viscous effects are negligible, and an intermediate region in which the viscid-inviscid results match. Mathematically, the measured composite profile is the sum of a boundary layer profile and an inviscid profile, less what appears in both. The last quantity is commonly called the boundary layer edge velocity, U_e. That is,

$$u_{\text{meas}} = u + u_{\text{inv}} - U_e \ .$$

Clearly, both the boundary layer velocity, u, and the measured velocity, u_{meas}, must go to zero at the wall, so that

$$U_e = (u_{\text{inv}})_{\text{wall}}$$

and the scheme reduces to finding the value of the inviscid velocity at the wall.

The validity of applying this procedure to velocity data is difficult to establish. However, it does allow for a consistent method to analyze measured velocity profiles provided that the

inviscid region can be properly identified from the data. There does not appear to be a rigorous way to do this, so a consistent method which produces plausible results is adopted.

A least-squares technique is used to fit a polynomial to the inviscid velocity profile. Since the inviscid profiles may have significant curvature, the analysis provides an option of fitting the inviscid profile with a linear, quadratic, or cubic polynomial. The difficulty lies in choosing the data points to be included in the least-squares analysis. To minimize this problem, the number of data points used in the polynomial fit was varied. First, the maximum number of points, $N_{\max}$, which could possibly be within the inviscid region was determined. For $\partial p/\partial y > 0$ (as an example, see figure 21a), $N_{\max}$ is taken to be the number of points between the point furthest from the wall and the point of maximum velocity. For $\partial p/\partial y < 0$ (as an example, see figure 20a), the data point at which the profile slope changes by at least 50% is used instead of the point of maximum velocity. For the data in figure 21a, $N_{\max}$ was determined to be 20, while $N_{\max}$ was found to be 24 for the data of figure 20a. Many applications have shown that for the region of $0.55N_{\max} \leq N_{\text{inv}} \leq 0.95N_{\max}$, the value of U_e is relatively independent of the number of points in the fit. This is clearly shown for the data of figures 20a and 21a in table 3 where polynomials were extrapolated to the wall to obtain values of U_e. Table 3 also gives the mean and 95% confidence bands of all values of U_e. The degree of the polynomial was chosen to minimize the 95% confidence bands of U_e. These 95% confidence bands have been observed to be quite small (~0.5%).

A u profile was calculated using the mean value of U_e and a polynomial fit of u_{inv}. We used $N_{\text{inv}} = 0.75N_{\max}$ as the number of data points in the fit to determine u_{inv} as the U_e found in this way was consistently close to the average U_e. A smoothed spline fit of the boundary layer velocity profile was used to calculate the boundary layer thickness, δ. δ is taken at the position at which

$$u = 0.99U_e \, .$$

Table 3. Variation of U_e and δ with the number of data points used in the polynomial fits of the inviscid regions at (a) 57.2% chord of the pressure surface for $i = 5.0$ degrees and (b) 53.6% chord of the suction surface for $i = 5.0$ degrees (linear fits were used for both of these boundary layers)

(a)

N_{inv}	U_e, m/sec	δ, mm
13	23.36	2.30
14	23.37	2.31
15	23.38	2.33
16	23.39	2.34
17	23.41	2.37
18	23.40	2.35
19	23.40	2.35
20	23.40	2.35
21	23.40	2.35
22	23.40	2.35
23	23.40	2.36
	23.39 ± 0.01	2.34 ± 0.01

(b)

N_{inv}	U_e, m/sec	δ, mm
11	33.81	11.50
12	33.82	11.51
13	33.83	11.53
14	33.85	11.58
15	33.83	11.54
16	33.82	11.52
17	33.80	11.47
18	33.79	11.44
19	33.78	11.44
	33.81 ± 0.02	11.50 ± 0.04

Figures 20b and 21b show the reconstructed boundary layer profiles using linear polynomial fits in the inviscid regions. As might be anticipated, the effect of the normal pressure gradient does not penetrate far into the boundary layer.

After comparing plots of the shape of the resulting turbulence intensity for several boundary layers versus normalized distance from the wall (y/δ) against classical measurements,[12] we concluded that the technique does indeed give reasonable results. Remember that the values of U_e are only a result of this technique for analyzing boundary layers with a normal pressure gradient; these values of velocity may not exist in the actual flow. For instance, boundary layers with $\partial p/\partial y > 0$ give a U_e larger than any measured values of u. Therefore, if we use these values of U_e to compute C_p from the inviscid equation

$$C_p = 1.0 - \left(\frac{U_e}{V_1}\right)^2 ,$$

we will obtain a value of C_p that is less than the measured value of C_p. It should be noted that Kiock [1983] developed an alternate method of accounting for the effects of the normal pressure gradient using the equations for the boundary layer parameters. Compared to the technique just described, however, we found the technique of Kiock [1983] to be more difficult to employ.

General Curve Fit of the Data

Comparisons between boundary layers are often made in terms of simple integral thicknesses or their ratios (shape factors). In order to calculate the boundary layer integral parameters, the analysis fits the velocity data points with a mathematical curve. A parametric cubic spline was used for the curve fit. This curve parametrically develops the u and y ordered pairs as

[12] The turbulent boundary layer measurements of Klebanoff [1954] show that turbulence intensity levels should increase from freestream levels as y is decreased to between 100% and 120% of the boundary layer thickness.

independent functions of the overall arc length of the curve. Even this curve fit tends to oscillate when a cusp appears in the profile. Therefore, a smoothing routine was added to the spline fit. Near the wall, a parametric cubic spline was fit between the data point nearest to the wall and the zero velocity point that would occur at the wall. For boundary layer profiles not well resolved in the near-wall region, this latter fit represents the largest potential error in the calculation of the integral parameters. Figures 20c and 21c show the calculated spline fits to the boundary layer profiles in each example.

Integral Parameters

The most common of the parameters which characterize the boundary layer are integral thicknesses based on the conservation of mass, momentum, and energy. In effect, the boundary layer acts to displace the streamlines in the flow outside the boundary layer away from the wall. A displacement thickness, δ^*, can be defined as the distance by which the solid surface would have to be displaced to maintain the same mass flowrate in a hypothetical inviscid flow. For steady, incompressible flow, δ^* can be defined as

$$\delta^* = \int_0^\infty \left(1 - \frac{u}{U_e}\right) dy \, .$$

δ^* is commonly used as a normalizing factor in presenting data since the alternative, the boundary layer thickness, is difficult to measure. A momentum thickness, θ, can be determined from the steady, incompressible momentum equation as

$$\theta = \int_0^\infty \frac{u}{U_e}\left(1 - \frac{u}{U_e}\right) dy \, .$$

The momentum thickness represents the momentum loss due to the presence of the boundary layer and is proportional to the drag when no streamwise pressure gradient exists. Many empirical

correlations use the momentum thickness. Finally, a steady, incompressible energy thickness can be defined as

$$\delta_3 = \int_0^\infty \frac{u}{U_e}\left[1 - \left(\frac{u}{U_e}\right)^2\right] dy \, .$$

Reynolds numbers can be formed based on all three of these integral thicknesses using the boundary layer edge velocity. They are especially useful in describing the boundary layers just before, during, and just after transition.

Some parameters describe the shape of the velocity profile. The first and second shape factors of the velocity profile are defined as

$$H_{12} = \frac{\delta^*}{\theta}$$

and

$$H_{32} = \frac{\delta_3}{\theta} \, .$$

Note that the definitions require that both shape factors be greater than unity. Schlichting [1979] gives some traditional values for H_{12} based on approximate integral solutions of the boundary layer equations. For laminar boundary layers, H_{12} lies between 3.5 and 2.3. Transition brings about a considerable drop in H_{12} giving a turbulent boundary layer in which H_{12} lies between 1.3 and 2.2. Laminar separation takes place at a value of H_{12} near 3.5 while turbulent separation takes place at a value of H_{12} near 2.2.

In the current study, the integral parameters and shape factors were found by integrating the spline fit using a trapezoidal rule with very fine spacing. Values of these parameters and the associated Reynolds numbers are given in appendix B for each of the profiles shown in figures 20c and 21c as well as all of the other measured boundary layers. A value for H_{12} of 2.86 indicates that the boundary layer in figure 20c is laminar while a value of H_{12} of 1.95 indicates that the boundary layer in figure 21c is turbulent. Based on the work of Purtell, Klebanoff, and Buckley [1981] and Murlis, Tsai, and Bradshaw [1982], one would anticipate that the Re_θ of 452 for the profile of figure 20c is too low to support turbulence.

Laminar Boundary Layers

For a constant streamwise pressure gradient, laminar boundary layers can be plotted in such a way as to collapse them all to the same curve. Such laminar boundary layers are said to be self-similar and solutions to the boundary layer momentum equations may be solved using a similarity solution. A similarity solution reduces the number of variables in the equation by using a coordinate transformation. The boundary layer momentum equation for steady, incompressible flow can be written as

$$u\frac{\partial u}{\partial x} + v\frac{\partial u}{\partial y} = -\frac{1}{\rho}\frac{dp_e}{dx} + \nu\frac{\partial^2 u}{\partial y^2} .$$

Several different coordinate transformations have been used for similarity solutions. One such transformation is the Levy-Lees transformation (see Cebeci and Smith [1974]) which is given as

$$\xi = \int_0^{x/\ell_{\text{ref}}} \frac{U_e}{U_{\text{ref}}}\, d\left(\frac{x}{\ell_{\text{ref}}}\right)$$

and

$$\eta = \frac{1}{\sqrt{2\xi}}\frac{U_e}{U_{\text{ref}}}\frac{y}{\ell_{\text{ref}}}\sqrt{Re}$$

where

$$Re = \frac{\ell_{\text{ref}} U_{\text{ref}}}{\nu} .$$

These transformation variables are for an incompressible flow with a constant value of viscosity. The variables U_{ref} and ℓ_{ref} refer to a reference velocity and a reference length, respectively. A similarity function, f, can then be defined from the streamfunction, ψ, as

$$\psi(x,y) = \sqrt{2\xi}\, f(\xi,\eta)$$

where

$$u = \frac{\partial \psi}{\partial y}$$

and

$$v = -\frac{\partial \psi}{\partial x} .$$

The boundary layer momentum equation for steady, incompressible flow can now be transformed into the following differential equation

$$f''' + f f'' + \beta(1 - f'^2) = 2\xi (f' f'_\xi - f_\xi f'')$$

where

$$\beta = \frac{2\xi}{U_e} \frac{dU_e}{d\xi} .$$

β is a streamwise pressure gradient parameter and can be determined from the measured streamwise static-pressure distribution. These measurements are also required to determine the values of ξ. When f has a prime for a superscript, it refers to a derivative with respect to η. A derivative with respect to ξ is noted by a subscript ξ.

Falkner and Skan [1931] developed a similarity solution for laminar boundary layers flowing over wedges with constant streamwise pressure gradients. In terms of the Levy-Lees coordinates, the Falkner-Skan solution involves no changes in the ξ direction. Thus all derivatives with respect to ξ (of f) are zero and the boundary layer momentum equation for steady, incompressible flow reduces to the following ordinary differential equation:

$$f''' + f f'' + \beta(1 - f'^2) = 0 .$$

The present boundary layer analysis solves this equation using the solution scheme of Hoffman [1983]. The Falkner-Skan solution represents a very good approximation of the laminar boundary layer solution in two cases: first, when the streamwise pressure gradient changes only slowly in the streamwise direction, and second, near the leading edge of the boundary layer surface (since ξ is very small and the Levy-Lees transformed equation is approximated quite well by the Falkner-Skan equation). In the previous equation when β is equal to zero, the Falkner-Skan solution reduces to the original similarity solution of Blasius [1908] for laminar boundary layers with no

streamwise pressure gradient. Separation of the laminar boundary layer will occur for a β with a value of -0.199.

Figure 20d compares the profile of figure 20c with a Falkner-Skan profile at an equivalent β. Although the streamwise pressure gradient is not constant here, the comparison is quite good. The profile of figure 20c is laminar. Integral parameters and skin friction values can be computed from the Falkner-Skan solution. These values are presented in appendix B; where appropriate, they are compared to the values calculated from the spline fit.

Transition

Transition represents the region in which a laminar boundary layer becomes turbulent. Within this region the flow is intermittently turbulent and we can define an intermittency factor as the fraction of time during which the flow at a given position remains turbulent. A fast-response, continuous measuring device, such as a hot-wire or hot-film probe, can be used to measure the intermittency. In "natural" transition, laminar flow instabilities lead to the onset of transition where the intermittency factor first becomes larger than zero. At some point after this onset, changes occur to the mean-velocity profiles as the profiles gradually transition into fully turbulent profiles and the intermittency factor becomes one. The length of the transition region depends strongly on, among other parameters, the streamwise pressure gradient and the freestream turbulence intensity. As we shall see in chapter 7, the presence of a separation "bubble" can instigate transition from laminar to turbulent flow since the separated shear layer can be very unstable. In this case, the length of the transition is much shorter than is the case for "natural" transition.

Abu-Ghannam and Shaw [1980] developed empirical equations to help determine the onset and completion of "natural" transition. Here, transition is defined as the region where the

intermittency factor goes from zero to one. These relationships include the effect of freestream turbulence, $(\sqrt{u'^2}/U_e)_e$, and a streamwise pressure gradient parameter,

$$\lambda_\theta = \frac{\theta^2}{\nu}\frac{dU_e}{dx} .$$

The value of Re_θ at the onset of transition is found from

$$Re_{\theta,s} = 163 + \exp\left[F(\lambda_\theta) - \frac{F(\lambda_\theta)}{6.91}\left(\frac{\sqrt{u'^2}}{U_e} \times 100\right)_e\right]$$

where

$$F(\lambda_\theta) = 6.91 + 12.75\,\lambda_\theta + 63.64\,\lambda_\theta^2$$

for adverse pressure gradients ($\lambda_\theta < 0$) and

$$F(\lambda_\theta) = 6.91 + 2.48\,\lambda_\theta - 12.27\,\lambda_\theta^2$$

for favorable pressure gradients ($\lambda_\theta > 0$). Comparing $Re_{\theta,s}$ with measured values of Re_θ gives the location of the onset of transition and $Re_{x,s}$. The value of Re_θ at the completion of transition is found from

$$Re_{\theta,e} = 540 + 183.5\,(0.000168\,Re_{x,s}^{0.8} - 1.5)(1 - 1.4\,\lambda_\theta) .$$

Once again, this value can be compared with measured values of Re_θ to locate the end of transition.

The incomplete transition of the pressure surface profiles for the 5 degree incidence angle is shown in figure 22. Here the transition is termed incomplete as the value of Re_θ for the profile at 97.9% chord is below that believed capable of sustaining full turbulence. The value of Re_θ is 413 while we computed $Re_{\theta,e} = 549$ from the empirical equations of Abu-Ghannam and Shaw [1980].[13] Note the comparison with the Falkner-Skan profiles, particularly the thickening of the profile in the near-wall region.

---

[13] Later, we observed no discernible logarithmic region within this boundary layer–a region that characterises all turbulent boundary layers.

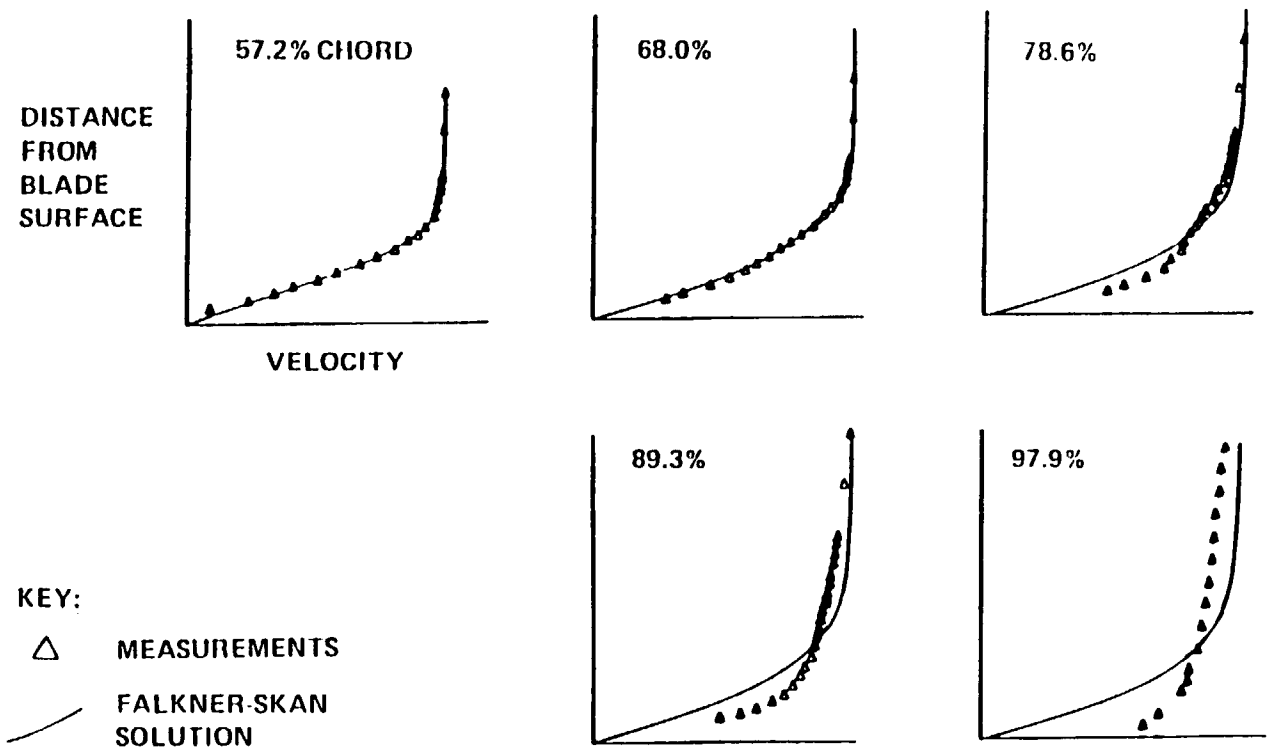

Figure 22. Incomplete transition of the pressure surface boundary layers for $i = 5.0$ degrees

Turbulent Boundary Layers

Turbulent boundary layers are commonly divided into different regions. The innermost region is dominated by viscous shear and is self-similar for all turbulent boundary layers. This region is call the viscous sublayer and is described by

$$\frac{u}{u_\tau} = \frac{y u_\tau}{\nu}$$

or

$$u^+ = y^+$$

where u^+ and y^+ are called inner variables. u_τ is called the shear or friction velocity. Outside of the sublayer but still very close to the wall, the velocity is logarithmic with distance as

$$u^+ = \frac{1}{\kappa} \ln(y^+) + C .$$

Turbulent shear dominates viscous shear in this logarithmic region. The viscous sublayer and logarithmic region overlap in a region called the buffer layer. Collectively the viscous sublayer, buffer layer, and logarithmic layer are called the "law of the wall." Streamwise pressure gradients have essentially no effect on this region. Outside of this wall region, the streamwise pressure gradients are important and the velocity profile exhibits a wake-like form. Coles [1956] developed an equation for the wake region called the "law of the wake." His composite equation included a wake-like function added to the logarithmic equation. This wall-wake equation can be written as

$$u^+ = \frac{1}{\kappa} \ln y^+ + C + \frac{\Pi}{\kappa} W\left(\frac{y}{\delta}\right)$$

where

$$W\left(\frac{y}{\delta}\right) = 2 \sin^2\left(\frac{\pi y}{2\delta}\right) = 1 - \cos\left(\frac{\pi y}{\delta}\right) .$$

$W(\ )$ is called Coles' universal wake function and is normalized to be zero at the wall and to be two at $y = \delta$. Coles' wake parameter Π brings in the effect of the streamwise pressure gradient and has a value from 0.5 to 0.6 for a zero pressure gradient flow. Coles and Hirst [1968] later examined the data from a number of turbulent boundary layer experiments and determined that the von Karman mixing length parameter, κ, should be 0.41 and the law-of-the-wall constant, C, should be 5.0.

The analysis of turbulent boundary layers should include a fit of the data to the wall-wake equation. A least-squares fit of the data to the equation was chosen with u_τ and Π as the variables to be determined and δ considered to be a known quantity.[14] The error between each data point and the wall-wake equation is

$$E_n = \frac{u_\tau}{\kappa} \ln\left(\frac{y_n u_\tau}{\nu}\right) + u_\tau C + \frac{u_\tau \Pi}{\kappa}\left[1 - \cos\left(\frac{\pi y_n}{\delta}\right)\right] - u_n \, .$$

Now the minimum error squared of all the data points must be found with respect to both u_τ and Π. Taking the partial derivative of the error squared for each data point with respect to u_τ and Π yields

$$\frac{\partial E_n^2}{\partial u_\tau} = 2E_n \left\{\frac{1}{\kappa} \ln\left(\frac{y_n u_\tau}{\nu}\right) + \frac{1}{\kappa} + C + \frac{\Pi}{\kappa}\left[1 - \cos\left(\frac{\pi y_n}{\delta}\right)\right]\right\}$$

and

$$\frac{\partial E_n^2}{\partial \Pi} = 2E_n \left\{\frac{u_\tau}{\kappa}\left[1 - \cos\left(\frac{\pi y_n}{\delta}\right)\right]\right\} \, .$$

Summing for all the data points and setting the two expressions equal to zero give two equations

$$\sum_{n=1}^{N} \frac{\partial E_n^2}{\partial u_\tau} = 0$$

and

$$\sum_{n=1}^{N} \frac{\partial E_n^2}{\partial \Pi} = 0$$

---

[14] An attempt to use all three variables (u_τ, Π, and δ) in a least squares scheme produced inconsistent results.

which can be solved simultaneously for u_τ and Π to give the minimum squared error. A secant method is used to solve the simultaneous non-linear equations. Sun and Childs [1976] presented a similar method for compressible turbulent boundary layers using the velocity transformation of van Driest [1951]. Coles and Hirst [1968] used a least squares-fit using u_τ and δ as the unknown variables with an initial guess of Π. Then, at the position $y = \delta$, they substituted U_e, u_τ, and δ into the wall-wake equation to obtain a new value for Π. They repeated this process until the solution converged.

In order to use the fit of the wall-wake equation, the range of data points to be used in the fit must be considered. White [1974] states that the logarithmic region does not hold for $y^+ < 35$ (corresponding roughly to $y/\delta < 0.02$). For a large wake component, Coles and Hirst [1968] state that the region being fit should not include $y/\delta > 0.9$. They suggest that this number should be reduced to 0.75 for a zero streamwise pressure gradient and 0.6 for a vanishing wake component. Here the region $0.05 \leq y/\delta \leq 0.75$ was used: Sensitivity to the specific range of data points was not large.

Figure 21d shows the data of figure 21c in inner variables where $u_\tau = 0.825$ m/sec and $\Pi = 4.49$. Parameters determined from the wall-wake fit are given in appendix B.

Streamwise pressure gradients can have a strong effect on the outer region of a turbulent boundary layer. We illustrate this in figure 23a by presenting typical profiles for an Re_θ of 5000 and several values of Π. The logarithmic region decreases in size as Π increases and the streamwise pressure gradient becomes more adverse. The size of the logarithmic region also decreases as Re_θ decreases. For illustration, figure 23b shows typical profiles for a Π of 0.5 and several values of Re_θ. Note the difficulty in discerning a logarithmic region for an Re_θ of 500.

Others have made attempts to characterize the turbulent boundary layer profiles. Perry and Schofield [1973] developed a similarity defect law based on the maximum shear stress, $\tau_{\max}$, rather than the wall shear stress, τ_w. The defect law was originally developed for attached boundary

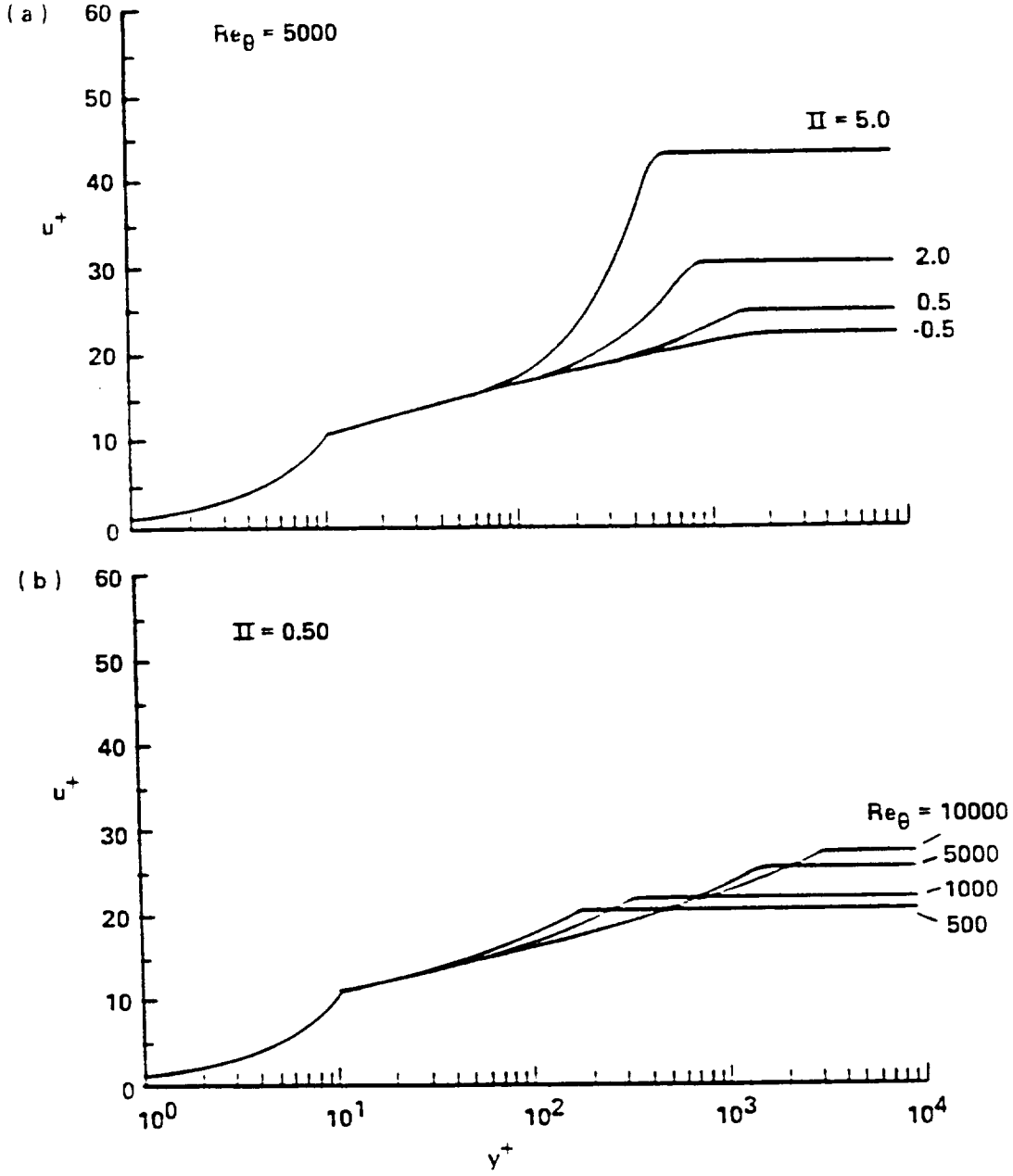

Figure 23. Variation of the wall-wake composite velocity profile with Π and Re_θ

layers under moderate to strong adverse pressure gradients where $\tau_{max}/\tau_w > 1.5$. The defect law is

$$\frac{U_e - u}{U_s} = 1.0 - 0.4\left(\frac{y}{B}\right)^{\frac{1}{2}} - 0.6\sin\left(\frac{\pi y}{2B}\right)$$

where

$$U_s = 8.0\left(\frac{B}{L}\right)^{\frac{1}{2}} U_m$$

and

$$B = 2.86\,\delta^*\left(\frac{U_e}{U_s}\right) .$$

U_m is a velocity scale based on the maximum shear stress ($U_m = \sqrt{\tau_{max}/\rho}$) and L is the distance from the wall to τ_{max}. The velocity scale U_s is found using the methodology that Clauser [1954] used to determine u_τ. A half-power equation is used near the wall,

$$\frac{u}{U_e} = 0.47\left(\frac{U_s}{U_e}\right)^{\frac{3}{2}}\left(\frac{y}{\delta^*}\right)^{\frac{1}{2}} + 1.0 - \frac{U_s}{U_e} .$$

Perry and Schofield [1973] suggested using the defect law for the outer 90% of the boundary layer with the half-power equation forming the innermost portion of that defect law. They recommended the law of the wall as an inner wall matching condition.

Figure 24 shows an example of how to obtain the proper scales for the similarity defect law of Perry and Schofield [1973]. First, we plot the measured boundary layer data as u/U_e versus $(y/\delta^*)^{1/2}$ and then find a value of U_s/U_e such that the half-power equation of Perry and Schofield [1973] is somewhere tangent to the distribution of data points. Figure 24a shows this procedure. Note that this procedure can be very difficult to employ since the half-power equation only intersects the data points in some cases. Now we can compute B and plot the data as $(U_e - u)/U_s$ versus y/B along with the similarity defect law. Figure 24b shows similarity in the outer 90% of the boundary layer.

Most analyses, short of direct computation, consider boundary layers in which the pressure gradient is constant, so that the profiles are self-similar with downstream distance–so called

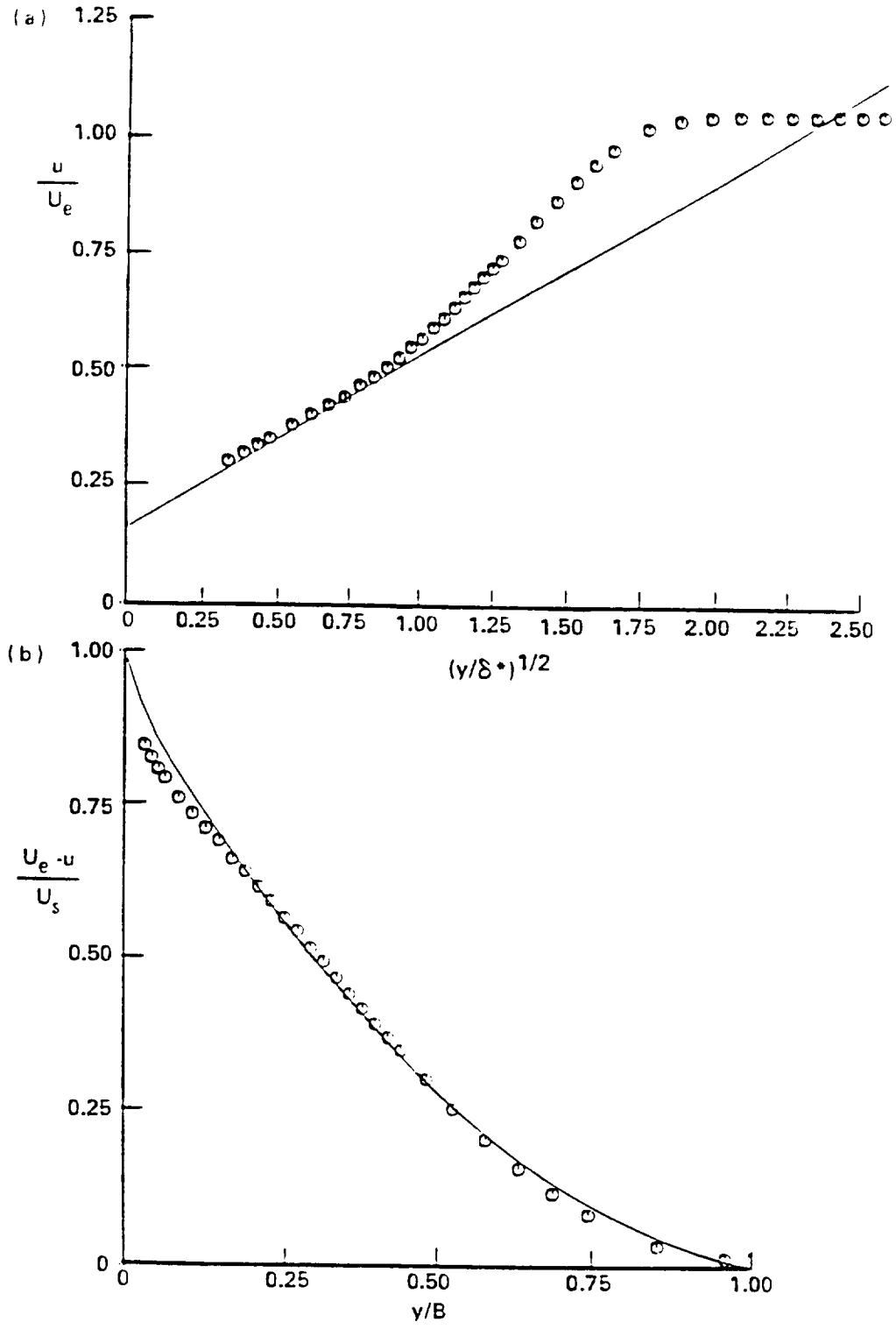

Figure 24. Turbulent boundary layer at 53.6% chord on the suction surface for $i = 5.0$ degrees showing (a) the half-power equation of Perry and Schofield and (b) the similarity defect law of Perry and Schofield

equilibrium layers. Clauser [1954, 1956] conceived of a parameter

$$\beta_c = \frac{\delta^*}{\tau_w}\frac{dp_e}{dx}$$

to characterize equilibrium. A turbulent boundary layer with a constant β_c has outer region similarity and is called an equilibrium turbulent boundary layer. All of the gross properties of that boundary layer can be described with a single parameter. Clauser [1954, 1956] chose the parameter G, where

$$G = \frac{1}{\Delta}\int_0^\infty \left(\frac{U_e - u}{u_\tau}\right)^2 dy$$

and

$$\Delta = \int_0^\infty \left(\frac{U_e - u}{u_\tau}\right)^2 dy \, .$$

G is called Clauser's shape factor and Δ is termed the defect thickness. For the turbulent boundary layer in figure 21c, we computed $\beta_c = 7.63$, $G = 19.41$, and $\Delta = 141.76$ mm. Most of the turbulent boundary layer profiles on the cascade blade are nonequilibrium. In practice, one expects nonequilibrium to be the rule rather than the exception.

Another parameter used to characterize equilibrium turbulent boundary layers is Π. Coles [1956] suggested an equation for Π,

$$\Pi = \kappa\left(\frac{\delta^*}{\delta}\right)\left(\frac{U_e}{u_\tau}\right) - 1.0 \, .$$

For the data in figure 21c, this equation gives $\Pi = 4.12$ while the least-squares fit of the data to the wall-wake equation gives $\Pi = 4.49$.

Ludweig and Tillman [1949] developed an empirical expression for the skin friction coefficient, C_f, of a turbulent boundary layer. The curve-fit expression from their experimental data is

$$C_f = 0.246\, Re_\theta^{-0.268}\, 10^{-0.678 H_{12}} \, .$$

The skin friction coefficient, shear velocity, and wall shear stress can be related by

$$C_f = \frac{\tau_w}{\frac{1}{2}\rho U_e^2}$$

and

$$u_\tau = \sqrt{\frac{\tau_w}{\rho}} .$$

Using this empirical expression, we can compute $u_\tau = 0.852$ m/sec for the data in figure 21c. Remember that we obtained $u_\tau = 0.825$ m/sec by using the least-squares fit of this same data to the wall-wake equation.

Separation

Separation is the entire process of the breakdown of boundary layer flow. For laminar boundary layers, this definition simply refers to the history of the boundary layer leading to a vanishing wall shear stress. However, even for laminar boundary layers, separation might not always occur for a specific shape factor. For turbulent boundary layers, Sandborn and Kline [1961] describe separation as an unsteady, three-dimensional region within the flow. Before the time-average wall shear stress vanishes, local, intermittent separation occurs which gives rise to streaks of instantaneous backflow. For intermittent separation, Sandborn and Kline [1961] proposed the relation

$$H_{12} = 1 + \frac{1}{1 - \frac{\delta^*}{\delta}} .$$

Simpson, Chew, and Shivaprasad [1981a] quantified the various stages of separation with the instantaneous backflow near the wall. Incipient detachment occurs with 1% instantaneous backflow; intermittent transitory detachment occurs with 20% instantaneous backflow; transitory detachment occurs with 50% instantaneous backflow; and detachment occurs when the wall shear stress becomes zero.

Numerical Methods

A primary objective of this research project is to provide very detailed experimental data for future comparisons to numerical, viscous flow computations. As a means of both analysis and comparison, we have selected a "standard" numerical method–namely, the STAN5 code for solving the boundary layer equations.

Crawford and Kays [1976] developed a numerical method (STAN5) for solving the compressible boundary layer equations for both two-dimensional and axisymmetric flows. In our case, we solve the incompressible equations for two-dimensional boundary layers. STAN5 solves the time-averaged continuity equation,

$$\frac{\partial u}{\partial x} + \frac{\partial v}{\partial y} = 0 ,$$

and the time-averaged, boundary layer momentum equation,

$$u\frac{\partial u}{\partial x} + v\frac{\partial u}{\partial y} + \frac{\partial \overline{u'v'}}{\partial y} = -\frac{1}{\rho}\frac{dp_e}{dx} + \nu\frac{\partial^2 u}{\partial y^2} .$$

Crawford and Kays [1976] use the familiar assumption of Boussinesq [1877] that perceives the turbulence as producing stresses on the mean flow. Furthermore, the apparent turbulent Reynolds stress is related to the rate of mean strain through an apparent scaler turbulent or "eddy" viscosity,

$$-\rho\overline{u'v'} = \rho\nu_t\frac{\partial u}{\partial y} .$$

The momentum equation now becomes

$$u\frac{\partial u}{\partial x} + v\frac{\partial u}{\partial y} = -\frac{1}{\rho}\frac{dp_e}{dx} + (\nu + \nu_t)\frac{\partial^2 u}{\partial y^2}$$

and a turbulence model is required to determine ν_t.

Crawford and Kays [1976] use another analogy that relates turbulent action with viscous action, namely, the "mixing length" model of Prandtl [1926]. Prandtl [1926] relates the molecular

kinetic theory for finding the viscosity of a gas to turbulent "kinetic theory" in order to determine the "eddy" viscosity,

$$\nu_t = \ell^2 \left| \frac{\partial u}{\partial y} \right| ,$$

where the length scale ℓ is called the "mixing length." Caution must be taken in using the analogies of Boussinesq [1877] and Prandtl [1926]: No physical reasoning exists for the analogy between viscous and apparent turbulent stresses and the variables ν_t and ℓ are not true fluid properties but flow dependent quantities that can vary throughout the flow field. STAN5 uses very simple models for this variation–models based on experiments for specific flow conditions.

Von Karman [1930] showed empirically that

$$\ell = \kappa y$$

for the logarithmic region. This relation fails in the viscous sublayer and buffer layer, so van Driest [1956] used a damping function to help model ℓ throughout the inner region,

$$\ell = \kappa y \left(1 - e^{-y^+/A^+} \right) .$$

The empirical constant A^+ can be considered to be an effective sublayer thickness (combined thickness of the viscous sublayer and buffer layer). As we discussed earlier, streamwise pressure gradients affect the size of the logarithmic region and thus the effective sublayer thickness. Using data from various experiments, Crawford and Kays [1976] developed a relationship for A^+ when no mass transfer exists,

$$A^+ = \frac{25.0}{\frac{51.475\nu}{\rho u_\tau^3} \frac{dp_e}{dx} + 1.0}$$

for favorable or zero streamwise pressure gradients ($dp_e/dx \leq 0$) and

$$A^+ = \frac{25.0}{\frac{20.59\nu}{\rho u_\tau^3} \frac{dp_e}{dx} + 1.0}$$

for adverse streamwise pressure gradients ($dp_e/dx > 0$). These equations show that favorable streamwise pressure gradients have larger values of A^+ than adverse gradients. Launder and Jones

[1968] felt that the effective sublayer thickness does not change instantaneously to a changing streamwise pressure gradient and suggested the use of a "lagging equation,"

$$\frac{dA^+}{dx^+} = \frac{A^+_{eq} - A^+}{4000.0} .$$

Outside of the wall region of a turbulent boundary layer, Prandtl [1942] observed the empirical approximation

$$\ell = \lambda\delta .$$

However, flows with a low Re_θ have an inner layer which is a fixed fraction of the boundary layer thickness. Therefore, viscous stresses become increasingly more important for lower Re_θ and evidence shows that values of λ are larger for flows with $Re_\theta < 5000$. Crawford and Kays [1976] proposed

$$\lambda = \max \begin{cases} 0.085 \\ 0.25 Re_\theta^{-0.125} \end{cases}$$

for the case with no mass transfer.

STAN5 solves the parabolic boundary layer problem using the finite-difference approximation suggested by Patankar and Spalding [1967]. For laminar boundary layers, STAN5 should give better solutions than the solution of Falkner and Skan [1931] since the streamwise pressure gradient is allowed to vary by providing the outer boundary condition of U_e varying with x. For this boundary condition, we can simply use our measured blade static-pressure distribution. The no-slip condition is applied at the blade surface. For our boundary layers, we used the inner region turbulence models within the viscous sublayer instead of using the optional "wall functions." STAN5 uses the inner region turbulence model when $y \leq \lambda\delta/\kappa$ and uses the outer region turbulence model when $y > \lambda\delta/\kappa$. Since little information exists for modeling the turbulent-like motion within the transition region, Crawford and Kays [1976] use an *ad hoc* model. In the inner region, they create a gradual transition by modifying A^+ when Re_θ exceeds $Re_{\theta,s}$,

$$A^+ = A^+ + (300.0 - A^+)\left\{1.0 - \sin\left[\frac{1.57}{Re_{\theta,s}}(Re_\theta - Re_{\theta,s})\right]\right\}^2 .$$

They employ this equation until $Re_{\theta,e} = 2Re_{\theta,s}$, where the full turbulence model becomes effective in the inner region. Since the boundary layer equations are parabolic, the STAN5 solution becomes unstable for separation of either laminar or turbulent boundary layers.

Wakes

Initially, the analysis of the wake profiles proceeds in the same manner as the analysis of the boundary layer profiles. Since the static pressure is normally constant across the wake, the analysis does not have to account for a normal pressure gradient. A spline is used to curve fit the data points from the point of minimum velocity to the last point in the freestream on one side of the wake. Integral parameters can then be calculated for this side of the wake. The analysis is repeated on the other side of the wake. The integral thicknesses for the entire wake can be found simply by summing the parameters for each side of the wake.

Turbulent wakes show a strong dependence on their history. Near the origin of a turbulent wake, the mean flow and turbulent structure must undergo a drastic change from the characteristics of a boundary layer to the characteristics of a wake. We call this region the near-wake region. Downstream of this near-wake region, the wake begins to show similarity or self-preservation. The mean-velocity profile shows self-preservation well before the turbulent structure. First, the mean static pressure must reach a state of equilibrium, leaving no pressure gradient across the wake. If the static pressure within the two boundary layers forming the wake is quite different, the wake centerline within the near wake will show a significant curvature until the static pressure reaches equilibrium. Next, the mean-velocity profile will become self-preserving and a far-wake region will emerge. Finally, the turbulent structure will become self-preserving. One would expect H_{12} to decay asymptotically to 1.0 as the wake mixes out.

C-2

Wake similarity requires different length scales on the pressure side, L_p, and the suction side, L_s, of the wake. L_p and L_s are the distances on the pressure and suction sides of the wake centerline from the point of minimum velocity to a point where the velocity defect is $\frac{1}{2}(U_e - u_{cl})$. Lakshminarayana and Davino [1980] suggested a Gaussian distribution to correlate the wake data,

$$\frac{U_e - u}{U_e - u_{cl}} = e^{-0.693\eta^2},$$

where η is the distance across the wake normalized by the appropriate length scale. One would expect that only far wakes would show similarity with this type of correlation.

Random Data

Most boundary layer and wake flows vary with time and cannot be described by an explicit mathematical equation. Measurements of these flows result in the acquisition of random data. For random data acquired with a continuous, fast-responding measuring device such as a hot wire or hot film, information can be obtained from the characteristics of the time history. Each time history includes a finite time interval and represents a sample record of a random or stochastic process. The collection of these sample records is called an ensemble. We can take the first moment of each sample record to obtain the mean value and the joint moment of the same random process with a time delay to obtain the autocorrelation function. If the moments are time invariant, the random process is stationary. Furthermore, if the moments for the entire ensemble equal the moments of each sample record, the stationary random process is ergodic.

Histograms of the digitized values of analog sample records can be plotted in a similar manner to the discrete LDV data. As with the LDV data histograms, we can compute the mean value, variance, skewness, and kurtosis. These values allow us to study the time-average properties of

an unsteady process such as the signal of the wall shear stress within a turbulent or separated shear layer.

A fast Fourier transform (FFT) can decompose the finite discrete time series into a set of frequency components. Since the time series is of finite length, the FFT assumes that this finite time series is repeated periodically for all time. Thus, if the amplitudes at the two end points were not equal, many higher frequencies would be necessary to represent this abrupt change in amplitude. Therefore, the FFT requires the signal to be tapered with the use of a spectral "window." Gade and Herlufsen [1988] suggest the use of a Hanning "window" when analyzing most continuous signals. Use of an FFT allows us to observe our sample record in the frequency domain. Thus, we can examine a spectrum of either the amplitude or phase of any time varying property such as the wall shear stress.

Time signals of some unsteady phenomena may contain a range of significant frequencies which is obscured by a broadband signal. In order to extract information from the range of significant frequencies, we can use a digital filter to filter out frequencies not in this range. For instance–as we shall see in chapter 7–the unsteady wall shear stress in the vicinity of a separation "bubble" has a characteristic range of low frequencies which may be difficult to detect because of the presence of many higher frequencies. In that case, we numerically build a low-pass, Butterworth filter with a given cutoff frequency and filter the time signals.

Besides analyzing a single stationary random process, we may want to analyze the relationship between two stationary random processes. If two flush-mounted, hot-film probes measure the time varying values τ_{w_a} and τ_{w_b}, the fluctuations of these simultaneous measurements about the time-average values are related through the correlation coefficient,

$$C_{ab} = \frac{\frac{1}{N}\sum_{n=1}^{N}(\tau_{w_a} - \overline{\tau_{w_a}})(\tau_{w_b} - \overline{\tau_{w_b}})}{\frac{1}{N}\sum_{n=1}^{N}(\tau_{w_a} - \overline{\tau_{w_a}})^2 \cdot \frac{1}{N}\sum_{n=1}^{N}(\tau_{w_b} - \overline{\tau_{w_b}})^2}.$$

The correlation coefficient is normalized such that $C_{ab} = 1$ for identically correlated signals, $C_{ab} = 0$ for uncorrelated signals, and $C_{ab} = -1$ for identically correlated signals with a 180

degree phase shift. The relationship between the two signals can also vary with time. A cross-correlation function is the joint moment of two random processes over the same time span. Both the autocorrelation and cross-correlation functions are time dependent. To obtain information of how random processes are related in frequency, we can use an FFT of these functions to obtain the autospectral density and cross-spectral density functions. Normalising the cross-spectral density function with the square root of the product of the the autospectral density functions for each random process yields the coherence function. These frequency dependent functions give information on both the amplitude and phase.

Chapter 7 Discussion

In the previous chapter, we presented a method for analyzing boundary layers and wakes. Now we can examine the data in light of this method of analysis in order to better understand the physics of the cascade flow field. Note that the value of ρ was taken as 1.205 kg/m^3 and the value of ν was taken as 0.150 cm^2/sec throughout the analysis.

Pressure Surface for a 5.0 Degree Incidence

Figure 6 showed the boundary layers measured on the pressure surface for $i = 5.0$ degrees. After removing the influence of the normal pressure gradient, we compared the reconstructed boundary layer data with a Falkner-Skan velocity profile at the local streamwise pressure gradient. For the velocity profiles measured near the trailing edge, we also attempted to fit the results to the wall-wake equation of Coles [1956]. The velocity profiles are replotted nondimensionally in figure 25. In spite of the influence of both curvature and a changing streamwise pressure gradient on the flow field, the Falkner-Skan approximation appears to reasonably represent the

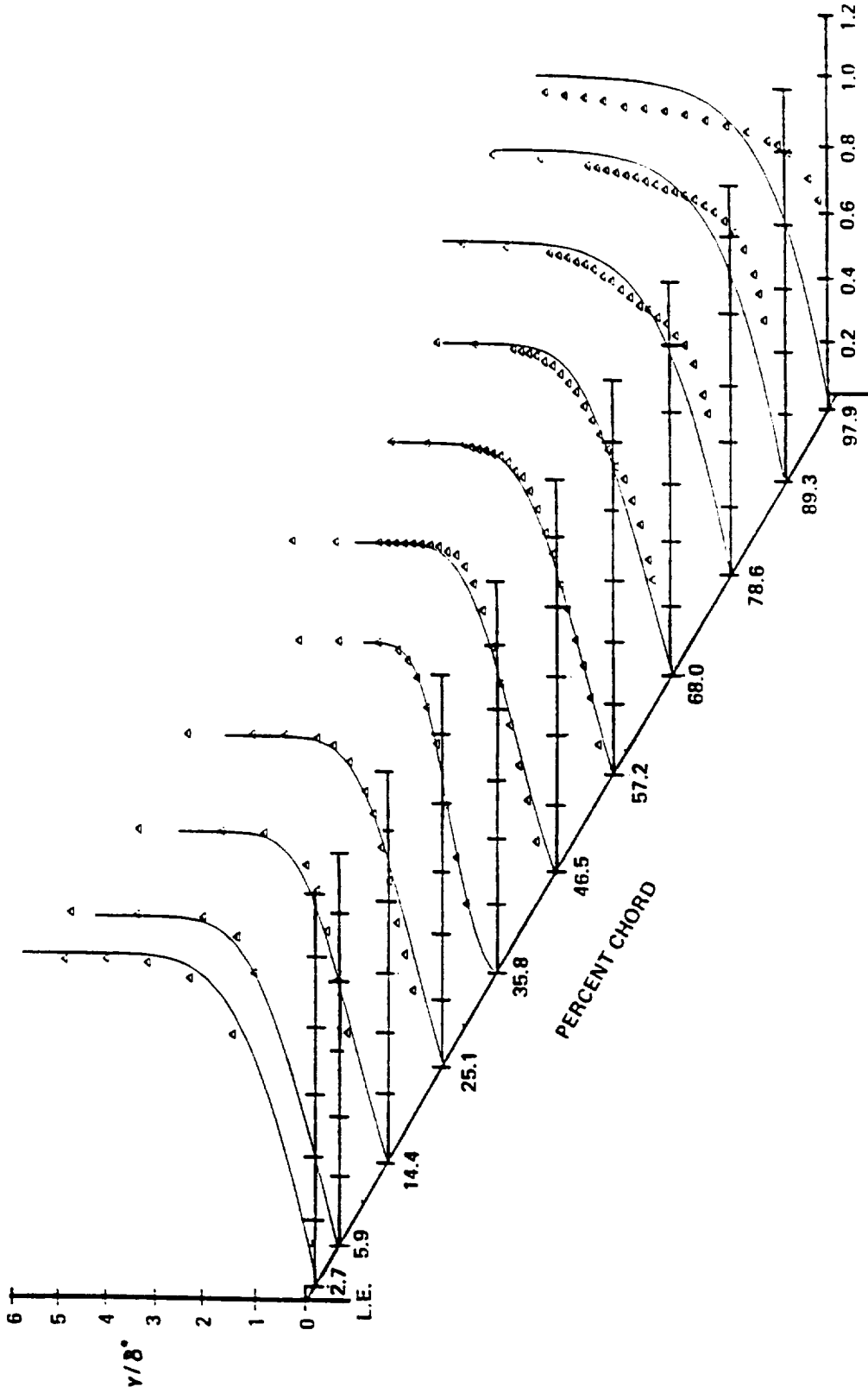

Figure 25. Reconstructed pressure surface boundary layers for $i = 5.0$ degrees in outer variables with the Falkner-Skan solutions (solid lines)

mean velocity profiles through about 57.2% chord. At 68.0% chord and beyond, there is an increased thickening of the measured profiles relative to the Falkner-Skan solution which indicates transitional boundary layers (also shown in figure 22).

Empirical relationships have been developed for the prediction of the beginning and end of transition; these relationships include the effects of freestream turbulence and streamwise pressure gradient. Using the relationships of Abu-Ghannam and Shaw [1980], for example, we predicted the onset of transition for the pressure surface data using the measured pressure distribution and a freestream turbulence intensity of 1.5%.[15] Onset of transition was predicted to be at a momentum thickness Reynolds numbers (Re_θ) of 342, and comparison with the Re_θ found from the profiles put this onset at 47.8% chord. By onset here, we mean the first location at which the intermittency, as measured with a flush-mounted hot-film probe for example, would be greater than zero. Because of the strong favorable gradient near the trailing edge, the scheme also predicted that a fully-turbulent boundary layer would not develop on the pressure surface. There do not seem to be any empirical prediction schemes which include the effect of surface curvature. While convex curvature apparently has no effect on transition, the concave curvature of the pressure surface can promote the generation of Görtler vortices (see Görtler [1940]), which can cause transition to occur earlier.

Sublimation flow visualization studies helped determine the transition point on the pressure surface. The average of five flow visualization tests placed the transition point at 64.2% $\pm$ 3.9% chord with 95% confidence. Figure 26 shows a plot of mean velocity, normalized by the edge velocity, for a fixed distance ($y = 0.508$ mm) above the blade and a varying chord location. At this distance above the surface, the measurement volume is above the boundary layer for the first two chord locations. The decrease in mean velocity with chord location over the first half of

---

[15] This turbulence intensity value was measured just outside of the leading edge boundary layers with a hot wire inserted from downstream. The difference between this value and the 0.18% found in the approach flow is probably due to the interaction of the flow with the blade pack.

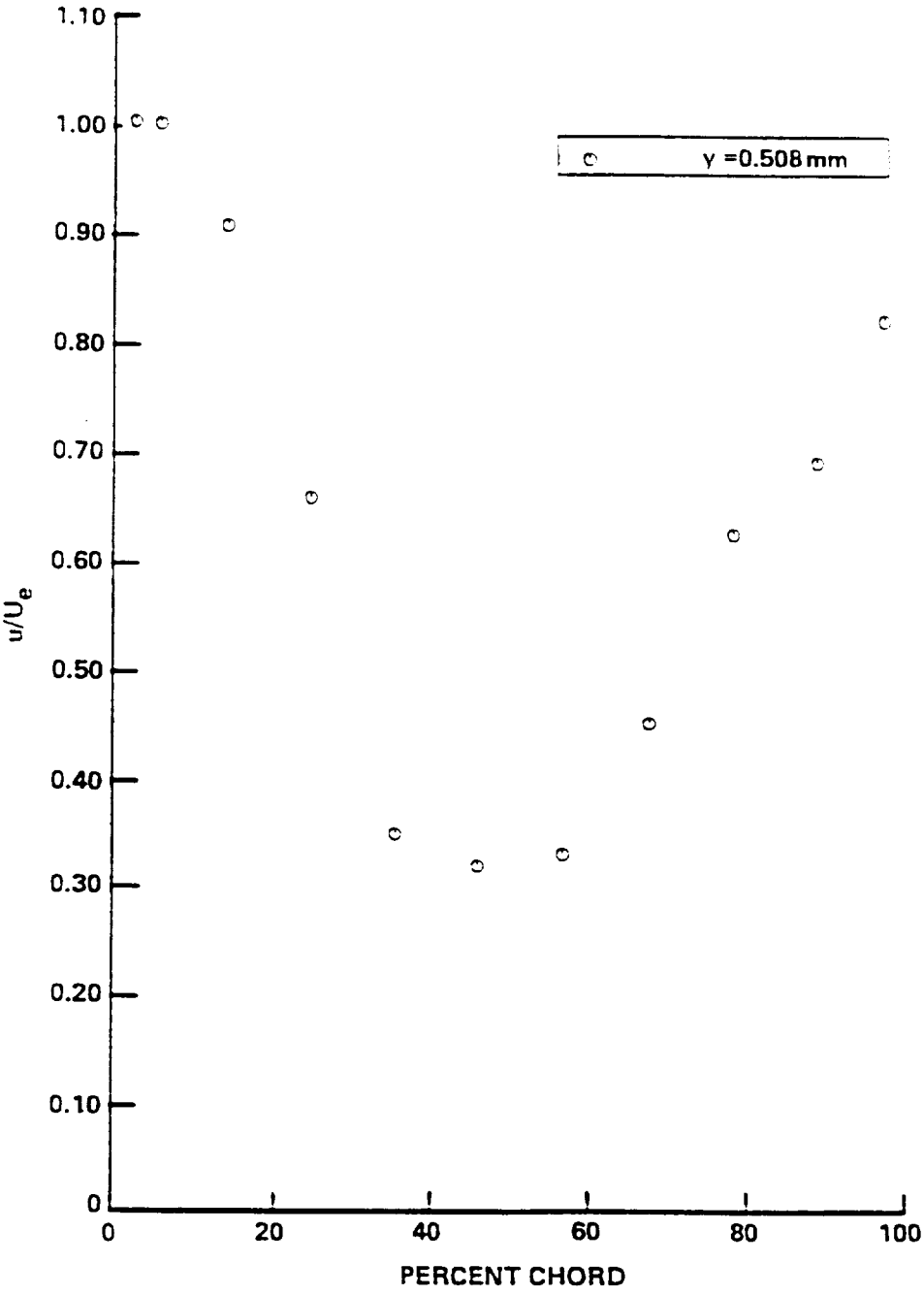

Figure 26. Variation of velocity, 0.508 mm from the blade, on the pressure surface for $i = 5.0$ degrees

the blade reflects the growth of the boundary layer relative to the fixed distance. The rapid rise in mean velocity near 60% chord indicates the onset of transition (see for example, Klebanoff, Tidstrom, and Sargent [1962]). Agreement with the flow visualization studies appears to be quite good. In this case, onset means the first location where transition affects the mean velocity profile. Since the intermittency of the flow becomes greater than zero before the mean velocities are affected, our calculations based on the empirical equations of Abu-Ghannam and Shaw [1980] pick a smaller chord value for the onset of transition. The fact that the mean velocity does not reach a constant (or decreasing) value with increasing chord location indicates that the transition process is not complete.

Integral parameters can also characterize transitional boundary layers. As shown in figure 27, the plots of δ^* and Re_θ show the boundary layer growth.[16] Calculating these parameters using a spline fit of the data gives values nearly the same as both the Falkner-Skan and STAN5 solutions through at least 35.1% chord. Because of the lack of near-wall measurements for some of the extremely thin layers near the leading edge, we felt that the values of momentum thickness obtained from the spline fit were not accurate.[17] At 35.1% chord, STAN5 computes a value for Re_θ of 250 and activates a transition turbulence model.[18] STAN5 never activates a full turbulence model since a value for Re_θ of 500 is never reached. Downstream of 35.1% chord, the boundary layer begins to transition and the most satisfactory values of the integral parameters are calculated from the spline fit. The Falkner-Skan solution yields laminar values that give steadily worse comparisons. The numerical computations of STAN5 give only slightly better results–so that we might infer that the transition model is not adequate here. Note that

---

[16] The parameters δ^* and Re_θ were plotted on logarithmic scales so that the plots from both the pressure and suction surfaces from all three incidence angles could be plotted using the same scales.

[17] For figure 27 and all the subsequent figures of boundary layer parameters, we include a dashed line as a visual aid to represent our best estimate of the actual values of the various parameters. These best estimates result from our experience with the analysis.

[18] Crawford and Kays [1976] suggest a value of $Re_{\theta,s}$ between 200 and 300.

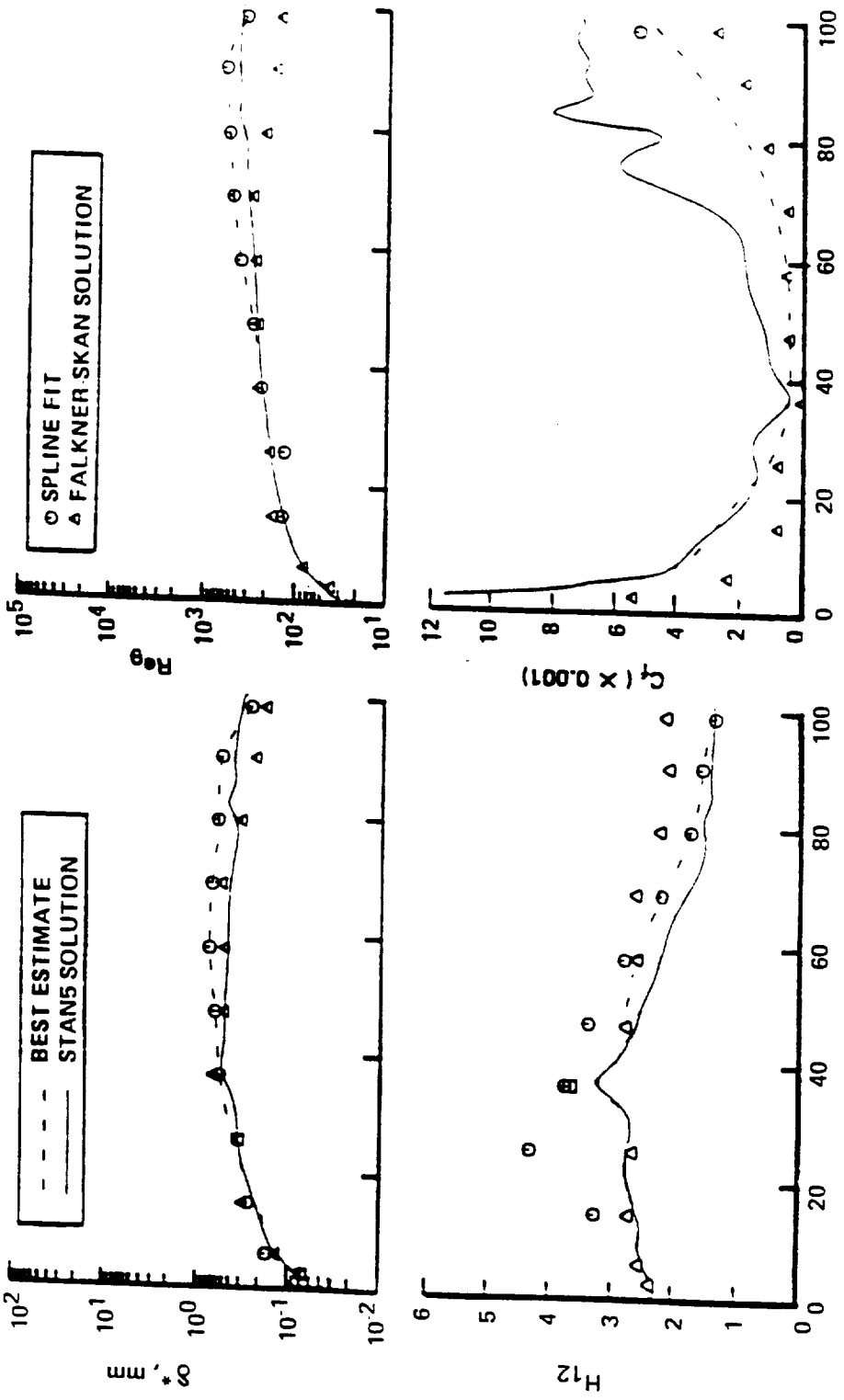

Figure 27. Variation of displacement thickness, first shape factor, momentum thickness Reynolds number, and skin friction coefficient on the pressure surface for $i = 5.0$ degrees

the favorable streamwise pressure gradient near the trailing edge causes the boundary layers to become thinner.

Figure 27 shows how H_{12} varies with percent chord. Again, the very thin boundary layers near the leading edge result in questionable calculations using the spline fit. Here the Falkner-Skan solution gives better results. Note that the STAN5 solution begins to have problems just before the transition model is activated. As transition begins, the values of H_{12} calculated from the spline fit give the best results. H_{12} leaves the laminar regime and enters the turbulent regime near 68% chord.

Near the leading edge, figure 27 shows that the skin friction for the laminar boundary layers, as computed with STAN5, begins at "infinity" and then decreases sharply with downstream chord position. We cannot compute C_f in the transition region downstream of 35.1% chord. To indicate how large C_f might become near the trailing edge, a value based on the spline fit and the Ludweig-Tillman empirical expression is given for the 97.9% chord location. Use of the Ludweig-Tillman expression here is not strictly valid, as the boundary layer profile is probably not fully turbulent at 97.9% chord. Values of δ^*, Re_θ, H_{12}, C_f, and other boundary layer parameters are given for both the pressure and suction surfaces at $i = 5.0$ degrees in appendix B.

An attempt was made to fit the boundary layer profile at 97.9% chord to the wall-wake equation, but no logarithmic region was obtained. Purtell, Klebanoff, and Buckley [1981] concluded that the logarithmic region seems to be an inherent characteristic of the turbulent boundary layer. That is, for fully-developed turbulent boundary layers, they found the extent of the logarithmic region to be roughly a constant fraction of the boundary layer thickness as Re_θ was decreased. Murlis, Tsai, and Bradshaw [1982] found strong evidence for the validity of the logarithmic law of the wall, at zero pressure gradient, for Re_θ values as low as 700, while Smits, Matheson, and Joubert [1983] found a logarithmic region, for favorable pressure gradients, at Re_θ as low as 261. Since no logarithmic region was found for the boundary layer at 97.9% chord, it must be

concluded that either the boundary layer was not fully turbulent at a Re_θ of 413, or (less likely) that the logarithmic region was so small that it could not be detected.

Turbulence intensity data for the pressure surface boundary layer are shown in figure 28. As the Falkner-Skan approximation has been shown to be reasonable for the profiles to 57.2% chord, the large turbulence intensities near the wall are disturbing. A typical profile of the skewness versus y/δ^*, which is shown for the 5.9% chord location in figure 29, adds considerably to the problem in that this profile might reasonably resemble the shape of a skewness profile one might expect to find from measurements of a turbulent boundary layer.

This problem was examined in some detail. Using both calibrated hot-wire probes in the boundary layer and uncalibrated hot films flush-mounted on the surface, we determined that the profiles near the leading edge were indeed laminar. Typically, at the edge of these leading edge boundary layers, the intensity was found to be near 1.5%. Having shown the boundary layers to be laminar, we next suspected that the intensity measurements might be contaminated by mean-velocity-gradient broadening. This problem has been considered previously by Edwards, Angus, French, and Dunning [1971], Goldstein and Adrian [1971], and Kried [1974]. For simplicity in the current study, the laser intensity was taken to be constant for the entire measurement volume. In the present case then, error estimates could be easily made by assuming the Falkner-Skan approximate profiles or by using the smoothed cubic spline fit. Similar results are obtained for either estimate. In figure 30a, an estimate of the turbulence intensity caused by mean-velocity-gradient broadening is shown against percent chord for a measurement volume roughly as large as the volume previously calculated (33 μm). As it seemed plausible that the actual measurement volume might be larger than the volume found theoretically, we repeated the calculations for a measurement volume roughly twice that of the estimated volume. These results are shown in figure 30b. Figure 30 shows estimates for a constant y/δ^* of roughly 1.70; the measurement points are also given. It is clear from a comparison of the turbulence intensity calculated from the velocity-gradient broadening against the measured data, that the gradient broadening alone

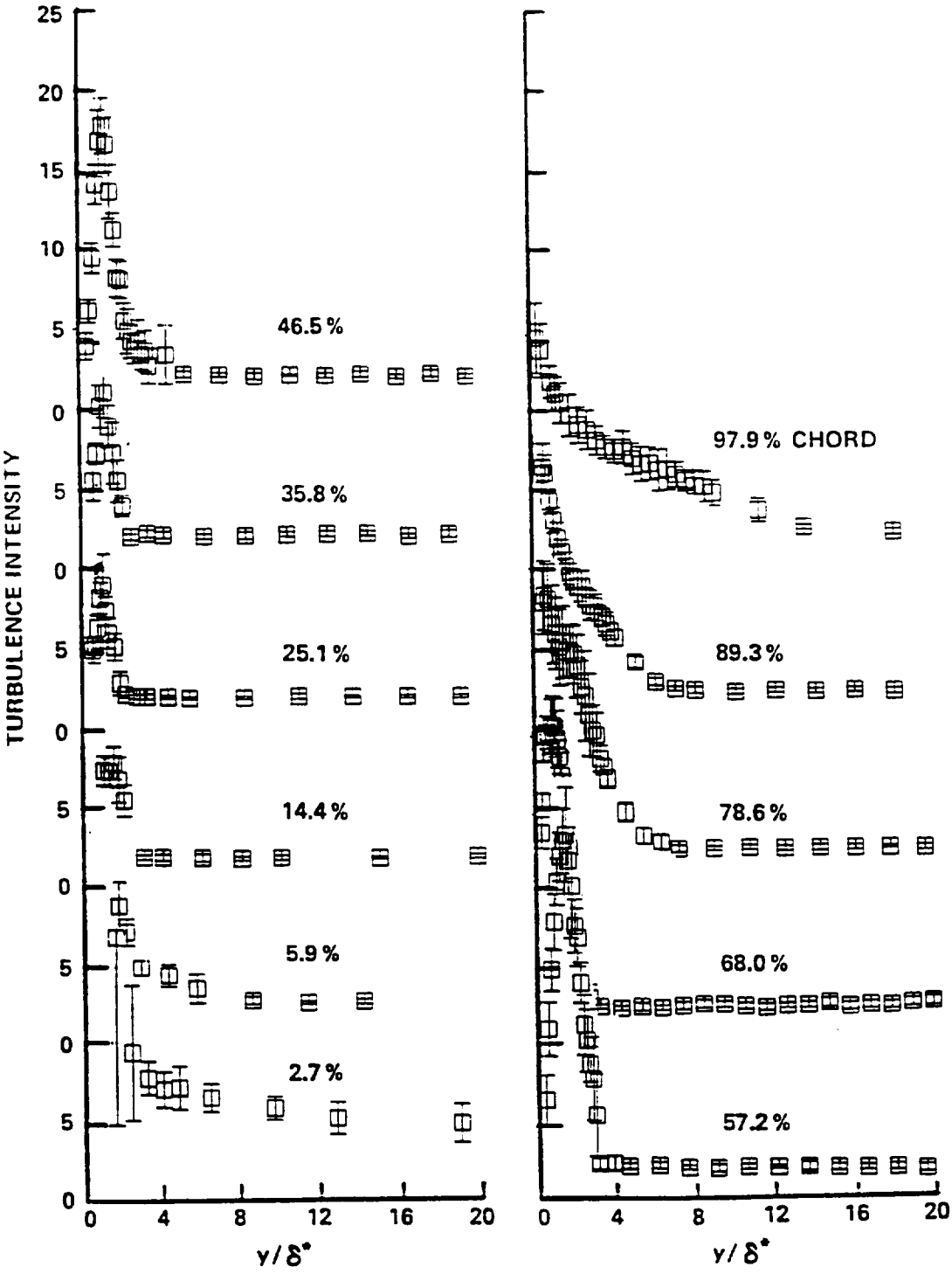

Figure 28. Turbulence intensity data for the pressure surface boundary layers at $i = 5.0$ degrees

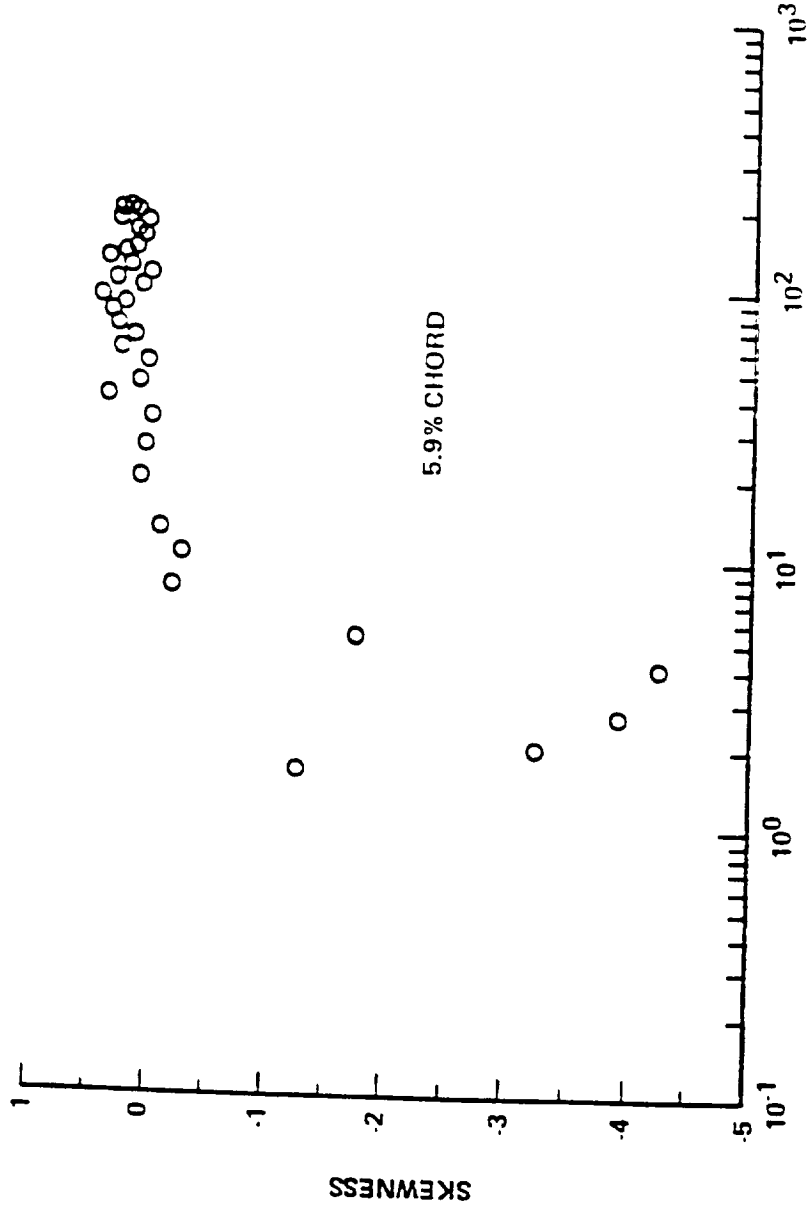

Figure 29. Skewness distribution for the pressure surface boundary layer at 5.9% chord and $i = 5.0$ degrees

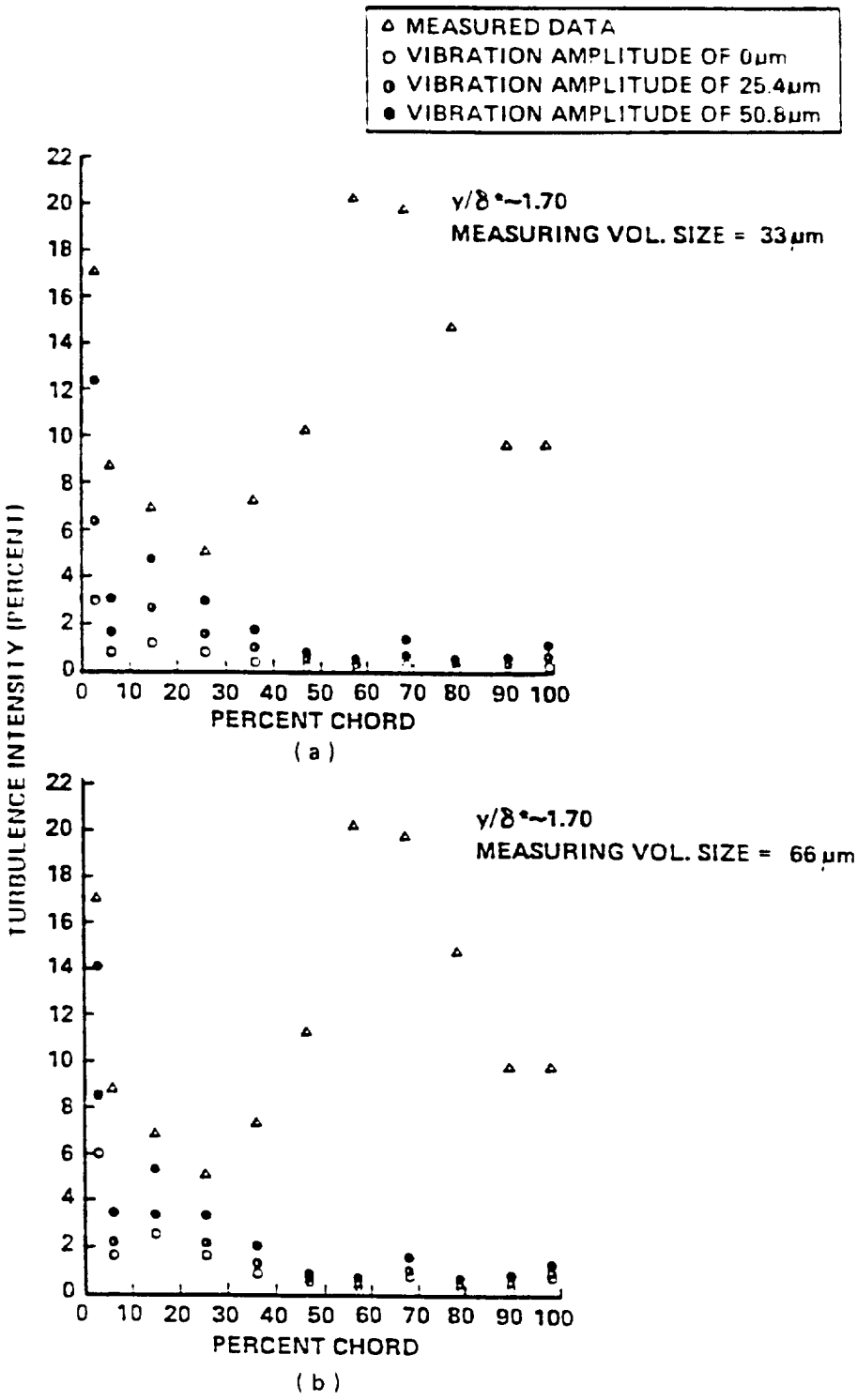

Figure 30. Pressure surface turbulence intensities at $y/\delta^* \approx 1.70$ and $i = 5.0$ degrees, both measured data and data estimated by mean-velocity-gradient broadening and measurement volume vibration

cannot account for the entire intensity. In addition, the skewness when calculated from an assumption of velocity-gradient broadening is much smaller than that observed experimentally.

As a second approach to the problem, we assumed that in addition to the gradient broadening problem, a small vibration may have contaminated the velocity signal. Calculations are again straightforward using either the spline fit or the Falkner-Skan approximations. Results for vibration amplitudes of 25.4 mm and 50.8 mm are again given in figure 30. With the exception of the points at 5.9% chord, which appear to have been biased by an inaccurate calculation of δ^* (see figure 27), the calculations agree reasonably well with the data for a measurement volume of 66 mm and a vibration amplitude of 50.8 mm. Comparison between the measured and calculated skewness is also much closer. Some simple measurements with an accelerometer indicated that vibration amplitudes of this magnitude were not unreasonable to expect, so that a combination of velocity-gradient broadening with a vibration of the measurement volume seems a likely cause for the elevated turbulence levels. As shown in figure 30 (and as can be shown for the suction surface turbulent profiles), the effect becomes quite small as the boundary layer grows. In the present situation, the bias can probably be considered negligibly small for chord positions larger than about 25%.

Turbulence intensity profiles are shown for the transitioning boundary layers on the pressure surface in figure 28. The data show classical shape (see Klebanoff, Tidstrom, and Sargent [1962]) and agree reasonably well with the measurements of Wang, Simon, and Buddhavarapu [1985]. For transitional boundary layers, the peaks in turbulence intensity can be even greater than the peaks for turbulent boundary layers. Also, these peaks occur at some distance from the blade as transition begins and move closer to the blade surface as transition progresses.

Suction Surface for a 5.0 Degree Incidence

All of the measured suction surface boundary layers shown in figure 7 are turbulent. This implies that transition took place before the measurement station at 2.6% chord, which is not surprising considering the very large adverse pressure gradient near the leading edge. The separation of a laminar boundary layer under an adverse pressure gradient results in a free shear layer, which is unstable. The transition to turbulence takes place very rapidly. Once turbulent entrainment increases, the shear layer is enlarged which results in a pressure recovery and a rapid reattachment. Thus, the separation "bubble" can be quite short and close to the leading edge.

Although the transition takes place very close to the leading edge, the recovery process extends some distance downstream. This process can be seen from the mean-velocity profiles plotted in dimensionless outer variables. These plots are shown in figure 31 where the normal pressure gradients have been taken into account as described previously. The recovery process can be seen to extend through the 2.6% and 7.6% chord locations by observing the shape of the profiles. As we will show later, the shape of the velocity profiles results in higher values of H_{12} during the recovery process. The local turbulence intensity profile at 2.6% chord also indicates recovery. This turbulent boundary layer was the only one measured at this incidence angle in which there was a maximum value of local turbulence intensity away from the surface.

The mean velocity data were fit to the wall-wake equation of Coles [1956] through a least squares technique. Figure 32 shows the velocity profiles in inner variables. The logarithmic region reaches a maximum and the wake region reaches a minimum at 12.7% chord. This seems to be a second indication of complete recovery from the leading edge separation "bubble." Moving further downstream, we find that Π (which controls the size of the wake region) and Re_θ both increase. Since the extent of the logarithmic region decreases, Π must influence the logarithmic

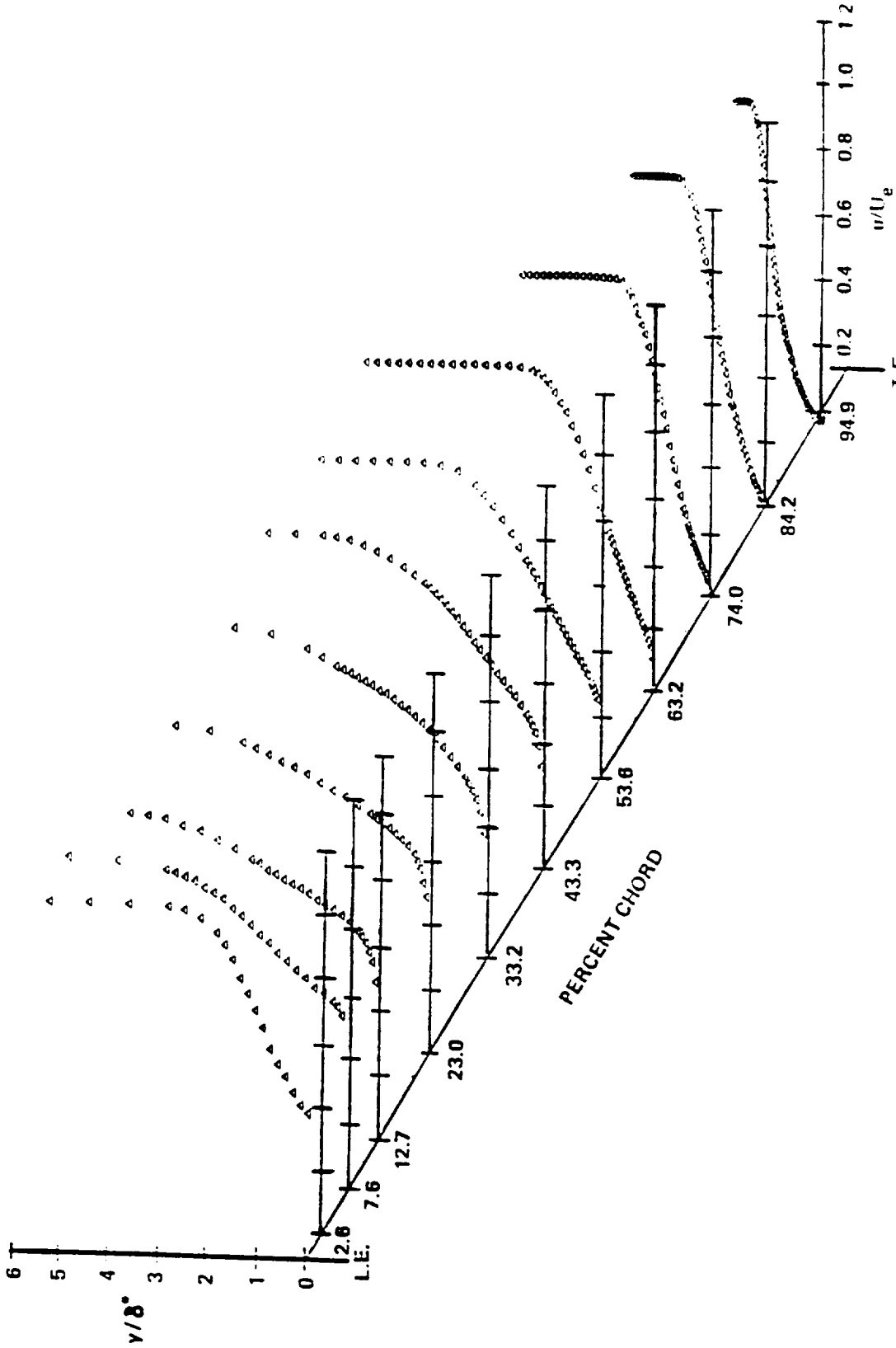

Figure 31. Reconstructed suction surface boundary layers for $i = 5.0$ degrees in outer variables

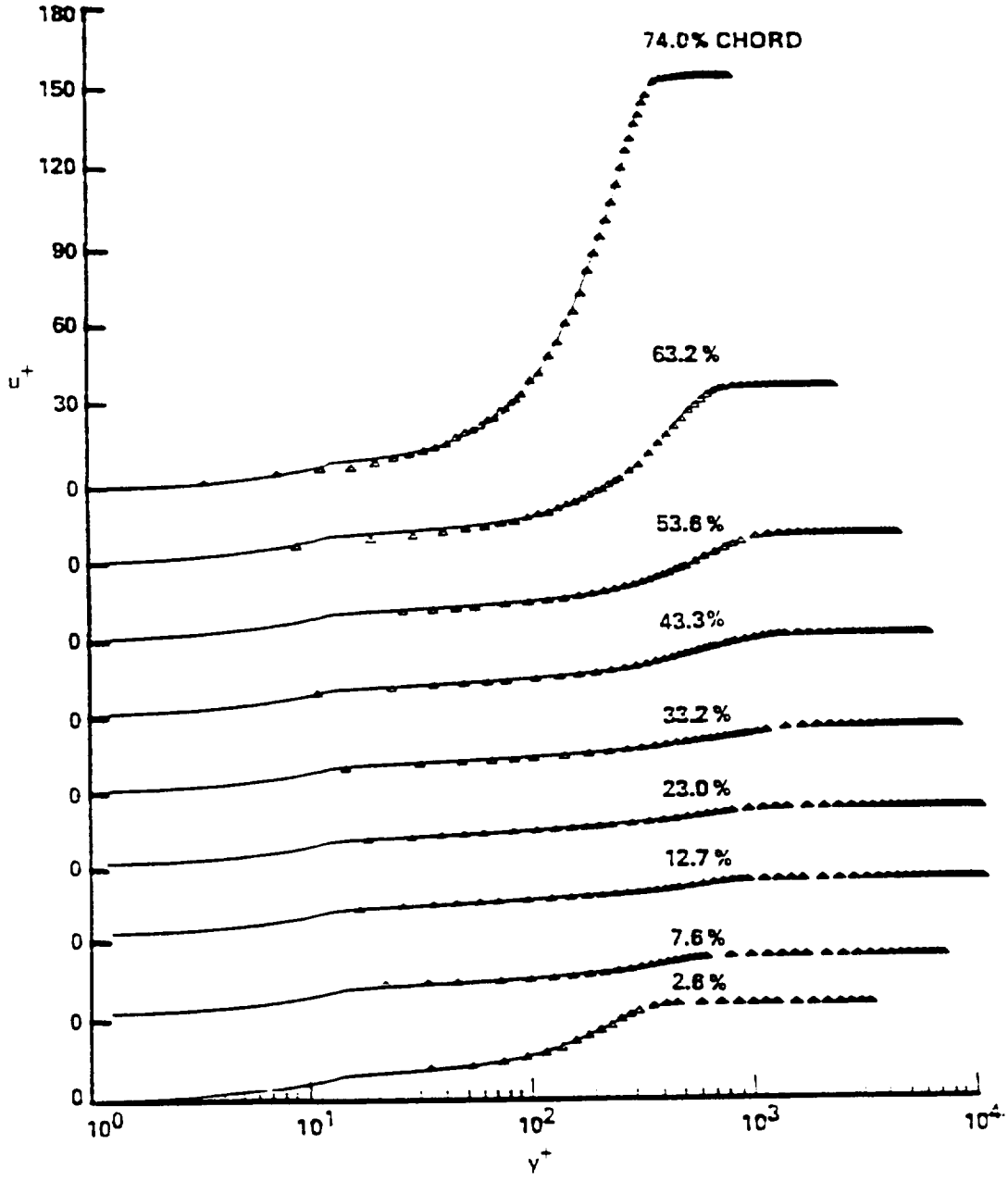

Figure 32. Reconstructed suction surface boundary layers for $i = 5.0$ degrees in inner variables

region more than Re_θ for this flow.[19] As separation is reached, the logarithmic region disappears and the wall-wake equation cannot be fit to the data.

Although the influence of surface curvature cannot be extracted from the data, one must suspect that this influence is indeed present. The convex curvature on the suction surface ($0.01 < |\delta/R_c| < 0.2$) and the concave curvature on the pressure surface ($0.002 < |\delta/R_c| < 0.02$) have opposite effects on turbulent boundary layers. Ramaprian and Shivaprasad [1977] show that convex curvature reduces the logarithmic region and increases the relative strength of the wake component. Except for the initial region of curvature, convex curvature increases the rate of growth of Re_θ and decreases C_f. Shivaprasad and Ramaprian [1978] claim that the effects of convex curvature on the behavior of the turbulent boundary layer are even stronger than the effects of concave curvature at the same value of $|\delta/R_c|$. Their measurements showed that convex curvature reduces turbulence intensity and Reynolds shear stress. Measurements by So and Mellor [1973], Gillis and Johnston [1983], and Gibson, Verriopoulos, and Vlachos [1984] agreed. These results indicate that for very strong convex curvature effects, regions can be found where turbulence cannot exist. Bradshaw [1969] showed that the behavior of the turbulent boundary layer is very sensitive to streamline curvature as mild as $|\delta/R_c| = 0.003$. He used an analogy between the effects of streamline curvature and buoyancy to estimate quantitatively the effect of curvature on mixing length distribution in the boundary layer. So [1975] verified this buoyancy analogy mathematically. Shivaprasad and Ramaprian [1978] made measurements which support the buoyancy analogy of Bradshaw [1969] for mild convex curvature. For concave curvature, they found the buoyancy analogy useful only for values of $|\delta/R_c|$ near 0.01.

After fitting the data to both a spline and the wall-wake equation, we calculated the major boundary layer parameters (as seen in appendix B). Calculations from both types of fits give similar results. As shown in figure 33, the displacement thickness increases gradually at first and then increases rapidly through separation. Figure 33 also shows this growth in the plot of

[19] Refer back to figure 23 for the influence of Π and Re_θ on the extent of the logarithmic region.

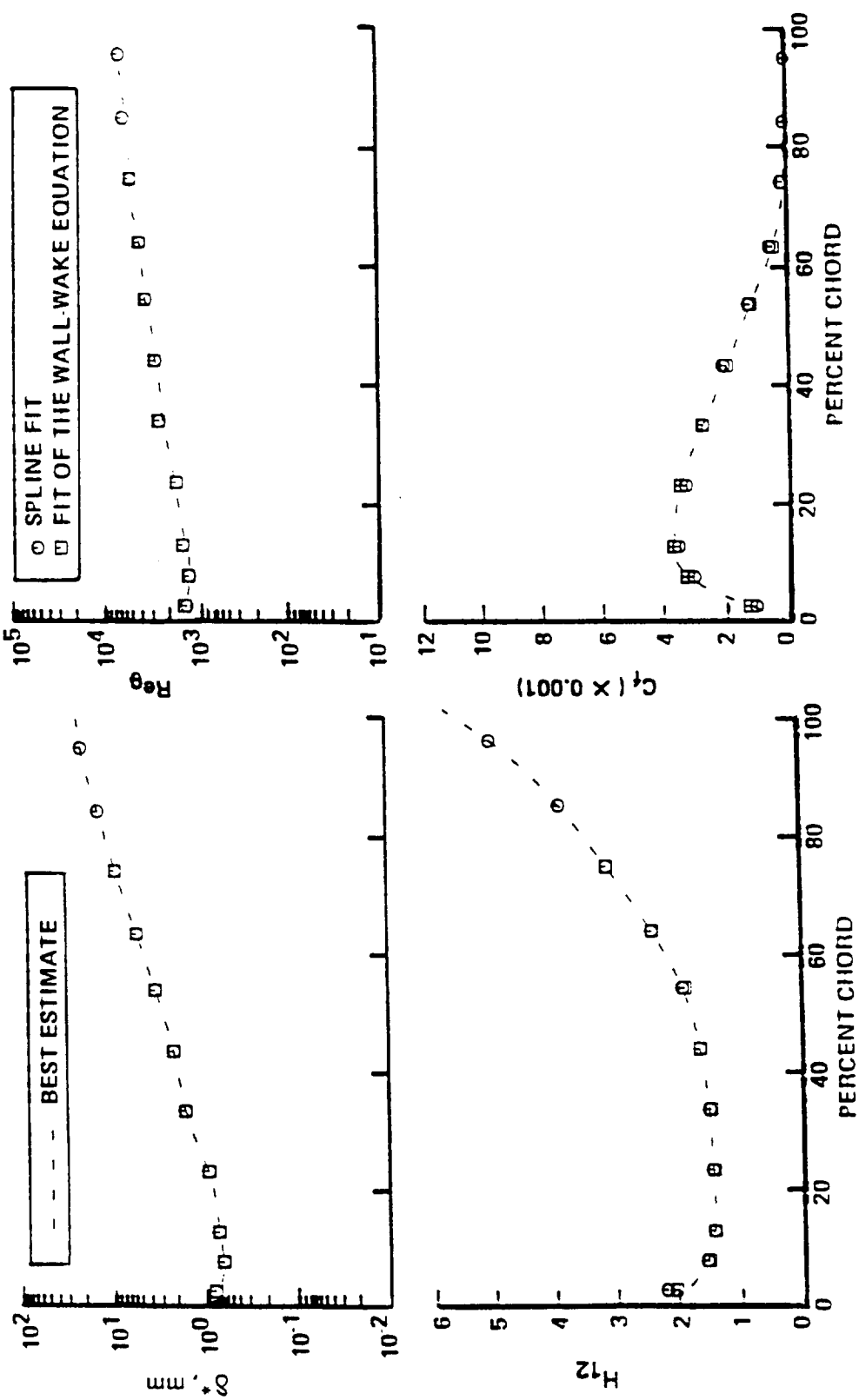

Figure 33. Variation of displacement thickness, first shape factor, momentum thickness Reynolds number, and skin friction coefficient on the suction surface for $i = 5.0$ degrees

Re_θ. All of the values of Re_θ are greater than 1200, even near the leading edge, and this again indicates that all of the boundary layers are turbulent. Figure 33 shows turbulent values of H_{12} beginning near the leading edge. Recovery from the leading edge separation "bubble" results in an initial decrease of H_{12}. Separation of turbulent boundary layers is usually approximated using values of H_{12} near 2.2 which corresponds here to a suction surface location near 59.0% chord. Sandborn and Kline [1961] proposed a relation for intermittent separation,

$$H_{12} = 1 + \frac{1}{1 - \frac{\delta^*}{\delta}},$$

which yields 67.4% chord (corresponding to $H_{12} = 2.73$) as the location of intermittent separation for the data presented here.

Values of C_f come directly from the least squares fit of the data to the wall-wake equation while the spline fit calculations must use the Ludweig-Tillman equation. From Figure 33, values of C_f appear to be near zero at the leading edge which corresponds to the vanishing skin friction at the beginning of the leading edge separation "bubble." C_f reaches a maximum after the boundary layer has totally recovered from the leading edge separation and then decreases as the trailing edge separation of the turbulent boundary layer is reached. C_f vanishes near 81.5% chord.

Attempts to compute boundary layer parameters from numerical solutions using STAN5 failed. Starting with a laminar solution fails because separation occurs immediately–as expected. Starting with a turbulent solution gives poor results since an "infinite" value of C_f is computed at the leading edge instead of the actual value of zero. Also, a problem arises from our use of the measured blade static-pressure distribution as a boundary condition for STAN5, which is a parabolic computer code. Physically, the trailing edge separation leads to a decreasing and eventually vanishing adverse pressure gradient. STAN5 sees the decreasing adverse pressure gradient as a change in the inviscid core flow between the blades and thus manages to avert the trailing edge separation altogether.

Defining separation as the entire process of the breakdown of boundary layer flow, Simpson, Chew, and Shivaprasad [1981a] quantified the various stages of separation with the maximum instantaneous backflow. Incipient detachment occurs with 1% instantaneous backflow; intermittent transitory detachment occurs with 20% instantaneous backflow; transitory detachment occurs with 50% instantaneous backflow; and detachment occurs when the wall shear stress becomes zero. The percent backflow is easily calculated as the portion of the measured velocity distribution that includes negative velocities. Figure 34 shows the instantaneous backflow measurements at several distances from the blade as a function of percent chord. Using the nomenclature of Simpson, Chew, and Shivaprasad [1981a], we can locate incipient detachment at 61.1% chord, intermittent transitory detachment at 69.1% chord, and transitory detachment at 83.7% chord. The sublimation flow visualization tests showed separation to occur at 65.6% $\pm$ 3.5% chord, and a comparison with the maximum instantaneous backflow data of figure 34 shows that flow visualization yields a value for separation which is only slightly downstream of incipient detachment. Locating turbulent separation by observing when H_{12} nears 2.2 also seems to indicate incipient detachment. We might note that although Simpson, Chew, and Shivaprasad [1981a] state that detachment and transitory detachment need not be at the same location, our skin friction calculations show that the chordwise locations of detachment and transitory detachment are quite close to one another.

Restrictions in applying the wall-wake equation in the vicinity of separation result from the velocity scale, u_τ, approaching zero. A vanishing u_τ leads to a vanishing logarithmic region, which would not cause concern if the separated flow profiles would follow the law of the wake. Unfortunately, experimental data prove otherwise (see Simpson, Chew, and Shivaprasad [1981a] for example). Schofield [1983,1986] extended the model of Perry and Schofield [1973] to detached flows by suggesting that the similarity would hold provided that the origin of the normal coordinate has been moved from the wall to the location (away from the wall) at which $u = 0$.

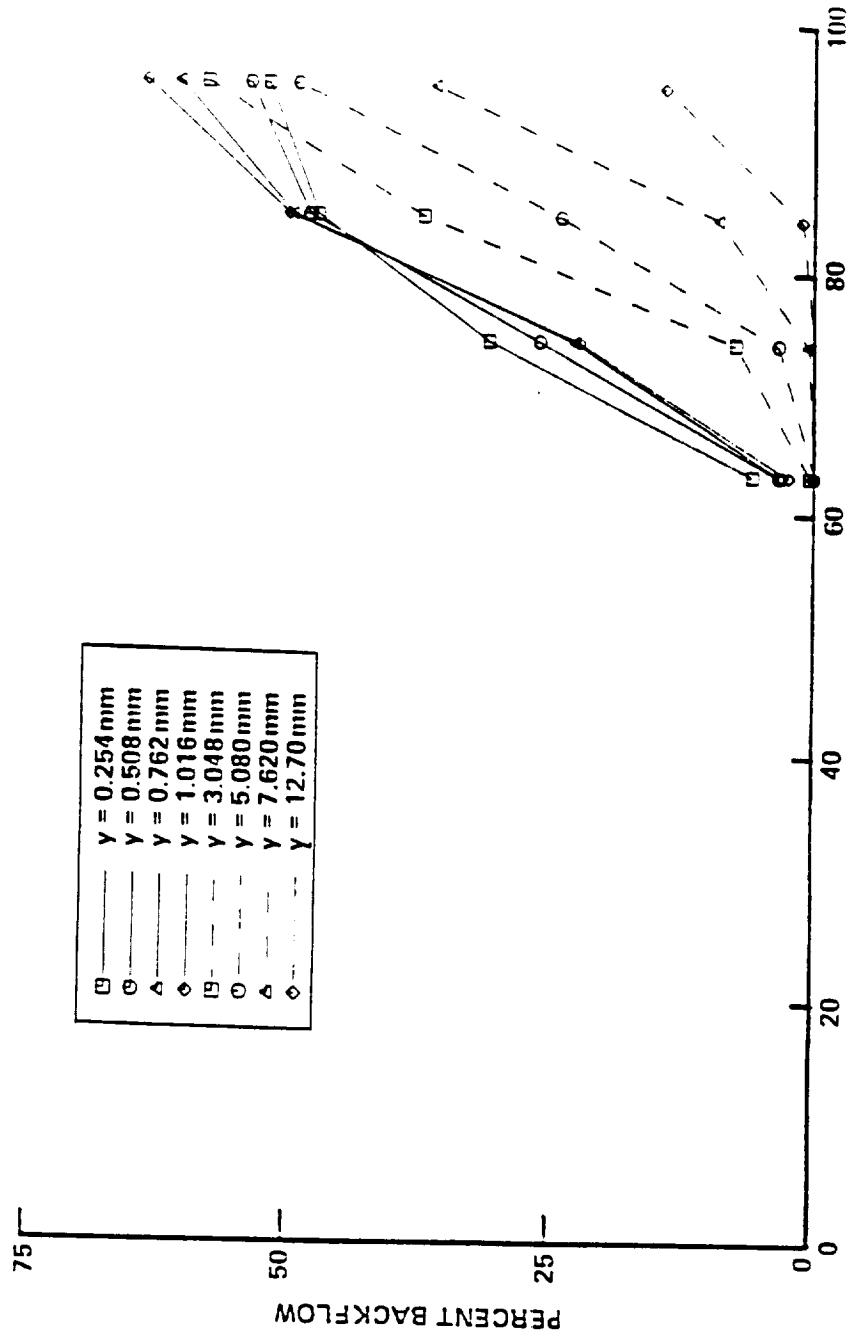

Figure 34. Instantaneous backflow measurements on the suction surface for $i = 5.0$ degrees

The suction surface boundary layers are plotted using the similarity relation of Perry and Schofield [1973] in figure 35. In the outer 90% of the boundary layer, the similarity relation collapses the data quite well for chord locations upstream of the separated region. As the amount of instantaneous backflow increases, however, the data deviates more and more from the similarity relation. This deviation is in seeming contrast to the conclusions made by Schofield [1983,1986]. A close examination of his defect plots, however, shows similar trends in his analyzed data and the data shown in figure 35. The wall-wake equation appears to be the best of the similarity techniques for profiles approaching detachment.

No outer region similarity seems to exist downstream of detachment. Many researchers have attempted a law of the wake correlation without success (see Simpson, Chew, and Shivaprasad [1981a] for example). For a turbulent boundary layer subjected to a streamwise pressure gradient, Mellor and Gibson [1966] suggested replacing the shear velocity with a pressure velocity, $(\delta^*/\rho)(dp/dx)$, as the velocity scale. However, Schofield [1981] has shown this scaling to be inadequate. Using the velocity scale corresponding to the maximum shear stress as suggested by Schofield [1983,1986] has been shown to give poor similarity in figure 35. Mehta and Goradia [1984] had some success by assuming the outer region velocity profile behaves like a two-dimensional mixing layer. Their similarity variables were not found to give outer region similarity with the data measured here.

Similarity in the backflow region seems to show more promise. Simpson, Chew, and Shivaprasad [1981a] found good backflow similarity by normalizing the velocity by the maximum backflow velocity, and the distance from the wall by the distance to the maximum backflow velocity. Schofield [1983,1986] found that this backflow similarity could be improved by using the total backflow thickness as the length scale. Figure 36 shows this backflow similarity for the data at 94.9% chord. Despite the scatter, the backflow data seems to collapse fairly well with the data measured by Simpson, Strickland, and Barr [1977] and Simpson, Chew, and Shivaprasad

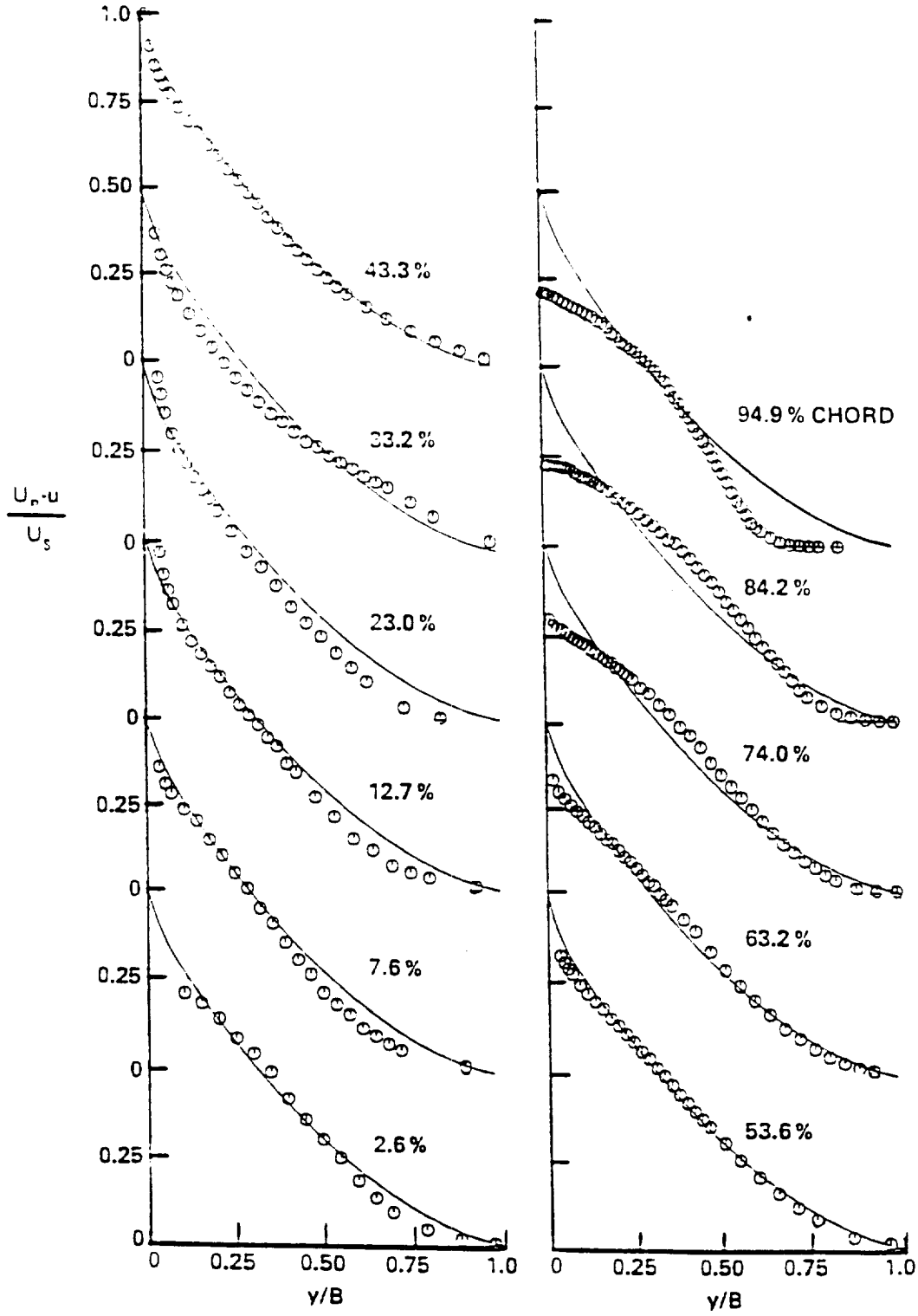

Figure 35. Reconstructed suction surface boundary layers for $i = 5.0$ degrees in defect form with Perry-Schofield similarity

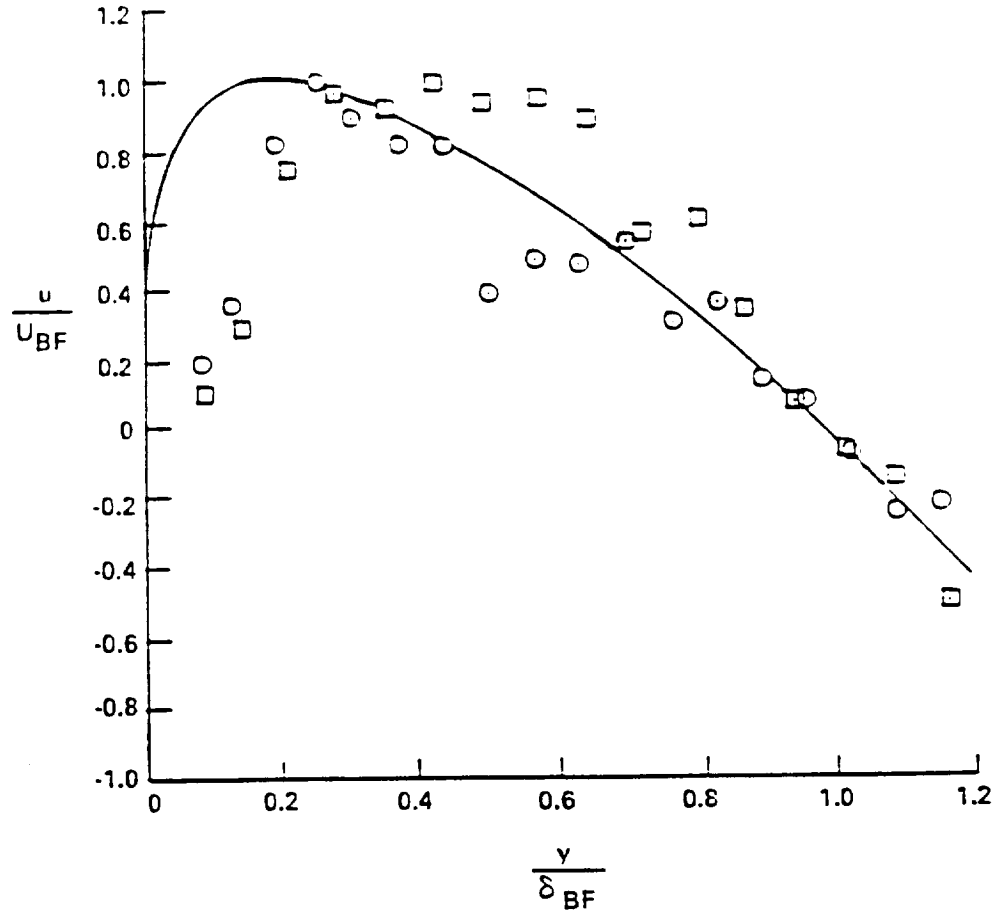

——— AVERAGE OF DATA MEASURED BY SIMPSON, STRICKLAND, AND BARR [1977] AND SIMPSON, CHEW, AND SHIVAPRASAD [1981a]

⊙ 94.9 % CHORD ON THE SUCTION SURFACE FOR THE 5.0° INCIDENCE

⊡ 90.3 % CHORD ON THE SUCTION SURFACE FOR THE -1.5° INCIDENCE

Figure 36. Backflow similarity of the reconstructed suction surface boundary layers at 94.9% chord for $i = 5.0$ degrees and at 90.3% chord for $i = -1.5$ degrees

[1981a]. The only exceptions are the two data points closest to the wall–data for which the 95% confidence bands are larger than the magnitude of the mean velocity.

The turbulence intensity on the suction surface is shown for all 11 chord positions in figure 37. Recovery from the leading edge separation is apparent from the peaks in turbulence intensity that occur away from the surface for the 2.6% and 7.6% chord locations. These peaks also occur in the separation region from 63.2% chord through 94.9% chord. This shape reflects the movement in the location of the maximum mean-shear rate outward from the near-wall region. Close to the blade surface at 94.9% chord, in the region with mean backflow, the 95% confidence bands are very large.

Wakes for a 5.0 Degree Incidence

Figure 8 shows the measured near wakes at 105.4% and 109.6% chord and the measured far wake at 152.6% chord. Wakes become similar only at distances far downstream of their source. A Gaussian distribution can be used to correlate these far-wake data. Lakshminarayana and Davino [1980] suggested the correlation

$$\frac{U_e - u}{U_e - u_{cl}} = e^{-0.693\eta^2}$$

where η is the normalized distance across the wake. The suction and pressure sides of the wake use different length scales, L_s and L_p. L_s and L_p are the distances on the suction and pressure sides of the wake centerline from the point of minimum velocity to a point where the velocity defect is $\frac{1}{2}(U_e - u_{cl})$. The far-wake data of Lakshminarayana and Davino [1980] showed similarity away from the wake edge for both inlet guide vane wakes and stator blade wakes. This similarity was corroborated by Hobbs, Wagner, Dannenhoffer, and Dring [1982] for distances greater than 30% axial chord downstream of the trailing edge of their compressor cascade blades. Figure 38 shows

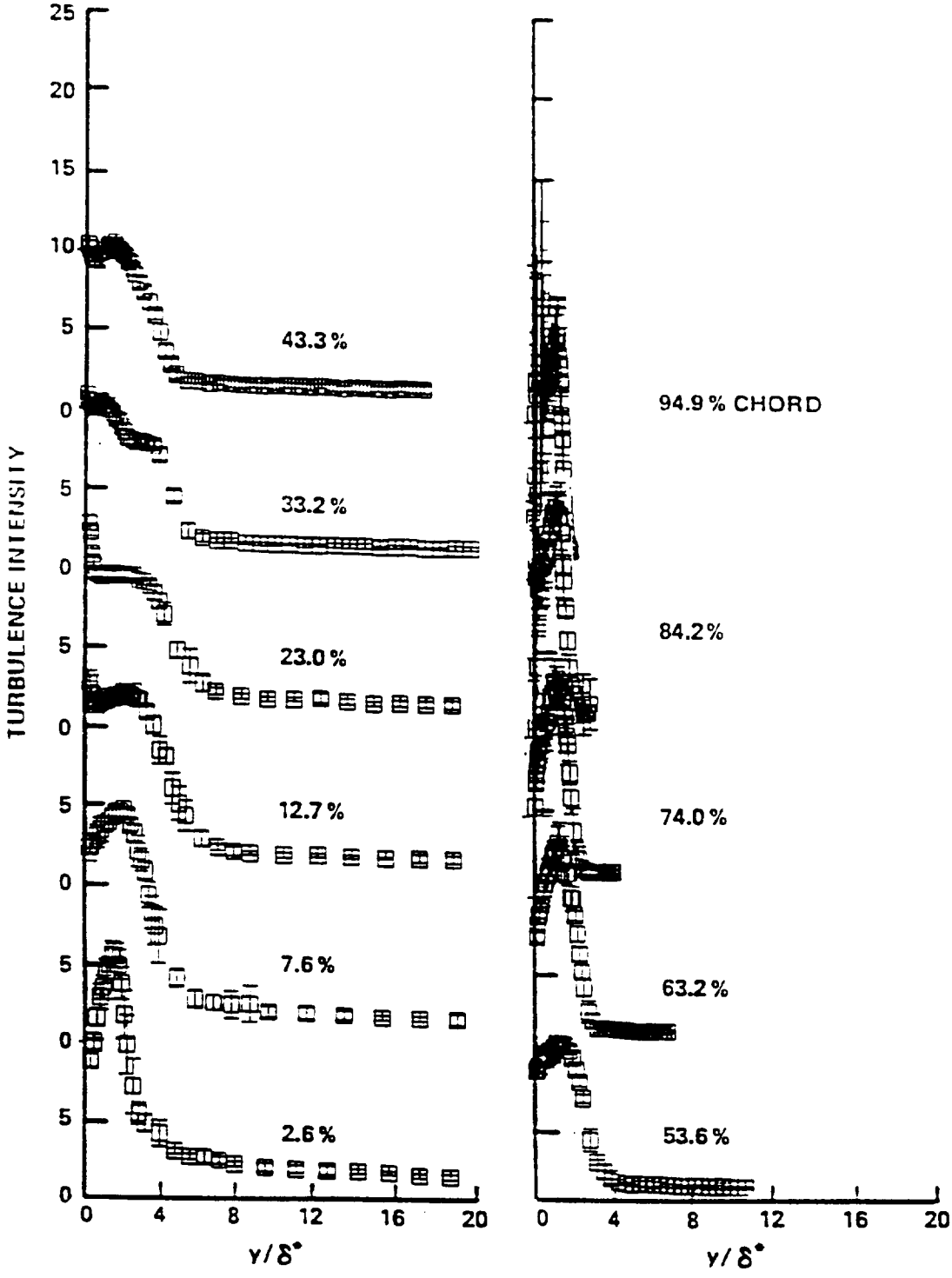

Figure 37. Turbulence intensity data for the suction surface boundary layers at $i = 5.0$ degrees

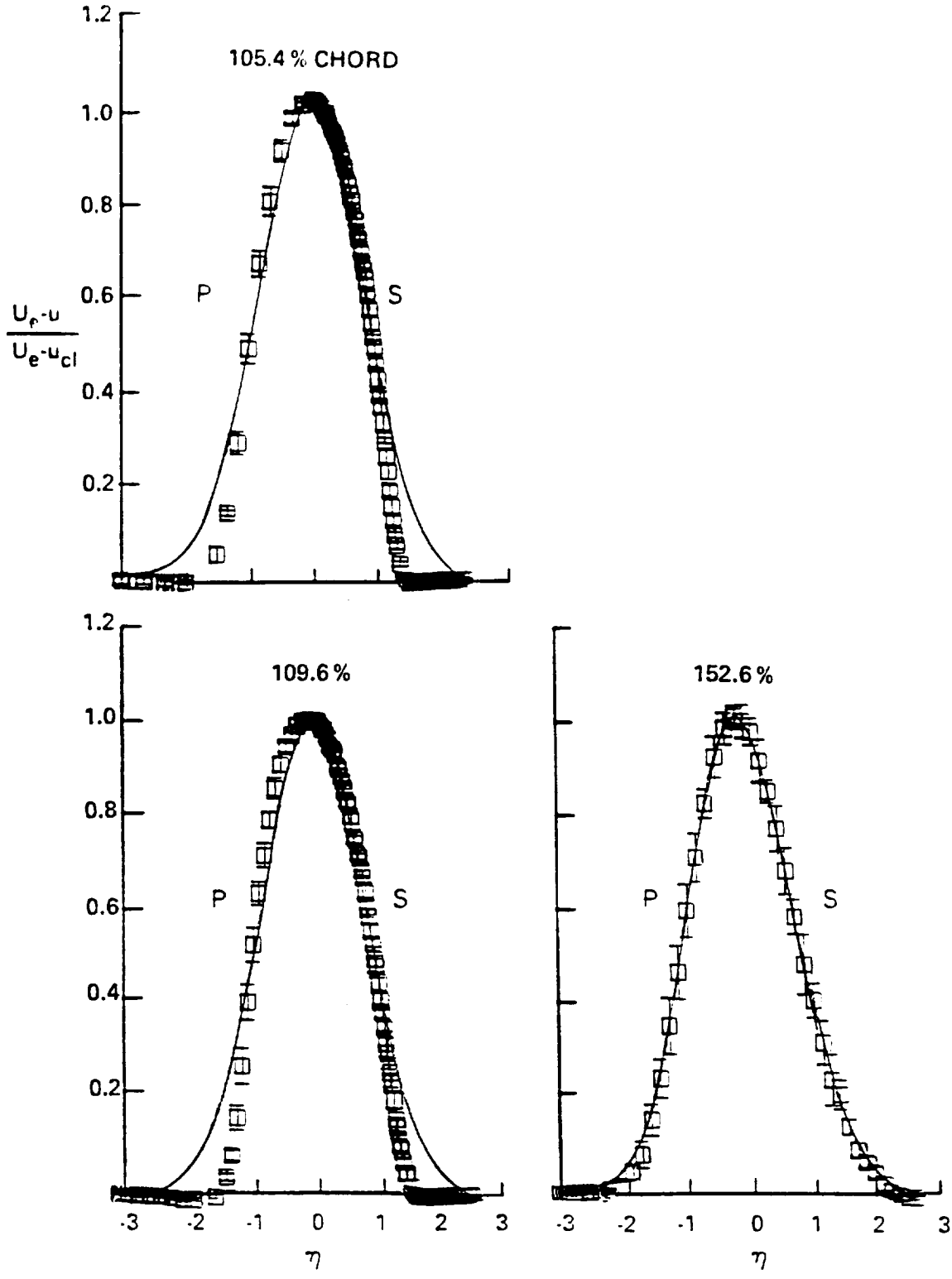

Figure 38. Wakes for $i = 5.0$ degrees in defect form with Gaussian similarity

that our wake data has Gaussian similarity in the far wake. However, the two near-wake profiles exhibit no similarity.

Integral parameters can be calculated from the wake velocity profiles. Using the location of the wake centerline and displacement thicknesses on either side of the centerline, the displacement surface can be drawn as seen in figure 39. The curvature of the displacement surface in the near-wake region can be explained by the pressure difference between the two blade surfaces at the trailing edge. The location of the displacement surface in the far-wake region can be partly explained by the large amount of separation on the suction surface of the neighboring blades. However, another explanation for this curvature of the displacement surface in the far-wake region is the confinement of the far wakes between the two tailboards. The effects of the tailboards must be taken into account when considering this displacement surface for wake modeling.

Turbulence intensity profiles are presented for the two near wakes in figure 40. As with the turbulence intensity profiles in the separating boundary layers, the turbulence intensity peaks are displaced outward, essentially tracking the regions of large mean-velocity gradients. These data, although more detailed, are quite similar to the data of Hah and Lakshminarayana [1982] for the near wake of an isolated airfoil. As was the case at 94.9% chord, a large amount of scatter exists in the turbulence intensity data within the regions of mean backflow.

Pressure Surface for a -1.5 Degree Incidence

The blade static-pressure distribution of figure 10 and the measured velocity profiles of figure 11 showed some differences between the pressure surface flow fields for $i = -1.5$ degrees and $i = 5.0$ degrees. After accounting for the normal pressure gradient and determining U_e and δ^*, we plotted the velocity profiles in outer variables in figure 41. Figure 41 also shows a Falkner-Skan solution for the first four chord positions. For the boundary layers at 4.3%

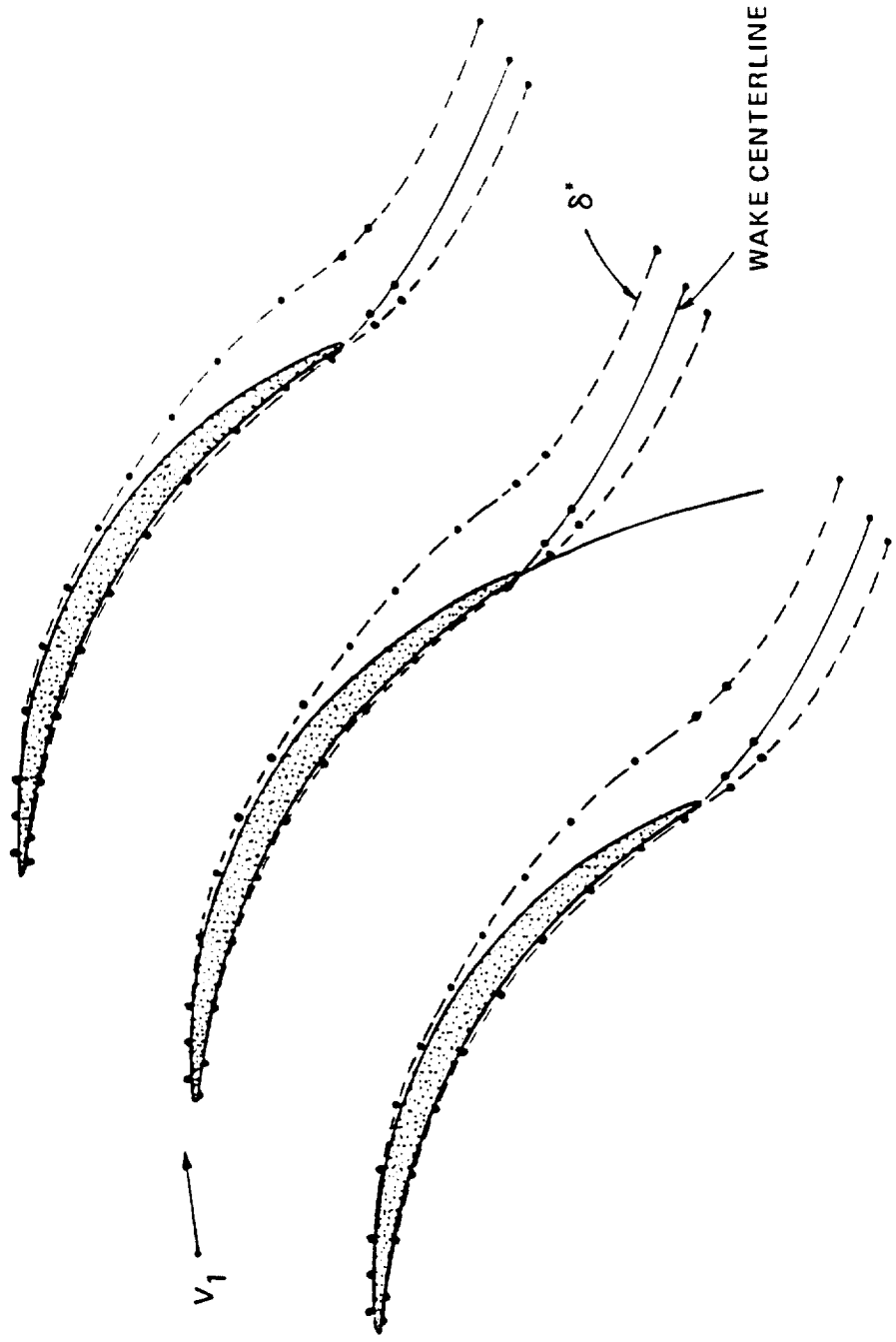

Figure 39. Cascade blades with the wake centerline and displacement thicknesses for $i = 5.0$ degrees (the two near wakes were measured with respect to the extended pressure surface arc which is shown)

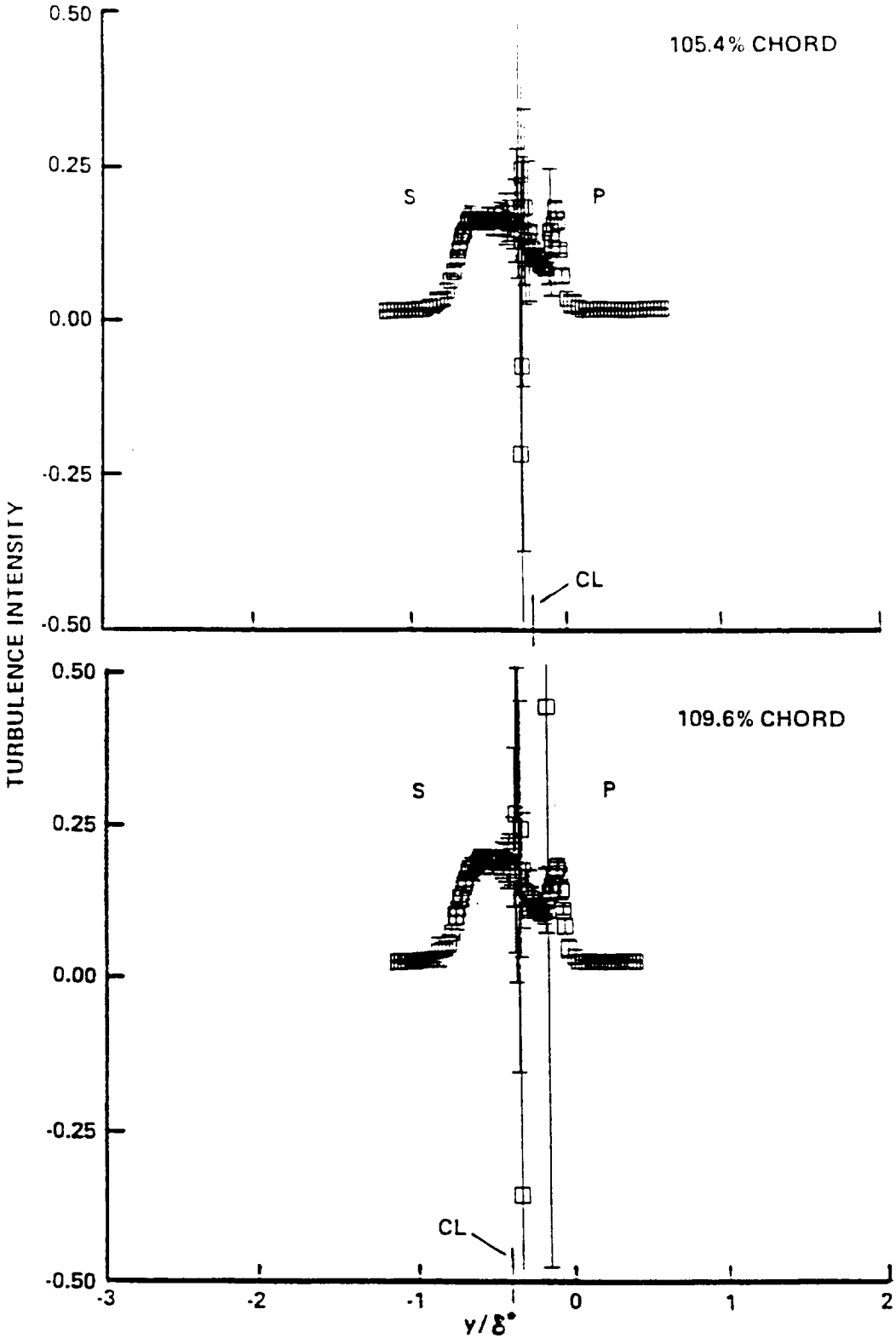

Figure 40. Turbulence intensity data for the near wakes at $i = 5.0$ degrees

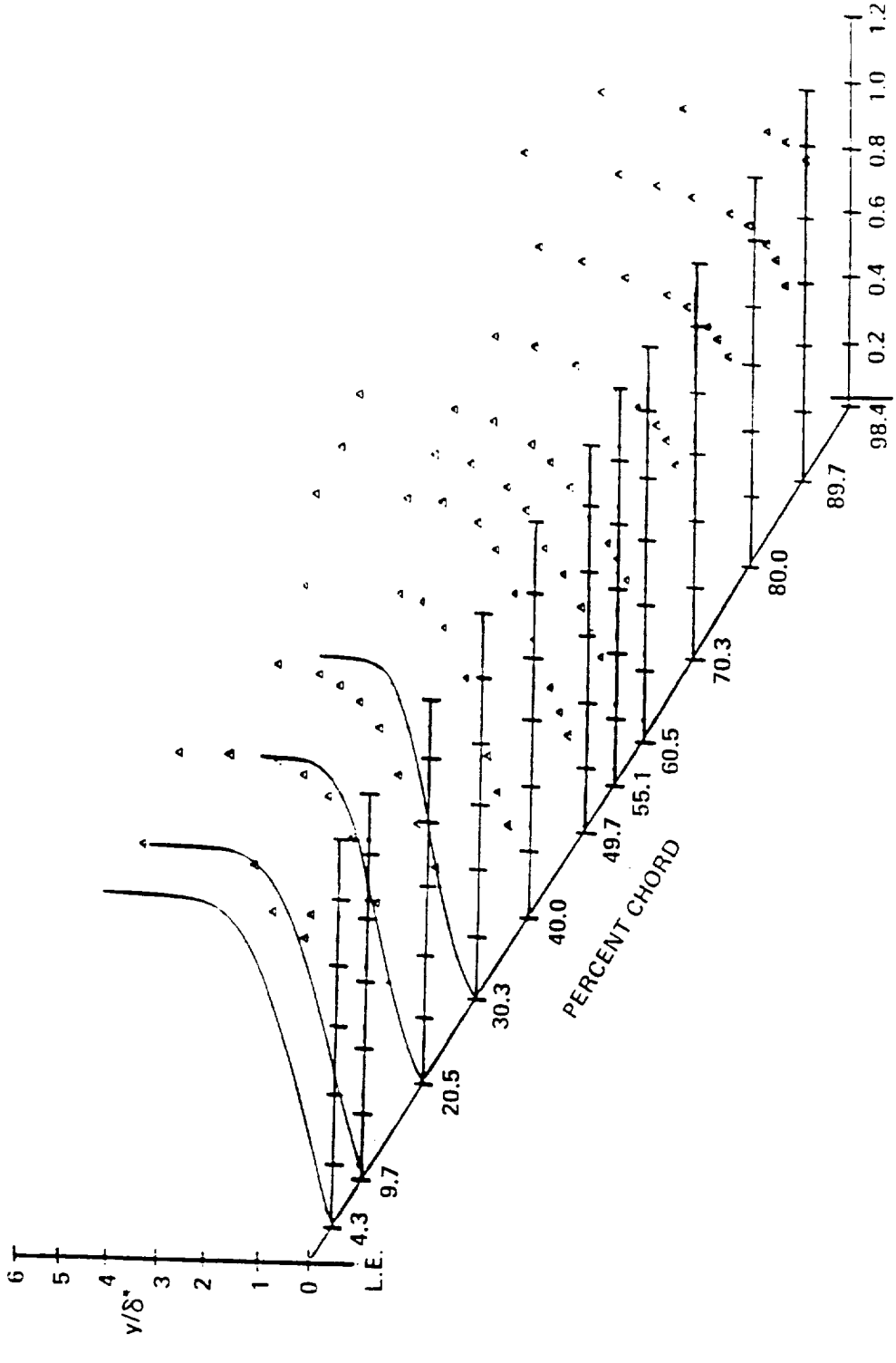

Figure 41. Reconstructed pressure surface boundary layers for $i = -1.5$ degrees in outer variables with the Falkner-Skan solutions (solid lines)

and 9.7% chord, the comparisons between the data and the Falkner-Skan solution are poor because the calculated values of δ^* used to normalize y are questionable in these extremely thin boundary layers. Comparisons at 20.5% and 30.3% chord show a continuing decrease in streamwise momentum of the measured profiles relative to the Falkner-Skan profiles: Falkner-Skan solutions could not be computed at 40.0% chord and downstream since the values of β indicated that laminar boundary layers would separate at these chord locations. The profiles at 40.0% and 49.7% chord are similar to the profiles on the suction surface at $i = 5.0$ degrees where the boundary layers are recovering from a leading edge separation "bubble."

At chord locations 49.7% chord and downstream, we successfully fit the data to the wall-wake equation. The fits at 49.7% chord and 55.1% chord, however, were marginal. Figure 42 shows the turbulent-like boundary layers plotted in inner variables. The wake region vanishes near the 80.0% chord location (Π=0). Downstream, the values of Π become negative–corresponding to the increasingly strong favorable streamwise pressure gradient. After calculating values of δ^*, we compared the data to the similarity defect law of Perry and Schofield [1973]. These comparisons were good at 49.7% and 55.1% chord and reasonable at 60.5% chord. Further downstream, the increasingly strong acceleration made it impossible to determine the velocity scale U_s from the half-power equation–giving no Perry-Schofield similarity.

A review of the sublimation flow visualization results show a region of low shear stress between 14.0% $\pm$ 5.5% chord and 38.2% $\pm$ 5.2% chord. These results, in conjunction with the outer variable plots of figure 41, seem to indicate the presence of a laminar flow separation "bubble" with at least a partial transition to turbulence. Completion of the transition to turbulence may take place downstream of the separation "bubble." This speculation may seem strange since we found no flow reversal in any of the boundary layers measured on this surface. Later results,[20] however, seem to indicate that we may not have penetrated the boundary layers far enough to find any backflow. The empirical relationships of Abu-Ghannam and Shaw [1980] place the onset

[20] See the discussion of the boundary layers on the suction surface when $i = -8.5$ degrees.

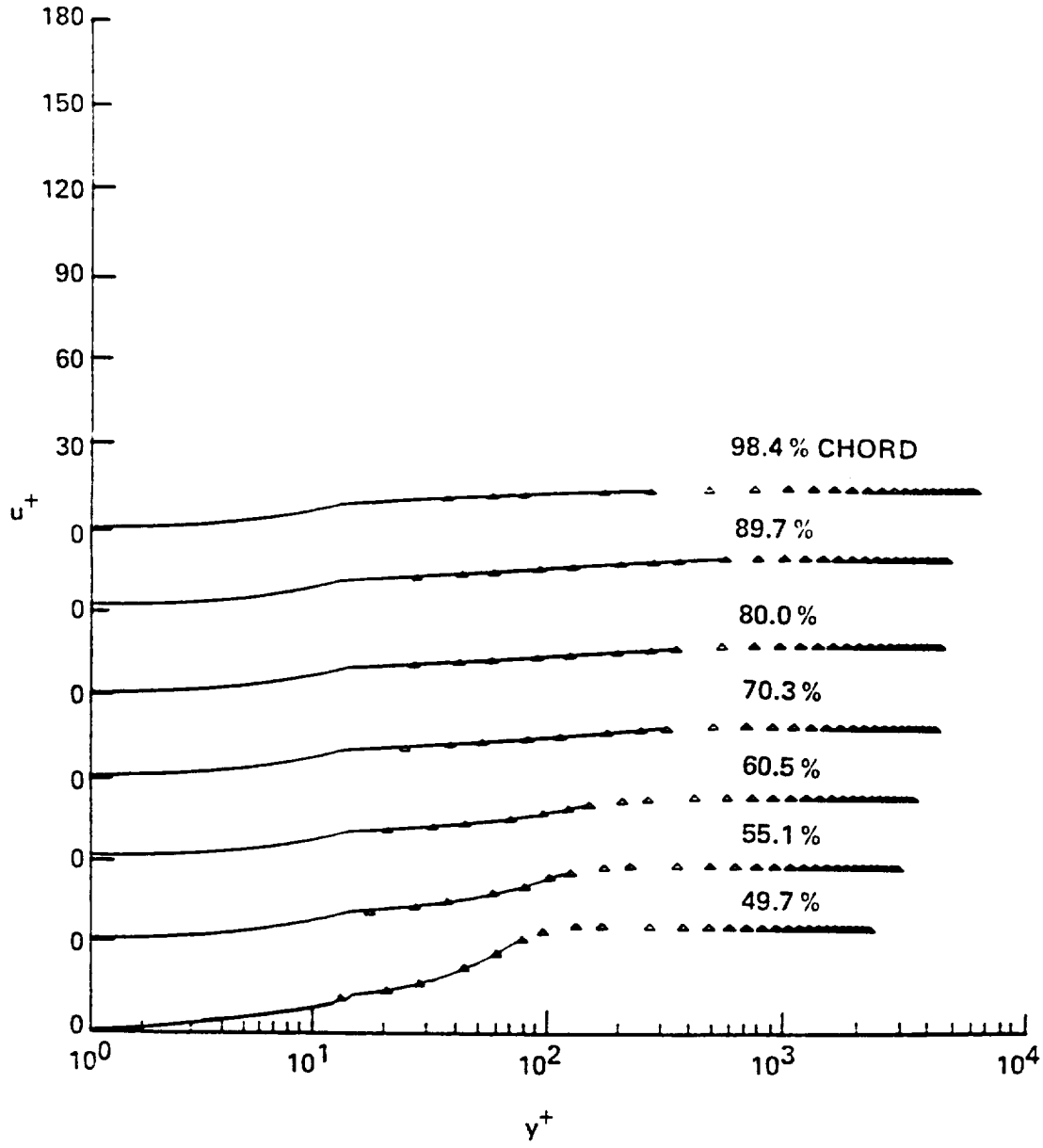

Figure 42. Reconstructed pressure surface boundary layers for $i = -1.5$ degrees in inner variables

of transition at 40.6% chord. This location may be in the correct vicinity, but we should ignore it since these empirical relationships come from data of "natural" transition with no separation "bubble." Transition, however, does take place. Because the transition to turbulence results in boundary layers with more streamwise momentum, a plot of mean velocity versus percent chord at a fixed distance above the blade surface can help determine the location of transition. Figure 43 shows this plot for $y = 0.254$ mm. The intial decrease corresponds to boundary layer growth. A sharp rise from the 55.1% chord location to the 70.3% chord location corresponds to transitional boundary layers. Unlike figure 26 for $i = 5.0$ degrees, the mean velocity stops increasing and begins decreasing–indicating that transition to turbulence is complete.

In order to better determine the locations of separation and transition, we computed integral parameters using spline fits of the data, Falkner-Skan solutions, a STAN5 solution, and least-squares fits of the data to the wall-wake equation (see appendix B). The plots of δ^* and Re_θ in figure 44 give only a little evidence of any separation or transition. Upstream of the 40.0% chord location, spline fits of the very thin boundary layers give questionable values of the integral thicknesses and the STAN5 solution seems to be the most reliable. At 30.4% chord, STAN5 computes a Re_θ of 250 and activates its transition turbulence model. At 36.5% chord, the STAN5 solution fails to converge–indicating the onset of separation. Downstream of the 40.0% chord location, the calculations using both the spline fits and the wall-wake fits give similar results. Note that the boundary layers become thinner near the trailing edge as the streamwise pressure gradient becomes more favorable.

Just before the separation "bubble" is reached and the STAN5 solution diverges, a sharp rise in H_{12} occurs as seen in figure 44. Separation of a laminar boundary layer is normally approximated when $H_{12} = 3.5$ and this corresponds to 35.1% chord. Downstream of the peak value of H_{12} (near 37.3% chord where $H_{12} \approx 3.9$), the values of H_{12} do not leave the laminar regime and enter the turbulent regime until 52.0% chord.

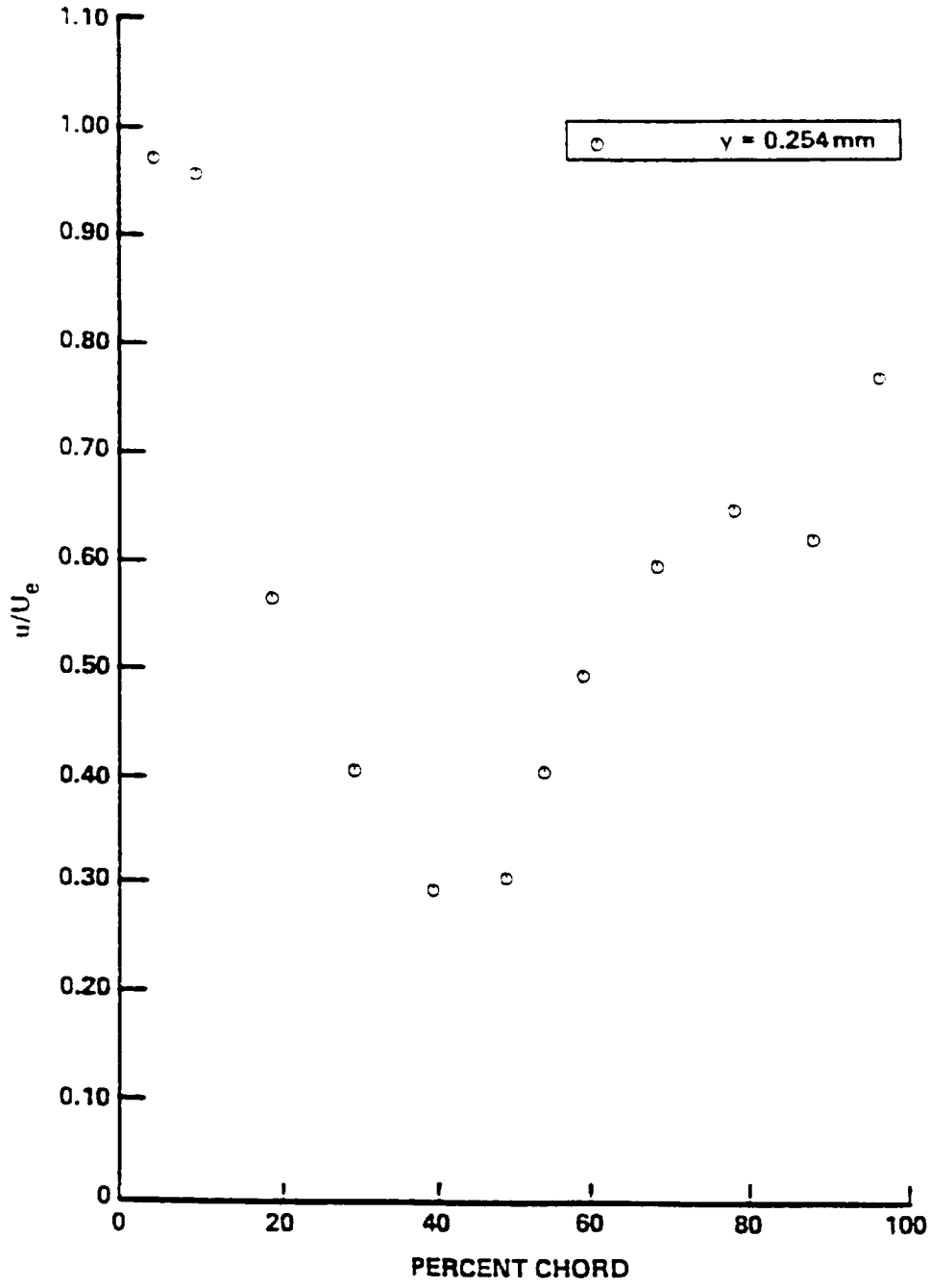

Figure 43. Variation of velocity, 0.254 mm from the blade, on the pressure surface for $i = -1.5$ degrees

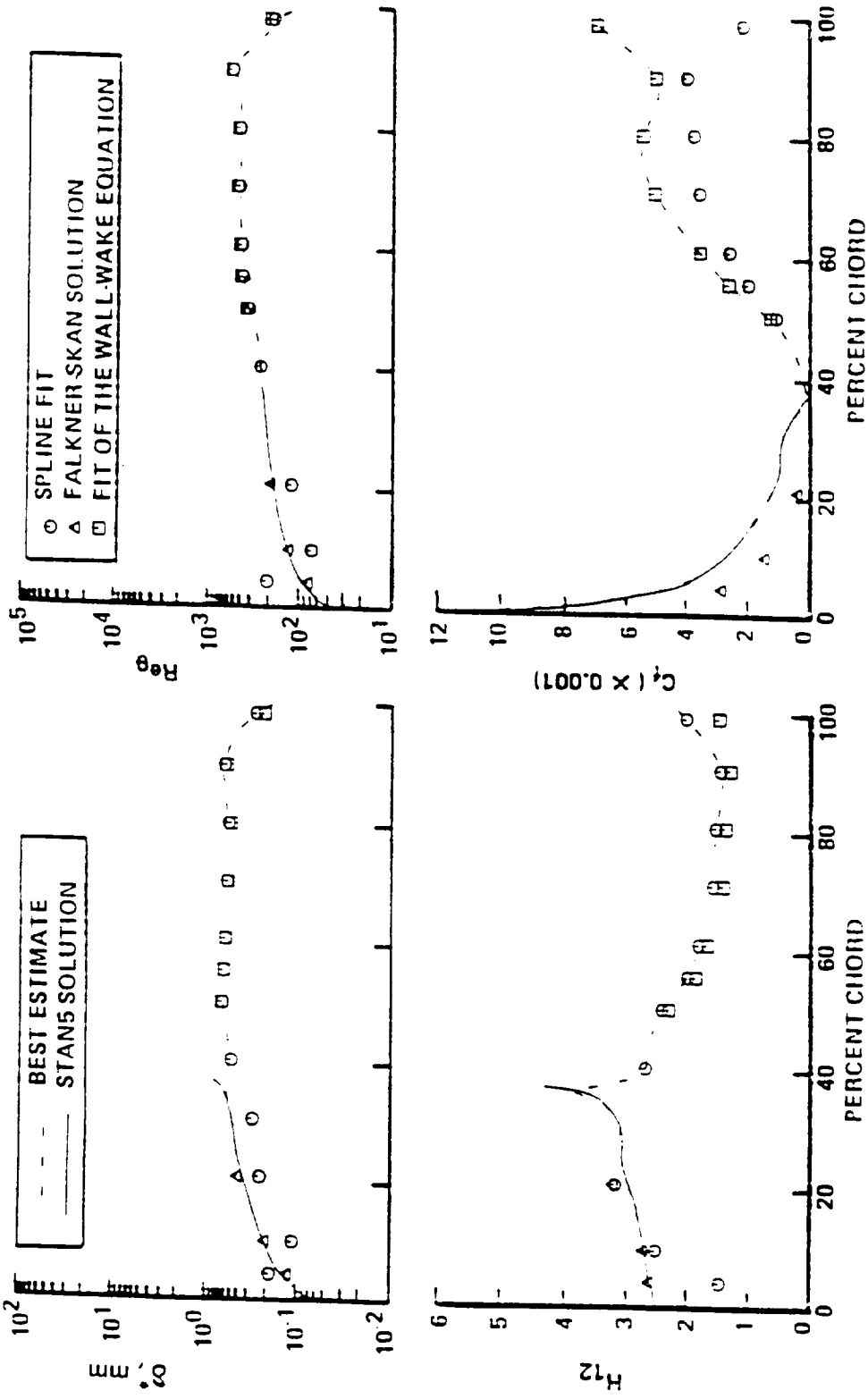

Figure 44. Variation of displacement thickness, first shape factor, momentum thickness Reynolds number, and skin friction coefficient on the pressure surface for $i = -1.5$ degrees

The clearest indication that a separation "bubble" truly exists is shown in the plot of skin friction coefficient in figure 44. Observing the STAN5 solution, we see that C_f starts at "infinity" at the leading edge, decreases rapidly, and finally vanishes near 37.3% chord. Downstream, the values of C_f computed from a fit of the wall-wake equation increase rapidly as we might expect of transitional boundary layers. A further increase in C_f occurs near the trailing edge where a large favorable pressure gradient exists. We decided to use the values of C_f that come directly from the fit of the wall-wake equation, since the calculations using the spline fit must employ the Ludweig-Tillman equation which may not be valid in this region.

The plots of turbulence intensity in figure 45 show similar trends to the turbulence intensity plots in figure 28 for the pressure surface boundary layers when $i = 5.0$ degrees. The intial boundary layers had velocity distributions with larger standard deviations than one would deem as physically possible for laminar boundary layers. As we discussed previously, the reason for these enlarged velocity distributions is not turbulence intensity, but a combination of mean-velocity-gradient broadening and a vibration of the LDV measurement volume. From 30.3% chord to 60.5% chord, a peak in turbulence intensity occurs away from the blade. Then, as the transition to turbulence ends, the the peaks move closer to the blade surface. These peaks move to the blade surface sooner for $i = -1.5$ degrees than for $i = 5.0$ degrees.

Suction Surface for a -1.5 Degree Incidence

After observing the measured velocity profiles of figure 12, we concluded that the suction surface boundary layers for $i = -1.5$ degrees and $i = 5.0$ degrees were similar. Both surfaces included a leading edge separation "bubble" and a trailing edge separation of the turbulent boundary layer. However, the turbulent boundary layers for $i = -1.5$ degrees were thinner

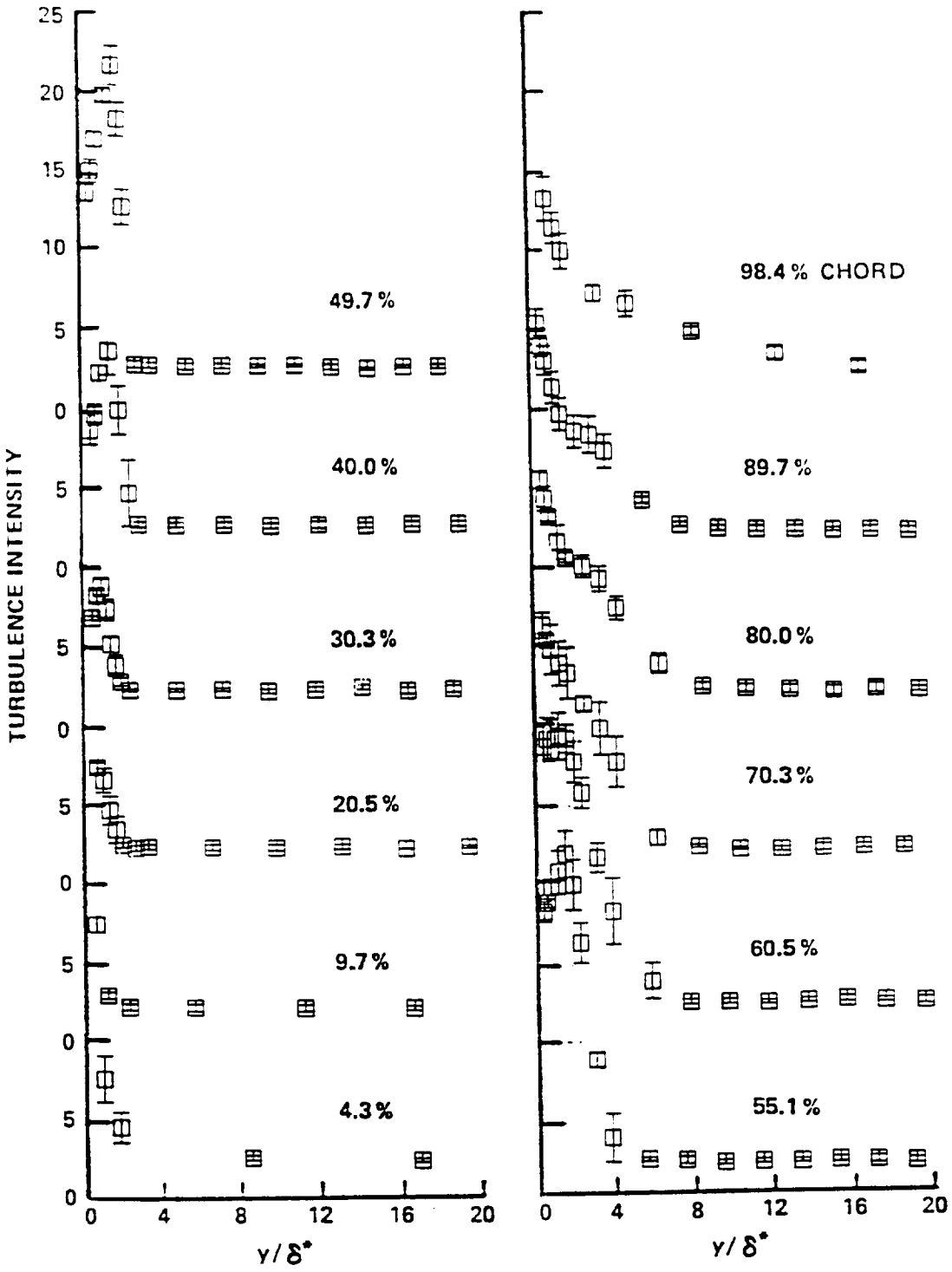

Figure 45. Turbulence intensity data for the pressure surface boundary layers at $i = -1.5$ degrees

because of the small region, with a favorable streamwise pressure gradient, from 3% chord to 9% chord.

Since all the boundary layers on this surface were turbulent, we fit all of the profiles to both a spline and the wall-wake equation. Figure 46 shows the velocity profiles in outer variables while figure 47 shows the profiles in inner variables. The outer variable plot shows us another difference between this flow field and the suction surface flow field for $i = 5.0$ degrees. The boundary layers immediately downstream of the leading edge separation "bubble" do not show signs of recovery–even though the boundary layers have clearly transitioned to turbulent. The small region of accelerated flow seems to have hastened the recovery process. Downstream, the boundary layer at 60.2% chord shows a slight inflection; the inflections become larger and finally negative mean velocities become evident at 90.3% chord. Another difference in the suction surface boundary layers for $i = -1.5$ degrees and $i = 5.0$ degrees is evident in the inner variable plots of figures 47 and 32, respectively. While the wall-wake equation fit the data for $i = 5.0$ degrees well for all the boundary layers prior to detachment, we see that this is not the case for $i = -1.5$ degrees. The boundary layers at 7.3% and 9.3% chord have a substantial logarithmic region and fit the wall-wake equation well. For 14.5% and 19.7% chord, the logarithmic region becomes quite small and the fit to the wall-wake equation worsens. While we could fit the boundary layers at 30.1%, 40.5%, and 49.8% chord, the fits were poor and no discernable logarithmic region is evident. Further downstream, the boundary layers at 60.2% and 70.6% chord fit the wall-wake equation well in the region just upstream of detachment.

Both the wall-wake and spline fits were used to compute various boundary layer parameters (see appendix B). Figure 48 shows the boundary layer growth in terms of δ^* and Re_θ. Except that the boundary layers are thinner, they grow in much the same manner as the suction surface boundary layers for $i = 5.0$ degrees. The shape factors in figure 48 show turbulent values from the leading edge until 62.0% chord where the H_{12} takes on a value of 2.2–an initial indicator of turbulent separation. Using the relation of Sandborn and Kline [1961] for intermittent separation

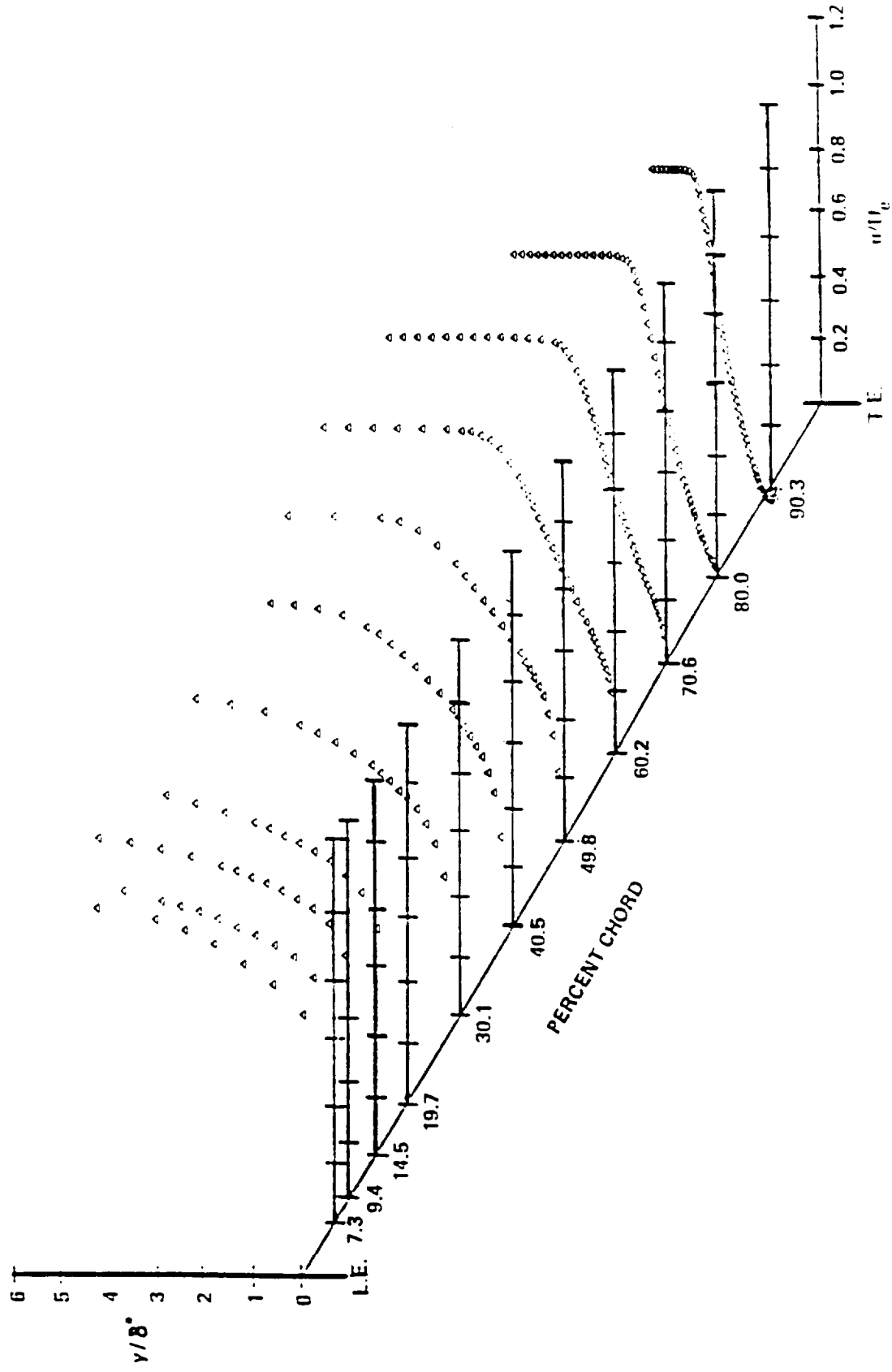

Figure 46. Reconstructed suction surface boundary layers for $i = -1.5$ degrees in outer variables

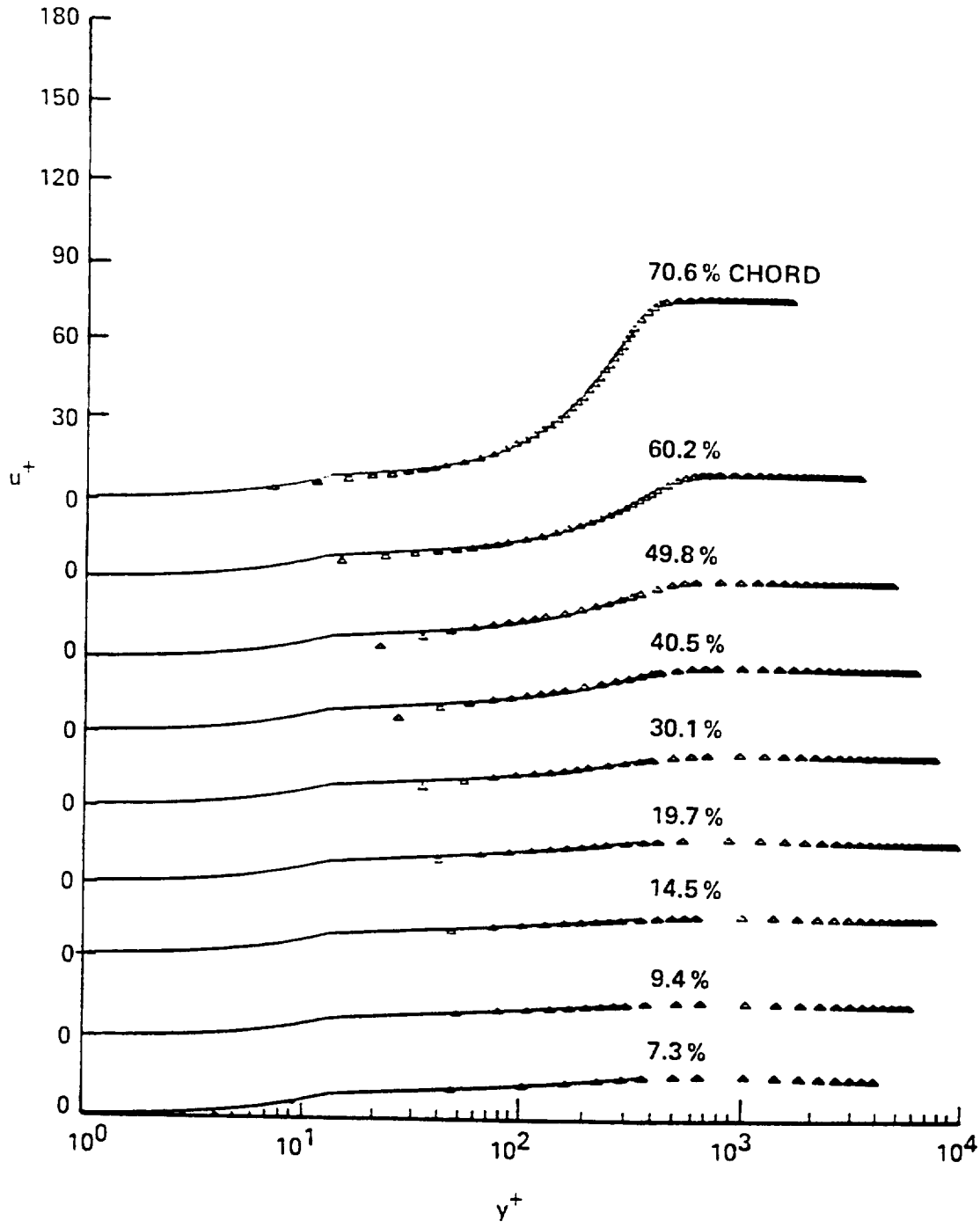

Figure 47. Reconstructed suction surface boundary layers for $i = -1.5$ degrees in inner variables

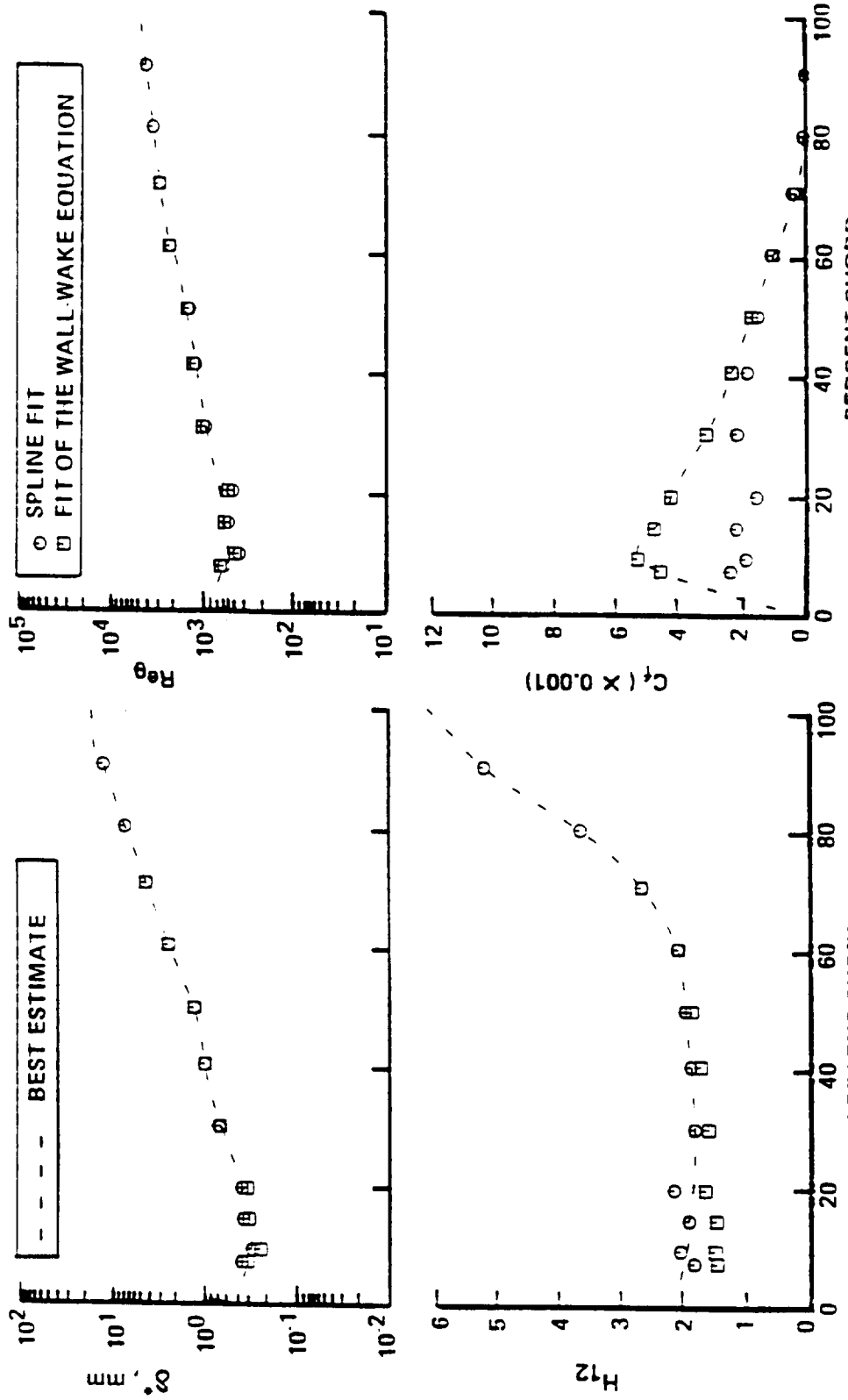

Figure 48. Variation of displacement thickness, first shape factor, momentum thickness Reynolds number, and skin friction coefficient on the suction surface for $i = -1.5$ degrees

gives a location of 70.9% chord and a first shape factor of 2.73. Both of these indicators show separation for $i = -1.5$ degrees to be slightly downstream of the corresponding locations for $i = 5.0$ degrees. Remember that the flow visualization showed a region of low shear stress at $45.1\% \pm 2.3\%$ chord–indicating that separation for $i = -1.5$ degrees is slightly upstream of separation for $i = 5.0$ degrees. Because of the difficulty in finding a satisfactory run time for the flow visualization tests, we might conclude that locating separation from flow visualization is less accurate than locating separation by analyzing the LDV data.

Figure 48 shows how the skin friction coefficient changes with chord location. Similarly to the suction surface for $i = 5.0$ degrees, C_f is zero at the leading edge because of the separation "bubble." The values of C_f rise sharply to a peak value larger than was the case for $i = 5.0$ degrees: Again, we might expect this larger value of C_f because of the region of accelerated flow. The skin friction vanishes near 85.8% chord. Unfortunately, the calculations of C_f using the spline fit and the Ludweig-Tillman equation give smaller and more scattered values. Despite the very small logarithmic regions in many of the boundary layers, we still have more confidence in the values of C_f that come directly from fitting the data to the wall-wake equation.

Since separation of turbulent boundary layers occurs over a finite region and not just where $C_f = 0$, we can examine the entire process of separation by plotting the instantaneous backflow in figure 49. Figure 49 shows the instantaneous backflow at each LDV measurement station for several distances from the blade. The data are very similar to the data in figure 34 for $i = 5.0$ degrees. Using the definitions of Simpson, Chew, and Shivaprasad [1981a], we can locate incipient detachment at 60.8% chord and intermittent transitory detachment at 72.1% chord. The position where $H_{12} = 2.2$ seems to indicate incipient detachment while the relation of Sandborn and Kline [1961] seems to indicate intermittent transitory detachment. Also, transitory detachment occurs at 82.1% chord–very near the detachment point where $C_f = 0$. These indications of the various stages of turbulent separation agree with the results on the suction surface for $i = 5.0$ degrees.

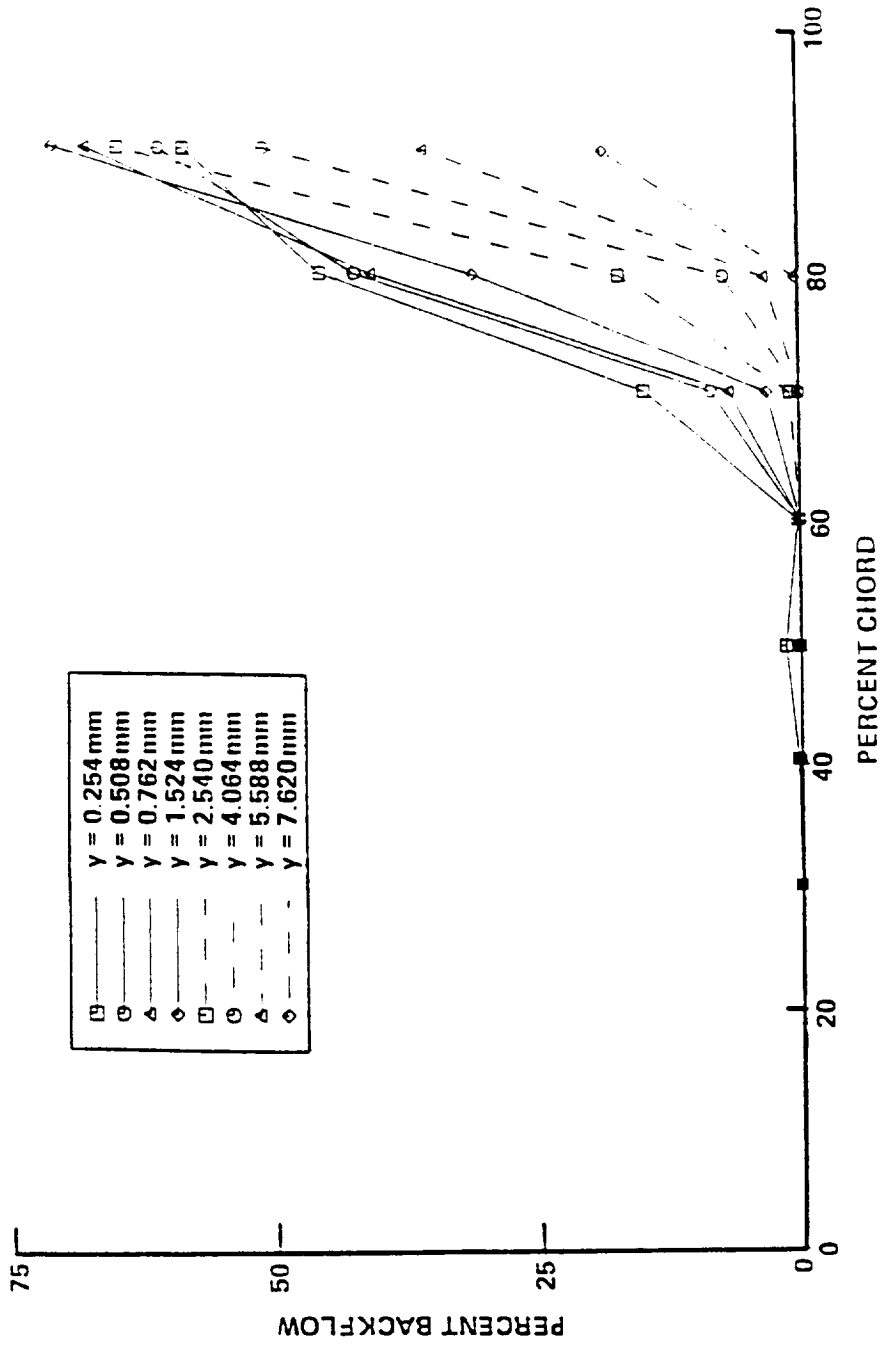

Figure 49. Instantaneous backflow measurements on the suction surface for $i = -1.5$ degrees

As we did for the suction surface at $i = 5.0$ degrees, we can examine the similarity of the velocity profiles at $i = -1.5$ degrees. Just as the fits to the wall-wake equation became slightly worse for the second incidence angle, the boundary layers for each incidence angle also showed worse similarity using the relation of Perry and Schofield [1973], as seen in figure 50. Again, the data deviates more and more from the similarity relation as the amount of instantaneous backflow increases–leading to no outer region similarity downstream of detachment. The mean backflow data at 90.3% chord has been plotted nondimensionally along with the mean backflow data at 94.9% chord for $i = 5.0$ degrees in figure 36. The velocity scale is the maximum backflow velocity and the length scale is the total backflow thickness. Both sets of data show some similarity when plotted in this manner. The data collapses fairly well with the curve that represents the average of several data sets measured by Simpson, Strickland, and Barr [1977] and Simpson, Chew, and Shivaprasad [1981a].

Some final physical insight can be obtained by observing the turbulence intensity plots of figure 51. With one exception, these plots look very similar to the turbulence intensity plots in figure 37 for the suction surface when $i = 5.0$ degrees. Again, the small region with a favorable streamwise pressure gradient seems to have accelerated the recovery from the leading edge separation "bubble." Therefore, the maximum mean-shear rate remains very close to the blade surface and the maximum turbulence intensity will also remain very close to the blade surface. Just like the turbulence intensities for $i = 5.0$ degrees, the turbulence intensities for $i = -1.5$ degrees track the location of maximum mean-shear rate in the turbulent separation region and the peaks move away from the blade surface. Notice the very large 95% confidence bands at 90.3% chord when the mean velocities become negative.

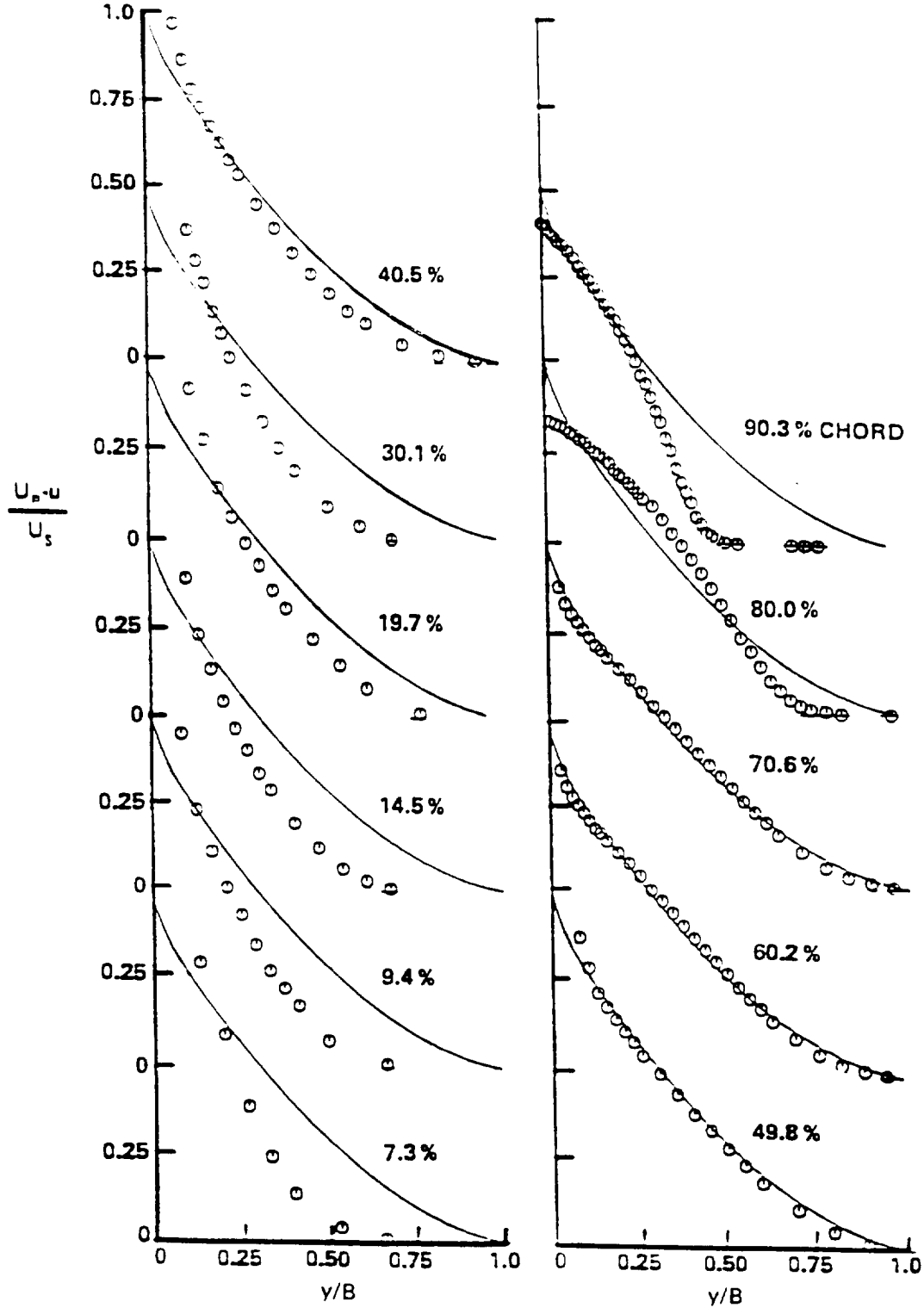

Figure 50. Reconstructed suction surface boundary layers for $i = -1.5$ degrees in defect form with Perry-Schofield similarity

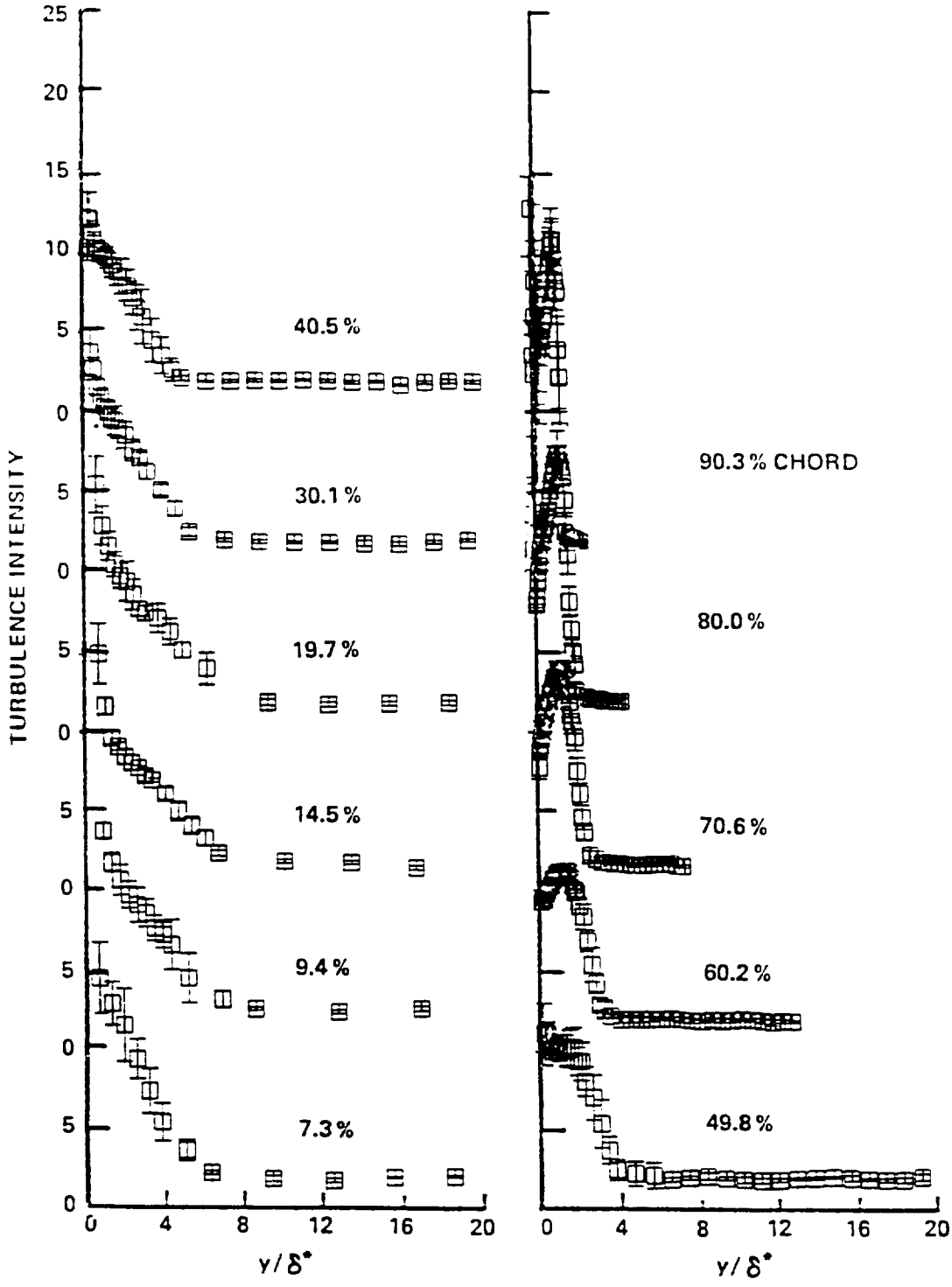

Figure 51. Turbulence intensity data for the suction surface boundary layers at $i = -1.5$ degrees

Wakes for a -1.5 Degree Incidence

A similarity analysis of the near and far wakes in figure 13 give results resembling the results for $i = 5.0$ degrees. As seen in figure 52, the near wakes at 106.0% and 109.7% chord fail to show similarity with the Gaussian distribution of Lakshminarayana and Davino [1980]. Similarity does hold for the far wake at 131.9% chord.

After calculating the integral parameters for the near and far wakes, we located the boundary layers and wakes on a schematic of the cascade blades in figure 53. Since the displacement of the freestream fluid is smaller for $i = -1.5$ degrees than for $i = 5.0$ degrees, the wake is not forced to migrate as far from the extended chord line. Some strong curvature of the wake centerline is evident in the near-wake region and this indicates that some trailing edge loading does exist (as seen in the blade static-pressure distribution in figure 10).

Turbulence intensity profiles for the two near wakes are shown in figure 54. These profiles look very similar to the near wake profiles for $i = 5.0$ degrees. Both sets of profiles show asymmetric wakes with the turbulence intensity peaks displaced from the wake centerline. All of these wakes show a large scatter in turbulence intensity data in the regions of mean backflow.

Pressure Surface for a -8.5 Degree Incidence

From the blade static-pressure distribution in figure 15, we can see that the large adverse pressure gradient near the suction surface leading edge for the 5.0 and -1.5 degree incidence angles has shifted to the pressure surface leading edge for the -8.5 degree incidence angle. Thus, the

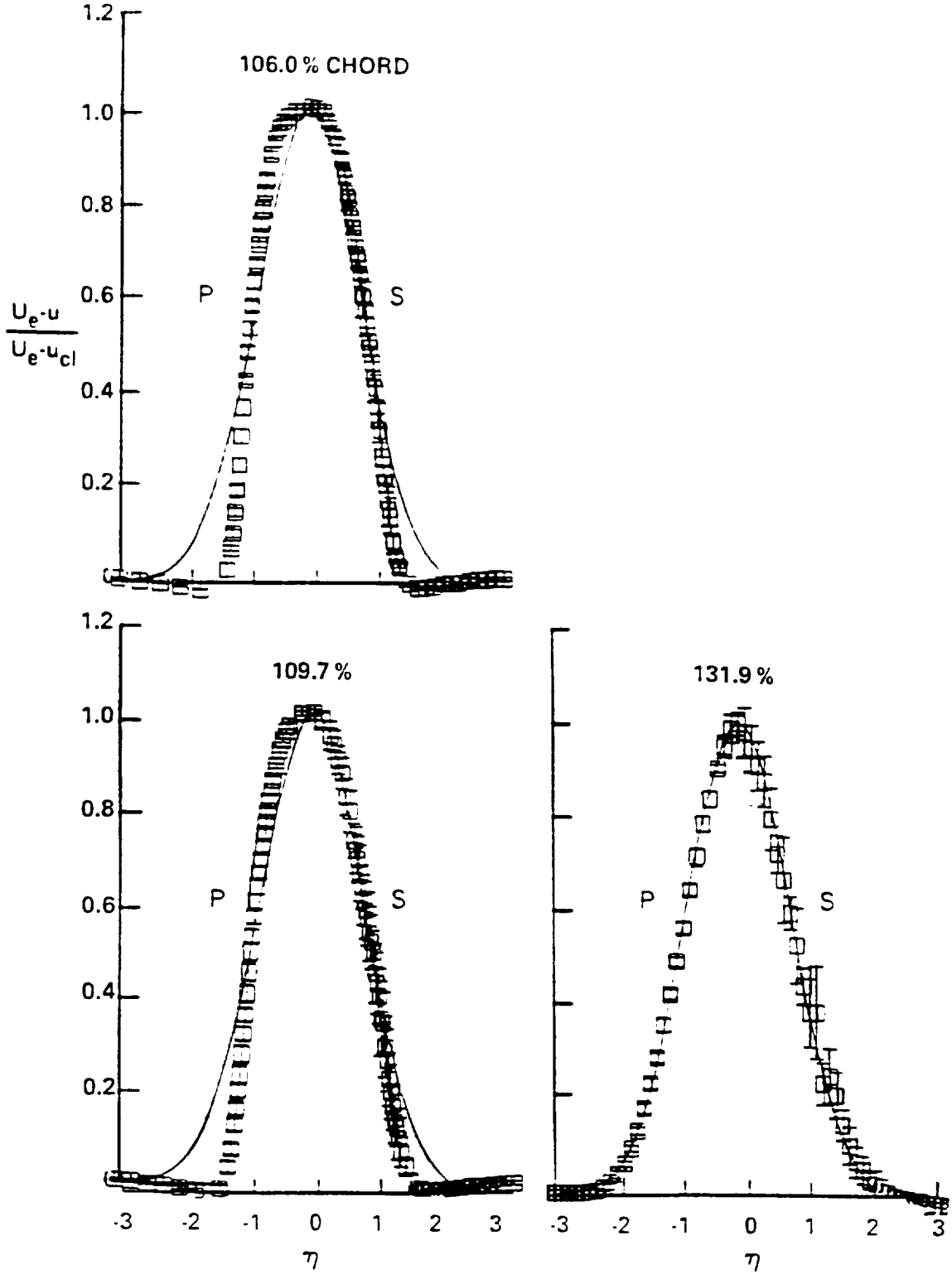

Figure 52. Wakes for $i = -1.5$ degrees in defect form with Gaussian similarity

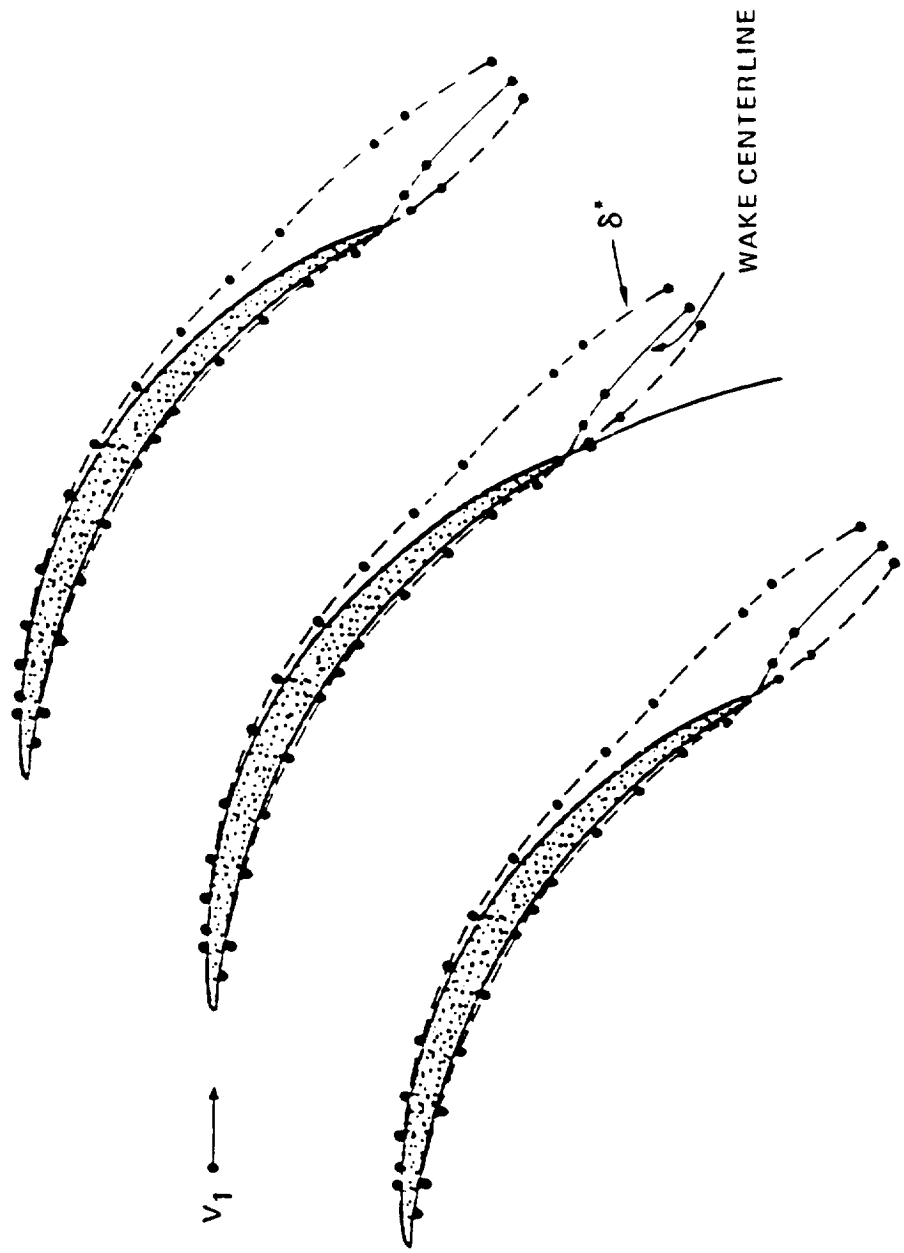

Figure 53. Cascade blades with the wake centerline and displacement thicknesses for $i = -1.5$ degrees (the two near wakes were measured with respect to the extended pressure surface arc which is shown)

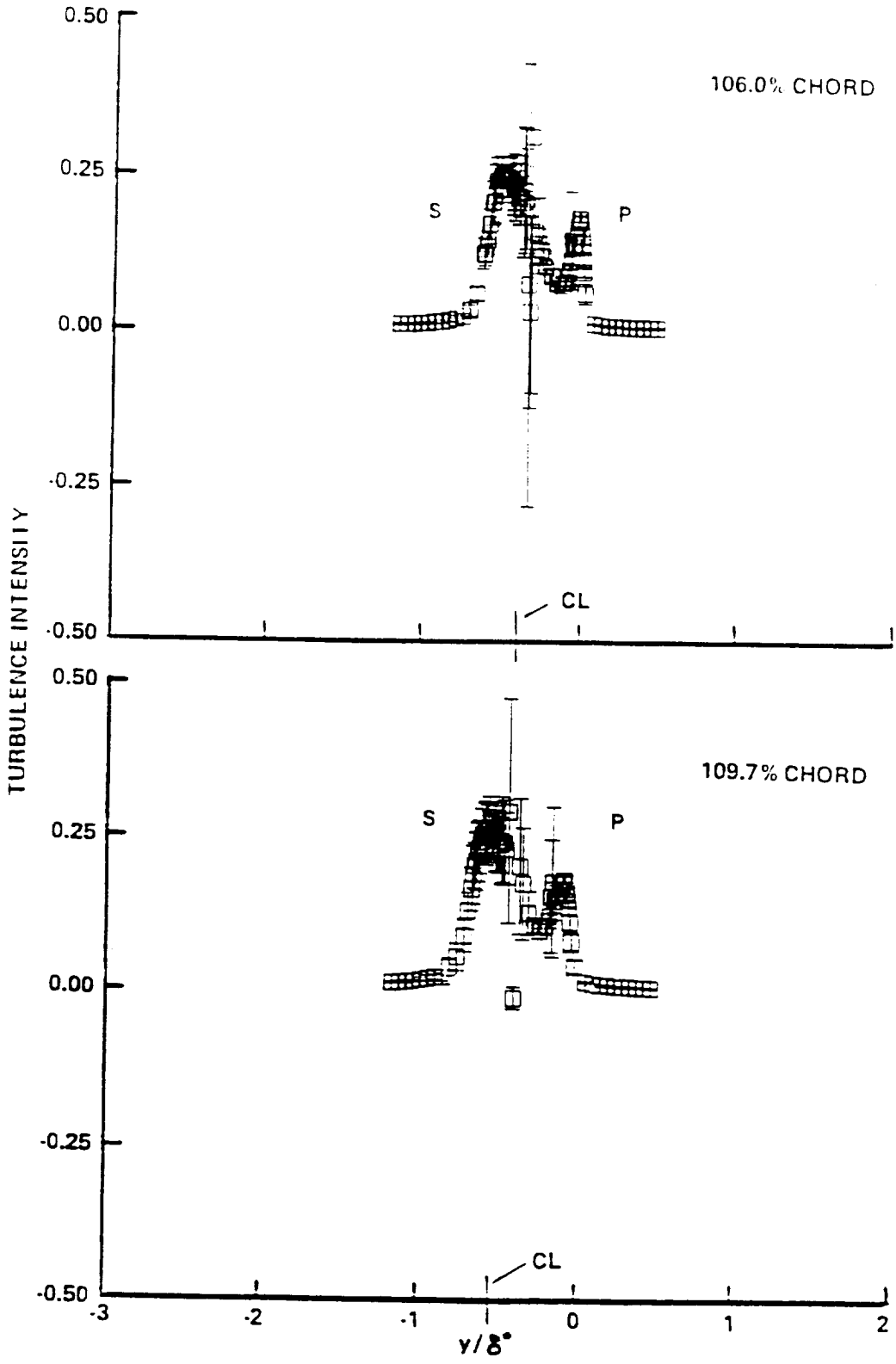

Figure 54. Turbulence intensity data for the near wakes at $i = -1.5$ degrees

separation "bubble" is now on the pressure surface as indicated with the oil film flow visualization. This separation "bubble" leads to an immediate transition and causes all of the measured boundary layers in figure 16 to be turbulent. After accounting for the normal pressure gradient, we fit each velocity profile to both a spline and the wall-wake equation. Figure 55 shows the outer variable plots of all eleven boundary layers. Despite the expected transition caused by the leading edge separation "bubble," the first few boundary layers are very thin and only a few data points were acquired within the boundary layer. Because of these very few data points, we find it difficult to observe any evidence of a recovery from the leading edge separation "bubble." Downstream, all of the profiles look like typical turbulent boundary layers. The inner variable plots in figure 56 are also typical of turbulent boundary layers. The wake region is quite small for all of the boundary layers–although the size of the wake region is probably distorted near the leading edge because of the very few data points. Also, we could not compute U_s near the leading edge because of the very few data points. At 30.3% chord and downstream, the velocity profiles in defect form showed only fair similarity using the relation of Perry and Schofield [1973].

Data fits to both a spline and the wall-wake equation were used to calculate various boundary layer parameters as compiled in appendix B. Figure 57 shows the boundary layer growth in terms of δ^* and Re_θ. The boundary layers grow rapidly at first and then grow with a decreasing rate until the favorable streamwise pressure gradient near the trailing edge causes the boundary layers to become thinner. The values of Re_θ also present a dilemma. While we expect all turbulent boundary layers on this surface, the values of Re_θ for the first few boundary layers seem too small to support turbulence. Recall that Murlis, Tsai, and Bradshaw [1982] found no logarithmic region, at zero pressure gradient, for Re_θ less than 700 and Smits, Matheson, and Joubert [1983] found no logarithmic region, at favorable pressure gradients, for Re_θ less than 261. Near the leading edge, we could expect even larger minimum values of Re_θ since the streamwise pressure gradients are adverse. However, despite the limited amount of data, we did fit all of the boundary layers to the wall-wake equation even though Re_θ did not reach 700 until 49.7% chord.

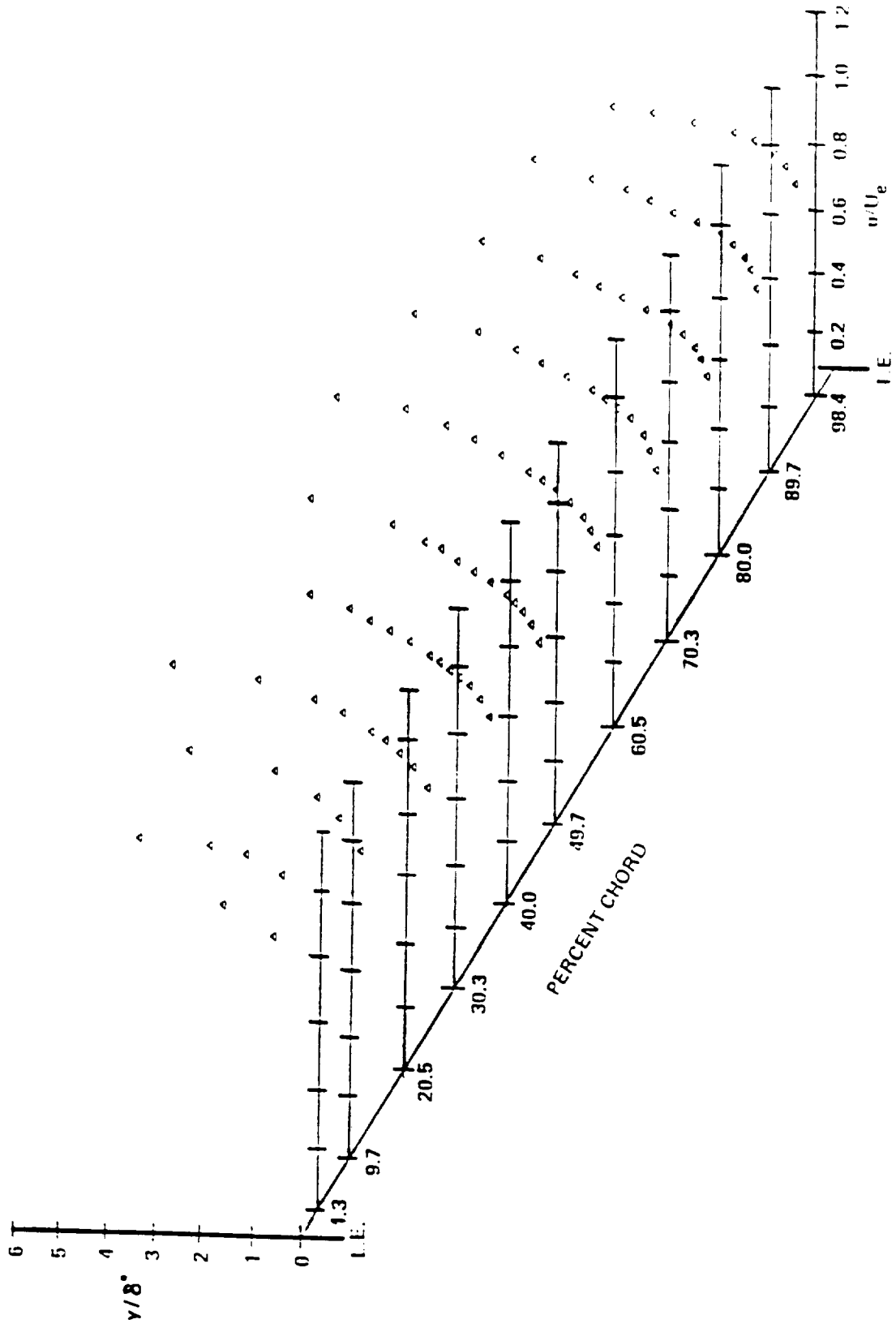

Figure 55. Reconstructed pressure surface boundary layers for $i = -8.5$ degrees in outer variables

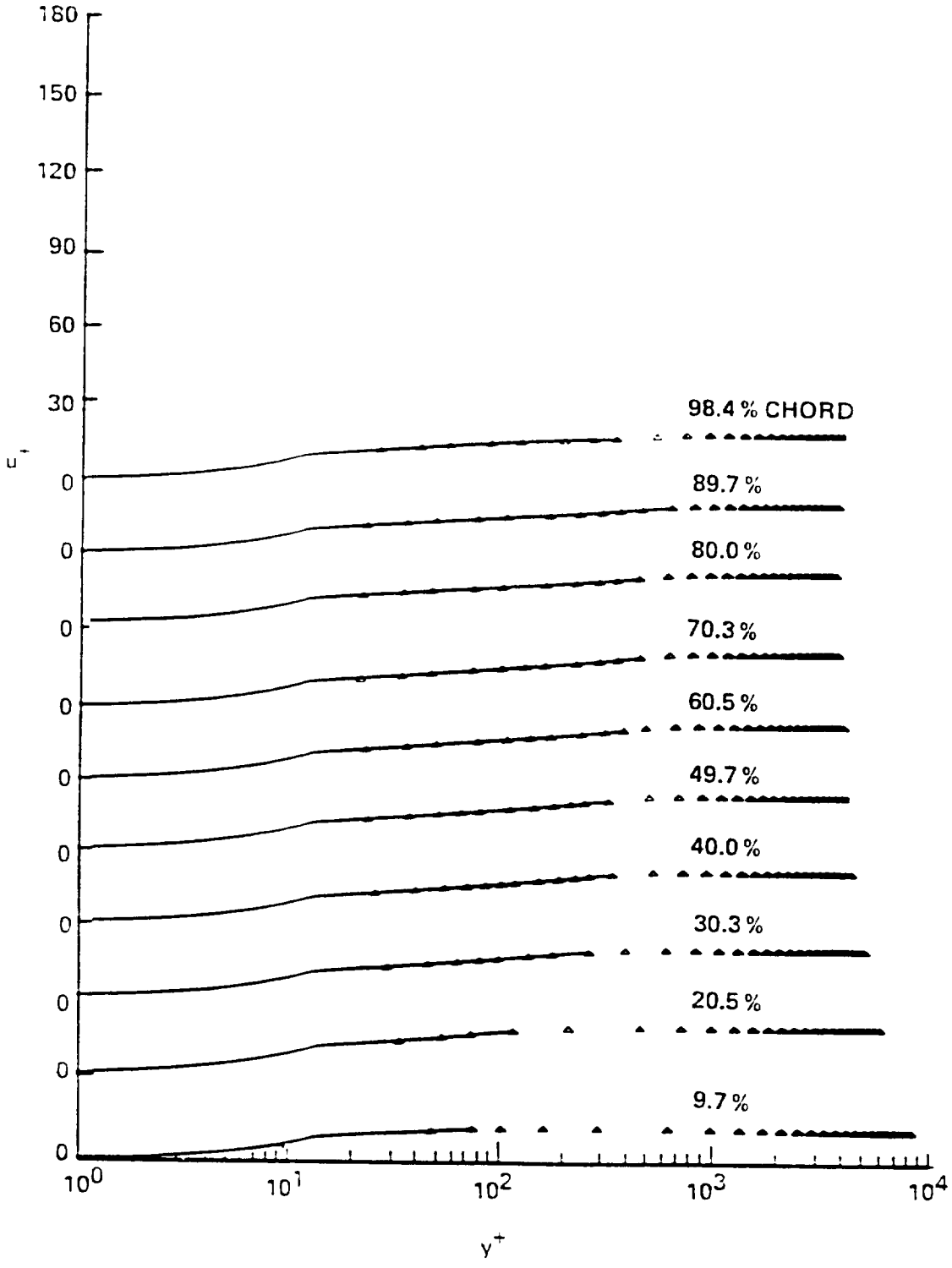

Figure 56. Reconstructed pressure surface boundary layers for $i = -8.5$ degrees in inner variables

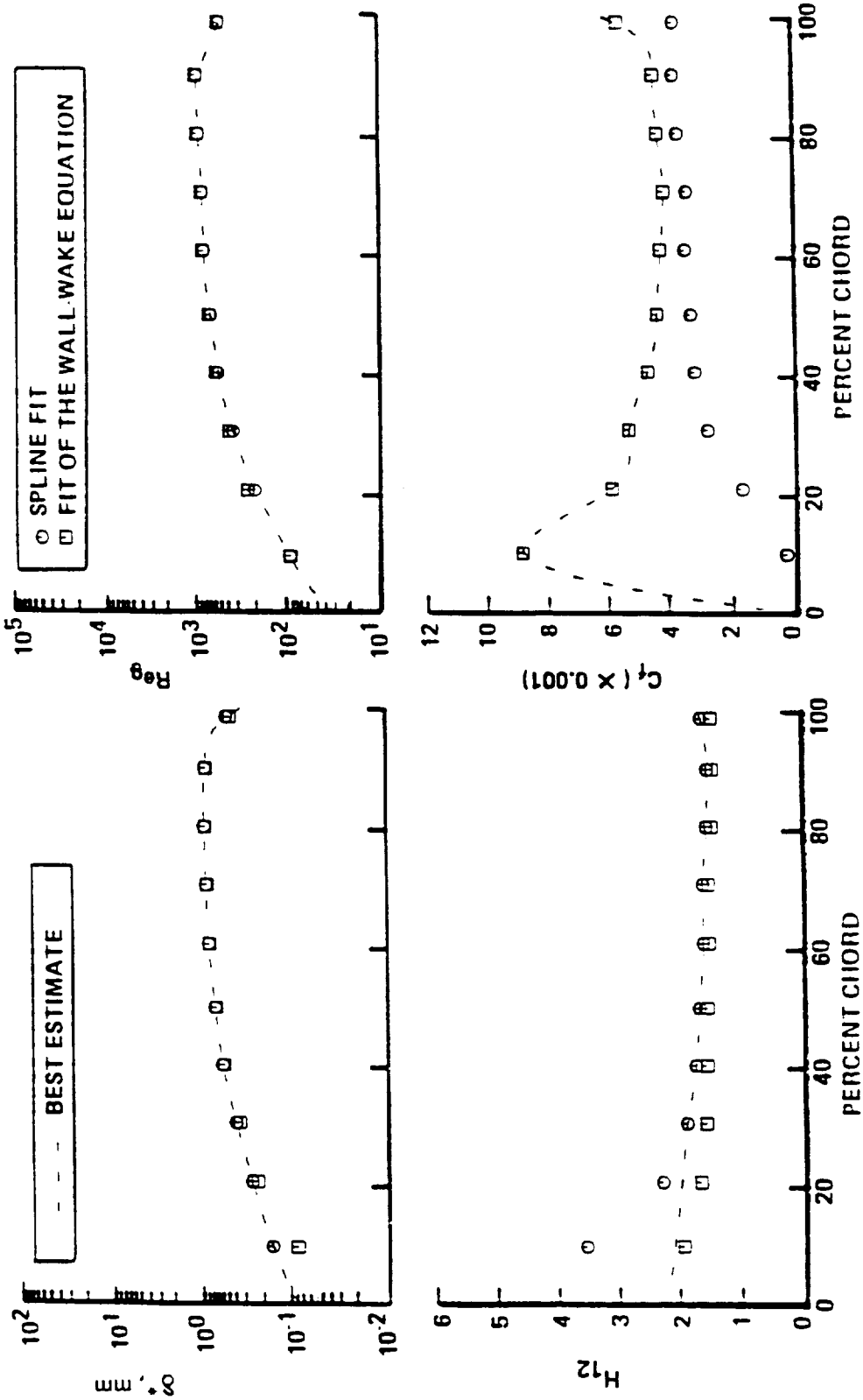

Figure 57. Variation of displacement thickness, first shape factor, momentum thickness Reynolds number, and skin friction coefficient on the pressure surface for $i = -8.5$ degrees

The first shape factor plot in figure 57 shows another interesting development. The values of H_{12} for all of the boundary layers lie within the turbulent regime when we use the fit to the wall-wake equation for calculating H_{12}. However, when we use the spline fit to calculate H_{12}, the boundary layers through 20.5% chord show values larger than 2.2. As seen in figure 57, differences also occur in calculating C_f when using the two types of fits. From analyzing the boundary layers on the previous surfaces and incidence angles, we have found that obtaining C_f directly from fitting the data to the wall-wake equation gives better results than obtaining C_f from the spline fit and Ludweig-Tillman equation. Since a leading edge separation "bubble" must exist, C_f should be zero very close to the leading edge. We assume then that C_f must rise to the value at 9.7% chord as obtained from the fit to the wall-wake equation–even though the values of C_f calculated this way do not imply a zero value of C_f at the leading edge. The recovery from the leading edge separation "bubble" may be complete before 9.7% chord. The values of C_f calculated from the spline fit and the Ludweig-Tillman equation do imply a zero value of C_f at the leading edge. However, these values fail to show the expected trends at other blade locations. Using the fit to the wall-wake equation, we see that C_f does decrease in the region of adverse pressure gradient, level off as the pressure gradient diminishes, and increase near the trailing edge where a favorable pressure gradient exists.

The turbulence intensity plots of figure 58 show typical results in the absence of transition and separation regions. The maximum value of turbulence intensity for all of these boundary layers lies very close to the blade surface. Note that the boundary layers close to the leading edge do not show any signs of the recovery from the leading edge separation "bubble."

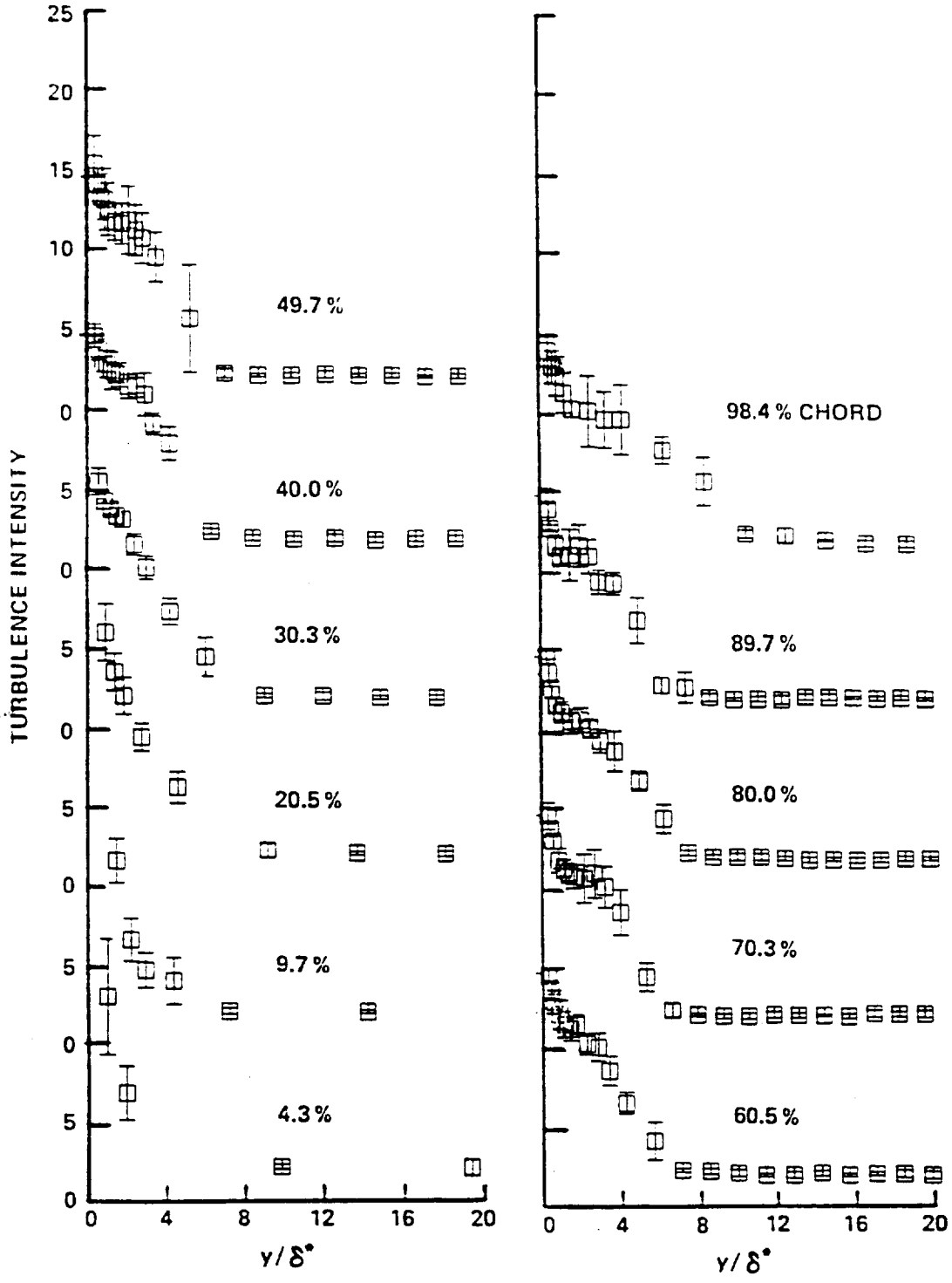

Figure 58. Turbulence intensity data for the pressure surface boundary layers at $i = -8.5$ degrees

Suction Surface for a -8.5 Degree Incidence

Recall that a strong favorable streamwise pressure gradient was found on the first 18% chord of the suction surface for $i = -8.5$ degrees (see figure 15). Expecting laminar boundary layers within this region, we found that the boundary layers at 10.4% and 19.7% chord were too thin to measure. Without these measurements, we could only use our Falkner-Skan and STAN5 solutions to study the behavior of the leading edge boundary layers. For all of the remaining boundary layers of figure 17, we fit the data to splines (after accounting for the normal pressure gradient) and attempted to fit the data to the wall-wake equation. After this initial analysis, we plotted the velocity profiles in outer variables in figure 59. The data at 30.1% chord compare very well to the Falkner-Skan solution which indicates the boundary layers remain laminar until this location. The Falkner-Skan solution failed at 40.5% chord and the outer variable plot here showed a slight point of inflection. At 49.8% and 55.0% chord, the outer variable plots showed that the boundary layers were separated. The boundary layer seemed to have recovered by 60.2% chord which signified the presence of a separation "bubble." Downstream, the boundary layers appeared turbulent and eventually, the adverse pressure gradient led to a slight point of infection in the profile at 97.6% chord. The inner variable plots of figure 60 show that we were able to fit all of the boundary layers from 60.2% chord to 97.6% chord to the wall-wake equation, but only the boundary layer at 70.6% chord gave a convincing fit. We can conclude that the separation "bubble" caused the laminar boundary layer to transition to turbulence. However, the recovery from this separation "bubble" and the near separation of the trailing edge turbulent boundary layer lead to a very small logarithmic region for most of the turbulent boundary layers downstream of reattachment. Also, we could only find the velocity scale U_s at 70.6% chord and

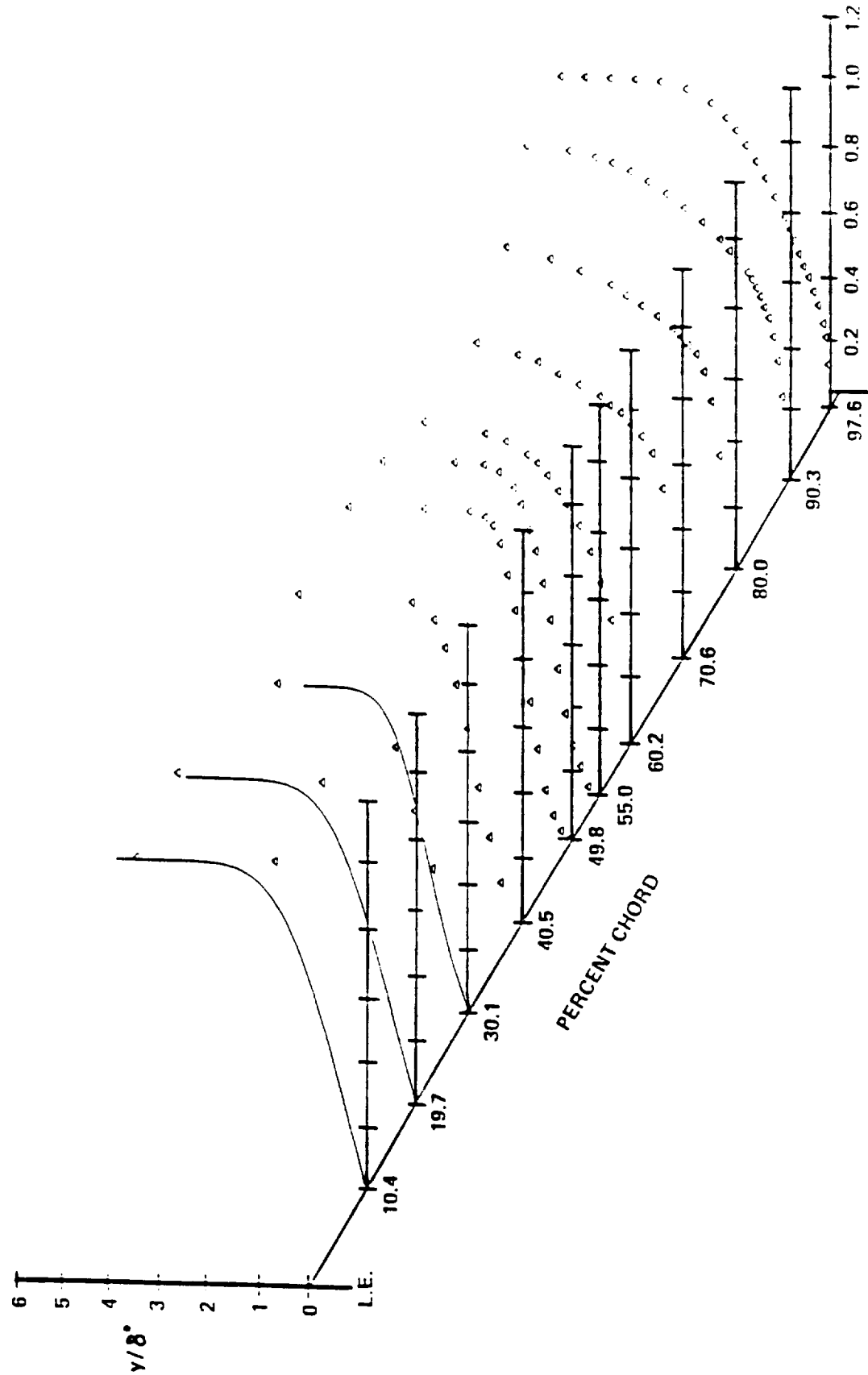

Figure 59. Reconstructed suction surface boundary layers for $i = -8.5$ degrees in outer variables with the Falkner-Skan solutions (solid lines)

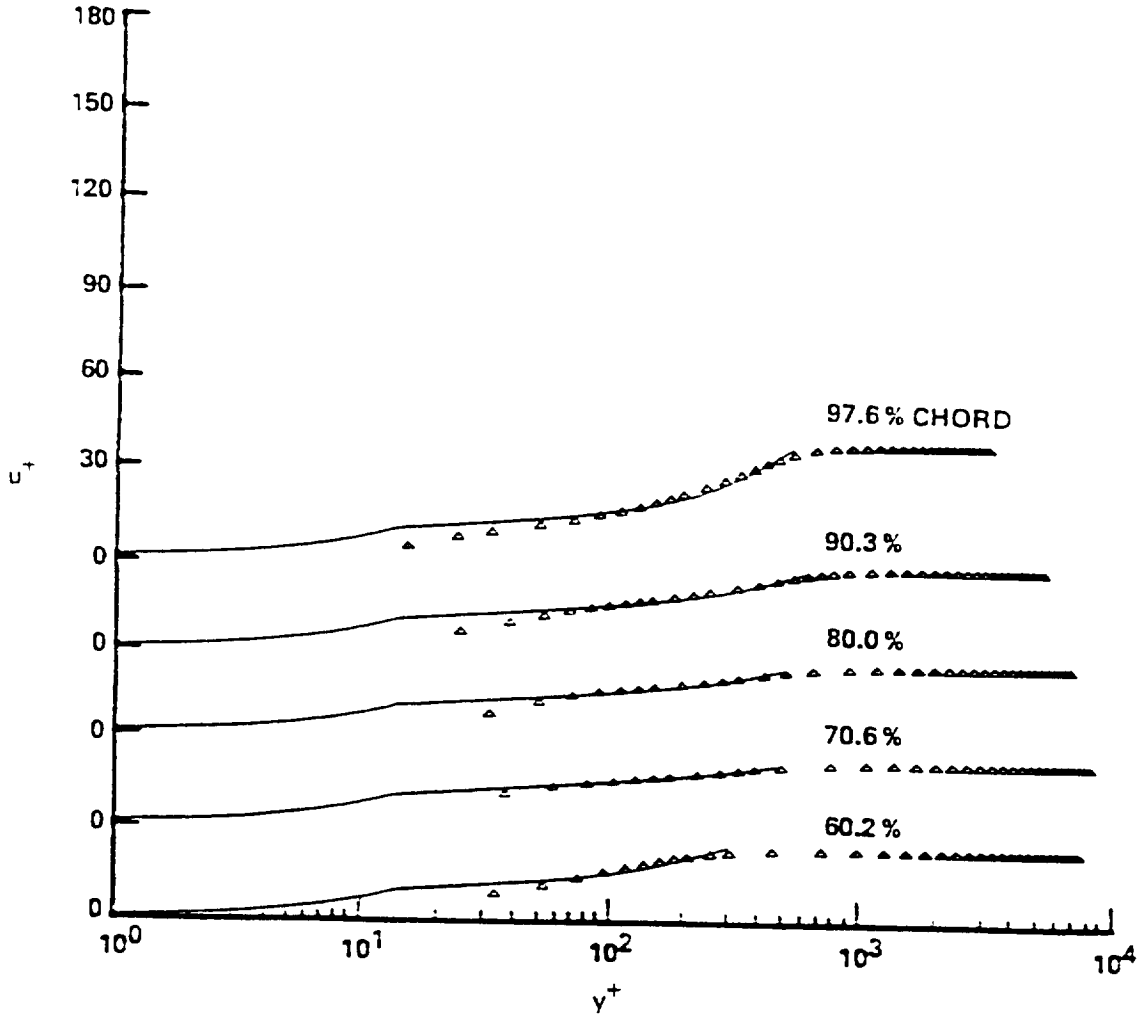

Figure 60. Reconstructed suction surface boundary layers for $i = -8.5$ degrees in inner variables

beyond–and even for these boundary layers, only the boundary layer at 97.6% chord showed reasonable agreement with the similarity relation of Perry and Schofield [1973].

The boundary layer growth on this surface is dominated by the existence of a substantial separation "bubble." The chordwise variation of δ^* in figure 61 shows a sudden rise in the boundary layer growth after the 30.1% chord location. The growth levels off and then suddenly δ^* decreases until just downstream of the 60.2% chord location. This type of shape led to the term separation "bubble." Since the separation "bubble" leads to a rapid transition to turbulence, we expect to see a sharp rise in Re_θ just before reattachment. Figure 61 shows this sharp rise between the 55.0% and 60.2% chord locations. The STAN5 solution fails to predict any evidence of separation. After the initially laminar boundary layer, STAN5 predicts that the adverse streamwise pressure gradient will induce a "natural" transition between 22.9% and 44.2% chord. The numerical solution predicts no "bubble" shape in the chordwise δ^* variation and only a gradual rise in Re_θ from the laminar region to the turbulent region.

The variation of H_{12} in figure 61 shows the most dramatic representation of the separation "bubble." Near the leading edge, the Falkner-Skan and STAN5 solutions show values of H_{12} in the laminar regime. Calculations using the spline fit, as well as the Falkner-Skan solution, show H_{12} increasing at the 30.1% chord location. H_{12} continues to rapidly increase–according to the spline fit calculation–with a laminar separation value of 3.5 occurring near 31.9% chord. As was the case of δ^*, H_{12} peaks near 51.9% chord at a value near 5.8. Between the 55.0% and 60.2% chord locations, H_{12} drops very rapidly as the separation "bubble" induces a sudden transition to turbulence. The values of H_{12} enter the turbulent regime near 59.0% chord. From 70.6% chord through 90.3% chord, H_{12} remains nearly constant before rising to the turbulent separation value of 2.2 at the trailing edge. Again, STAN5 gives values of H_{12} that decrease in a region of "natural" transition since no separation "bubble" was predicted.

The STAN5 solution gives the values of C_f near the leading edge. As shown in figure 61, C_f decreases asymptotically from "infinity" at the leading edge. As it did for the other boundary

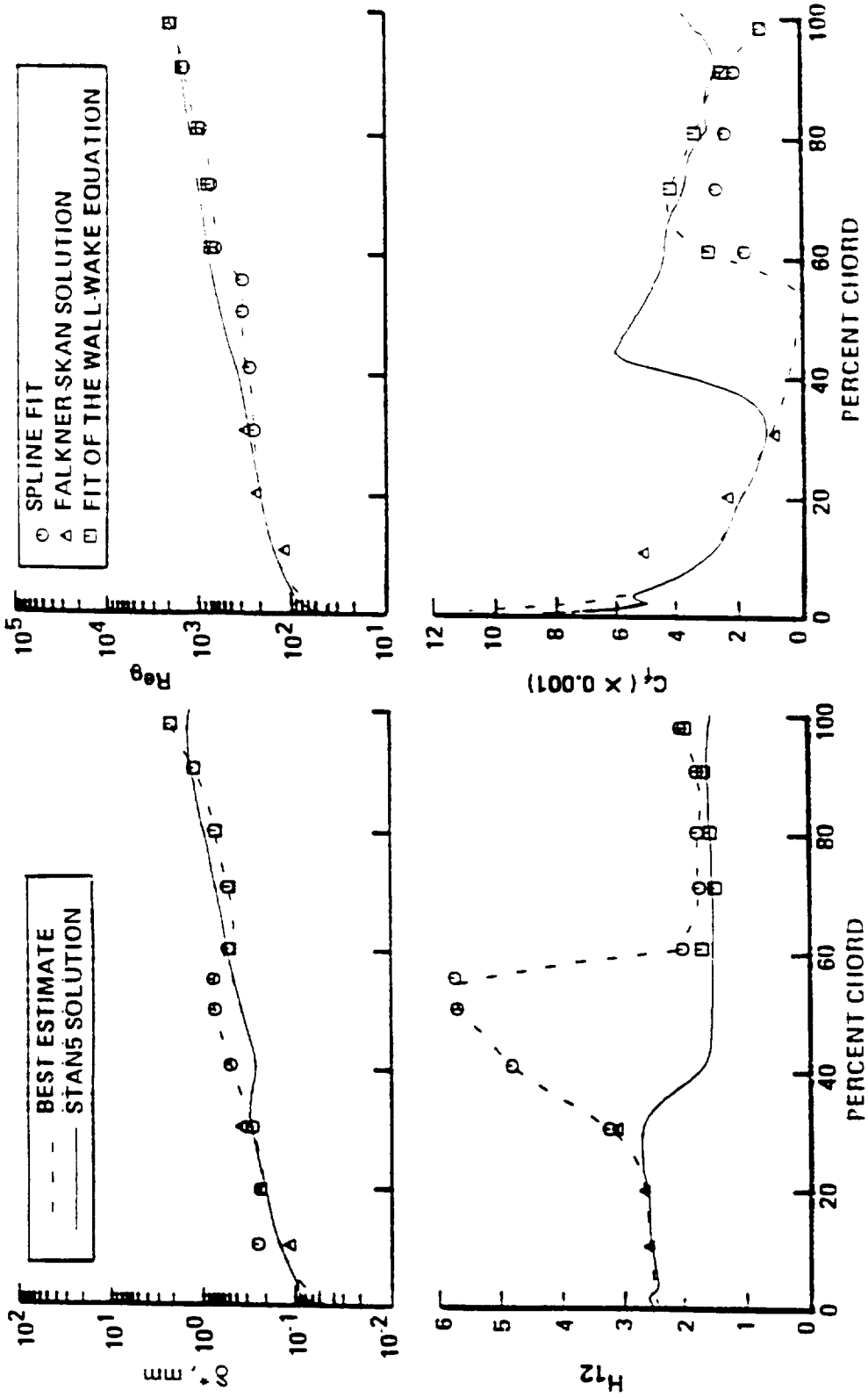

Figure 61. Variation of displacement thickness, first shape factor, momentum thickness Reynolds number, and skin friction coefficient on the suction surface for $i = -8.5$ degrees

layer parameters, however, STAN5 predicts a "natural" transition which results in a sharp rise in C_f. In actuality, this sharp rise in C_f should be delayed until C_f vanishes. Then, as transition takes place, C_f should rise to the values obtained from fitting the data to the wall-wake equation. After the 70.6% chord location, C_f decreases in the region of adverse streamwise pressure gradient and approaches a value of zero as the turbulent separation process begins near the trailing edge. Even using the LDV data and the numerical and analytical solutions, we still cannot obtain accurate magnitudes for the values of C_f in the vicinity of the separation "bubble." In fact, C_f might even become negative within the "bubble." Taking the values shown in figure 61, our best estimate of the magnitudes of C_f were later used in obtaining a rough calibration of our flush-mounted, hot-film probes.

On this surface, surface flow visualization tests proved especially useful in determining the location of the separation "bubble" as well as the location of peak transition within the "bubble." To 95% confidence, the oil film method placed the location of laminar detachment at 35.3% $\pm$ 2.0% chord and turbulent reattachment at 59.8% $\pm$ 2.3% chord. The chemical sublimation method located the peak transition at 56.0% $\pm$ 0.8% chord, to the same level of confidence. The oil film method also showed a possible separation of the turbulent boundary layer near the trailing edge. Note that the chemical sublimation method indicated transition for this separation "bubble" and separation and reattachment for the very small separation "bubble" on the pressure surface for $i = -1.5$ degrees.

To help locate the transition region within the separation "bubble," figure 62 shows a plot of mean velocity versus percent chord at a fixed distance above the blade surface ($y = 0.508$ mm). Most of the transition process takes place between 55.0% and 60.2% chord where a sharp increase occurs in mean velocity. Transition seems complete beyond the 70.6% chord location as the mean velocity decreases from this location to the trailing edge.

Besides the mean velocity data, the LDV measurements also provide information on flow reversal. Figure 63 shows the chordwise variation of percent backflow at several different distances

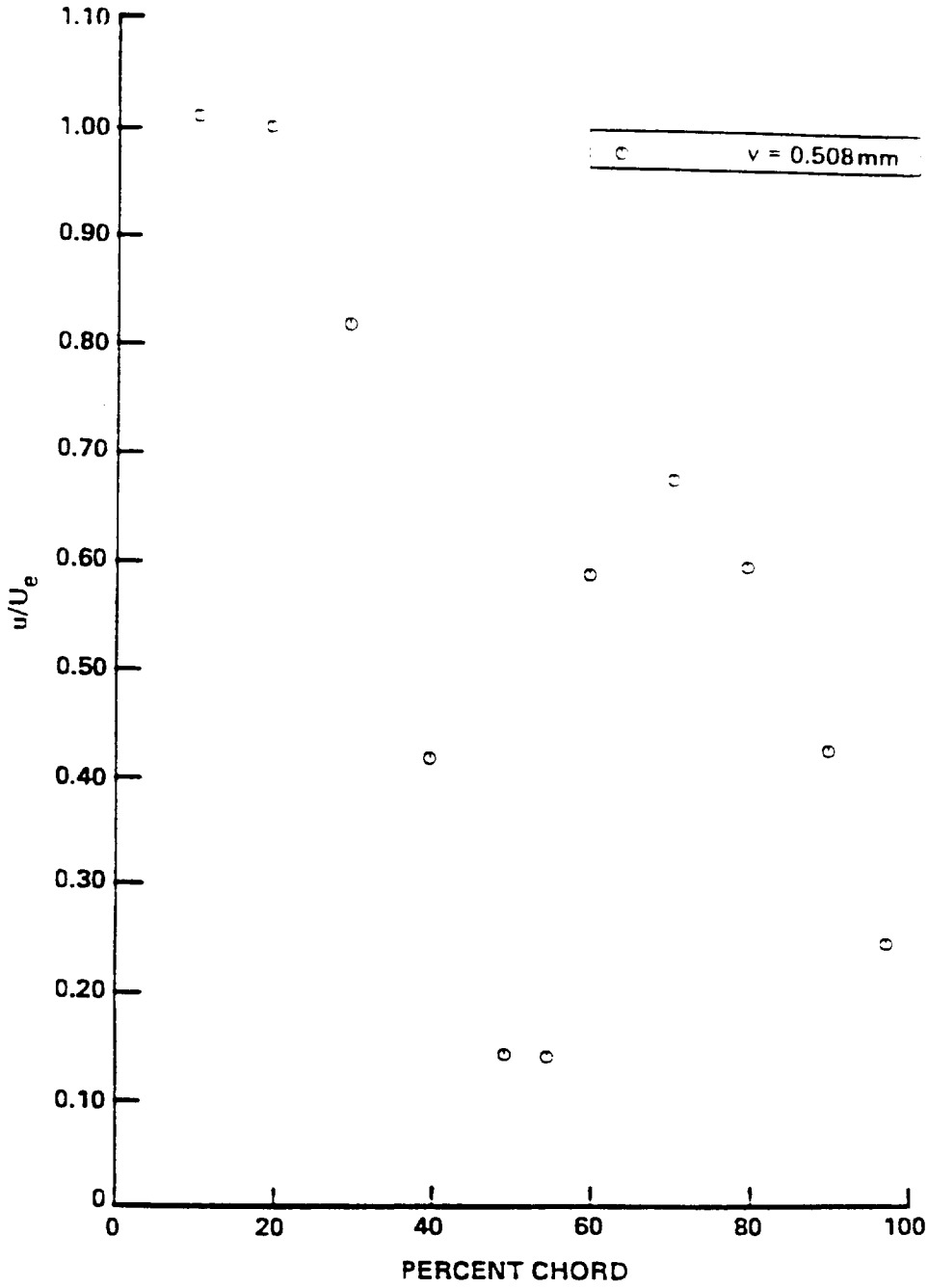

Figure 62. Variation of velocity, 0.508 mm from the blade, on the pressure surface for $i = -8.5$ degrees

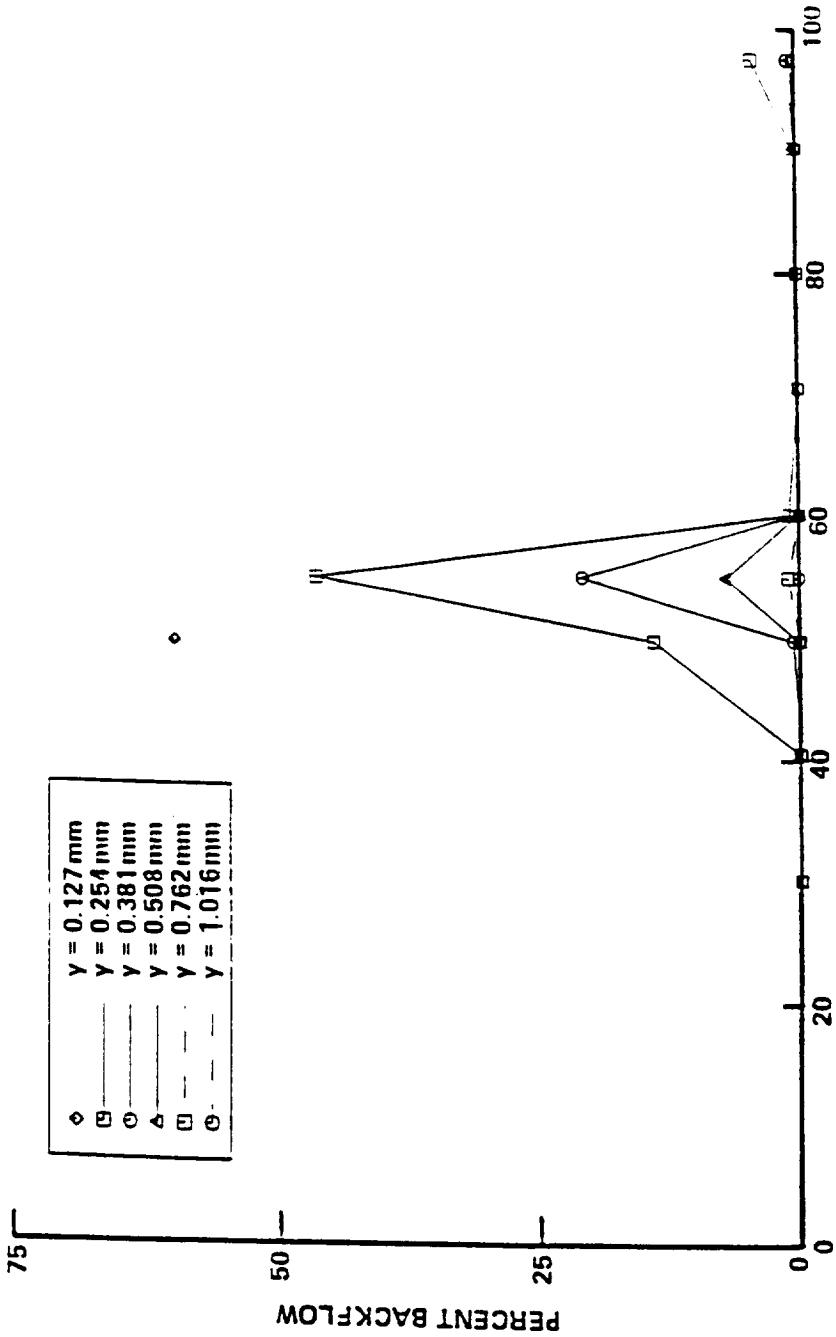

Figure 63. Instantaneous backflow measurements on the suction surface for $i = -8.5$ degrees

from the blade surface. Again, the backflow data between the 40.5% and 60.2% chord locations give the appearance of a "bubble." For all distances from the blade surface, the maximum percent backflow occurs at the 55.0% chord location where a value of 46.7% can be found 0.254 mm from the blade surface. However, larger values of maximum percent backflow might occur closer to the blade surface. For only one chord location could we measure the velocity closer than 0.254 mm from the surface with the LDV. At 49.8% chord, the percent backflow rose from 14.1% to 60.3% as we moved the LDV measurement volume from $y = 0.254$ mm to $y = 0.127$ mm. The major region of flow reversal seems to occur very close to the blade surface. This same flow phenomena seems to account for our failure to measure any backflow on the pressure surface at $i = -1.5$ degrees where a very small separation "bubble" almost certainly exists. Finally, as the turbulent boundary layer near the trailing edge approaches separation, we measured some backflow at 97.6% chord–leading to an incipient detachment point (with 1% instantaneous backflow) near 91.7% chord.

Figure 64 shows how the turbulence intensity profiles vary with chord location. Within the initial laminar boundary layers, the turbulence intensity levels are low–the problems with mean-velocity-gradient broadening and vibration of the LDV measurement volume are not evident since we just barely penetrated these boundary layers. By 30.1% chord, the levels of turbulence intensity rise, with a peak value located away from the blade surface. This trend continues through 60.2% chord as expected in regions of transition and separation. Note the small turbulence intensity very close to the blade surface at 49.8% chord. This location corresponds to the point of maximum H_{12} and percent backflow, just as the separation "bubble" induces transition to turbulence. Beyond 60.2% chord, the peak in turbulence intensity lies very close to the blade surface since the boundary layers are fully turbulent. Near the trailing edge, at 97.6% chord, the peak once again moves away from the blade surface as intermittent separation of the turbulent boundary layers has begun.

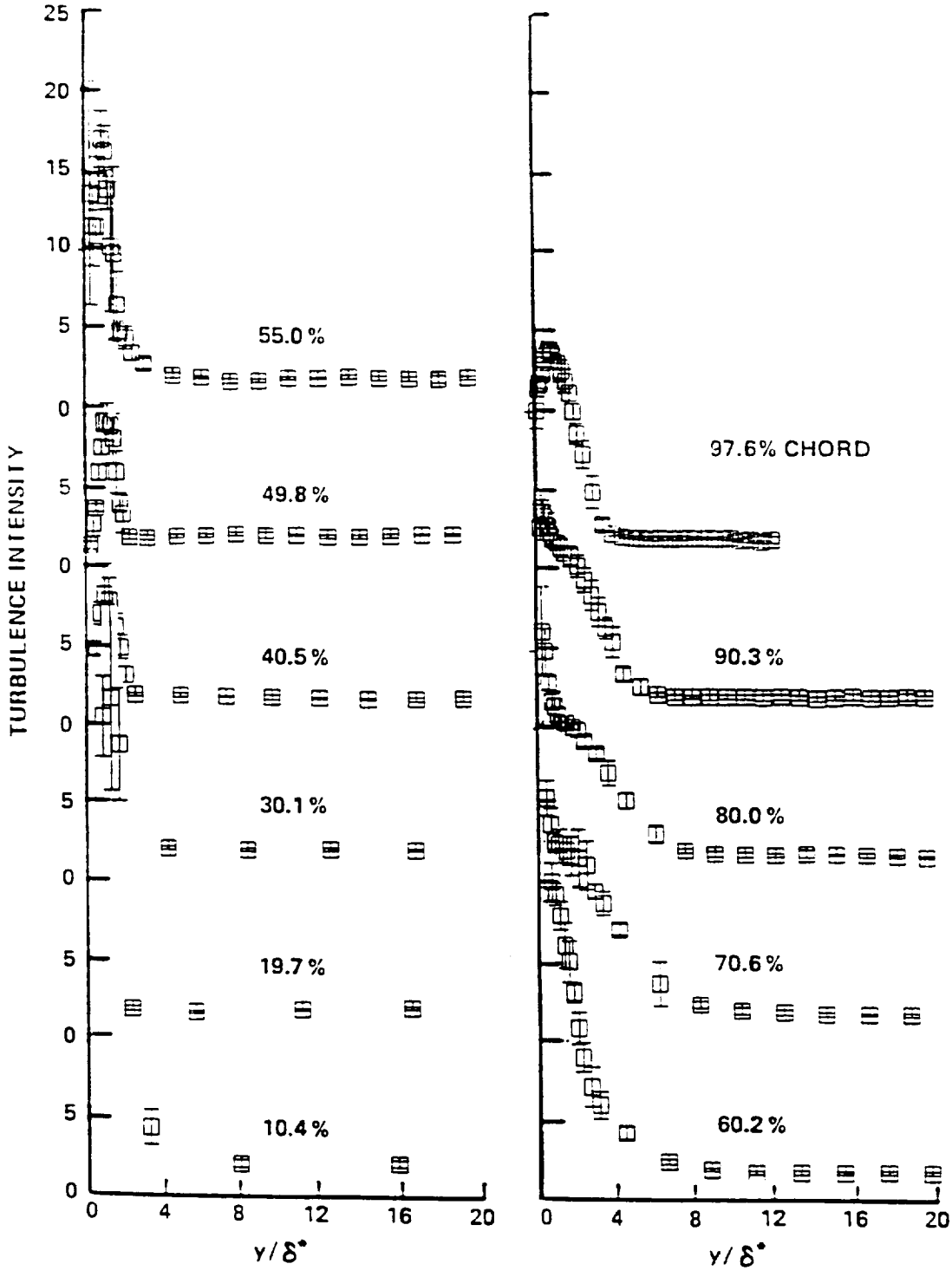

Figure 64. Turbulence intensity data for the suction surface boundary layers at $i = -8.5$ degrees

For most of the surfaces evaluated here, transition results from the occurrence of a separation "bubble" as opposed to the occurrence of "natural" transition. Although it is quite small, the separation "bubble" on the suction surface for $i = -8.5$ degrees appears to be large enough to warrant further investigation. Before proceeding, however, let us review some other experiments involving separation "bubbles." These experiments have led to our current knowledge concerning the physics of separation "bubbles." Some have contributed to models of the size and location of the "bubbles" as well as transitional aspects, turbulence characteristics, and the recovery of the reattached boundary layer. In addition, we shall examine the unsteady and three-dimensional aspects of separation "bubbles."

A laminar boundary layer separates when it encounters an adverse pressure gradient of sufficient magnitude. The laminar shear layer breaks away from the surface leaving a stagnant region between the shear layer and the surface. Our data acquisition supported this occurrence since it proved very difficult to entrain seeding particles into this region. Except for the close proximity to a solid surface which can damp out disturbances, the laminar shear layer behaves according to inviscid stability theory with curved streamlines. Basically, the inflectional velocity profile is inherently unstable, although the convex curvature of the streamlines could offer some stability. Disturbances should amplify and cause transition over a very short region. The increased momentum transfer due to turbulent mixing eventually eliminates the reverse flow near the surface and the flow reattaches. Figure 65 shows a sketch of a typical separation "bubble" and the corresponding pressure distribution. If the "bubble" is large enough, one can expect the adverse pressure gradient to vanish in the upstream portion of the "bubble" since this flow cannot sustain a pressure gradient. However, the short region of transition energizes the flow causing an increase in static pressure. In our measurements, all of the separation "bubbles" proved to be too small to cause a recognizable change in the pressure distribution.

Very little data are available concerning separation "bubbles" on blades within a turbomachine or a cascade. However, several researchers have studied separation "bubbles" on isolated

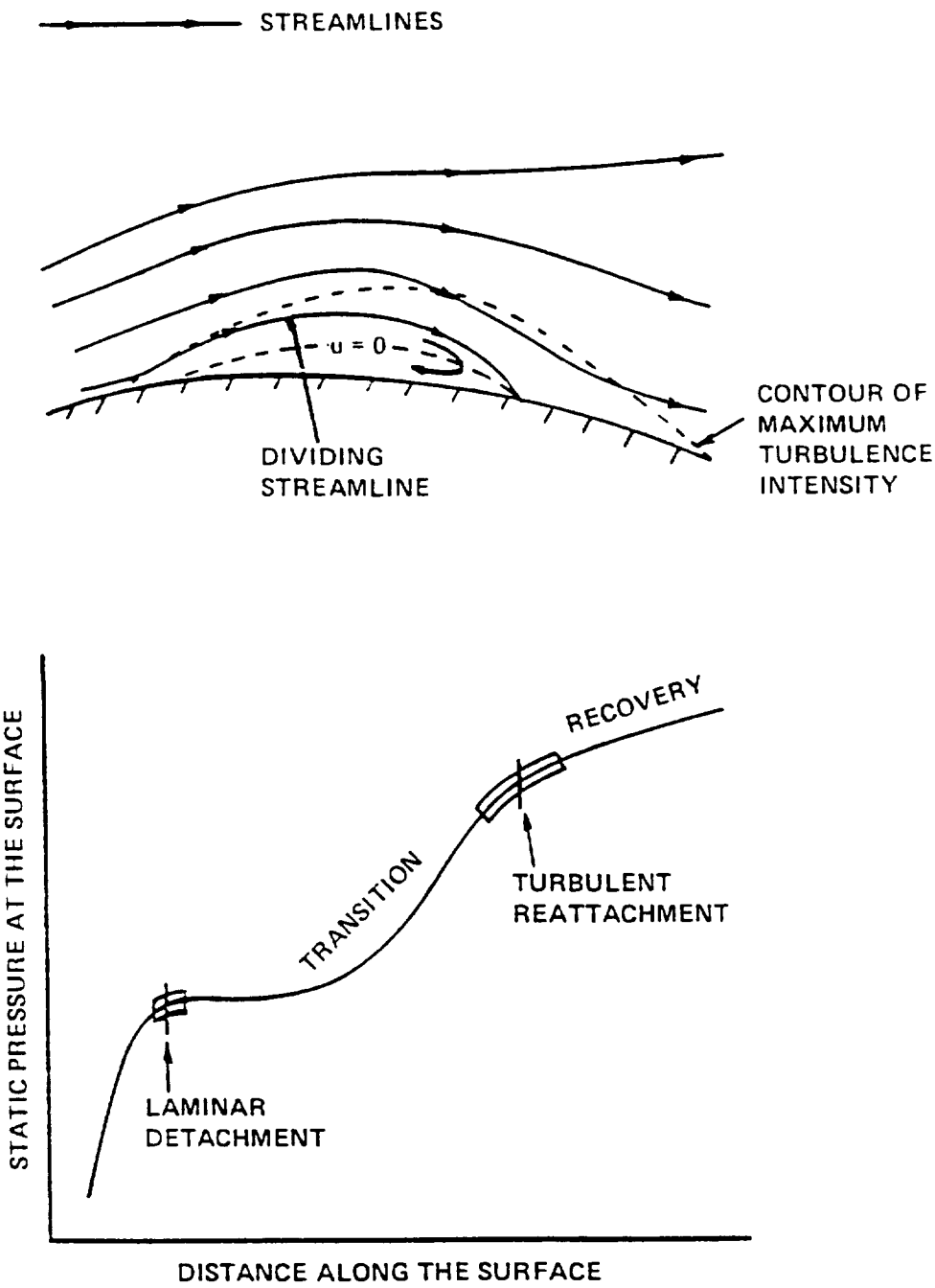

Figure 65 Time-average description of a separation "bubble" caused by laminar detachment and turbulent reattachment

airfoils. O'Meara and Mueller [1987] performed parameter studies to help create empirical models of separation "bubbles." Their low Re_c airfoil had a minimum pressure point near the leading edge of the suction surface–similar to our cascade blade–that led to a separation "bubble." As one might expect, the severity of the adverse pressure gradient near the leading edge of the suction surface determines the size and location of the separation "bubble." They noted that increases in chord Reynolds number and freestream turbulence lead to a more pronounced minimum in static pressure near the leading edge of the suction surface and thus reduce both the length and thickness of the separation "bubble." It is generally recognized that increases in freestream turbulence reduce the length of the separation "bubble" for various test geometries (for example, see Nakamura and Osono [1987] and Castro and Haque [1988]). Comparing the results of Arena and Mueller [1980], O'Meara and Mueller [1987], and Brendel and Mueller [1988] give no clear indication of the effect of incidence angle on the size and location of separation "bubbles." Since the local streamwise pressure gradient essentially controls these characteristics, the blade shape and Re_c affect how variations in incidence angle change the local pressure gradient.

Since transition results from the inherently unstable shear layer that has separated from the surface, we can make an analogy between transition caused by separation "bubbles" and transition caused by surface roughness. For various types of roughness with some characteristic height, h, a large enough ratio of h to the displacement thickness at separation, δ_s^*, can cause local transition before reattachment. Crimi and Reeves [1976] and O'Meara and Mueller [1987] used a roughness analogy to find h/δ_s^* as a function of $\delta_s^* U_{e_s}/\nu$ where h is some required height of the separation "bubble" to cause transition before reattachment. O'Meara and Mueller [1987] also give empirical functions to find the lengths of laminar, transitional, and turbulent flow within the separation "bubble" relative to the total length of the "bubble." Goldstein, Eriksen, Olson, and Eckert [1970] found empirical criteria for transition within the flow over a downstream-facing step. For a step of height h, they found that transition would occur before reattachment if either $h/\delta_s^* > 2.5$ or $hU_{e_s}/\nu > 520$.

Much of the data involving separation "bubbles" involves the size, location, and transitional aspects of the "bubbles." These data help in the formation of empirical models. Other researchers have been concerned with turbulence characteristics in order to both understand the physics and create appropriate turbulence closure models for the time-averaged governing equations. The low Re_c airfoil, LDV data of Bell and Cornelius [1987] show similar trends of δ^*, θ, H_{12}, and $\sqrt{u'^2}/U_e$ to the data presented here. Figure 65 shows a result reported by several investigators: The maximum value of $\sqrt{u'^2}/U_e$ can occur well away from the surface–essentially near the center of the shear layer since the velocity profiles have a point of inflection there. Using pulsed-wire anemometry, Castro and Haque [1987] measured very extensive turbulence data of a separation "bubble." The flow separated off a flat plate normal to the flow and reattached on a long splitter plate. They found that the features of a separated shear layer bounding a highly turbulent reverse-flow region are quite different from those of the plane mixing layer between two streams. Other separation "bubbles" have been measured on upstream-facing, blunt plates and downstream-facing steps.

In an attempt to model a turbine blade separation "bubble," Patrick [1987] created a large separation "bubble" on a flat plate test surface of a wind tunnel with an imposed pressure distribution. He modeled the "cove" separation caused by the large curvature on the pressure surface of a turbine blade. The separated boundary layer was an equilibrium turbulent boundary layer and not a laminar boundary layer. Also, a favorable pressure gradient existed downstream of the separation "bubble." Patrick [1987] made extensive two-component LDV measurements and has seemingly measured the only separated region with 100% instantaneous backflow. He found that this backflow shear layer even had a logarithmic region. From observations of our data, we might conclude that no others have found 100% instantaneous backflow because no one else had created a large enough separation "bubble" to make measurements close enough to the surface.

Downstream of the separation "bubble," measurements have shown how the reattached boundary layer recovers from separation. Mueller, Korst, and Chow [1964] show that these redeveloping turbulent boundary layers are similar to those for a turbulent boundary layer developing toward separation except that they are traversed in reverse. For the rare case of a reattached laminar boundary layer, Goldstein, Eriksen, Olson, and Eckert [1970] measured the same trend as for redeveloping turbulent boundary layers. Patrick [1987] showed that the inner region of the newly developed turbulent boundary layer quickly reached equilibrium on the basis of the formation of a logarithmic region. However, the relaxation of the outer region occurred more slowly. Despite the local pressure gradient–which became favorable downstream of reattachment–a very large wake region was evident just downstream of reattachment and this wake region slowly decayed with downstream distance. Our data shows the importance of the streamwise pressure gradient on the recovery process: An adverse pressure gradient will lengthen the recovery region.

Thus far, all of our observations of separation "bubbles" concern the time-average aspects. However, as Eaton and Johnston [1982] point out, the fact that the flow near the wall can be instantaneously moving either upstream or downstream suggests that a large-scale unsteadiness is present in the flow. As an introductory analysis, let us examine the separation "bubble" in the manner that Kline [1966] examined the flow over a downstream-facing step. In order for a fluid particle upstream of the separation "bubble" to flow past the reattachment point, the particle must have a stagnation pressure larger than the static pressure at reattachment. This criterion may not be satisfied for particles deep within the upstream boundary layer and hence such particles can pass beyond reattachment only if shear work is done on them by laminar or turbulent mixing from fluid particles in the freestream after separation. Kline [1966] claims that this mixing is insufficient to energize all such particles and therefore, the dividing streamline passes above the separation point as shown in figure 65. Then, a certain fraction of the boundary layer fluid passes into the backflow region. Without an escape path via continuity, the separation region grows in time until finally an interaction occurs between the recirculating region and

the outer flow. In a recurring process, some of the recirculating region is "torn away" and the separation region is very rapidly reduced in size.

Theoretical observations–such as the one made by Kline [1966]–went unobserved experimentally until researchers developed more sophisticated means of measurement. Although its nature has not been fully explained, experiments have now shown us that a large-scale, low-frequency unsteadiness does accompany separation "bubbles." On the separation "bubble" at the entrance to a pipe, McGuiness [1978] used smoke visualization to observe that the separation "bubble" was occasionally cut roughly in two and that the downstream portion proceeded downstream as a "divorced eddy." Eaton and Johnston [1982] used hot-wire and thermal-tuft probes to show that the reattachment point beyond a downstream-facing step moves upstream and downstream at some low frequency with no regular periodicity. They felt that the "flapping" motion is caused by an instantaneous imbalance between the shear-layer entrainment from the recirculating zone on the one hand and reinjection of fluid near reattachment on the other.

For flow over an upstream-facing, blunt plate, Kiya and Sasaki [1983] and Cherry, Hillier, and Latour [1984] observed a low-frequency "flapping" of the shear layer. Using "x"-configuration hot wires and split-film probes, Kiya and Sasaki [1983] claimed that the "flapping" of the shear layer is closely related to the shrinkage and enlargement of the separation "bubble." The the outer shear layer provides a shearing motion to the reverse flow region; thus increasing the vorticity in the separation "bubble." In a range of fairly low frequencies, Kiya and Sasaki [1983] found some small-scale structures to break away from the "bubble." However, they felt that some unknown mechanisms hindered this very weak, regular shedding and as a result, a large amount of vorticity is accumulated within the "bubble." This is accompanied by a considerable increase of the "bubble" length and outward motion of the shear layer. When a sufficient amount of vorticity is accumulated, an extremely large structure breaks away from the "bubble" and the "bubble" then rapidly shrinks and the shear layer moves inwards. This large-scale unsteadiness occurs at a very low frequency. The shed "vorticies" travel downstream without significantly changing

their structure within a certain distance after reattachment. From instantaneous smoke visualizations and fast-response, static-pressure measurements at the surface, Cherry, Hillier, and Latour [1984] also observed structures of various scales breaking away from the separation "bubble" at various low frequencies. Large-scale motion with recurring "bursts" and the shedding of small-scale structures appeared to indicate a temporary interruption to the shear-layer-structure growth/coalescence process. Showing similar results, the pulsed-wire anemometry data of Castro and Haque [1987] found a low-frequency motion most noticeable near separation.

A low-frequency unsteadiness has also been observed for separation "bubbles" without a salient edge to fix the location of separation. We have already observed the intermittency of the separation of a turbulent boundary layer. However, the separation point of a laminar boundary layer can also vary unsteadily because of the ellipticity of the flow. Any disturbances–including any low-frequency unsteadiness–can cause a "jitter" of the laminar separation point. Patrick [1987] used flow visualization to show unsteadiness at both turbulent detachment and turbulent reattachment. Because his separation "bubble" had a very vigorous region of backflow, Patrick [1987] observed an unusual occurrence. His smoke flow visualization movies showed a random streamline "flapping" near reattachment with large-scale eddies being convected alternately upstream and downstream from the impingement point on the test surface. The upstream motion might be a manifestation of the reinjection of fluid near reattachment.

A few researchers have found a low-frequency unsteadiness involved with the separation "bubbles" on laminar flow airfoils. These low Re_c airfoils have a large extent of laminar flow and are designed for low drag and high performance under cruise conditions. The adverse pressure gradient downstream of the midchord location on the suction surface results in a separation "bubble." Zaman, Bar-Sever, and Mangalam [1987] made hot-wire velocity spectra measurements in the airfoil far wake. The measurements showed a low-frequency, sharp peak, indicating a vortex shedding for flow just prior to stall (shown by smoke flow visualization). They speculated that the origin of this unsteadiness can be traced to a bursting of the separation "bubble"

and the associated instability. Also, they found that acoustic excitation at an appropriately high frequency could eliminate this shedding completely and they postulated that the acoustic excitation eliminated energetic vortical structures from the separated shear layer.

Another interesting experiment also involved laminar flow airfoils. Stack, Mangalam, and Kalburgi [1988] used a multi-element heat transfer sensor to obtain simultaneous, directionally sensitive measurements of the dynamic shear stress conditions on the suction surface. In the vicinity of a separation "bubble," the time history plots of their signals showed that the root-mean-square values were a minimum at separation, became the largest at peak transition, and then reduced toward turbulent reattachment. After applying a low-pass filter with a cutoff frequency of 10 Hz, they discovered a "phase reversal phenomenon" from both the filtered time signals and some cross-correlations of these signals. Looking at the low-frequency variation in wall shear stress near the detachment and reattachment points, they found that probes completely within the "bubble" correlated at a phase nearly 180 degrees differently than with probes completely out of the "bubble." Resolution of the cross-correlations and the "phase reversal phenomenon" is a function of sensor spacing. They felt that the "phase reversal phenomenon" was related to the unsteady nature of laminar separation and turbulent reattachment. This type of measurement proved to be a desirable method to find the detachment and reattachment points without the need for probe calibration.

Some differences remain as to the magnitudes of both the length scale and the frequency of this separation "bubble" unsteadiness. For the largest turbulent eddies, Eaton and Johnston [1982] use δ for a length scale and define a Strouhal number as

$$St = \frac{f\delta}{\frac{1}{2}U_e} .$$

However, since the length of a separation "bubble" is typically five to ten times the boundary layer thickness, they feel that the low-frequency motions have time scales greater than or equal to the time it takes freestream fluid particles to pass over the separation "bubble." From their

spectrum data, we can determine that the low-frequency motion has a frequency of 4.8 Hz and we can define a Strouhal number as

$$St = \frac{f x_{sb}}{U_{e_s}} \approx 0.15$$

where x_{sb} is the length of the separation "bubble." Using this definition of St and their surface pressure spectra, Kiya and Sasaki [1983] found a "flapping" frequency of 39.6 Hz and $St \approx 0.12$ while Cherry, Hillier, and Latour [1984] obtained values less than 7.2 Hz and 0.125. Both groups estimated $St \approx 0.6$ to 0.7 for the very weak regular shedding of smaller-scale structures from the "bubble."

For the low-frequency unsteadiness associated with the separation "bubbles" on laminar flow airfoils, researchers report smaller values of St–possibly because a salient edge no longer fixes the location of detachment. Zaman, Bar-Sever, and Mangalam [1987] measured frequency peaks in the velocity spectra within the far wake of 4.5, 7.8, 10.2, and 14.8 Hz at successively increasing values of freestream velocity. Using V_1 instead of U_{e_s} and c instead of x_{sb}, they obtain a Strouhal number of 0.07. With the previous definition of St, one would certainly believe that the value of St would be an order of magnitude smaller than 0.07. Remember that Stack, Mangalam, and Kalburgi [1988] found their "phase reversal phenomenon" at a frequency less than 10 Hz which corresponds to a value of St less than 0.02.

While experiments have shown that a large-scale, low-frequency unsteadiness does accompany separation "bubbles," these same experiments have been unable to determine the interrelations between this unsteadiness and any three-dimensional flow effects. Although three-dimensional flow effects probably accompany separation "bubbles," the various experimental setups will also affect the three-dimensionality. Goldstein, Eriksen, Olson, and Eckert [1970] found that three-dimensional secondary flows caused smoke entering near their side walls to travel spanwise into the separation "bubble" in the middle of the test section before being convected downstream. Eaton and Johnston [1982], Kiya and Sasaki [1983], and Cherry, Hillier, and

Latour [1984] all noticed a spanwise system of large-scale, counterrotating vorticies which Cherry, Hillier, and Latour [1984] claimed began very rapidly after separation and were not particularly accentuated by the reattachment process. Cherry, Hillier, and Latour [1984] also found that various shedding frequencies from the separation "bubble" occurred across the span and that the three-dimensionality can affect any correlations. Eaton and Johnston [1982] postulated that the low-frequency unsteadiness could be tied into the breakdown of the spanwise vorticies.

Now, let us proceed with the analysis of the separation "bubble" on the suction surface for $i = -8.5$ degrees. Figure 66 shows a summary of some of the LDV data in the vicinity of the separation "bubble" along with the chordwise locations of the flush-mounted, hot-film probes. Because of the small thickness of the separation "bubble," we could not integrate the mass flow to adequately locate the dividing streamline. After converting the hot-film voltage signals into dynamic shear stress signals (see chapter 4), we plotted the first 0.2 seconds of the surface shear stress time history in figure 67. The probe at 30.0% chord lies within the laminar region and consequently, τ_w varies very little with time. At 40.6% and 45.0% chord, the probes lie within a region where some instantaneous backflow was measured. These probes measured some low-frequency variation in τ_w. Some higher frequency variation is noticeable at 50.2% chord, but the values of τ_w remain near zero at all times. From our LDV data at 55.0% chord, figure 66 shows the instantaneous backflow reaches a maximum, δ^* begins to decrease, and θ begins to increase causing us to speculate that transition occurs abruptly near this location. The hot-film signal at 55.8% chord confirms this speculation as the near zero values of τ_w intermittently become quite large.[21] By 57.9% chord, both low- and high-frequency unsteadiness in τ_w becomes evident, while the mean value of τ_w grows larger. These trends continue through 60.0% chord and 69.8% chord, where the signal looks turbulent.

---

[21] Several values of τ_w at both 55.8% and 57.9% chord occasionally stop abruptly at a maximum value. At these locations, we mistakenly set our voltage gains too high on the constant-temperature anemometer and the output voltage was occasionally amplified to values greater than the maximum allowed input voltage on our analog-to-digital converter. Nonetheless, the output signals can be reasonably interpreted. This same effect will later be noticed on the histogram for 55.8% chord.

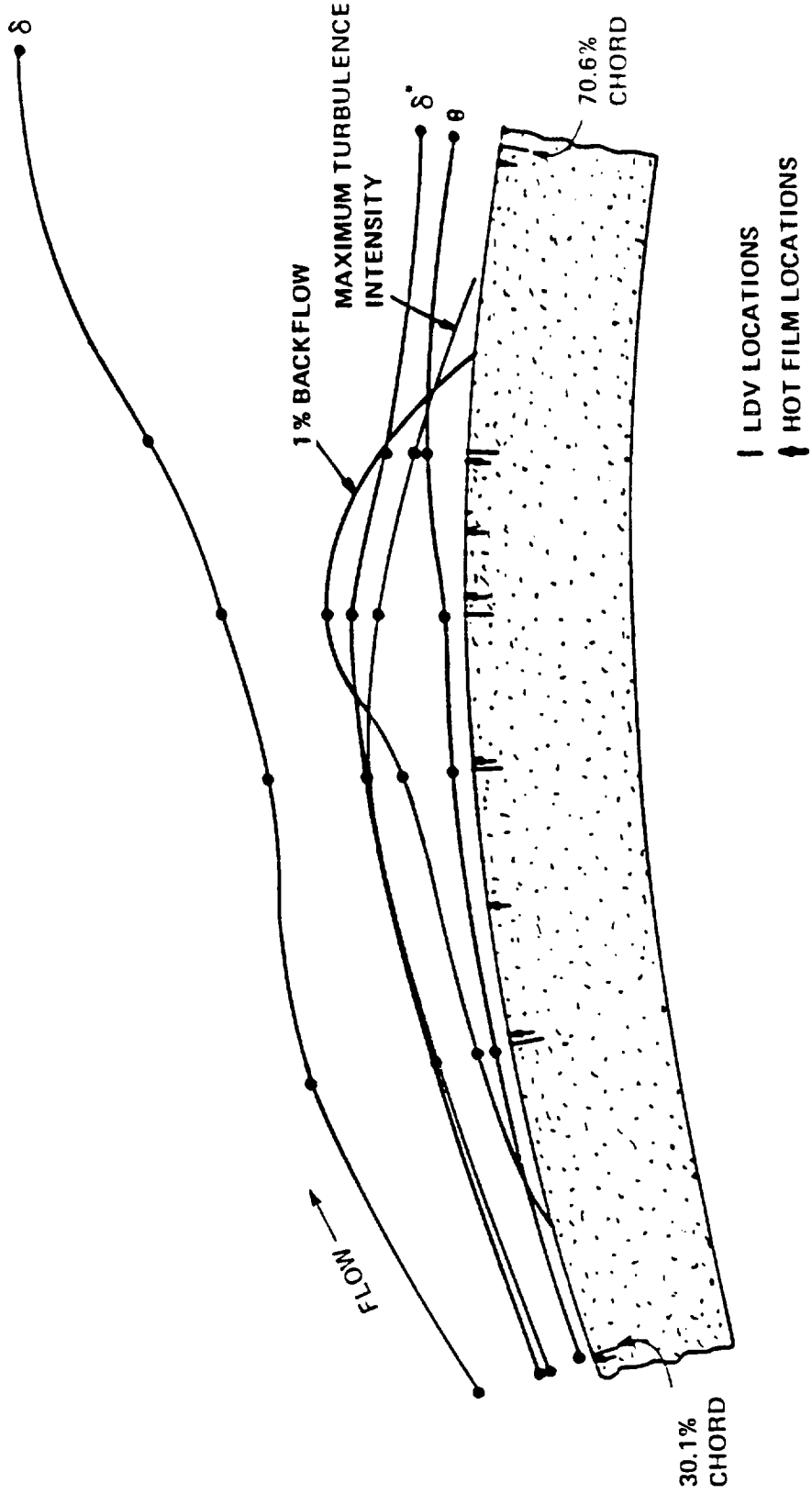

Figure 66. Flow characteristics and locations of the flush-mounted, hot-film probes in the vicinity of the separation "bubble" on the suction surface for $i = -8.5$ degrees

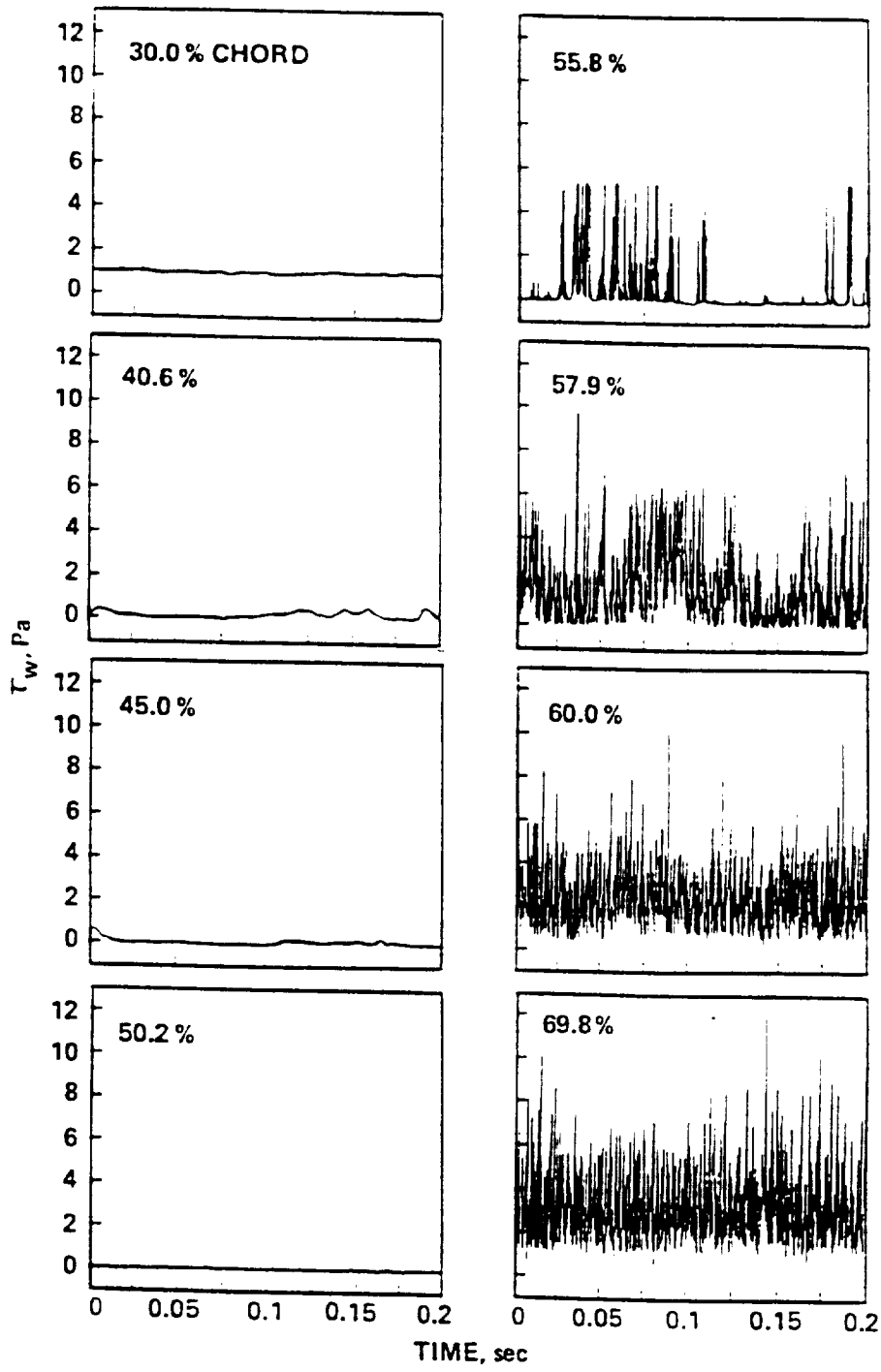

Figure 67. Time signals of the dynamic shear stress on the suction surface for $i = -8.5$ degrees

We can summarize these time history signals by plotting the chordwise variation of the root-mean-square values of τ_w normalized by the mean values of τ_w. Figure 68 shows this variation in $\sqrt{\tau_w'^2}/\overline{\tau_w}$. $\sqrt{\tau_w'^2}/\overline{\tau_w}$ rises from near zero in the laminar boundary layer to large, irregular values in the transition region of the separation "bubble." Finally, $\sqrt{\tau_w'^2}/\overline{\tau_w}$ decreases and begins to level off near a value of 0.446. Earlier, we analyzed the LDV data in this region as turbulent and the work of Alfredsson, Johansson, Haritonidis, and Eckelmann [1988] confirms this. They measured the fluctuating values of τ_w with various types of hot-wire and hot-film sensors in turbulent boundary layers. They concluded that $\sqrt{\tau_w'^2}/\overline{\tau_w} = 0.40$ for turbulent boundary layers while the values of skewness and kurtosis were 1.0 and 4.8, respectively.

Continuous time signals can be plotted as histograms in a similar manner as the discrete time signals from LDV measurements. Figure 69 shows histograms of the signals from all eight of our flush-mounted, hot-film probes. For probes where the flow is either laminar or τ_w is small, the values of τ_w remain concentrated around the mean value. As transition begins, the distributions show a positive skewness which gradually lessens. The positive skewness remains for the turbulent τ_w distribution at 69.8% chord–giving values of skewness and kurtosis of 1.37 and 6.29, respectively. Again, these values are near the turbulent values reported by Alfredsson, Johansson, Haritonidis, and Eckelmann [1988].

After taking an FFT of each time signal, we can examine the spectra of τ_w from each probe in figure 70. The decibel (dB) values showing the amplitude of τ_w is defined as

$$\text{dB value} = 20\log(\tau_w)$$

where τ_w has units of Pa. As indicated in the time signals of figure 67, the spectra of figure 70 show that most of the fluctuations of τ_w for 30.0%, 40.6%, and 45.0% chord occur at frequencies of 400 Hz or less. Further downstream, the amplitude of the higher frequency fluctuations increases as transition begins. The high frequency fluctuations at 50.2% chord are 15 dB (or 6 times) greater than the high frequency fluctuations at 45.0% chord. Then as the peak transition is

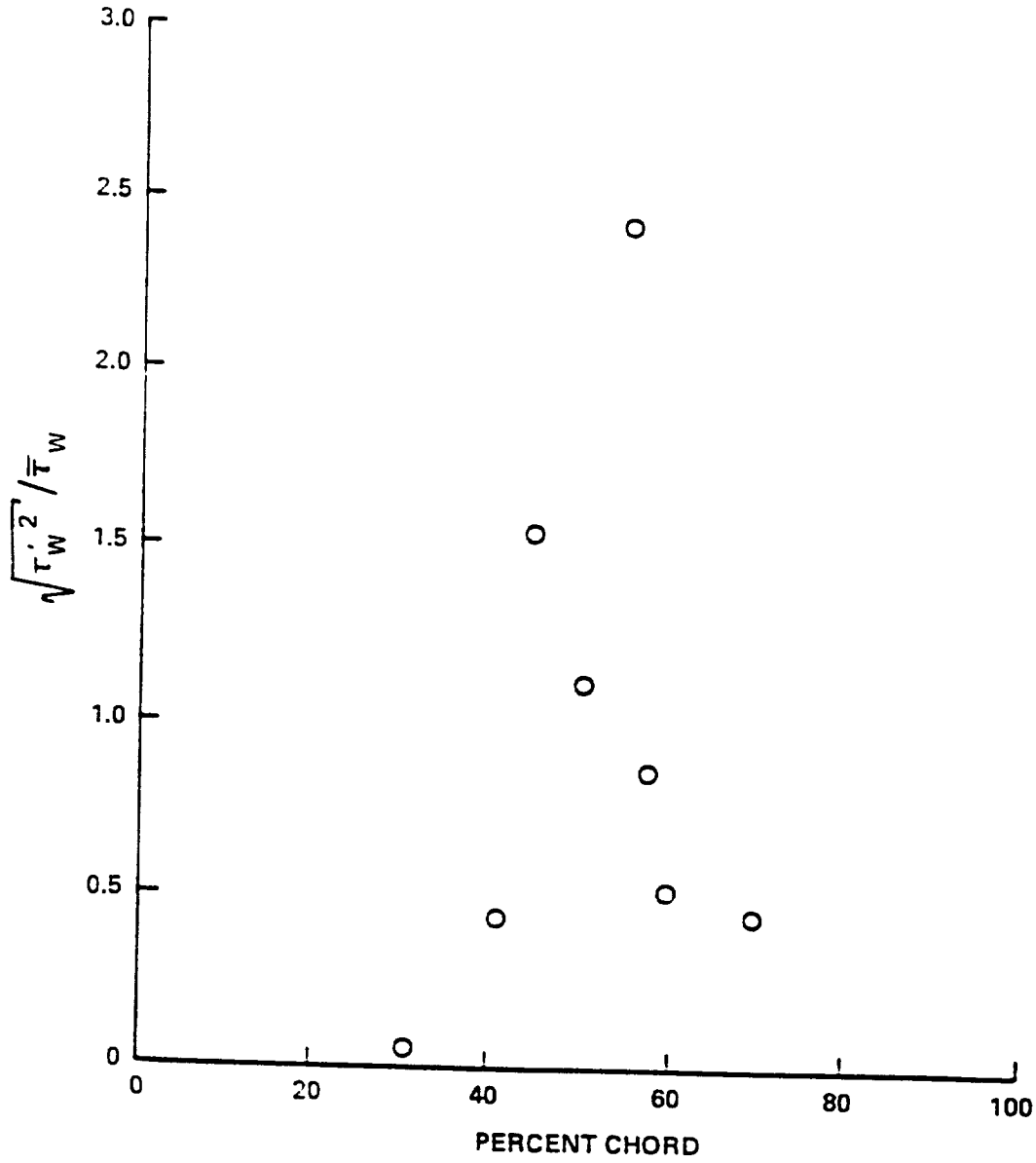

Figure 68. Chordwise variation of $\sqrt{\tau_w'^2}/\overline{\tau_w}$ on the suction surface for $i = -8.5$ degrees

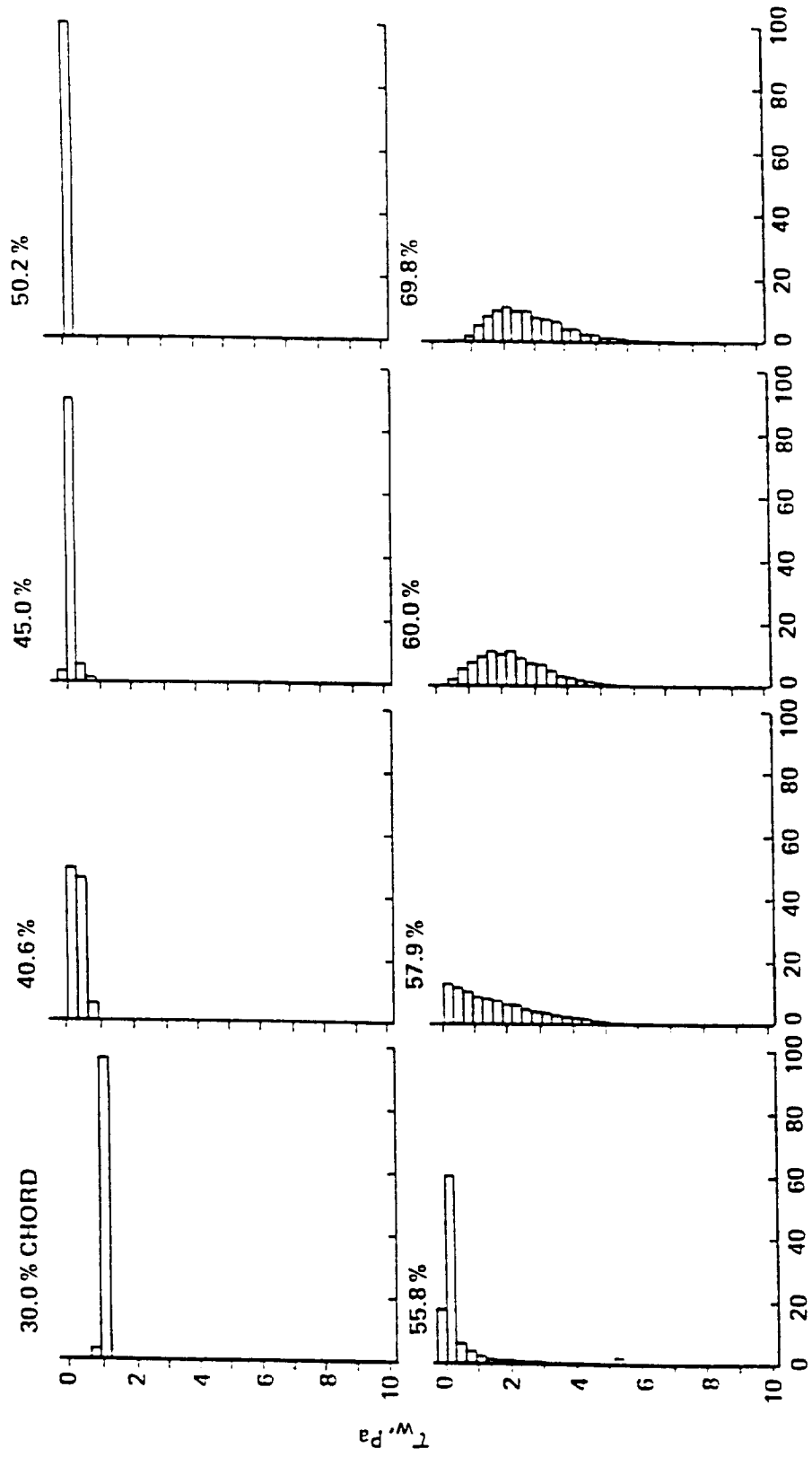

Figure 69. Histograms of the dynamic shear stress on the suction surface for $i = -8.5$ degrees

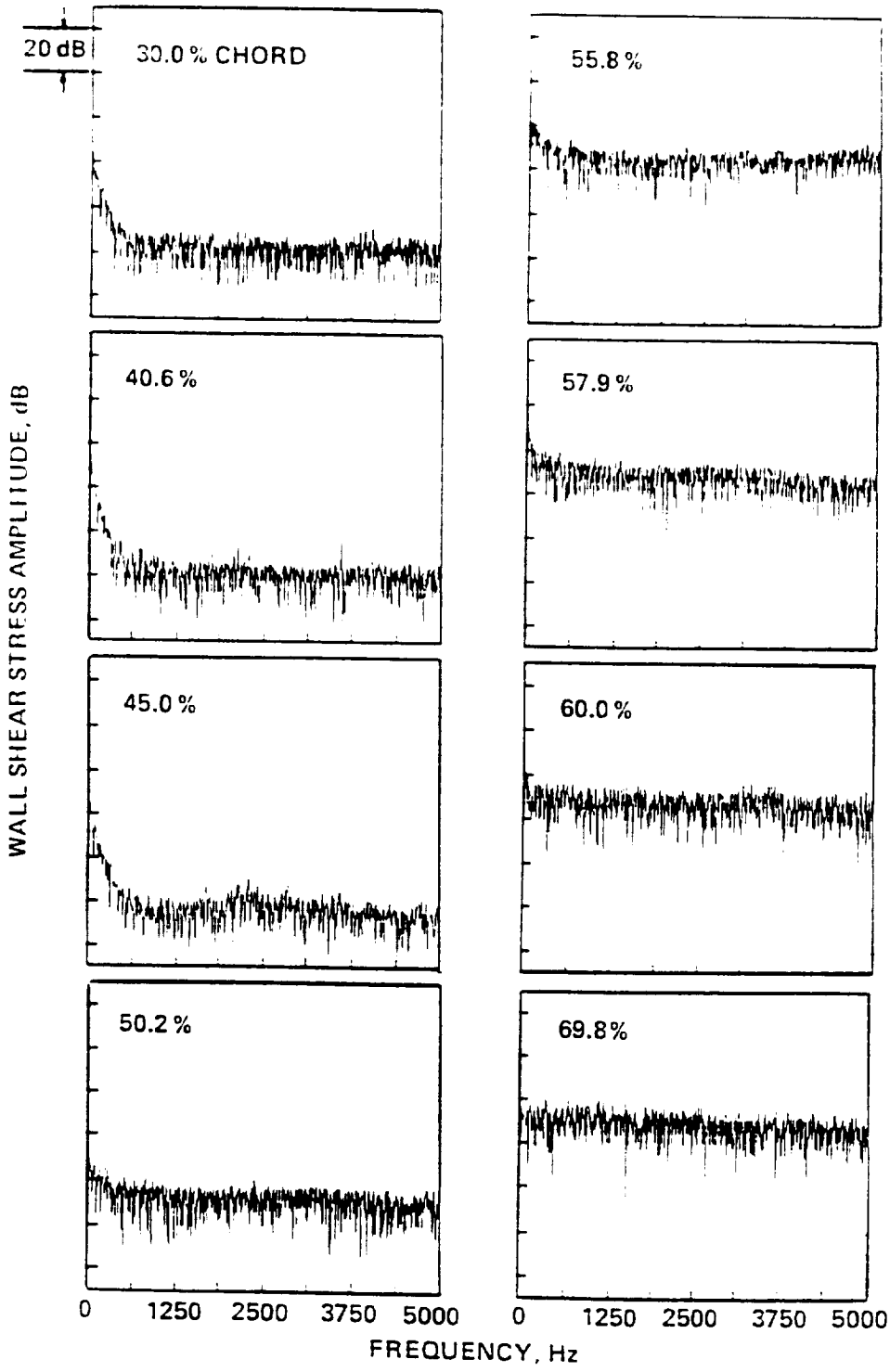

Figure 70. Spectra of the dynamic shear stress on the suction surface for $i = -8.5$ degrees

reached, the high frequency fluctuations at 50.2% chord increase by 34 dB (or a factor of 50) to the high frequency fluctuations at 55.8% chord. As expected, the transitional and turbulent shear layers have broadband fluctuations of τ_w

From the time signals and spectra of the dynamic shear stress, we cannot directly obtain any information on the large-scale, low-frequency unsteadiness associated with separation "bubbles." Emphasizing the regions near detachment and reattachment, we computed correlation coefficients from signals of selected probe pairs. Table 4 shows that only the probes at 40.6% and 45.0% chord show a significant positive correlation. Remember that the signals at these two locations both showed fairly low frequency fluctuations of τ_w in figure 67. The signals from the probes at 30.0% chord and 45.0% chord showed some negative correlation. From our previous discussion, these two probes appear on either side of the detachment point and they should show the "phase reversal phenomenon" of Stack, Mangalam, and Kalburgi [1988]. Following their lead, we filtered the time signals using a low-pass, Butterworth filter with a cutoff frequency of 10 Hz. Figure 71 shows the filtered time signals while table 4 shows the new correlation coefficients computed from the filtered time signals. Near detachment, C_{ab} between probe signals at 30.0% and 45.0% chord becomes more negative when the time signals are filtered–thus showing that the "phase reversal phenomenon" does occur at a very low frequency. Surprisingly, the probe signal at 40.6% chord does not have a negative correlation with either the upstream or downstream probe signals. Possibly, this probe lies very close to the detachment point–even though the oil film flow visualization located the detachment point at 35.3% $\pm$ 2.0% chord.

The "phase reversal phenomenon" is more evident near the reattachment point using our filtered time signals. As seen in table 4, a strong negative C_{ab} occurs between the filtered time signals at 60.0% and 69.8% chord while a less negative C_{ab} occurs between the filtered time signals at 57.9% and 69.8% chord. Also, the filtered signals at 57.9% and 60.0% chord are very positively correlated. The filtered time signals in figure 71 show the same trends. In the same manner of Stack, Mangalam, and Kalburgi [1988], our observations of the filtered time signals

Table 4. Correlation coefficients between various time signals and filtered time signals from the suction surface for $i = -8.5$ degrees

percent chord location of probe pair		C_{ab} of unfiltered time signals	C_{ab} of filtered time signals
30.0	40.6	-0.038	0.040
30.0	45.0	-0.159	-0.539
40.6	45.0	0.336	0.280
57.9	60.0	0.044	0.604
57.9	69.8	-0.008	-0.098
60.0	69.8	-0.023	-0.368

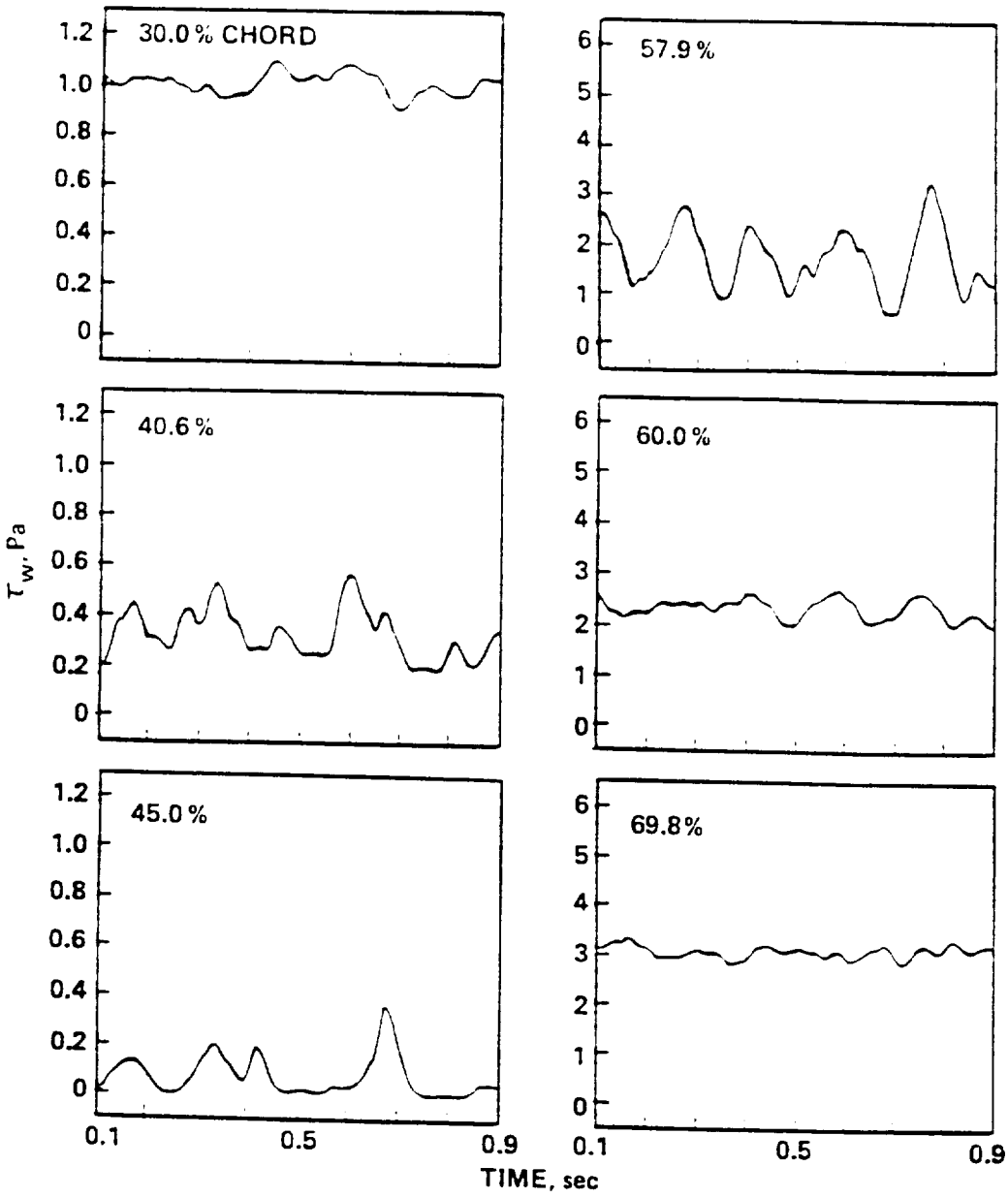

Figure 71. Time signals of the dynamic shear stress on the suction surface for $i = -8.5$ degrees–filtered using a low-pass Butterworth filter with a cutoff frequency of 10 Hz

and C_{ab} place reattachment between 60.0% and 69.8% chord. The oil film visualization place the reattachment point at 59.8% ± 2.3% chord.

As a final analysis, we examined the cross-spectra between the signals from various probes near detachment and reattachment. Near detachment, the probe signals at 30.0% and 40.6% chord and the probe signals at 40.6% and 45.0% chord showed no definite correlation. The probe signals at 30.0% and 45.0% chord showed a strong negative correlation near 2.4 Hz. Just before reattachment, the probe signals at 57.9% and 60.0% chord showed a very strong positive correlation near 6.0 Hz. Across the reattachment point, the probe signals at 60.0% and 69.8% chord showed some negative correlation near 6.0 Hz while the probe signals at 57.9% and 69.8% chord showed a small amount of negative correlation near 3.6 Hz.

Stack, Mangalam, and Kalburgi [1988] used very high quality, directionally sensitive heat transfer sensors that were spaced close together to study the "phase reversal phenomenon." Even using a simple technique, we uncovered some evidence of this large-scale, low-frequency unsteadiness. For this separation "bubble," we can characterize this unsteadiness with a Strouhal number. From the oil film flow visualization, we can obtain $x_{sb} \approx 60$ mm while we can estimate $U_{e_s} \approx 38$ m/sec from the LDV data. Then, using $f \approx 6$ Hz from the cross-spectra results in

$$St = \frac{f x_{sb}}{U_{e_s}} \approx 0.01$$

which compares well with the results of Stack, Mangalam, and Kalburgi [1988] and Zaman, Bar-Sever, and Mangalam [1987] for separation "bubbles" on laminar flow airfoils.

Wakes for a -8.5 Degree Incidence

In figure 18, both the near wakes at 106.0% and 109.7% chord and the far wakes at 131.9% and 152.6% chord were nearly symmetric. After replotting these wakes as velocity defects in figure

72, we find that all four wakes show good similarity with respect to the Gaussian distribution of Lakshminarayana and Davino [1980] (away from the wake edge). Having near-wake similarity seems in contrast with our data from the first two incidence angles as well as the data of Hobbs, Wagner, Dannenhoffer, and Dring [1982]. However, these data all showed larger regions of trailing edge separation on the suction surface than did the data for the current flow field. Evidently, the distance required for the wakes to show self-preservation is extended farther downstream as the size of the trailing edge separation region is enlarged.

Aside from showing better similarity, the wakes for $i = -8.5$ degrees are much smaller and show much less curvature of the wake centerline. After calculating the integral parameters, we can plot the displacement surface in figure 73. Without the large displacement caused by the trailing edge separation, the wake centerline shows little curvature.

The turbulence intensity profiles in figure 74 are quite different than the profiles for the near wakes at $i = 5.0$ degrees and $i = -1.5$ degrees. Although these profiles are not as symmetric as the mean-velocity profiles, they show more symmetry than the turbulence intensity profiles at the two previous incidence angles. Also, the 95% confidence bands on the turbulence intensity measurements are much smaller for $i = -8.5$ degrees. As with all wakes, however, the peaks in turbulence intensity track the regions of large mean-velocity gradients and occur away from the wake centerline.

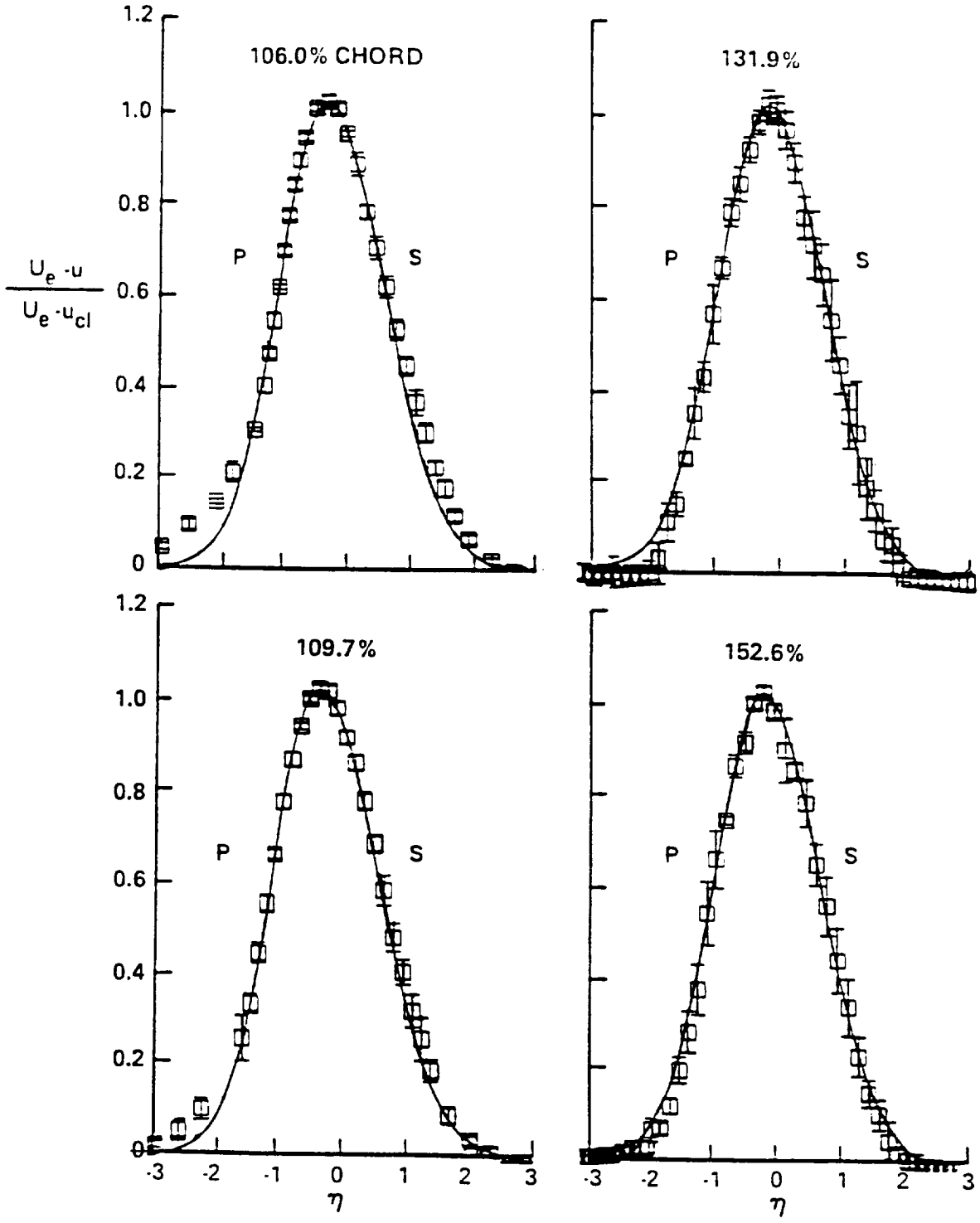

Figure 72. Wakes for $i = -8.5$ degrees in defect form with Gaussian similarity

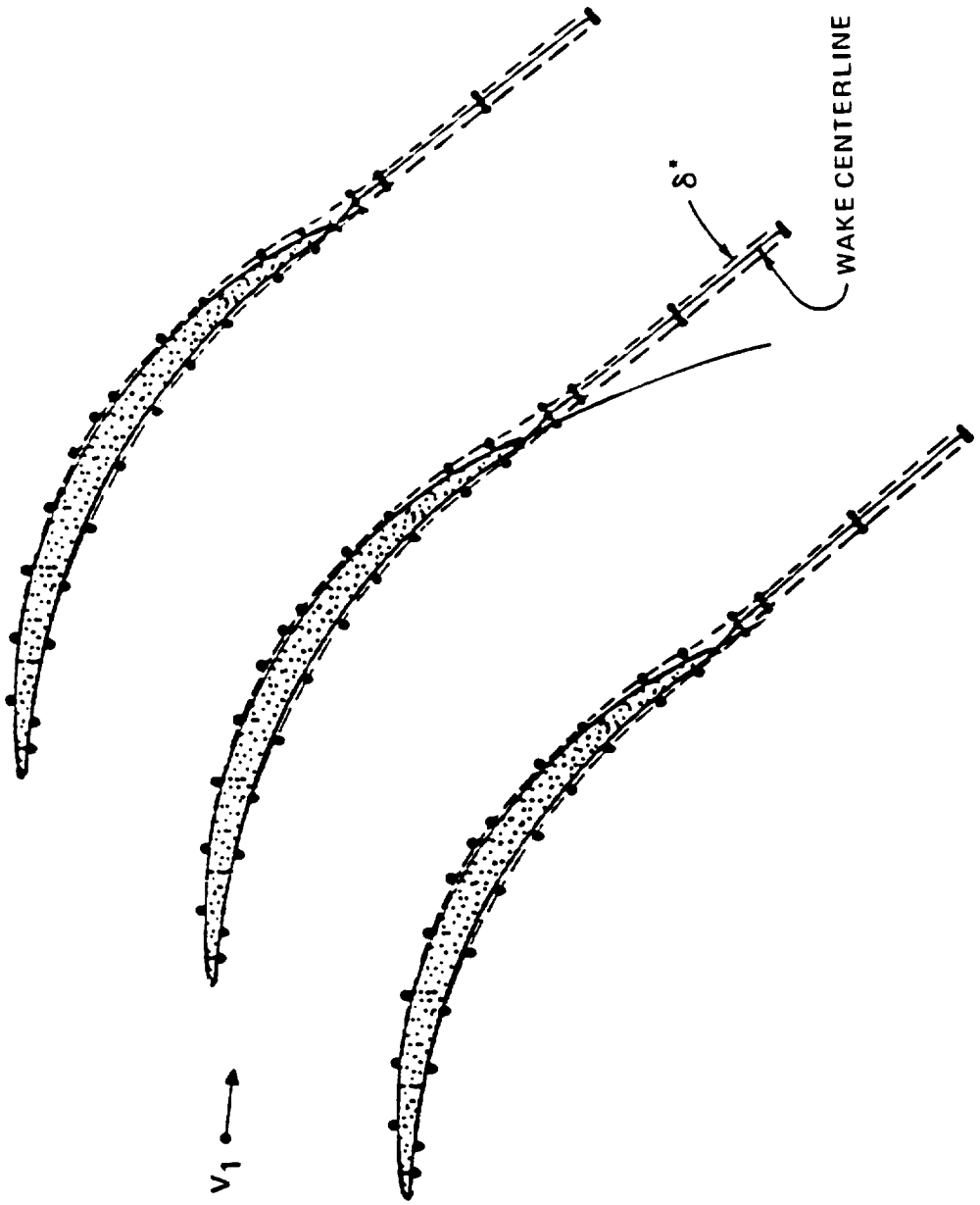

Figure 73. Cascade blades with the wake centerline and displacement thicknesses for $i = -8.5$ degrees (the two near wakes were measured with respect to the extended pressure surface arc which is shown)

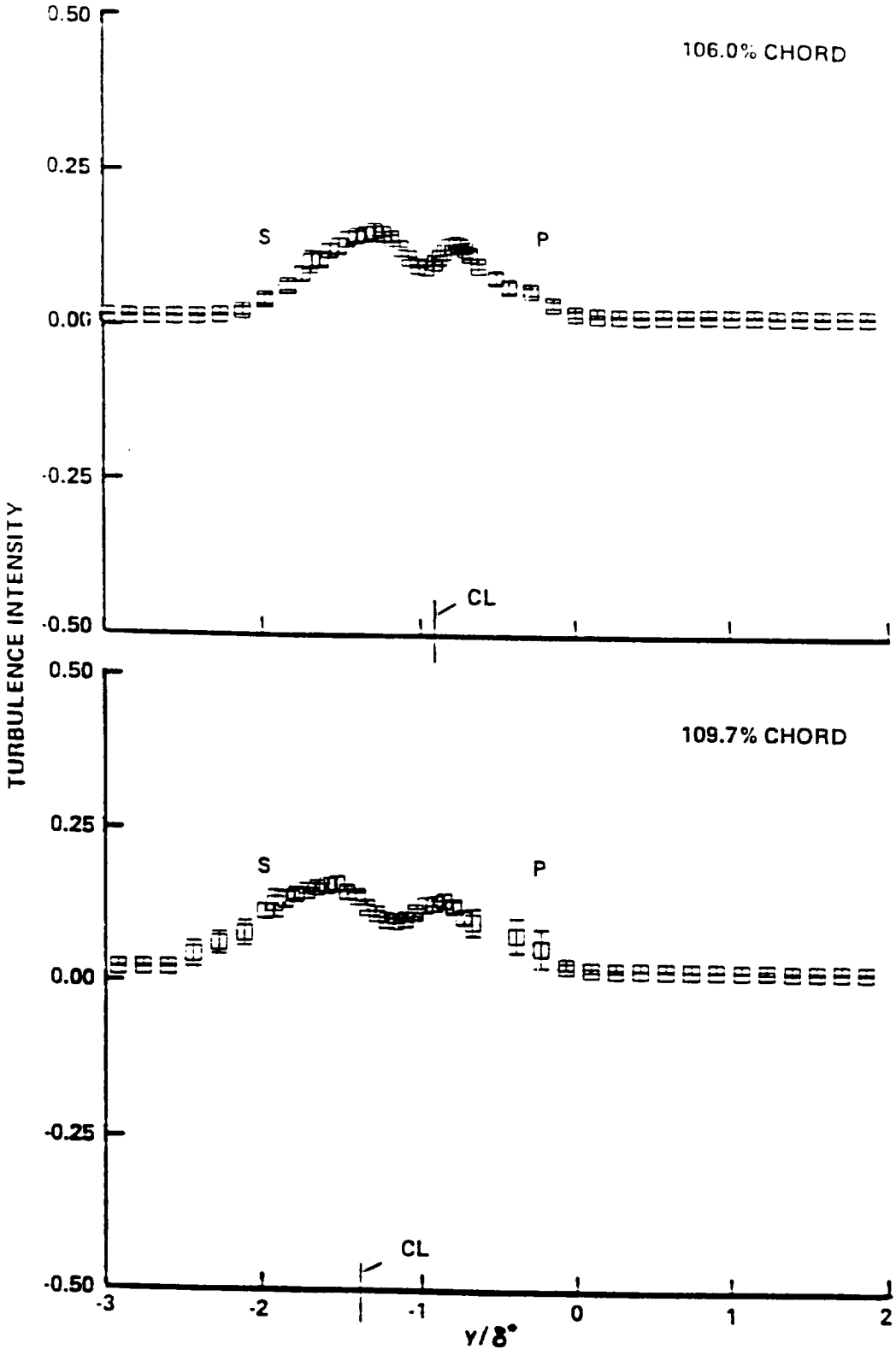

Figure 74. Turbulence intensity data for the near wakes at $i = -8.5$ degrees

Chapter 8 Summary and Conclusions

The numerical calculations of turbomachinery flow fields require the computing of many unsteady and three-dimensional flow phenomena. Before computing these complex flow fields with confidence, one must be able to compute the periodic, two-dimensional flow over a turbomachine blade in cascade. In either case, viscous calculations for turbomachinery applications have been handicapped by both a lack of sufficiently detailed and precise data against which these calculations can be compared and a lack of understanding of the physics involved within this complex flow field. In order to help overcome this problem, we designed an experiment to measure the boundary layers and wakes about a double-circular-arc, compressor blade in cascade. The measurements about these highly loaded blades have been made at a Re_c near 500,000 and at three incidence angles–for comparisons of computations at off-design conditions.

A periodic, two-dimensional cascade flow has been developed without the use of continuous side wall suction. Instead, a combination of strong suction just upstream of the blade pack and tailboards are used to create the desired flow–allowing the measurements to be made with a non-intrusive, one-component LDV system. Since a consensus opinion on how to correct velocity bias in a highly turbulent flow is still lacking, we have used simple arithmetic averaging to

determine the streamwise components of mean velocity and turbulence intensity. However, in measurements of very thin laminar boundary layers, we have shown that a combination of mean-velocity-gradient broadening and a vibration of the LDV measurement volume results in elevated turbulence levels. Aside from the LDV measurements, several other experimental techniques have helped characterize the flow fields. Static-pressure taps, Pitot-static probes, and five-hole probes were used in conjunction with pressure transducers to measure flow quantities upstream and downstream of the blade pack as well as on the blade surface. Flow visualization has also helped quantify the blade surface flow characteristics through a chemical sublimation method and an oil film method. We have also made dynamic wall shear stress measurements with hot films and turbulence intensity measurements with hot wires.

To help understand the physics of the cascade flow field we have presented a method by which we can analyze the raw data in regions of laminar, transitional, turbulent, and separated flows. Included are methods that allow one to account for a pressure gradient that occurs normal to the blade surface, to compute important boundary layer and wake parameters, and to fit or compare the data with empirical or theoretical equations for velocity profiles. Different methods to account for the normal pressure gradient need further investigation–perhaps through second-order boundary layer theory.

Near the leading edge, the incidence angle causes the stagnation point to lie on either the pressure or suction surface of the blade. On this stagnation surface, the streamwise pressure gradient begins as favorable and results in a region where the boundary layer is laminar. Falkner-Skan solutions describe this region fairly well, although the numerical, parabolic computations of STAN5 show even better comparisons. Further downstream, an adverse streamwise pressure gradient will either cause the laminar boundary layer to separate or initiate "natural" transition. Freestream turbulence intensity, concave surface curvature, and the continuing variation of the streamwise pressure gradient all can strongly affect "natural" transition. On the surface opposite of the stagnation point, a severe adverse pressure gradient results in the presence of a separation

"bubble" which transitions the flow to turbulence. One must take note that these highly loaded, double-circular-arc blades have a small leading edge radius and may not be typical of modern compressor blades. Further investigation is required of blade leading edge flows.

For these blade profiles with a Re_c of 500,000, we found that the boundary layer transition was usually initiated by the separation of the laminar boundary layer and the subsequent reattachment of either a fully turbulent boundary layer or possibly an intermittently turbulent boundary layer. It seems reasonable to conclude that transition through a separation "bubble" occurs much more often than "natural" transition on most compressor blades. Recently, Schulz and Gallus [1988] made several types of measurements and determined that transition occurred on the suction surface of their annular compressor cascade blade. They also made predictions with a boundary layer integral method using empirical criteria given by Dunham [1972] to predict boundary layer transition and turbulent separation. At all span locations and all incidence angles, they predicted that transition always occurred via a laminar separation "bubble."

Separation "bubbles" lead to sudden transition because the outer shear layer is inherently unstable. Numerical computations must either model overall characteristics of the "bubble"–such as size, location, and transitional aspects–or rely on very complex turbulence models. In either case, the computations will be affected by the unsteady and three-dimensional state of the "bubble." A recurring enlargement and shrinkage of the separation "bubble" seems to occur at a very low frequency. The recirculating region of the "bubble" grows either from fluid deep within the upstream boundary layer entering near detachment, from fluid being entrained from the freestream by the outer shear layer, or from fluid being reinjected upstream near reattachment. The outer region continually shears this recirculating region and some small-scale structures do break away. However, the "bubble" continually grows until instabilities cause large-scale structures to break away and convect downstream at a very low frequency. Also, this unsteadiness can interact with three-dimensional flow effects within the "bubble." The nature of this low-frequency unsteadiness warrants much additional research–both experimentally and computationally. This

research should attempt to determine how the separation "bubble" grows, what leads to the eventual instability, and what length scale best characterizes the unsteadiness.

After transition, nonequilibrium turbulent boundary layers develop because of the continually changing streamwise pressure gradient. If the turbulent boundary layer develops downstream of a separation "bubble," the velocity profiles are similar to the inflectional profiles developing toward separation except that they are traversed in reverse. This recovery process can be extended downstream if the streamwise pressure gradient is adverse. On the suction surface of compressor blades, these turbulent boundary layers can encounter a strong adverse pressure gradient and the boundary layers will begin to intermittently separate near the trailing edge. Even for intermittent separation, the wall-wake equation of Coles [1956] describes the turbulent velocity profiles quite well. After some region of intermittent separation, the turbulent boundary layer can detach. In the inner region of the separated shear layer, the mean backflow data shows some similarity using the maximum backflow velocity as the velocity scale and the total backflow thickness as the length scale. However, no similarity has been found to adequately describe the outer region of separation. Similarity should be investigated further in both regions.

As the turbulent shear layers reach the trailing edge, a near wake develops where its structure shows no similarity or self-preservation. A significant curvature of the wake centerline can develop if the blade has any trailing edge loading. Downstream, a far wake develops where the velocity profile shows Gaussian similarity. If a significant amount of separation occurs upstream of the trailing edge, the development of this Gaussian similarity is delayed until further downstream. An additional examination of the velocity profile in the near wake region is needed. In addition, different length scales for similarity are required if we want to describe the wake profiles from the characteristics of the trailing edge boundary layers.

These measurements form a good foundation for a data base on blade boundary layers.[22]

---

[22] Data tables and computer tapes of the data are available at the Applied Research Laboratory from either William C. Zierke or Steven Deutsch, at the NASA Lewis Research Center from Nelson Sanger, or from COSMIC.

C3

Eventually this database of boundary layer measurements on cascades should be extended to other blade shapes–representative of both compressor and turbine blades. Multi-component measurements could be used to extract turbulence characteristics. To continually increase the three-dimensional effects on the blade boundary layers, researchers should extend their measurements to annular cascades. These measurements might also include different levels of freestream turbulence. Finally, more research is required in the area of unsteady blade boundary layers.

In conclusion, these very detailed and precise measurements should provide a challenging and yet necessary test for comparison with numerical, viscous computations within a turbomachinery flow field. These computations must compute laminar, transitional, turbulent, and separated boundary layers as well as near and far wakes. Our initial numerical computations with STAN5 show the difficulties a parabolic boundary layer code has in the frequent regions of separation. Better models of separation, transition, and near-wake flows appear necessary in order to compute these flow fields.

Bibliography

Abu-Ghannam, B. J. and Shaw, R., "Natural Transition of Boundary Layers–The Effects of Turbulence, Pressure Gradient, and Flow History," *Journal of Mechanical Engineering Science*, Vol. 22, No. 5, pp. 213–228, 1980.

Alfredsson, P. H., Johansson, A. V., Haritonidis, J. H., and Eckelmann, H., "The Fluctuating Wall-Shear Stress and the Velocity Field in the Viscous Sublayer," *Physics of Fluids*, Vol. 31, No. 5, pp 1026–1033, May 1988.

Anand, A. K. and Lakshminarayana, B., "An Experimental Study of Three-Dimensional Turbulent Boundary Layer and Turbulent Characteristics Inside a Turbomachinery Rotor Passage," Transactions of the ASME, *Journal of Engineering for Power*, Vol. 100, pp. 676–690, October 1978.

Arena, A. V. and Mueller, T. J., "Laminar Separation, Transition, and Turbulent Reattachment near the Leading Edge of Airfoils," *AIAA Journal*, Vol. 18, No. 7, pp. 747–753, July 1980.

Ball, C. L., Reid, L., and Schmidt, J. F., "End-Wall Boundary Layer Measurements in a Two Stage Fan," NASA TM 83409, June 1983.

Bammert, K. and Milsch, R., "Boundary Layers on Rough Compressor Blades," ASME Paper No. 72-GT-48, 1972.

Bammert, K. and Sandstede, H., "Measurements of the Boundary Layer Development Along a Turbine Blade with Rough Surfaces," Transactions of the ASME, *Journal of Engineering for Power*, Vol. 102, pp. 978–983, October 1980.

Beam, R. M. and Warming, R. F., "An Implicit Factored Scheme for the Compressible Navier-Stokes Equations," *AIAA Journal*, Vol. 16, No. 4, pp. 393–402, April 1982.

Bell, W. A. and Cornelius, K. C., "An Experimental Investigation of a Laminar Separation Bubble on a Natural Laminar Airfoil," AIAA Paper No. 87-0458, Presented at the AIAA 25th Aerospace Sciences Meeting, Reno, Nevada, January 12–15, 1987.

Bellhouse, B. J. and Schultz, D. L., "Determination of Mean and Dynamic Skin Friction, Separation, and Transition in Low-Speed Flow with a Thin-Film Heated Element," *Journal of Fluid Mechanics*, Vol. 24, Part 2, pp. 370–400, 1966.

Bellhouse, B. J. and Schultz, D. L., "The Measurement of Fluctuating Skin-Friction in Air with Heated Thin-Gages," *Journal of Fluid Mechanics*, Vol. 32, Part 4, pp. 675–680, 1968.

Blasius, H., "Grenzchichten in Flüssigkeiten mit kleiner Reibung," *Z. Angew. Math. Phys.*, Vol. 56, No. 1, pp. 1–37, 1908. (English Translation, NACA TM No. 1256.)

Boussinesq, J., "Essai Sur La Théorie Des Eaux Courantes," *Mem. Présentés Acad. Sci.*, Vol. 23, Paris, p.46, 1877.

Braden, J. A., Whipkey, R. R., Jones, G. S., and Lilley, D. E., "Experimental Study of the Separating Confluent Boundary-Layer," NASA Contractor Report 3655, June 1983.

Bradshaw, P., Ferriss, D. H., and Atwell, W. P., "Calculation of Boundary Layer Development Using the Turbulent Energy Equation," *Journal of Fluid Mechanics*, Vol. 28, pp. 593–616, 1967.

Bradshaw, P., "The Analogy Between Streamline Curvature and Buoyancy in Turbulent Shear Flow," *Journal of Fluid Mechanics*, Vol. 26, pp. 177–191, 1969.

Brendel, M. and Mueller, T. J., "Boundary-Layer Measurements on an Airfoil at Low Reynolds Numbers," *Journal of Aircraft*, Vol. 25, No. 7, pp. 612–617, July 1988.

Briley, W. R. and McDonald, H., "Three-Dimensional Viscous Flows With Large Secondary Velocity," *Journal of Fluid Mechanics*, Vol. 144, pp. 47–77, July 1984.

Castro, I. P. and Haque, A., "The Structure of a Turbulent Shear Layer Bounding a Separation Region," *Journal of Fluid Mechanics*, Vol. 179, pp. 439–468, 1987.

Castro, I. P. and Haque, A., "The Structure of a Turbulent Shear Layer Bounding a Separation Region. Part 2. Effects of Free-Stream Turbulence," *Journal of Fluid Mechanics*, Vol. 192, pp. 577–595, 1988.

Cebeci, T. and Smith, A. M. O., *Analysis of Turbulent Boundary Layers*, Academic Press, 1974.

Charney, G., Mathieu, J., and Comte-Bellot, G., "Response of a Turbulent Boundary Layer to Random Fluctuations in the External Stream," *Physics of Fluids*, Vol. 19, No. 9., September 1976.

Cherry, N. J., Hillier, R., and Latour, M. E. M. P., "Unsteady Measurements in a Separated and Reattaching Flow," *Journal of Fluid Mechanics*, Vol. 144, pp. 13–46, 1984.

Clauser, F. H., "Turbulent Boundary Layers in Adverse Pressure Gradients," *Journal of the Aeronautical Sciences*, Vol. 21, pp. 91–108, February 1954.

Clauser, F. H., "The Turbulent Boundary Layer," *Advances in Applied Mechanics*, Vol. 4, pp. 1–51, 1956.

Coles, D. E., "The Law of the Wake in the Turbulent Boundary Layer," *Journal of Fluid Mechanics*, Vol. 1, pp. 191–226, 1956.

Coles, D. E. and Hirst, E. A., "Computation of Turbulent Boundary Layers," Proceedings of the AFSOR-IFP-Stanford Conference, Vol. II, August 1968.

Crawford, M. E. and Kays, W. M., "STAN5–A Program for Numerical Computation of Two-Dimensional Internal and External Boundary Layer Flows," COSMIC Program No. LEW-13009, NASA CR-2742, 1976.

Crimi, P. and Reeves, B. L., "Analysis of Leading-Edge Separation Bubbles on Airfoils," *AIAA Journal*, Vol. 14, pp 1548–1555, November 1976.

Davis, R. T. and Werle, M. J., "Progress on Interacting Boundary-Layer Computations at High Reynolds Number," *Numerical and Physical Aspects of Aerodynamic Flows*, Edited by T. Cebeci, Springer-Verlag, 1981.

Dunham, J., "Prediction of Boundary Layer Transition on Turbomachinery Blades," AGARDograph No. 164, pp. 55–71, 1972.

Eaton, J. K. and Johnston, J. P., "Low Frequency Unsteadiness of a Reattaching Turbulent Shear Layer," *Turbulent Shear Flows 3*, Edited by L. J. S. Bradbury, F. Durst, B. E. Launder, F. W. Schmidt, and J. H. Whitelaw, Springer–Verlag, pp 162–170, 1982.

Edwards, D. E. and Carter, J. E., "A Quasi-Simultaneous Finite Difference Approach for Strongly Interacting Flow," Presented at the Third Symposium on Numerical and Physical Aspects of Aerodynamics Flow, January 21–29, 1985.

Edwards, R. V., Angus, J. C., French, M. J., and Dunning, J. W., Jr., "Spectral Analysis of the Signal From the Laser Doppler Flowmeter: Time-Dependent Systems," *Journal of Applied Physics*, Vol. 42, No. 3, pp. 837–850, February 1971.

Edwards, R. V., "A New Look at Particle Statistics in Laser-Anemometer Measurements," *Journal of Fluid Mechanics*, Vol. 105, pp. 317–325, 1981.

Edwards, R. V. and Jensen, A. S., "Particle-Sampling Statistics in Laser Anemometers: Sample-and-Hold Systems and Saturable Systems," *Journal of Fluid Mechanics*, Vol. 133, pp. 397–411, 1983.

Elazar, Y. and Shreeve, R. P., "Viscous Flow Behavior in a Controlled-Diffusion Compressor Cascade with Progressively Increasing Incidence," Submitted for Presentation at the 1989 ASME Gas Turbine Conference, Toronto, Ontario, Canada, June 4–8, 1989.

Evans, B. J., "Effects of Free-Stream Turbulence on Blade Performance in a Compressor Cascade," Ph.D. Dissertation, Cambridge University, 1971.

Evans, R. L., "Boundary Layer Development on an Axial-Flow Compressor Stator Blade," Transactions of the ASME, *Journal of Engineering for Power*, Vol. 100, pp. 287–293, April 1978.

Falkner, V. M. and Skan, S. W., "Some Approximate Solutions of the Boundary Layer Equations," *Phil. Mag.*, Vol. 12, No.7, pp. 865–896, 1931.

Gade, S. and Herlufsen, H., "Windows to FFT Analysis," *Sound and Vibrations*, pp. 14–22, March 1988.

Gibson, M. M., Verriopoulos, C. A., and Vlachos, N. S., "Turbulent Boundary Layer on a Mildly Curved Convex Surface–Part I: Mean Flow and Turbulence Measurements," *Experiments in Fluids*, Vol. 2, pp. 17–24, 1984.

Giel, T. V. and Barnett, D. O., "Analytical and Experimental Study of Statistical Bias in Laser Velocimetry," *Laser Velocimetry and Particle Sizing*, Edited by H. D. Thompson and W. H. Stevenson, Hemisphere Publishing Corporation, pp. 86–99, 1979.

Gillis, J. C. and Johnston, J. P., "Turbulent Boundary-Layer Flow and Structure on a Convex Wall and Its Redevelopment on a Flat Wall," *Journal of Fluid Mechanics*, Vol. 135, pp. 123-153, 1983.

Goldstein, R. J., Eriksen, V. L., Olson, R. M., and Eckert, E. R. G., "Laminar Separation, Reattachment, and Transition of the Flow Over a Downstream-Facing Step," Transactions of the ASME, *Journal of Basic Engineering*, pp. 732–741, December 1970.

Goldstein, R. J. and Adrian, R. J., "Measurement of Fluid Velocity Gradients Using Laser-Doppler Techniques," *The Review of Scientific Instruments*, Vol. 42, No. 9, pp. 1312–1320, September 1971.

Görtler, H., "Über eine dredimensionale Instabilität laminarer Grenzschichten an konkaven Wänden," Nachr. Ges. Wiss. Göttingen, Math. Phys. Klasse, New series 2, No. 1, 1940.

Gray, W. E., "A Chemical Method of Indicating Transition in the Boundary Layer," Royal Aircraft Establishment TN Aero 1466, June 1944.

Hah, C. and Lakshminarayana, B., "Measurement and Prediction of Mean Velocity and Turbulence Structure in the Near Wake of an Airfoil," *Journal of Fluid Mechanics*, Vol. 115, pp. 251–282, 1982.

Hobbs, D. E., Wagner, J. H., Dannenhoffer, J. F., and Dring, R. P., "Experimental Investigation of Compressor Cascade Wakes," ASME Paper No. 82-GT-299, 1982.

Hodson, H. P., "The Development of Unsteady Boundary Layers on the Rotor of an Axial-Flow Turbine," AGARD-CP-351, June 1983.

Hoessel, W. and Rodi, W., "New Biasing Elimination Method for Laser-Doppler Velocimeter Counter Processing," *Review of Scientific Instrumentation*, Vol. 48, No. 2, July 1977.

Hoffman, G. H., "A Rapid Method for Predicting Suction Distributions to Maintain Attached, Laminar Boundary Layers on Bodies of Revolution," ARL/PSU TM 83-201, Applied Research Laboratory, The Pennsylvania State University, December 1983.

Holmes, B. J. and Obara, C. J., "Observations and Implications of Natural Laminar Flow on Practical Airplane Surfaces," Thirteenth Congress of ICAS and AIAA, Aircraft Systems and Technology Conference, Seattle, Washington, ICAS-82-5.1.1, August 22–27, 1982.

Jessup, S. D., Schott, C. G., Jeffers, M. F., and Kobayashi, S., "Local Propeller Blade Flows in Uniform and Sheared Onset Flows Using LDV Techniques," David W. Taylor Naval Ship Research and Development Center, Report No. DTNSRDC-85/007, February 1985.

Johnson, D. A., Modarress, D., and Owen, F. K., "An Experimental Verification of Laser-Velocimeter Sampling Bias and Its Correction," Transactions of the ASME, *Journal of Fluids Engineering*, Vol. 106, pp. 5–12, March 1984.

Johnston, W. and Sockol, P., "Viscous-Inviscid Interactive Procedure for Rotational Flow in Cascades of Airfoils," *AIAA Journal*, Vol. 22, No. 9, pp. 1281–1282, September 1984.

Karlsson, R. I., "Turbulence Structure and Skin Friction in Turbulent Boundary Layers on Irregularly Rough Surfaces," ASME Paper No. 81-GT-14, 1981.

Kiock, R., "Evaluation of Boundary Layer Measurements in Two-Dimensional Compressible Subsonic Flow with a Pressure Gradient across the Boundary Layer," ESA-TT-810, European Space Agency, July 1983.

Kiya, M. and Sasaki, K., "Structure of a Turbulent Separation Bubble," *Journal of Fluid Mechanics*, Vol. 137, pp. 83–113, 1983.

Klebanoff, P. S., "Characteristics of Turbulence in a Boundary Layer with Zero Pressure Gradient," NACA Technical Note 3178, 1954.

Klebanoff, P. S., Tidstrom, K., D., and Sargent, L. M., "The Three-Dimensional Nature of Boundary-Layer Instability," *Journal of Fluid Mechanics*, Vol. 12, No. 1, pp. 1–34, 1962.

Kline, S. J., Discussion of a Paper by G. Hekestad, "Remarks on Snow Cornice Theory and Related Experiments with Sink Flows," Transactions of the ASME, *Journal of Basic Engineering*, Series D, Vol. 88, pp. 547–549, June 1966.

Kried, D. K., "Laser-Doppler Velocimeter Measurements in Nonuniform Flow: Error Estimates," *Applied Optics*, Vol. 13, No. 8, pp. 1872–1881, August 1974.

Lakshminarayana, B. and Davino, R., "Mean Velocity and Decay Characteristics of the Guide Vane and Stator Blade Wake of an Axial Flow Compressor," Transactions of the ASME, *Journal of Engineering for Power*, Vol. 102, pp. 50–60, January 1980.

Lakshminarayana, B., Govindan, T. R., and Hah, C., "Experimental Study of the Boundary Layer on a Turbomachine Rotor Blade," Three-Dimensional Turbulent Boundary Layers, IUTAM Symposium, Berlin, March 29–April 1, 1982.

Launder, B., and Jones, W. P., "On the Prediction of Laminarization," presented at the ARC Heat and Mass Transfer Subcommittee Meeting of April 5, 1968.

Launder, B. E., Reece, G. J., and Rodi, W., "Progress in the Development of a Reynolds Stress Turbulence Closure," *Journal of Fluids Mechanics*, Vol. 68, pp. 537–566, 1975.

Lieblein, S., Schwenk, F. C., and Broderick, R. L., "Diffusion Factor for Estimating Losses and Limiting Blade Loadings in Axial-Flow-Compressor Blade Elements," NACA RM E53 D01, June 8, 1953.

Lieblein, S. and Roudebush, W. H., "Theoretical Loss Relations for Low-Speed Two-Dimensional-Cascade Flow," NACA TN 3662, 1956.

Liepmann, H. W., and Skinner, G. T., "Shearing-Stress Measurements by Use of a Heated Element," NACA TN 3268, 1954.

Ludweig, H. and Tillman, W., "Untersuchungen über die Wandschubspannung in Turbulenten Reibungsschenhten", *Ing.-Arch.*, Vol. 17, pp. 288–299, 1949. (English Transaction, NACA TM 1285.)

Ludweig, H., "Investigation for Measuring the Wall Shearing Stress of Turbulent Boundary Layers," NACA TM 1284, May 1950.

McGuiness, M., "Flow with a Separation Bubble–Steady and Unsteady Aspects," Ph. D. Dissertation, Cambridge University, 1978.

McLaughlin, D. K. and Tiederman, W. G., "Biasing Correction for Individual Realization of Laser Anemometer Measurements in Turbulent Flows," *Physics of Fluids*, Vol. 16, No. 12, pp. 2082–2088, December 1973.

Meauzé, G., "Transonic Boundary Layer on Compressor Stator Blades as Calculated and Measured in Wind Tunnel," At the Fourth International Symposium on Air Breathing Engines–ISABE, April 1–6, 1979.

Mehta, J. M. and Goradia, S., "Experimental Studies of the Separated Flow Over a NASA GA(W)-1 Airfoil," *AIAA Journal*, Vol. 22, No. 4, pp. 552- -554, April 1984.

Mellor, G. L. and Gibson, D. M., "Equilibrium Turbulent Boundary Layers," *Journal of Fluid Mechanics*, Vol. 24, Part 2, pp. 225–253, 1966.

Mellor, G. L. and Wood, G. M., "An Axial Compressor End-Wall Boundary Layer Theory," Transactions of the ASME, *Journal of Basic Engineering*, Vol. 93, Series D, No. 1, pp. 300–316, June 1971.

Melnik, R. E. and Brook, J. W., "The Computation of Viscid/Inviscid Interaction on Airfoils With Separated Flow," Gruman Aerospace Corporation Report RE-697, April 1985.

Mueller, T. J., Korst, H. H., and Chow, W. L., "On the Separation, Reattachment, and Redevelopment of Incompressible Turbulent Shear Flow," Transactions of the ASME, *Journal of Basic Engineering*, pp. 221–226, June 1964.

Murlis, J., Tsai, H. M., and Bradshaw, P., "The Structure of Turbulent Boundary Layers at Low Reynolds Numbers," *Journal of Fluid Mechanics*, Vol. 122, pp. 13–56, 1982.

Nakamura Y., and Ozono, S., "The Effects of Turbulence on a Separated and Reattaching Flow," *Journal of Fluid Mechanics*, Vol. 178, pp 477–490, 1987.

Obara, C. J., "Sublimating Chemical Technique for Boundary-Layer Flow Visualization in Flight Testing," *Journal of Aircraft*, Vol. 25, No. 6, pp. 493–498, June 1988.

O'Meara, M. M. and Mueller, T. J., "Laminar Separation Bubble Characteristics on an Airfoil at Low Reynolds Numbers," *AIAA Journal*, Vol. 25, No. 8, pp 1033–1041, August 1987.

Patankar, S. V., and Spalding, D. B., *Heat and Mass Transfer in Boundary Layers*, 1st Edition, Morgan-Grampian, London, 1967.

Patrick, W. P., "Flowfield Measurements in a Separated and Reattached Flat Plate Turbulent Boundary Layer," NASA Contractor Report 4052, March 1987.

Perry, A. E. and Schofield, W. H., "Mean Velocity and Shear Stress Distributions in Turbulent Boundary Layers," *Physics of Fluids*, Vol. 16, No. 12, pp. 2068–2074, December 1973.

Peterson, C. R., "Boundary Layer on an Airfoil in a Cascade," Gas Turbine Laboratory Report No. 49, Massachusetts Institute of Technology, December 1958.

Pollard, D. and Gostelow, J. P., "Some Experiments at Low Speed on Compressor Cascades," Transactions of the ASME, *Journal of Engineering for Power*, Vol. 89, Series A, pp. 427–436, June 1967.

Pouagare, M., Galmes, J. M., and Lakshminarayana, B., "An Experimental Study of the Compressor Rotor Blade Boundary Layer," Transactions of the ASME, *Journal of Engineering for Gas Turbines and Power*, Vol. 107, pp. 364–373, April 1985.

Prandtl, L., "Ueber die ausgebildete Turbulenz," Proceedings of the 2nd International Congress for Applied Mechanicx, Zürich, pp. 62–74, 1926.

Prandtl, L., "Bemeerkungen zur Theorie der freien Turbulenz," *Z. Angew. Math. Mech.*, Vol. 22, pp. 241–243, 1942.

Purtell, L. R., Klebanoff, P. S., and Buckley, F. T., "Turbulent Boundary Layers at Low Reynolds Numbers," *Physics of Fluids*, Vol. 24, pp. 802–811, 1981.

Ramaprian, B. R. and Shivaprasad, B. G., "Mean Flow Measurements in Turbulent Boundary Layers Along Mildly Curved Surfaces," *AIAA Journal*, Vol. 15, No. 2, pp. 189-196, February 1977.

Reichert, J. K. and Azad, R. S., "Features of a Developing Turbulent Boundary Layer Measured in a Bounded Flow," *Canadian Journal of Physics*, p. 477, 1979.

Rubin, S. G. and Khosla, P. K., "Navier-Stokes Calculations With a Coupled Strongly Implicit Method. Part I–Finite Difference Solutions," *Computers and Fluids*, Vol. 9, No. 2, p. 163, 1981.

Rubin, S. G. and Khosla, P. K., "A Composite Velocity Procedure for the Incompressible Navier-Stokes Equations," 8th International Conference on Numerical Methods in Fluid Mechanics, Springer-Verlag, pp. 448–454, 1982.

Sandborn, V. A. and Kline, S. J., "Flow Models in Boundary Layer Stall Inception," Transactions of the ASME, *Journal of Basic Engineering*, Vol. 83, pp. 317-327, May 1961.

Sanger, N., Double-Circular-Arc Compressor Blades, NASA Lewis DCA4, 65 Degree Camber Centerline and Thickness Equations, Private Communication, November 1980.

Schlichting, H., *Boundary-Layer Theory*, Seventh Edition, McGraw-Hill, Inc., 1979.

Schofield, W. H., "Equilibrium Boundary Layers in Moderate to Strong Adverse Pressure Gradients," *Journal of Fluid Mechanics*, Vol. 113, pp. 91-122, 1981.

Schofield, W. H., "On Separating Turbulent Boundary Layers," Mechanical Engineering Report 162, Department of Defense, Defense Science and Technology Organization, Aeronautical Research Laboratories, September 1983.

Schofield, W. H., "Two-Dimensional Separating Turbulent Boundary Layers," *AIAA Journal*, Vol. 24, No. 10, pp. 1611–1620, October 1986.

Schulz, H. D. and Gallus H. D., "Experimental Investigation of the Three-Dimensional Flow in an Annular Compressor Cascade," Transactions of the ASME, *Journal of Turbomachinery*, Vol. 110, pp. 467–478, October 1988.

Shivaprasad, B. G. and Ramaprian, B. R., "Turbulence Measurements in Boundary Layers Along Mildly Curved Surfaces," Transactions of the ASME, *Journal of Fluids Engineering*, Vol. 100, pp. 37–46, March 1978.

Simpson, R. L., Strickland, J. H., and Barr, P. W., "Features of a Separating Turbulent Boundary Layer in the Vicinity of Separation," *Journal of Fluid Mechanics*, Vol. 79, Part 3, pp. 553–594, 1977.

Simpson, R. L., Chew, Y.-T., and Shivaprasad, B. G., "The Structure of a Separating Turbulent Boundary Layer. Part 1. Mean Flow and Reynolds Stresses," *Journal of Fluid Mechanics*, Vol. 113, pp. 23–51, 1981a.

Simpson, R. L., Chew, Y.-T., and Shivaprasad, B. G., "The Structure of a Separating Turbulent Boundary Layer. Part 2. Higher-Order Turbulence Results," *Journal of Fluid Mechanics*, Vol. 113, pp. 53–73, 1981b.

Smits, A. J., Matheson, N., and Joubert, P. N., "Low Reynolds-Number Turbulent Boundary Layers in Zero and Favorable Pressure Gradients," *Journal of Ship Research*, Vol. 27, No. 3, pp. 147–157, September 1983.

So, R. M. C. and Mellor, G. L., "Experiment on Convex Curvature Effects in Turbulent Boundary Layers," *Journal of Fluid Mechanics*, Vol. 60, pp. 43–62, 1973.

So, R. M. C., "A Turbulence Velocity Scale for Curved Shear Flows," *Journal of Fluid Mechanics*, Vol. 70, Part 1, pp. 37–57, 1975.

Stack, J. P., Mangalam, S. M., and Kalburgi, V., "The Phase Reversal Phenomenon at Flow Separation and Reattachment," AIAA Paper No. 88-0408, Presented at the AIAA 26th Aerospace Sciences Meeting, Reno, Nevada, January 11–14, 1988.

Steger, J. L., "Implicit Finite-Difference Simulation of Flow About Arbitrary Two Dimensional Geometries," *AIAA Journal*, Vol. 16, pp. 679–686, 1978.

Stevenson, W. H., Thompson, H. D., and Craig, R. R., "Laser Velocimeter Measurements in Highly Turbulent Recirculating Flows," Transactions of the ASME, *Journal of Fluids Engineering*, Vol. 106, pp. 173–180, June 1984.

Sun, C. C. and Childs, M. E., "Wall-Wake Velocity Profile for Compressible Nonadiabatic Flows," *AIAA Journal*, Vol. 14, No. 6, pp. 820–822, June 1976.

Thompson, J., "Numerical Solution of Flow Problems Using Body-Fitted Coordinate Systems," in Computational Fluid Dynamics, Lecture at von Karman Institute, edited by W. Kollmann, Hemisphere Publication, New York, NY, p. 1. 1980.

Toyokura, T., Kurokawa, J., and Kimoto, Y., "Three-Dimensional Boundary Layer Flow on Rotating Blades," *Transactions of the JSME*, Vol. 25, 1982.

Treaster, A. L. and Yocum, A. M., "The Calibration and Application of Five-Hole Probes," *Transactions of the Instrument Society of America*, Vol. 18, No. 3, pp. 23–24, 1979.

Van Driest, E. R., "Turbulent Boundary Layer in Compressible Fluids," *Journal of the Aeronautical Sciences*, Vol. 18, pp. 145–160 and 216, 1951.

Van Driest, E. R., "On Turbulent Flow Near a Wall," *Journal of Aero. Sci.*, Vol. 23, pp. 1007–1011, 1956.

Von Kármán, Th., "Mechanishe Ähnlichkeit und Turbulenz," *Nachrichten der Akademie der Wissenschaften*, Math.-Phys. Klasse, Vol. 58, 1930.

Wadcock, A. J., "Simple Turbulence Models and Their Application to Boundary Layer Separation," NASA Contractor Report 3283, May 1980.

Walker, G. J., "The Turbulent Boundary Layer on an Axial Compressor Blade," ASME Paper No. 82-GT-52, 1982.

Wang, T., Simon, T. W., and Buddhavarapu, J., "Heat Transfer and Fluid Mechanics Measurements in Transitional Boundary Layer Flows," ASME Paper No. 85-GT-113, 1985.

White, F. M., *Viscous Fluid Flow*, McGraw-Hill, Inc., 1974.

Wills, J. A. B., "Correction of Hot Wire Readings for Proximity to a Solid Boundary," *Journal of Fluid Mechanics*, Vol. 12, pp. 388–296, 1962.

Zaman, K. B. M. Q., Bar-Sever, A., and Mangalam, S. M., "Effect of Acoustic Excitation on the Flow over a Low-*Re* Airfoil," *Journal of Fluid Mechanics*, Vol. 182, pp. 127–148, 1987.

Appendix A Blade Profile

The equations for the pressure surface, suction surface, and camberline of the double-circular-arc blades used in the current study can be written as

$$x_p^2 + (y_p + 219.7)^2 = 246.8^2 ,$$

$$x_s^2 + (y_s + 149.5)^2 = 189.1^2 ,$$

and

$$x_c^2 + (y_c + 179.4)^2 = 212.8^2 .$$

All of the dimensions are in millimeters. The origin of the coordinate system used here is located on the chord line at midchord. The x coordinate is parallel to the chord, while the y coordinate is normal to the chord. Figure 75 shows the double-circular-arc blade where the camber angle (ϕ) is 65 degrees and the blade chord length (c) is 228.6 mm. This value of c is measured from the center of the leading edge circle to the center of the trailing edge circle. Both the leading edge and trailing edge radii were 0.9144 mm and the corresponding circles met the two blade surfaces at the tangency points.

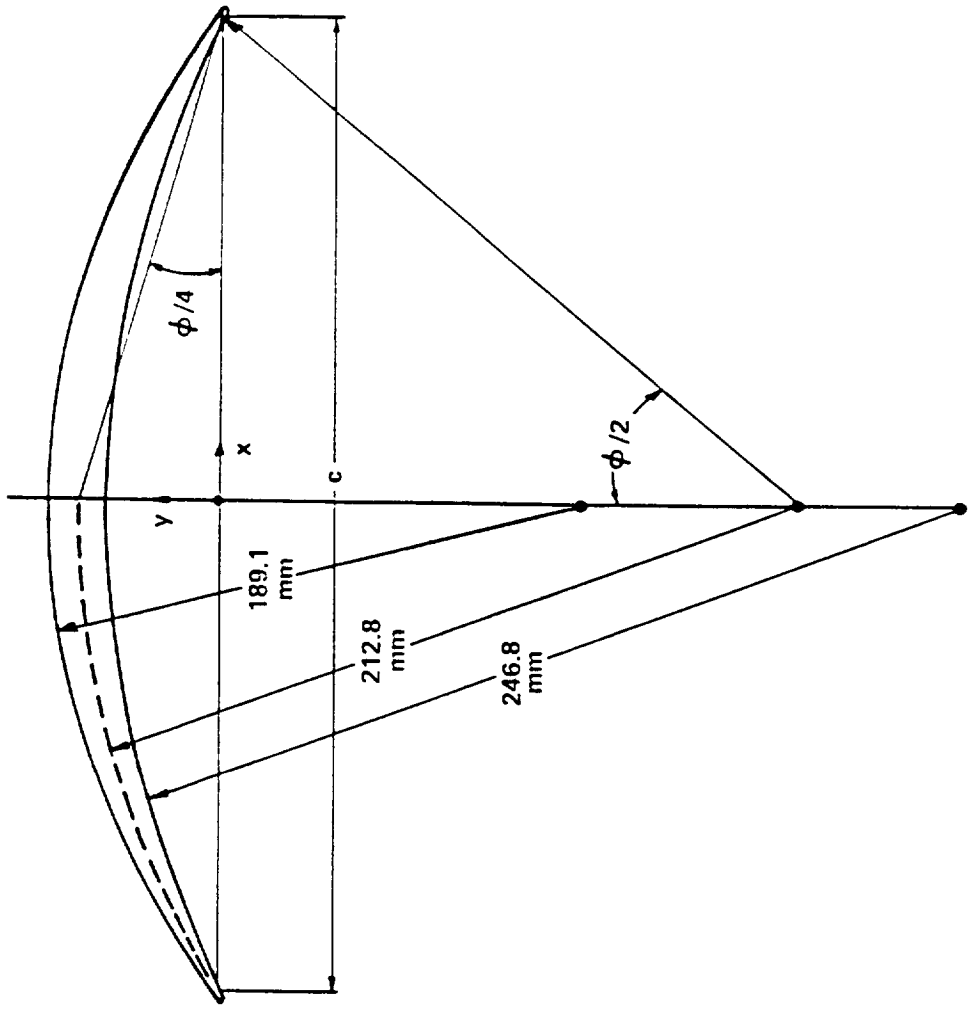

Figure 75. Double-circular-arc blade profile

Appendix B Parameter Tables

The boundary layer and wake parameters mentioned in chapter 6 have been computed for all of the shear layers presented in chapters 5 and 7. This appendix includes tables of all these parameters, as well as the measured static-pressure coefficients for all three incidence angles. The values of U_e that accompany these measured values of C_p were computed from the inviscid equation

$$U_e = V_1\sqrt{1.0 - C_p}\,.$$

Table 5. Static-pressure coefficients for $i = 5.0$ degrees

Pressure Surface			Suction Surface		
Percent Chord	C_p	U_e (m/sec)	Percent Chord	C_p	U_e (m/sec)
1.0	0.685	18.58	1.0	-1.346	50.72
3.0	0.547	22.28	2.0	-1.302	50.24
4.0	0.523	22.87	3.0	-0.936	46.08
5.0	0.508	23.22	5.0	-0.481	40.30
6.0	0.508	23.22	6.0	-0.453	39.92
12.2	0.509	23.20	12.2	-0.349	38.46
18.3	0.526	22.80	18.3	-0.270	37.32
24.5	0.545	22.33	24.5	-0.167	35.77
30.7	0.553	22.14	30.7	-0.067	34.20
36.8	0.574	21.61	36.8	0.038	32.48
43.0	0.583	21.38	43.0	0.097	31.47
49.2	0.588	21.25	49.2	0.153	30.48
55.3	0.588	21.25	55.3	0.196	29.69
61.5	0.590	21.20	61.5	0.243	28.84
67.7	0.597	21.02	67.7	0.260	28.51
73.8	0.584	21.36	73.8	0.292	27.89
80.0	0.565	21.84	80.0	0.301	27.71
82.5	0.551	21.19	82.5	0.309	27.55
85.4	0.543	22.38	88.3	0.297	27.79
88.3	0.523	22.87	94.5	0.307	27.59
91.3	0.494	23.55	97.3	0.308	27.57
94.5	0.456	24.42			
97.3	0.400	25.65			

Table 6. Shear layer thicknesses for $i = 5.0$ degrees

		Spline Fit					Falkner-Skan Solution		Fit of the Wall-Wake Equation			
Percent Chord	Region	U_e (m/sec)	δ (mm)	δ^* (mm)	θ (mm)	δ_3 (mm)	δ^* (mm)	θ (mm)	δ^* (mm)	θ (mm)	δ_3 (mm)	Δ (mm)
2.7	P	21.45	0.68(?)	0.074	0.005(?)	–	0.071	0.029	–	–	–	–
5.9	P	23.62	0.49	0.187	0.028(?)	0.027(?)	0.144	0.056	–	–	–	–
14.4	P	24.65	0.68	0.301	0.090	0.140	0.349	0.126	–	–	–	–
25.1	P	24.14	1.04	0.390	0.089	0.121	0.377	0.139	–	–	–	–
35.8	P	23.84	1.36	0.622	0.163	0.246	0.740	0.199	–	–	–	–
46.5	P	23.58	1.64	0.707	0.206	0.316	0.569	0.202	–	–	–	–
57.2	P	23.39	2.34	0.830	0.290	0.458	0.567	0.214	–	–	–	–
68.0	P	23.56	2.77	0.798	0.353	0.577	0.628	0.236	–	–	–	–
78.6	P	24.07	3.45	0.699	0.388	0.677	0.385	0.169	–	–	–	–
89.3	P	25.51	4.61	0.648	0.400	0.718	0.272	0.124	–	–	–	–
97.9	P	28.14	2.90	0.312	0.220	0.407	0.214	0.098	–	–	–	–
2.6	S	55.98	2.28	0.804	0.362	0.574	–	–	0.786	0.380	0.601	30.75
7.6	S	45.98	3.25	0.657	0.418	0.720	–	–	0.648	0.423	0.727	15.91
12.7	S	44.70	4.00	0.734	0.505	0.890	–	–	0.728	0.509	0.893	16.86
23.0	S	41.77	5.26	0.940	0.638	1.116	–	–	0.926	0.643	1.123	22.14
33.2	S	37.79	8.26	1.660	1.092	1.878	–	–	1.646	1.104	1.900	44.25
43.3	S	35.33	9.28	2.214	1.326	2.206	–	–	2.203	1.328	2.207	69.93
53.6	S	33.82	11.50	3.500	1.796	2.885	–	–	3.460	1.821	2.915	141.76
63.2	S	31.77	14.40	5.557	2.261	3.471	–	–	5.550	2.279	3.484	375.77
74.0	S	31.22	20.00	9.495	2.975	4.442	–	–	9.479	2.982	4.459	1486.44
84.2	S	30.45	27.50	14.718	3.718	5.483	–	–	–	–	–	–
94.9	S	29.44	36.36	22.446	4.375	6.360	–	–	–	–	–	–
105.4	W	29.09	53.00	27.238	3.885	5.980	–	–	–	–	–	–
109.6	W	29.15	56.00	29.306	4.345	6.865	–	–	–	–	–	–
152.6	W	26.18	85.60	29.050	15.45	24.549	–	–	–	–	–	–

Table 7. Shear layer parameters for $i = 5.0$ degrees

		Spline Fit			Falkner-Skan Solution			Fit of the Wall-Wake Equation					
Percent Chord	Region	H_{12}	H_{32}	Re_θ	β	H_{12}	Re_θ	H_{12}	H_{32}	Re_θ	β_c	G	II
2.7	P	–	–	–	0.181	2.43	43	–	–	–	–	–	–
5.9	P	6.74(?)	0.98(?)	44(?)	0.000	2.60	86	–	–	–	–	–	–
14.4	P	3.33	1.54	149	-0.090	2.77	194	–	–	–	–	–	–
25.1	P	4.37	1.36	143	-0.064	2.71	207	–	–	–	–	–	–
35.8	P	3.81	1.50	260	-0.197	3.72	288	–	–	–	–	–	–
46.5	P	3.43	1.53	324	-0.106	2.82	286	–	–	–	–	–	–
57.2	P	2.86	1.58	452	-0.032	2.65	304	–	–	–	–	–	–
68.0	P	2.26	1.64	555	-0.040	2.66	331	–	–	–	–	–	–
78.6	P	1.80	1.74	623	0.623	2.28	244	–	–	–	–	–	–
89.3	P	1.62	1.80	680	1.664	2.19	191	–	–	–	–	–	–
97.9	P	1.42	1.85	413	2.570	2.18	170	–	–	–	–	–	–
2.6	S	2.22	1.58	1353	–	–	–	2.07	1.58	1418	19.14	20.21	4.18
7.6	S	1.57	1.72	1282	–	–	–	1.53	1.72	1297	0.53	8.52	1.14
12.7	S	1.45	1.76	1505	–	–	–	1.43	1.76	1516	0.56	6.98	0.49
23.0	S	1.47	1.75	1778	–	–	–	1.44	1.75	1790	1.18	7.31	0.62
33.2	S	1.52	1.72	2752	–	–	–	1.49	1.72	2782	3.46	8.85	1.18
43.3	S	1.67	1.66	3122	–	–	–	1.66	1.66	3128	3.55	12.60	2.59
53.6	S	1.95	1.61	4049	–	–	–	1.90	1.60	4105	7.63	19.41	4.49
63.2	S	2.46	1.53	4789	–	–	–	2.44	1.53	4827	13.53	39.90	10.19
74.0	S	3.19	1.49	6193	–	–	–	3.18	1.50	6207	138.43	107.48	26.93
84.2	S	3.96	1.47	7547	–	–	–	–	–	–	–	–	–
94.9	S	5.13	1.45	8589	–	–	–	–	–	–	–	–	–
105.4	W	7.01	1.54	7534	–	–	–	–	–	–	–	–	–
109.6	W	6.74	1.58	8444	–	–	–	–	–	–	–	–	–
152.6	W	1.88	1.59	26965	–	–	–	–	–	–	–	–	–

Table 8. Boundary layer friction parameters for $i = 5.0$ degrees

		Spline Fit and Ludweig-Tillman Equation			Falkner-Skan Solution			Fit of the Wall-Wake Equation		
Percent Chord	Region	u_τ (m/sec)	τ_w (Pa)	C_f	u_τ (m/sec)	τ_w (Pa)	C_f	u_τ (m/sec)	τ_w (Pa)	C_f
2.7	P	–	–	–	1.151	1.595	0.00559	–	–	–
5.9	P	–	–	–	0.824	0.818	0.00252	–	–	–
14.4	P	–	–	–	0.479	0.277	0.00086	–	–	–
25.1	P	–	–	–	0.454	0.248	0.00083	–	–	–
35.8	P	–	–	–	0.132	0.021	0.00007	–	–	–
46.5	P	–	–	–	0.324	0.126	0.00046	–	–	–
57.2	P	–	–	–	0.355	0.152	0.00056	–	–	–
68.0	P	–	–	–	0.329	0.131	0.00049	–	–	–
78.6	P	–	–	–	0.527	0.335	0.00118	–	–	–
89.3	P	–	–	–	0.718	0.621	0.00193	–	–	–
97.9	P	–	–	–	0.972	1.140	0.00282	–	–	–
2.6	S	1.322	2.104	0.00111	–	–	–	1.430	2.465	0.00131
7.6	S	1.814	3.966	0.00311	–	–	–	1.872	4.221	0.00331
12.7	S	1.892	4.315	0.00358	–	–	–	1.930	4.490	0.00373
23.0	S	1.703	3.496	0.00333	–	–	–	1.747	3.678	0.00350
33.2	S	1.405	2.380	0.00277	–	–	–	1.406	2.383	0.00277
43.3	S	1.145	1.579	0.00210	–	–	–	1.113	1.492	0.00198
53.6	S	0.852	0.875	0.00127	–	–	–	0.825	0.821	0.00119
63.2	S	0.526	0.333	0.00055	–	–	–	0.469	0.265	0.00044
74.0	S	0.281	0.095	0.00016	–	–	–	0.199	0.048	0.00008
84.2	S	0.147	0.026	0.00005	–	–	–	–	–	–
94.9	S	0.056	0.004	0.00001	–	–	–	–	–	–

Table 9. Static-pressure coefficients for $i = -1.5$ degrees

Pressure Surface			Suction Surface		
Percent Chord	C_p	U_e (m/sec)	Percent Chord	C_p	U_e (m/sec)
1.0	0.462	24.12	1.0	-1.047	47.04
3.0	0.449	24.40	2.0	-0.306	37.57
4.0	0.451	24.36	3.0	-0.233	36.51
5.0	0.456	24.25	6.0	-0.268	37.02
6.0	0.460	24.16	12.2	-0.254	36.82
12.2	0.486	23.58	18.3	-0.186	35.81
18.3	0.512	22.98	24.5	-0.111	34.66
24.5	0.536	22.39	30.7	-0.014	33.12
30.7	0.554	21.97	36.8	0.064	31.81
36.8	0.574	21.47	43.0	0.117	30.90
43.0	0.590	21.06	49.2	0.169	29.97
49.2	0.603	20.71	55.3	0.228	28.90
55.3	0.610	20.53	61.5	0.275	27.99
61.5	0.618	20.33	67.7	0.311	27.30
67.7	0.614	20.43	73.8	0.333	26.86
73.8	0.608	20.58	80.0	0.354	26.43
82.5	0.589	21.08	82.5	0.355	26.41
85.4	0.579	21.32	88.3	0.372	26.06
88.3	0.566	21.66	94.5	0.369	26.12
91.3	0.544	22.20	97.3	0.360	26.29
94.5	0.513	22.94			
97.3	0.463	24.10			

Table 10. Shear layer thicknesses for $i = -1.5$ degrees

		Spline Fit					Falkner-Skan Solution		Fit of the Wall-Wake Equation			
Percent Chord	Region	U_e (m/sec)	δ (mm)	δ^* (mm)	θ (mm)	δ_3 (mm)	δ^* (mm)	θ (mm)	δ^* (mm)	θ (mm)	δ_3 (mm)	Δ (mm)
4.3	P	24.62	–	0.198(?)	0.134(?)	0.258(?)	0.128	0.049	–	–	–	–
9.7	P	24.44	0.49	0.113(?)	0.045(?)	0.077(?)	0.226	0.083	–	–	–	–
20.5	P	23.63	0.82	0.256	0.080	0.123	0.455	0.141	–	–	–	–
30.3	P	22.78	1.26	0.311	–	–	–	–	–	–	–	–
40.0	P	22.32	1.74	0.539	0.199	0.312	–	–	–	–	–	–
49.7	P	21.88	1.94	0.676	0.276	0.433	–	–	0.695	0.298	0.474	25.65
55.1	P	21.87	2.19	0.662	0.326	0.540	–	–	0.663	0.352	0.582	18.30
60.5	P	21.61	2.69	0.642	0.347	0.588	–	–	0.629	0.370	0.627	14.87
70.3	P	21.80	3.61	0.613	0.377	0.669	–	–	0.590	0.405	0.718	11.72
80.0	P	22.46	4.20	0.591	0.370	0.660	–	–	0.554	0.388	0.694	10.61
89.7	P	23.96	5.13	0.662	0.436	0.788	–	–	0.614	0.450	0.815	11.81
98.4	P	26.49	2.94	0.296	0.142	0.243	–	–	0.241	0.156	0.273	4.09
7.3	S	42.91	2.30	0.409	0.221	0.384	–	–	0.355	0.240	0.423	7.36
9.4	S	41.93	1.90	0.316	0.153	0.262	–	–	0.256	0.169	0.296	4.93
14.5	S	41.33	2.30	0.392	0.203	0.351	–	–	0.338	0.226	0.396	6.85
19.7	S	40.19	2.56	0.405	0.186	0.304	–	–	0.354	0.212	0.351	7.60
30.1	S	38.32	3.57	0.722	0.392	0.664	–	–	0.688	0.427	0.721	17.27
40.5	S	36.19	4.44	1.024	0.539	0.897	–	–	0.999	0.574	0.943	29.10
49.8	S	34.41	4.68	1.338	0.671	1.090	–	–	1.323	0.703	1.131	45.01
60.2	S	31.94	7.47	2.505	1.182	1.862	–	–	2.498	1.195	1.873	110.17
70.6	S	30.11	10.52	4.405	1.629	2.460	–	–	4.406	1.635	2.469	351.62
80.0	S	29.02	14.23	7.481	2.030	2.987	–	–	–	–	–	–
90.3	S	28.34	20.87	13.117	2.489	3.677	–	–	–	–	–	–
106.0	W	27.22	–	28.275	1.713	3.783	–	–	–	–	–	–
109.7	W	26.76	–	27.600	2.710	5.164	–	–	–	–	–	–
131.9	W	25.09	–	17.411	7.411	11.453	–	–	–	–	–	–

Table 11. Shear layer parameters for $i = -1.5$ degrees

		Spline Fit			Falkner-Skan Solution			Fit of the Wall-Wake Equation					
Percent Chord	Region	H_{12}	H_{32}	Re_θ	β	H_{12}	Re_θ	H_{12}	H_{32}	Re_θ	β_c	G	II
4.3	P	1.48(?)	1.93(?)	220(?)	-0.029	2.64	79	–	–	–	–	–	–
9.7	P	2.53(?)	1.72(?)	73(?)	-0.077	2.74	131	–	–	–	–	–	–
20.5	P	3.19	1.53	126	-0.175	3.23	214	–	–	–	–	–	–
30.3	P	–	–	–	–	–	–	–	–	–	–	–	–
40.0	P	2.71	1.57	296	–	–	–	–	–	–	–	–	–
49.8	P	2.45	1.57	402	–	–	–	2.33	1.59	434	0.61	21.10	4.97
55.1	P	2.03	1.65	476	–	–	–	1.89	1.66	513	0.31	12.96	2.52
60.5	P	1.85	1.69	500	–	–	–	1.70	1.69	533	0.15	9.73	1.75
70.3	P	1.63	1.77	548	–	–	–	1.46	1.77	588	-0.10	6.24	0.35
80.0	P	1.59	1.78	555	–	–	–	1.43	1.79	582	-0.24	5.72	0.03
89.7	P	1.52	1.81	696	–	–	–	1.36	1.81	718	-0.67	5.14	-0.08
98.4	P	2.09	1.71	251	–	–	–	1.55	1.76	275	-0.28	6.01	-0.55
7.3	S	1.85	1.74	631	–	–	–	1.48	1.76	688	-0.03	6.69	0.51
9.4	S	2.07	1.71	427	–	–	–	1.51	1.75	474	0.04	6.51	0.14
14.5	S	1.93	1.73	560	–	–	–	1.49	1.75	624	0.20	6.68	0.36
19.7	S	2.17	1.63	500	–	–	–	1.67	1.66	568	0.27	8.62	0.69
30.1	S	1.84	1.69	1003	–	–	–	1.61	1.69	1091	1.04	9.52	1.62
40.5	S	1.90	1.66	1301	–	–	–	1.74	1.64	1384	1.17	12.40	2.60
49.8	S	1.99	1.62	1540	–	–	–	1.88	1.61	1613	2.73	15.94	3.45
60.2	S	2.12	1.58	2517	–	–	–	2.09	1.57	2544	7.36	23.01	5.23
70.6	S	2.70	1.51	3270	–	–	–	2.69	1.51	3282	22.77	50.19	12.47
80.0	S	3.69	1.47	3927	–	–	–	–	–	–	–	–	–
90.3	S	5.27	1.48	4703	–	–	–	–	–	–	–	–	–
106.0	W	16.51	2.21	3109	–	–	–	–	–	–	–	–	–
109.7	W	10.18	1.90	4835	–	–	–	–	–	–	–	–	–
131.9	W	2.35	1.55	12396	–	–	–	–	–	–	–	–	–

Table 12. Boundary layer friction parameters for $i = -1.5$ degrees

		Spline Fit and Ludweig-Tillman Equation			Falkner-Skan Solution			Fit of the Wall-Wake Equation		
Percent Chord	Region	u_τ (m/sec)	τ_w (Pa)	C_f	u_τ (m/sec)	τ_w (Pa)	C_f	u_τ (m/sec)	τ_w (Pa)	C_f
4.3	P	–	–	–	0.924	1.028	0.00288	–	–	–
9.7	P	–	–	–	0.640	0.494	0.00145	–	–	–
20.5	P	–	–	–	0.311	0.117	0.00037	–	–	–
30.3	P	–	–	–	–	–	–	–	–	–
40.0	P	–	–	–	–	–	–	–	–	–
49.7	P	0.506	0.309	0.00107	–	–	–	0.593	0.423	0.00126
55.1	P	0.689	0.571	0.00198	–	–	–	0.793	0.757	0.00263
60.5	P	0.778	0.730	0.00260	–	–	–	0.913	1.004	0.00357
70.3	P	0.923	1.026	0.00358	–	–	–	1.098	1.451	0.00507
80.0	P	0.973	1.142	0.00376	–	–	–	1.172	1.656	0.00545
89.7	P	1.067	1.372	0.00397	–	–	–	1.245	1.734	0.00501
98.4	P	0.868	0.909	0.00215	–	–	–	1.557	2.923	0.00691
7.3	S	1.491	2.679	0.00241	–	–	–	2.072	5.172	0.00466
9.4	S	1.294	2.019	0.00191	–	–	–	2.180	5.729	0.00541
14.5	S	1.378	2.290	0.00222	–	–	–	2.038	5.004	0.00486
19.7	S	1.126	1.528	0.00157	–	–	–	1.870	4.214	0.00433
30.1	S	1.267	1.935	0.00219	–	–	–	1.526	2.808	0.00317
40.5	S	1.103	1.466	0.00186	–	–	–	1.243	1.860	0.00236
49.8	S	0.952	1.093	0.00153	–	–	–	1.012	1.234	0.00173
60.2	S	0.750	0.678	0.00110	–	–	–	0.724	0.632	0.00103
70.6	S	0.433	0.226	0.00041	–	–	–	0.377	0.172	0.00031
80.0	S	0.189	0.043	0.00008	–	–	–	–	–	–
90.3	S	0.052	0.003	0.00001	–	–	–	–	–	–

Table 13. Static-pressure coefficients for $i = -8.5$ degrees

Pressure Surface			Suction Surface		
Percent Chord	C_p	U_e (m/sec)	Percent Chord	C_p	U_e (m/sec)
1.0	-0.339	38.51	1.0	-0.177	36.10
3.0	0.151	30.66	2.0	-0.180	36.15
4.0	0.186	30.02	3.0	-0.235	36.98
5.0	0.194	29.89	6.0	-0.346	38.61
6.0	0.200	29.77	12.2	-0.389	39.23
12.2	0.284	28.15	18.3	-0.398	39.34
18.3	0.345	26.93	24.5	-0.362	38.85
24.5	0.386	26.07	30.7	-0.297	37.91
30.7	0.419	25.36	36.8	-0.230	36.92
36.8	0.451	24.65	43.0	-0.170	35.99
43.0	0.476	24.09	49.2	-0.114	35.12
49.2	0.494	23.68	55.3	-0.051	34.12
55.3	0.507	23.37	61.5	0.010	33.11
61.5	0.523	23.00	67.7	0.055	32.35
67.7	0.536	22.67	73.8	0.121	31.20
73.8	0.540	22.57	80.0	0.182	30.10
82.5	0.532	22.77	82.5	0.217	29.44
85.4	0.539	22.60	88.3	0.275	28.34
88.3	0.529	22.85	94.5	0.329	27.27
91.3	0.513	23.22	97.3	0.336	27.12
94.5	0.493	23.70			
97.3	0.453	24.60			

Table 14. Shear layer thicknesses for $i = -8.5$ degrees

		Spline Fit					Falkner-Skan Solution		Fit of the Wall-Wake Equation			
Percent Chord	Region	U_e (m/sec)	δ (mm)	δ^* (mm)	θ (mm)	δ_3 (mm)	δ^* (mm)	θ (mm)	δ^* (mm)	θ (mm)	δ_3 (mm)	Δ (mm)
4.3	P	30.36	0.72	–	–	–	–	–	–	–	–	–
9.7	P	29.26	0.65	0.170	0.048	0.075	–	–	0.092	0.047	0.080	1.37
20.5	P	26.93	1.62	0.285	0.126	0.214	–	–	0.246	0.151	0.263	4.52
30.3	P	25.48	2.38	0.428	0.232	0.402	–	–	0.391	0.255	0.446	7.56
40.0	P	24.30	3.47	0.605	0.357	0.620	–	–	0.574	0.379	0.661	11.81
49.7	P	23.54	4.20	0.740	0.453	0.788	–	–	0.710	0.473	0.823	15.11
60.5	P	22.99	4.89	0.881	0.563	0.986	–	–	0.851	0.581	1.081	18.34
70.3	P	22.64	5.53	0.954	0.610	1.066	–	–	0.926	0.629	1.097	20.24
80.0	P	22.76	6.29	1.018	0.683	1.211	–	–	0.987	0.701	1.244	21.02
89.7	P	23.53	6.78	1.031	0.708	1.266	–	–	0.986	0.717	1.282	20.72
98.4	P	24.76	4.99	0.607	0.392	0.701	–	–	0.554	0.400	0.716	10.37
10.4	S	39.97	–	0.272(?)	–	–	0.123	0.048	–	–	–	–
19.7	S	41.29	–	0.259(?)	–	–	0.249	0.094	–	–	–	–
30.1	S	41.06	0.87	0.312	0.097	0.145	0.406	0.132	–	–	–	–
40.5	S	39.89	1.47	0.539	0.112	0.145	–	–	–	–	–	–
49.8	S	38.54	1.54	0.803	0.140	0.193	–	–	–	–	–	–
55.0	S	37.73	1.83	0.831	0.144	0.187	–	–	–	–	–	–
60.2	S	36.41	2.46	0.588	0.291	0.492	–	–	0.556	0.328	0.552	14.48
70.6	S	34.54	3.73	0.602	0.346	0.601	–	–	0.564	0.379	0.660	12.34
80.0	S	32.78	4.47	0.828	0.469	0.807	–	–	0.797	0.511	0.872	19.32
90.3	S	29.94	6.32	1.421	0.802	1.353	–	–	1.392	0.846	1.413	39.16
97.6	S	27.46	8.68	2.521	1.240	2.007	–	–	2.503	1.285	2.056	97.60
106.0	W	25.60	–	4.376	2.647	4.412	–	–	–	–	–	–
109.7	W	25.31	–	3.939	2.566	4.328	–	–	–	–	–	–
131.9	W	24.71	–	2.674	2.131	3.844	–	–	–	–	–	–
152.6	W	23.95	–	2.317	1.946	3.590	–	–	–	–	–	–

Table 15. Shear layer parameters for $i = -8.5$ degrees

		Spline Fit			Falkner-Skan Solution			Fit of the Wall-Wake Equation					
Percent Chord	Region	H_{12}	H_{32}	Re_θ	β	H_{12}	Re_θ	H_{12}	H_{32}	Re_θ	β_c	G	II
4.3	P	–	–	–	–	–	–	–	–	–	–	–	–
9.7	P	3.52	1.56	94	–	–	–	1.93	1.70	92	0.10	7.24	-0.06
20.5	P	2.26	1.70	226	–	–	–	1.63	1.74	271	0.18	7.08	0.71
30.3	P	1.85	1.74	393	–	–	–	1.53	1.75	433	0.28	6.72	0.32
40.0	P	1.69	1.74	578	–	–	–	1.51	1.74	615	0.38	6.97	0.45
49.7	P	1.63	1.74	711	–	–	–	1.50	1.74	742	0.30	7.11	0.52
60.5	P	1.56	1.75	863	–	–	–	1.47	1.75	890	0.46	6.84	0.45
70.3	P	1.56	1.75	921	–	–	–	1.47	1.75	949	0.20	7.02	0.39
80.0	P	1.49	1.77	1037	–	–	–	1.41	1.77	1063	-0.12	6.17	0.23
89.7	P	1.46	1.79	1111	–	–	–	1.38	1.79	1124	-0.99	5.74	0.11
98.4	P	1.55	1.79	647	–	–	–	1.39	1.79	660	-0.63	5.21	-0.57
10.4	S	–	–	–	0.021	2.57	125	–	–	–	–	–	–
19.7	S	–	–	–	-0.029	2.64	247	–	–	–	–	–	–
30.1	S	3.22	1.49	266	-0.159	3.08	334	–	–	–	–	–	–
40.5	S	4.82	1.30	298	–	–	–	–	–	–	–	–	–
49.8	S	5.73	1.38	360	–	–	–	–	–	–	–	–	–
55.0	S	5.77	1.30	362	–	–	–	–	–	–	–	–	–
60.2	S	2.02	1.69	706	–	–	–	1.70	1.67	795	0.61	10.70	2.33
70.6	S	1.74	1.74	797	–	–	–	1.49	1.74	872	0.59	7.19	0.75
80.0	S	1.77	1.72	1025	–	–	–	1.56	1.71	1116	1.25	8.71	1.36
90.3	S	1.77	1.69	1601	–	–	–	1.65	1.67	1688	3.04	11.04	2.02
97.6	S	2.03	1.62	2270	–	–	–	1.95	1.60	2353	3.16	18.97	4.79
106.0	W	1.65	1.67	4517	–	–	–	–	–	–	–	–	–
109.7	W	1.54	1.69	4330	–	–	–	–	–	–	–	–	–
131.9	W	1.25	1.80	3510	–	–	–	–	–	–	–	–	–
152.6	W	1.19	1.84	3107	–	–	–	–	–	–	–	–	–

Table 16. Boundary layer friction parameters for $i = -8.5$ degrees

		Spline Fit and Ludweig-Tillman Equation			Falkner-Skan Solution			Fit of the Wall-Wake Equation		
Percent Chord	Region	u_τ (m/sec)	τ_w (Pa)	C_f	u_τ (m/sec)	τ_w (Pa)	C_f	u_τ (m/sec)	τ_w (Pa)	C_f
4.3	P	–	–	–	–	–	–	–	–	–
9.7	P	0.358	0.155	0.00030	–	–	–	1.953	4.596	0.00891
20.5	P	0.782	0.737	0.00169	–	–	–	1.464	2.582	0.00591
30.3	P	0.949	1.085	0.00277	–	–	–	1.318	2.093	0.00535
40.0	P	0.968	1.130	0.00318	–	–	–	1.180	1.678	0.00472
49.7	P	0.957	1.103	0.00330	–	–	–	1.107	1.475	0.00442
60.5	P	0.961	1.112	0.00349	–	–	–	1.066	1.371	0.00430
70.3	P	0.939	1.062	0.00344	–	–	–	1.036	1.294	0.00419
80.0	P	0.984	1.166	0.00374	–	–	–	1.068	1.376	0.00441
89.7	P	1.035	1.290	0.00387	–	–	–	1.120	1.512	0.00453
98.4	P	1.088	1.427	0.00386	–	–	–	1.322	2.107	0.00570
10.4	S	–	–	–	1.966	4.658	0.00506	–	–	–
19.7	S	–	–	–	1.343	2.174	0.00234	–	–	–
30.1	S	–	–	–	0.776	0.725	0.00083	–	–	–
40.5	S	–	–	–	–	–	–	–	–	–
49.8	S	–	–	–	–	–	–	–	–	–
55.0	S	–	–	–	–	–	–	–	–	–
60.2	S	1.093	1.441	0.00180	–	–	–	1.398	2.356	0.00295
70.6	S	1.273	1.953	0.00272	–	–	–	1.580	3.008	0.00419
80.0	S	1.145	1.579	0.00244	–	–	–	1.352	2.202	0.00340
90.3	S	0.980	1.157	0.00214	–	–	–	1.064	1.365	0.00253
97.6	S	0.700	0.590	0.00130	–	–	–	0.704	0.598	0.00132

Table 17. Wake parameters

			Spline Fit						
i (deg)	Percent Chord	Side of Wake	L_p, L_s (mm)	δ^* (mm)	θ (mm)	δ_3 (mm)	H_{12}	H_{32}	Re_θ
5.0	105.4	P	3.7	3.912	0.580	0.928	6.74	1.60	1125
5.0	105.4	S	22.8	23.318	3.308	5.058	7.05	1.53	6414
5.0	109.6	P	7.1	7.418	0.768	1.269	9.65	1.65	1490
5.0	109.6	S	20.9	21.801	3.513	5.477	6.21	1.56	6810
5.0	152.6	P	18.2	12.096	6.423	10.187	1.88	1.59	11210
5.0	152.6	S	24.7	16.983	9.039	14.380	1.88	1.59	15777
-1.5	106.0	P	7.8	8.682	0.109	0.624	79.51	5.72	198
-1.5	106.0	S	17.5	19.593	1.604	3.159	12.21	1.97	2911
-1.5	109.7	P	9.9	10.857	0.296	0.946	36.70	3.20	528
-1.5	109.7	S	14.9	16.744	2.414	4.218	6.94	1.75	4308
-1.5	131.9	P	9.7	8.426	3.529	5.436	2.39	1.54	5902
-1.5	131.9	S	10.0	8.989	3.882	6.017	2.32	1.55	6493
-8.5	106.0	P	2.7	2.125	1.329	2.259	1.60	1.70	2268
-8.5	106.0	S	3.4	2.251	1.318	2.153	1.71	1.63	2250
-8.5	109.7	P	3.2	1.911	1.274	2.175	1.50	1.71	2150
-8.5	109.7	S	3.7	2.028	1.292	2.153	1.57	1.67	2180
-8.5	131.9	P	4.6	1.338	1.064	1.918	1.26	1.80	1753
-8.5	131.9	S	4.6	1.336	1.067	1.926	1.25	1.81	1757
-8.5	152.6	P	4.8	1.075	0.902	1.663	1.19	1.84	1441
-8.5	152.6	S	5.4	1.242	1.044	1.927	1.19	1.85	1668

☆U.S. GOVERNMENT PRINTING OFFICE: 1989- 648162/ 00201

NASA
National Aeronautics and Space Administration

Report Documentation Page

1. Report No.	2. Government Accession No.	3. Recipient's Catalog No.
NASA CR-185118		

4. Title and Subtitle

The Measurement of Boundary Layers on a Compressor Blade in Cascade
Volume I—Experimental Technique, Analysis, and Results

5. Report Date
July 1989

6. Performing Organization Code

7. Author(s)
William C. Zierke and Steven Deutsch

8. Performing Organization Report No.
None

10. Work Unit No.
505-62-21

9. Performing Organization Name and Address
Pennsylvania State University
P.O. Box 30
State College, Pennsylvania 16801

11. Contract or Grant No.
NSG-3264

13. Type of Report and Period Covered
Contractor Report
Final

12. Sponsoring Agency Name and Address
National Aeronautics and Space Administration
Lewis Research Center
Cleveland, Ohio 44135-3191

14. Sponsoring Agency Code

15. Supplementary Notes
Project Manager, Nelson L. Sanger, Internal Fluid Mechanics Division, NASA Lewis Research Center.

16. Abstract

Measurements have been made of the boundary layers and wakes about a highly loaded, double-circular-arc compressor blade in cascade. These laser Doppler velocimetry measurements have yielded a very detailed and precise data base with which to test the application of viscous computational codes to turbomachinery. In order to test the computational codes at off-design conditions, the data have been acquired at a chord Reynolds number of 500,000 and at three incidence angles. Moreover, these measurements have supplied some physical insight into these very complex flows. Although some "natural" transition is evident, laminar boundary layers usually detach and subsequently reattach as either fully or intermittently turbulent boundary layers. These transitional separation "bubbles" play an important role in the development of most of the boundary layers and wakes measured in this cascade and the modeling or computing of these "bubbles" should prove to be the key aspect in computing the entire cascade flow field. In addition, the nonequilibrium turbulent boundary layers on these highly loaded blades always have some region of separation near the trailing edge of the suction surface. These separated flows, as well as the subsequent near wakes, show no similarity and should prove to be a challenging test for the viscous computational codes.

17. Key Words (Suggested by Author(s))	18. Distribution Statement
Boundary layer Cascade Compressor blades Laser velocimetry	Unclassified—Unlimited Subject Category 07

19. Security Classif. (of this report)	20. Security Classif. (of this page)	21. No of pages	22. Price*
Unclassified	Unclassified	223	A10

NASA FORM 1626 OCT 86

*For sale by the National Technical Information Service, Springfield, Virginia 22161